Continuation and Optimization of Gaits and Other Non-Smooth Orbits

Von der Fakultät Konstruktions-, Produktions- und Fahrzeugtechnik
der Universität Stuttgart zur Erlangung der Würde eines
Doktor-Ingenieurs (Dr.-Ing.) genehmigte Abhandlung

Vorgelegt von
Maximilian Raff
aus Herrenberg

Hauptberichter:	Prof. Dr. C. David Remy
Mitberichter:	Prof. Dr.-Ing. Christian Ebenbauer
	Assoc. Prof. Dr. Ludovic Righetti
Tag der mündlichen Prüfung:	02.07.2025

Institut für Adaptive Mechanische Systeme
der Universität Stuttgart

2025

To Emil

Preface

Most of the work in this monograph was carried out at the Institute for Nonlinear Mechanics, before I became the first Ph.D. graduate of the newly founded Institute for Adaptive Mechanical Systems. I am sincerely grateful to my doctoral advisor Prof. Dr. C. David Remy for his guidance and support throughout my research. Our discussions, his intuition, and his constructive ideas had a significant influence on this work.

I would like to thank Prof. Dr. Christian Ebenbauer and Prof. Dr. Ludovic Righetti for reviewing my manuscript and for their interest in my research. In addition to serving as co-examiners for my thesis, I especially appreciate their valuable feedback and advice during my Ph.D., during which they both served on my thesis advisory committee at the International Max Planck Research School for Intelligent Systems.

I am thankful to all my colleagues at the Institute for Nonlinear Mechanics for many insightful discussions and the joyful conference trips we shared. Special thanks go to Dr. Robin Bendfeld, Prof. Dr. Nelson Rosa, Dr. Giuseppe Capobianco, Fabia Bayer, and Dr. Simon Sailer for the often passionate debates about my work.

I am also deeply indebted to Iskandar Khemakhem, Nikola Velimirovic, Mohamed Abou-Taleb, and Yassine Karoui for reviewing parts of my manuscript. Further thanks go to all the students who wrote a thesis under my supervision or I had the pleasure to work with in building one-legged hoppers and passive-dynamic walkers.

I would also like to thank my new colleagues at the Institute of Adaptive Mechanical Systems and the Max–Planck–Institute in Stuttgart. Additional thanks go to the "nonlinear normal modes guys" from TU Munich for sharing their passion for exploiting natural dynamics.

Finally, I would like to thank my friends, family, and especially my dearest Lisa-Marie for their love and support.

Stuttgart, July 2025 *Maximilian Raff*

Contents

Abstract

Gaining insights into locomotion patterns in legged systems has broad implications, from advancing our understanding of animal movement to informing the design and control of prosthetics, exoskeletons, and legged robots. While nature often prioritizes minimizing metabolic cost through the body's morphology, engineers rely on optimization methods to accomplish similar efficiency. This dissertation presents mathematical tools that bridge these perspectives, systematically exploring the relationship between economical periodic motion patterns (gaits) and a system's morphology.

A primary focus in this dissertation is the generation of continuous families of gaits, considering that legged systems operate across a wide range of speeds and exhibit various locomotion patterns. A core insight underlying the generation of these gait families is that unactuated (passive) periodic motions in a dynamical system are inherently optimal from an energy perspective. Leveraging this, the dissertation formulates an inverse optimization problem in which passive motions are the globally optimal solutions in an optimal control framework, where the most efficient actuation is no actuation at all. In this context, this dissertation contributes to two key research areas.

The first is the analysis of periodic orbits in conservative hybrid dynamical systems, particularly in unforced systems that conserve energy or other quantities. In such systems, periodic orbits are shown to belong to families parameterized by their conserved quantities. The problem of identifying these motions is formulated as a parameterized root-finding problem, enabling their exploration through numerical continuation methods. Starting from trivial solutions, such as equilibria, families of periodic orbits can be constructed.

The second area of contribution comprises parameterized trajectory optimization problems that may also incorporate passive solutions. To extend the analysis of optimal and passive motions, a model homotopy is introduced to bridge energetically conservative and dissipative dynamics with a homotopy (dissipation) parameter. The first-order necessary conditions for optimality are also framed as a parameterized root-finding problem, allowing the use of continuation methods to generate families of optimal gaits. Crucially, the formulation of optimality conditions involves an infinite-dimensional actuation space, which is tackled using both direct and indirect methods, paired with a shooting approach. Extensions to the indirect method serve as a further contribution to the field of periodic trajectory optimization.

By generating and analyzing families of gaits, this dissertation offers a comprehensive view of energy economy in legged systems. Passive periodic motions are particularly valuable within these families, as they allow for an in-depth study of a system's inherent dynamics, independent of control influences, thereby revealing how morphology alone shapes gait efficiency.

Zusammenfassung

Ein tiefgehendes Verständnis von Bewegungsmustern in Systemen mit Beinen hat weitreichende Implikationen, von der Vertiefung unseres Wissens über Tierbewegungen bis hin zur Entwicklung und Steuerung von Prothesen, Exoskeletten und Laufrobotern. Während in der Natur die Minimierung des metabolischen Energieaufwands durch die Körpermorphologie im Vordergrund steht, greifen Ingenieure auf Optimierungsmethoden zurück, um eine ähnliche Effizienz zu erreichen. Diese Dissertation stellt mathematische Werkzeuge vor, die diese beiden Perspektiven verbinden, und untersucht systematisch die Beziehung zwischen ökonomischen periodischen Bewegungsmustern (Gangarten) und der Morphologie eines Systems.

Ein Schwerpunkt dieser Arbeit liegt auf der Generierung kontinuierlicher Familien von Gangarten, da Laufsysteme in einem breiten Geschwindigkeitsbereich operieren und verschiedene Bewegungsmuster aufweisen. Eine zentrale Erkenntnis für die Generierung solcher Gangfamilien ist, dass nicht aktuierte (passive) periodische Bewegungen von Natur aus energetisch optimal sind. Auf dieser Grundlage formuliert die Arbeit ein inverses Problem, bei dem passive Bewegungen als globale Lösungen eines Optimierungsproblems identifiziert werden. Somit ist die effizienteste Aktuation gerade kein Antrieb – die Bewegung erfolgt passiv. In diesem Kontext leistet diese Dissertation Beiträge zu zwei zentralen Forschungsbereichen.

Der erste Bereich umfasst die Analyse periodischer Orbits in konservativen hybriden dynamischen Systemen, insbesondere in nicht-aktuierten Systemen, die Energie oder andere Größen erhalten. In solchen Systemen gehören periodische Orbits zu Familien, die durch ihre Erhaltungsgrößen parametrisiert sind. Zur Identifikation dieser Orbits wird ein parametrisiertes Nullstellenproblem formuliert, das eine gezielte Exploration mittels numerischer Fortsetzungsmethoden ermöglicht. Ausgehend von trivialen Lösungen wie Gleichgewichtspunkten können so Familien periodischer Orbits konstruiert werden.

Der zweite Beitrag betrifft parametrisierte Trajektorienoptimierungsprobleme, die ebenfalls passive Lösungen enthalten können. Um die Analyse optimaler und passiver Bewegungen zu erweitern, wird eine Modell-Homotopie eingeführt, welche energetisch konservative und dissipative Dynamiken mit einem Homotopie- (Dissipations-)Parameter verbindet. Die notwendigen Optimalitätsbedingungen erster Ordnung werden ebenfalls als parametrisiertes Nullstellenproblem formuliert, sodass Fortsetzungsmethoden zur Generierung von Familien optimaler Gangarten genutzt werden können. Besonders relevant ist dabei, dass die Formulierung der Optimalitätsbedingungen einen unendlich-dimensionalen Aktuationsraum umfasst. Dieses Problem wird mit direkten und indirekten Methoden sowie einem Schießverfahren behandelt. Erweiterungen der indirekten Methode stellen einen weiteren Beitrag zum Bereich der periodischen Trajektorienoptimierung dar.

Durch die Generierung und Analyse von Gangfamilien bietet diese Arbeit einen umfassenden Einblick in die Energieeffizienz von Laufsystemen. Passive periodische Bewegungen sind innerhalb dieser Familien besonders wertvoll, da sie eine tiefgehende Untersuchung der inhärenten Dynamik eines Systems ermöglichen, unabhängig vom Antrieb. Dies zeigt, wie allein die Morphologie die Effizienz der Gangart bestimmt.

List of Acronyms

1-D / 2-D	one-dimensional / two-dimensional
ODE	ordinary differential equation
DAE	differential algebraic equation
BVP	boundary value problem
HDS	hybrid dynamical system
cHDS	conservative hybrid dynamical system
tb	time-based
eb	event-based
ss	single shooting
ms	multiple shooting
ECM	energetically conservative model
DoF	degrees of freedom
CoR	coefficient of restitution
SLIP	spring-loaded inverted pendulum
PCC	predictor-corrector continuation
SB	simple bifurcation
SVD	singular value decomposition
TP	turning point
EQ	equilibria
NLP	nonlinear program
ECO	equality-constrained optimization
TO	trajectory optimization
LICQ	linear independence constraint qualification

Chapter 1

Introduction

C'est même des hypothèses simples qu'il faut le plus se défier, parce que ce sont celles qui ont le plus de chances de passer inaperçues.[1]
It is even the simplest hypotheses that one must be most wary of, because these are the ones that have the highest chances of passing unnoticed.

—*Henri Poincaré*

A fundamental challenge for both animals and humans when traveling long distances is the limited energy available for movement. Observations in nature reveal that animals with similar body structures, such as quadrupeds (e.g., dogs, horses) and bipeds (e.g., humans), share common periodic motion patterns, like walking and running. Studies indicate that these gaits are closely linked to energy expenditure (metabolic cost) [4, 59, 64], suggesting that locomotion is inherently optimized for energetic economy.

A prevailing hypothesis posits that gait similarities among animals with the same number of legs arise primarily from their structural morphology rather than muscle-driven actuation. This hypothesis extends to legged robotic systems, where locomotion endurance is similarly limited by power supply. In robotic systems, optimizing energy consumption through mathematical modeling often results in gaits that exploit the robot's morphology, mirroring biological efficiency. Unlike in living organisms, however, robotic actuation can be isolated, enabling a focused study of unactuated (passive) dynamics alone.

Building on these insights, this dissertation leverages continuation and optimization techniques to generate diverse families of periodic orbits in

[1]This quote is taken from the book by Poincaré [106].

impulsive dynamical systems, particularly in legged locomotion. A key emphasis is placed on understanding and utilizing passive gaits, as they are essential for economic movement.

To rigorously analyze the role of actuation in dynamical systems, this work classifies energy transfer into four categories, as illustrated in Fig. 1.1. Depending on whether energy is transferred through the environment or the actuators, a system can be categorized as (1) passive-conservative, (2) passive-open, (3) actuated-closed, or (4) actuated-open.

A useful analogy for this classification is a child on a swing, where the child and swing form a dynamical system. If the child remains still, the system is passive. External influences such as wind, air resistance, friction within the swing's suspension, or a parent's push determine whether the system is closed (1) or open (2). In theory, without these external influences, the system remains energetically conservative. If the child actively rocks back and forth to change the swing's frequency and amplitude, the system becomes actuated yet remains closed/lossless (3). Finally, if external forces act on the moving child, the system is classified actuated-open (4).

This classification provides a structured framework for analyzing energy flow in dynamical systems, offering insights that are particularly relevant to the study of passive and actuated gaits in legged locomotion.

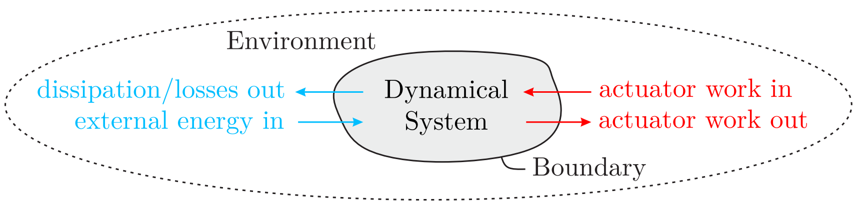

energy transfer		dynamics classification	
environment	actuators		
$\cancel{\rightleftarrows}$	$\cancel{\rightleftarrows}$	(passive) **conservative**	(1)
$\rightleftarrows$	$\cancel{\rightleftarrows}$	**passive** (open)	(2)
$\cancel{\rightleftarrows}$	$\rightleftarrows$	(actuated) **closed/lossless**	(3)
$\rightleftarrows$	$\rightleftarrows$	**actuated** (open)	(4)

Figure 1.1: Illustration of system dynamics as a thermodynamic model, classified into four categories based on energy transfer via the environment (blue) and actuator work (red).

1.1 Motivation

Improving the performance of prosthetic devices, exoskeletons, and legged robots requires a deeper understanding of how mechanical design influences motion. For instance, integrating springs into systems such as Anybotics' *ANYmal* [65] or the *emPOWER* bionic ankle [58] has been shown to support the emergence of economical gait patterns [127, 139, 141]. This approach draws inspiration from biological systems, where muscles, tendons, and ligaments naturally store and release energy during movement [114]. Given a particular morphology, the fundamental question is how to systematically identify and exploit the economical motions that the design inherently enables.

Fundamental Insights from Simplified Models

To uncover the core principles of locomotion, both biomechanics and robotics frequently rely on simplified models [5]. Classic examples such as the spring-loaded inverted pendulum (SLIP) [16] and the compass-gait walker [44] aim to capture key features of gait generation without the complexity of detailed multi-body models. Beyond their explanatory value, these models also serve a practical role in high-level motion planning and control [69]. This has led to the development of the template–anchor framework [41], where insights from simple models (templates) inform the behavior, design and control of more complex systems (anchors).

Yet, drawing systematic and quantitative links between simplified and full-order models remains a major challenge. This dissertation addresses this by developing continuation- and optimization-based tools that make these connections more accessible and interpretable.

The Role of Optimization

Optimization is a crucial tool for generating feasible motions in dynamical systems [135]. Beyond that, well-posed optimization problems can reveal meaningful relationships between design and motion, such as how gait economy in walking and running changes with speed in a monoped [126].

However, most existing approaches focus on isolated optimization problems that depend heavily on well-chosen initial guesses and offer little understanding of the broader solution landscape. This is especially limiting in legged locomotion, where problems are nonlinear, high-dimensional, and discontinuous due to impacts. To overcome this, the methods developed in this dissertation trace continuous families of optimal periodic gaits, providing a structured way to explore how behaviors vary with system parameters and offering a clearer picture of how morphology shapes periodic gaits.

1.2 Literature Overview

This section provides a concise overview of the literature relevant to this dissertation. It is structured into three main areas: natural dynamics in legged locomotion (Section 1.2.1), gait libraries (Section 1.2.2), and modeling and optimization techniques (Section 1.2.3).

1.2.1 Natural Dynamics in Legged Locomotion

Natural dynamics in legged systems refer to motion patterns that emerge directly from the mechanical design (morphology) and passive physical properties of the system, such as elastic and gravitational potential, with no or only minimal energy input from actuators. In particular, while elastic behavior can be shaped through the integration of springs, as introduced in Section 1.1, gravitational potential fundamentally contributes to the operation of a class of systems known as passive dynamic walkers.

Principles of Passive Dynamic Walkers

Passive dynamic walkers are legged robots capable of walking downhill without any power supply [28, 92, 93]. Driven purely by gravity, these systems range from simple compass gait robots (Fig. 1.2a) to more advanced prototypes with articulated knees and arms (Fig. 1.2b). Adding springs to the legs further enables these systems to perform running gaits (Fig. 1.2c). These prototypes already demonstrate how hardware design alone can

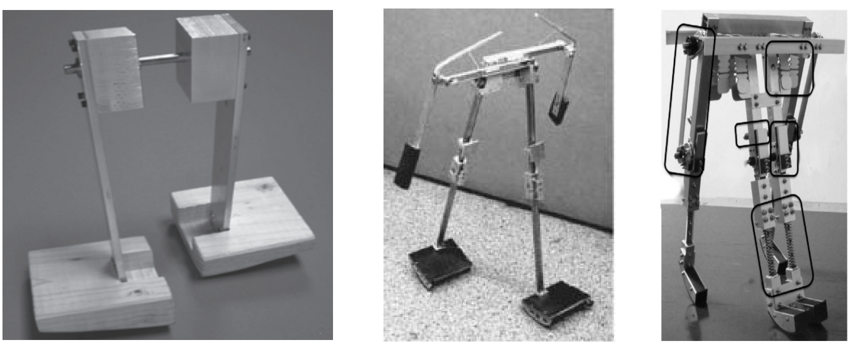

(a) (b) (c)

Figure 1.2: Three passive dynamic walkers: (a) A minimalist compass gait robot [134], (b) a passive dynamic walker with knees and arms [138], and (c) a running robot with springy legs [102].

produce a wide variety of gaits without any form of actuation. According to Figure 1.1, these systems are passive-open.

Although these robots do not require any motor actuation, their ability to walk successfully without falling is limited to a narrow range of initial conditions and slope inclinations. Within this range of attraction, however, they converge to a stable periodic motion, known as a limit cycle.

Characterization of Periodic Gaits

The number and configuration of legs, joints, and elastic components in a legged system allows for a wide variety of locomotion patterns. As a result, biologists have developed different methods to characterize and classify the repetitive motions observed in nature, such as walking and running [37, 59]. A complete cycle of such motion is commonly referred to as a *stride*. One of the most straightforward ways to classify gaits is by analyzing the *footfall pattern*, which describes the sequence in which the feet contact and leave the ground during a stride. Additional classification methods consider various metrics, including ground reaction force profiles [3], stride symmetry [60], and the exchange of energy throughout a stride [22].

Energy Economy in Locomotion

Another notable observation in biology is that animals with a similar morphology often share the same set of gaits. For example, dogs and horses both exhibit walking, trotting, and galloping. This similarity is closely linked to energy efficiency, as it is more economical to adapt the gait to specific operating conditions, such as changes in terrain or speed [64, 77, 128]. In particular, the pioneering work of Hoyt and Taylor [64] demonstrated that horses expend the least energy when walking at low speeds, trotting at moderate speeds, and galloping at high speeds. In these biological systems, energy consumption is measured by the metabolic cost. A low metabolic cost indicates reduced muscular effort and, consequently, greater exploitation of the system's natural dynamics.

A similar relationship between gait and energy economy has been observed in legged robots powered by electric motors. In these systems, energy-optimal gaits emerge by minimizing motor effort, and the choice of gait is likewise dependent on speed [40, 126]. Typical cost functions in robotic systems include copper losses in the motor, positive mechanical actuator work, and positive electrical work [112].

To facilitate comparisons of energy economy between biological and robotic systems, the cost of transport is often used [80]. This metric normalizes energy expenditure by the system's weight and the distance traveled.

Relevance to This Dissertation

In this dissertation, passive dynamic walkers and their passive gaits provide an important starting point for the systematic exploration and generation of energy-optimal gaits in actuated legged systems. This work emphasizes periodicity as a core property in the definition of gaits. Periodicity is especially useful in mathematical modeling because it significantly reduces the space of possible motions. Instead of analyzing an arbitrarily long time horizon with a somewhat repetitive (quasiperiodic) motion sequence, a periodic gait can simply be extended over the same time horizon.

1.2.2 Constructing Libraries of Gaits

Legged systems typically operate across a continuous range of conditions, which has led to significant interest in generating libraries of gaits for legged robots [85, 86, 111, 116, 137]. These conditions may reflect changes in the environment, such as slope or terrain, or variations in the robot's operating point, such as forward speed or step length.

To better understand and highlight the underlying natural dynamics within these actuated gait libraries, continuous families of passive gaits have received particular attention (Fig. 1.3). Extending the SLIP model,

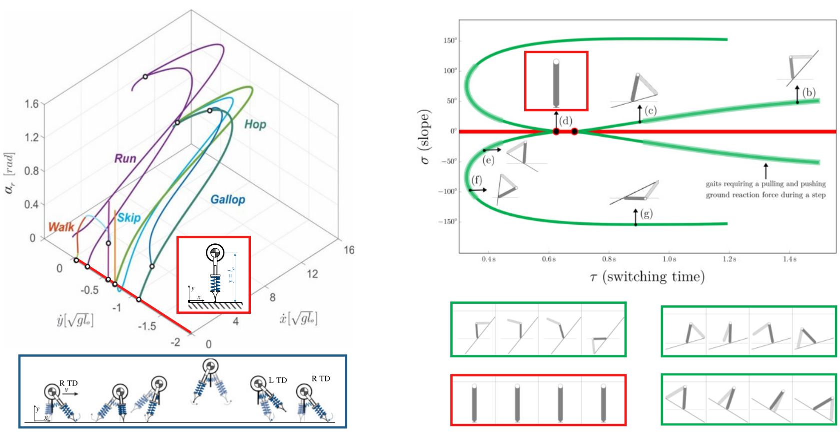

(a) (b)

Figure 1.3: Connected families of passive gaits originating from (a) oscillation in place and (b) standing still, both shown in red. Adapted from [42] (SLIP-like biped) and [116] (compass-gait walker).

Gan et al. [42] demonstrated that a bipedal robot can be designed to conserve energy. The authors further showed empirically that its periodic gaits continuously connect from an in-place oscillation to all common bipedal gaits, including walking, hopping, running, skipping, and galloping (Fig. 1.3a). Likewise, the work of Rosa and Lynch [115] demonstrates that continuous gait families of passive dynamic walkers on a slope can be systematically traced from a standstill pose (Fig. 1.3b).

Both works use numerical continuation methods to construct these families, where each point on the curve corresponds to a passive gait.

Numerical Continuation Methods

Conditions such as periodicity, operating points, and optimality define the motion within a dynamical system. Mathematically, these conditions yield a set of implicit constraints, leading to a root-finding problem. When this problem has a parameterized solution or a non-trivial null-space, numerical continuation methods can be used to generate the solution space of gaits [6]. These methods systematically construct additional solutions in the neighborhood of an initial solution point. They can be generally categorized into two types:

- Predictor-corrector continuation (PCC) methods rely on Newton-type solvers, which enjoy strong local convergence when tracing implicitly defined 1-D solution sets (curves). However, they require sufficient differentiability of the root-finding problem.

- Piecewise linear continuation (PLC) methods approximately follow the exact solution curves through a polygonal path relative to an underlying triangulation. They naturally extend to higher-dimensional solution spaces and do not rely on smoothness assumptions. However, detecting bifurcation points and singularities within the problem is more complex.

Relevance to This Dissertation

Particularly, the work of Gan et al. [42] highlights the explanatory power of energetically conservative models for passive gaits. Hence, this dissertation further explores the apparent connectedness of periodic orbits (gaits) in conservative dynamics. Additionally, the missing connection between passive and optimally actuated gait libraries is addressed through the use of PCC methods. PCC methods are employed in this monograph, as they prove particularly fast and robust in tracing 1-D gait families, including bifurcations at which different families meet.

1.2.3 Modeling and Optimization of Legged Systems

The mathematical study of legged locomotion requires several fundamental decisions in both modeling and optimization.

A primary modeling choice concerns whether components of the robot are treated as *compliant* or *rigid*. Since the main body and limbs are typically built from stiff materials, it is common to model them as rigid. This simplifies the equations of motion into a low-dimensional ordinary differential equation (ODE), which is easier to interpret and solve using standard numerical integrators. However, modeling the feet is more complex due to the sudden changes in velocity that occur when they contact the ground. Here, both rigid and compliant approaches have distinct advantages and drawbacks.

Soft vs. Hard Contacts

Compliant models capture more accurately the physical interactions at the foot-ground interface, especially when the feet are made from softer materials to enhance friction and reduce slippage [122]. This approach maintains the use of a single ODE for the entire system and enables gradient-based optimization, provided the contact forces are differentiable [110]. However, compliant models introduce stiff dynamics, which require careful numerical handling. This typically involves implicit integration methods with adaptive time-stepping, significantly increasing the computational effort for both simulation and optimization. To further simplify optimization, some approaches soften contact dynamics artificially, prioritizing differentiability over physical accuracy [45, 94, 99].

In contrast, hard contact models treat foot impacts as instantaneous, neglecting small deformations. While this avoids the stiffness issues of compliant models, it introduces discontinuities in velocity, making the system non-smooth and unsuitable for standard ODE formulations. These dynamics are instead modeled using either measure differential equations (MDEs) [19, 104] or hybrid dynamical systems (HDSs) [47, 52].

Measure Differential Equations vs. Hybrid Dynamical Systems

Measure differential equations generalize the concept of ODEs to include impulsive forces and set-valued dynamics, which are necessary to model rigid impacts.

In contrast, *hybrid dynamical systems* explicitly separate continuous and discrete behaviors. The system evolves continuously during each phase (e.g., when a leg is in contact or in the air), and discrete transitions occur at specific times due to impacts or liftoffs.

Neither MDEs nor HDSs can be solved analytically in general. For MDEs, time-stepping methods provide a robust numerical approach [18, 95]. Hybrid systems, on the other hand, are often simulated using event-driven ODE solvers, which can struggle with complex behavior such as Zeno behavior, i.e., infinite impacts in finite time [9]. Nevertheless, hybrid modeling offers greater flexibility in system design and control, particularly when such complexities are absent [136].

Collocation vs. Shooting Methods

Regardless of the chosen modeling approach, finding periodic orbits in these typically non-smooth systems involves a search over a finite time horizon, where periodicity is enforced by matching the initial and final states. Two common approaches are:

- *Shooting methods* [34], which evolve states through numerical integration from given initial conditions. These methods support variable time steps and adaptive error control, improving dynamic accuracy.

- *Collocation methods* [72], which define system states and inputs on a fixed time grid. They require iterative mesh refinement to achieve similar accuracy, increasing computational cost (Section 4.6.9 [14]).

A key advantage of collocation is its flexibility in handling path and inequality constraints, making it especially suitable for systems modeled with MDEs. In this context, complementarity conditions can encode set-valued contact forces, enabling so-called contact-invariant or contact-implicit collocation methods [91, 109, 132, 135]. These are particularly useful when the footfall pattern is not known in advance, as they can adaptively resolve the sequence of contact events during optimization. A drawback of this approach is slow convergence, largely due to the lack of regularity introduced by complementarity conditions. In contrast, when using hybrid dynamical models with a known footfall pattern, both collocation and shooting methods can be applied effectively. The known contact sequence ensures differentiability and improves convergence in root-finding and optimization problems.

Direct vs. Indirect Methods in Trajectory Optimization

The optimization methods discussed so far fall under the category of *direct* trajectory optimization. In this approach, the system is first discretized in time, transforming the continuous problem into a finite-dimensional nonlinear program (NLP). This NLP is then solved numerically to find an approximate local optimum. Most results in periodic optimization of

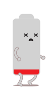

legged robots are based on the direct approach [135], due to its considerable flexibility in terms of implementation. As a drawback, the accuracy of the resulting optimal trajectory depends on the chosen parameterization of the input space, potentially missing better solutions that exist outside this discretization. This creates a trade-off between accuracy and problem size, while the true global optimum may remain unattainable due to the constraints imposed by the parameterization [62, 84].

In contrast, indirect methods work with the continuous-time problem before applying any discretization. For ODEs, the most comprehensive framework is Pontryagin's Maximum Principle [107], which provides first-order optimality conditions as a boundary value problem by implicitly defining the control inputs as functions of the system's states and additional costates. This approach often yields more accurate solutions, especially when using shooting methods with variable step-size integrators. While the introduction of costates helps formalize the first-order necessary conditions, it does not significantly increase the dimensionality of the optimization problem. However, these methods typically suffer from small regions of convergence and are less suitable for problems with path constraints [14, 34]. Although indirect methods in periodic trajectory optimization have been used in fields such as aerospace [46, 130], and in hybrid systems for chemical processes [61] and legged robots [23], they have not achieved the same level of popularity as direct methods.

Relevance to This Dissertation

Despite its limitations, hybrid dynamical modeling is well-suited for synthesizing periodic gaits in legged systems, where a finite number of impacts typically occur. When the footfall pattern is known, many challenges associated with hybrid systems become manageable.

Moreover, simplified hybrid models sometimes allow for analytical solutions, making them especially valuable in theoretical investigations. Therefore, this dissertation adopts hybrid dynamics as the preferred modeling approach. It offers the flexibility to use variable step-size shooting methods and provides the necessary regularity for tracing families of periodic gaits using PCC methods.

In the context of periodic trajectory optimization, and particularly the generation of optimal gait families, there remains considerable room for advancement in both direct and indirect approaches using shooting methods. In particular, the convergence issues associated with indirect shooting can be mitigated through the use of PCC methods and their strong local convergence properties.

1.3 Structure and Main Contributions

This section outlines the structure of the thesis and details the contributions made. The content of the publications [1, 2, 3, 4] constitutes the main body and key contributions of the dissertation. The contributions presented in these publications are visually summarized in Fig. 1.4 and elaborated systematically through the following chapter overview:

Chapter 2, Mathematical Tools: This chapter establishes the mathematical groundwork for subsequent developments. It introduces essential concepts from continuation methods and optimization theory. Drawing from existing literature, these preliminaries are reinterpreted through a geometric lens to support the methodologies introduced in later chapters.

Chapter 3, Recurrent Hybrid Dynamical Systems: This chapter introduces a general framework for time-variant recurrent hybrid dynamical systems (HDSs), enabling the formal modeling of non-smooth dynamics through a combination of continuous and discrete-time evolutions. It further provides definitions of recurrent and periodic trajectories (orbits) within these systems. A key innovation of this chapter is the comparison between time-based and event-based shooting approaches, assessing the challenges involved in computing orbits, as detailed in [3].

Chapter 4, Conservative Hybrid Dynamical Systems: The recurrent HDSs introduced before in Chapter 3 are refined to autonomous (time-invariant) dynamics. Furthermore, flow-invariant functions (first integrals) are investigated, which render the HDS conservative. The main objective of this chapter is to provide a systematic understanding of periodic orbits in a broader class of conservative hybrid dynamical systems (cHDSs), offering a robust framework and methodology for their analysis and generation. The theoretical advancements, fully derived from [3], comprise three principal contributions:

- Introduction of a hybrid first integral to characterize cHDSs.
- Proof of the local existence of families of periodic orbits in cHDSs based on the construction of a Poincaré map (Theorem 4.2.1).
- Extension of the concept of *normal* conservative orbits from Sepulchre and MacKay [124] to HDS.

Additionally, Section 4.3 contributes more on the practical side:

- Modification of the Poincaré map to introduce a (scalar) dissipation parameter, thereby regularizing its conservation-induced state dependencies.
- Extension of Theorem 1 in [124] and Lemma 6 in [97] to cHDS, proving that fixed points of the regularized Poincaré map are equivalent to the solution space of periodic orbits in the conservative HDS (Theorem 4.3.1).

Introducing a dissipation parameter enables the application of pseudo-arclength continuation methods to systematically trace continuous families of connected orbits. The chapter concludes with implementation details on the time-based shooting method used to explore periodic orbits, emphasizing its advantages over the state-based approach.

Chapter 5, Energetically Conservative Models: In this dissertation, a particularly important first integral is the energy of a system. Hence, this chapter focuses on energy conservation in mechanical systems with impulses. Section 5.1, based on [1], outlines the construction of energetically conservative models (ECMs). It addresses conditions for energy conservation in systems involving plastic collisions, common in legged locomotion. A scaling procedure for masses and inertias is introduced to ensure energy conservation during collisions. This process is demonstrated in Section 5.1.3 using a spring-loaded hopper, offering a more systematic derivation than that proposed by [43]. The chapter also includes a second contribution, based on [3], applying the time-based shooting method to four ECMs with non-smooth dynamics. It shows how equilibria can be leveraged to construct families of conservative orbits using continuation techniques.

Chapter 6, Optimization in Hybrid Dynamics: Building on the time-based framework, Section 6.1 formulates a general periodic trajectory optimization (TO) problem for HDSs. The contributions include:

- Definition of the class of economic cost functions (Section 6.1.1).
- Definition of passive-optimal solutions/gaits (Section 6.1.2), where periodic orbits with zero actuation constitute global minimizers under economic cost functions.

To address periodic TO problems in HDSs with a single hybrid phase, both direct and indirect numerical methods are introduced in Section 6.2, along with their associated first-order necessary conditions.

Building upon the work in [4], this chapter advances the field through:

- Extension of necessary conditions within the indirect approach to a broader class of cost functions and operating scenarios, addressing both legged and other hybrid robotic systems.

- Systematic reconstruction of Lagrange multipliers at passive-optimal solutions for both solution approaches.

The chapter concludes (Section 6.3) with remarks on conservation in indirect methods and an extension of direct methods to multi-phase HDSs.

Chapter 7, Parameterized Periodic Trajectory Optimization: This chapter integrates the continuation and optimization techniques developed previously to generate 1-D families of optimal periodic orbits. By formulating a parameterized periodic TO problem, this family is derived from parameterized zero-functions that encode first-order optimality conditions of these problems, using both direct and indirect methods (Section 7.1). Major contributions within these parameterized problems provide Section 7.2 and 7.3:

- Introduction of the *model homotopy* approach from [2], which systematically transitions from passive-optimal gaits of actuated but lossless models to locally optimal gaits in actuated-open systems with dissipation. This method provides a powerful alternative to traditional, labor-intensive optimization strategies by exploiting the topological properties of legged systems, where passive gaits serve as globally optimal seeds.

- Systematic expansion of optimal gait libraries from passive-optimal gaits of the compass-gait walker, using both direct and indirect methods. Particular emphasis is placed on the advantages of indirect shooting combined with variable step-size integrators, as demonstrated in [4].

Section 7.4 concludes with a comparative summary of Sections 7.2 and 7.3, highlighting their main differences.

Chapter 8, Conclusions and Outlook: The final chapter provides a concise summary of the dissertation's core contributions. It also discusses current limitations and outlines potential directions for future research, particularly regarding the extension of continuation and optimization techniques in hybrid dynamical systems.

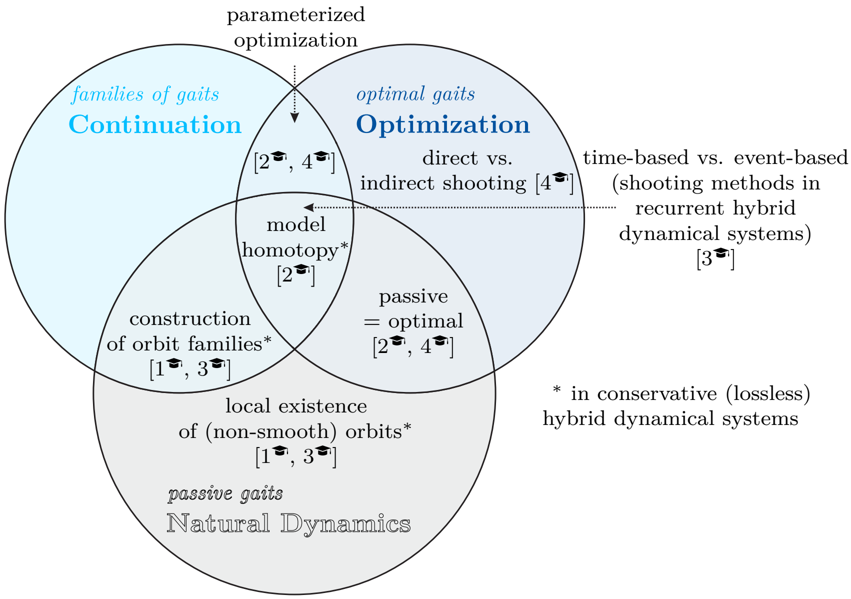

Figure 1.4: Visualization of the three overlapping main topics explored in this thesis: continuation, optimization, and natural dynamics. The primary contributions of this dissertation are emphasized in regular black font.

1.3.1 Supplementary Research Contributions

The following publications and preprints were (co)-authored during the course of my doctoral studies. While they are thematically related and influential to the research presented in this thesis, they do not directly contribute to its primary objectives or findings:

[110] **M. Raff**, C. D. Remy. *"Hard vs. soft contacts in trajectory optimization of legged robots: An example with a compliant rubber foot."* ICRA 2023 Workshop on Embracing Contacts. 2023.

[117] N. Rosa, B. Katamish, **M. Raff**, C. D. Remy. *"An approach for generating families of energetically optimal gaits from passive dynamic walking gaits."* IEEE/RSJ International Conference on Intelligent Robots and Systems (IROS). 2023.

[120] A. Sachtler. D. Calzolari, **M. Raff**, A. Schmidt, Y. P. Wotte, C. D. Santina, C. D. Remy, A. Albu-Schäffer. *"Swing-Up of a Weakly Actuated Double Pendulum via Nonlinear Normal Modes."* European Control Conference (ECC). 2024.

[36] H. Ebel, J. van Delden, T. Lüddecke, A. Borse, R. Gulakala, M. Stoffel, M. Yadav, M. Stender, L. Schindler, K. M. de Payrebrune, **M. Raff**, C. D. Remy, B. Röder, P. Eberhard. *"Data Publishing in Mechanics and Dynamics: Challenges, Guidelines, and Examples from Engineering Design."* Data-Centric Engineering. 2025.

[30] K. M. de Payrebrune, K. Flaßkamp, T. Ströhla, T. Sattel, D. Bestle, B. Röder, P. Eberhard, S. Peitz, M. Stoffel, G. Rutwik, B. Aditya, M. Wohlleben, W. Sextro, **M. Raff**, C. D. Remy, M. Yadav, M. Stender, J. van Delden, T. Lüddecke, S. C. Langer, J. Schultz, C. Blech. *"The impact of AI on engineering design procedures for dynamical systems."* Technische Mechanik. 2025.

[1] M. Abou-Taleb, **M. Raff**, K. Flaßkamp, C. D. Remy. *"Koopman Based Trajectory Optimization with Mixed Boundaries."* 7th Annual Learning for Dynamics & Control Conference (L4DC). 2025.

[74] I. Khemakhem, D. Tschemernjak, **M. Raff**, C. D. Remy. *"How Leg Stiffness Affects Energy Economy in Hopping."* The 12th International Symposium on Adaptive Motion of Animals and Machines (AMAM2025) and 2nd LokoAssist Symposium 2025.

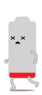

Chapter 2

Mathematical Tools

> The rules that describe nature seem to be mathematical.... Why nature is mathematical is, again, a mystery.[1]
>
> —*Richard Feynman*

This chapter presents the mathematical tools required for the methodologies developed in the subsequent chapters. After briefly explaining the notation used in this monograph in Section 2.1, Section 2.2 introduces predictor-corrector continuation (PCC) methods, and Section 2.3 derives the necessary conditions for a class of optimization problems.

2.1 Notation and Preliminaries

In this dissertation, scalars are represented using a standard math font such as α, a or A. Vectors, on the other hand, are typically denoted by lowercase bold symbols (e.g., $\boldsymbol{a}$), while matrices are represented by uppercase bold symbols (e.g., $\boldsymbol{A}$). With $\mathbb{R}^n \widehat{=} \mathbb{R}^{n \times 1}$ denoting the n-dimensional space of column vectors, a vector $\boldsymbol{a} \in \mathbb{R}^n$ is a column vector. Let $(\bullet)^{\mathrm{T}}$ denote the matrix transpose, so that $\boldsymbol{a}^{\mathrm{T}}$ is a row vector. A vector-valued function is defined as $\boldsymbol{a} : \mathbb{R}^n \to \mathbb{R}^m$, where n and m are positive integers, i.e., $n, m \in \mathbb{N}$. If $\boldsymbol{a}(\boldsymbol{x})$ is differentiable at a point $\boldsymbol{x}^* \in \mathbb{R}^n$, its Jacobian is expressed as $D\boldsymbol{a}(\boldsymbol{x}^*) = {}^{\partial \boldsymbol{a}}/_{\partial \boldsymbol{x}}\big|_{\boldsymbol{x}=\boldsymbol{x}^*}$, where D abbreviates the differential operator. The Jacobian $D\boldsymbol{a}$ is considered *regular* at $\boldsymbol{x}^*$ if $D\boldsymbol{a}(\boldsymbol{x}^*) \in \mathbb{R}^{n \times m}$ has maximum rank.

Throughout this monograph, implicit constraints of the form $\boldsymbol{a}(\boldsymbol{x}) = \boldsymbol{0}$ often define subsets in $\mathbb{R}^n$ for continuation and optimization problems.

[1] This quote is an excerpt from the first chapter of Feynman [39].

When $n > m$, the constraint $\boldsymbol{a}(\boldsymbol{x}) = \boldsymbol{0}$ defines the surface $\mathcal{S} = \boldsymbol{a}^{-1}(\boldsymbol{0})$, where a point $\boldsymbol{x}^* \in \mathcal{S}$ is termed a *regular point* if $D\boldsymbol{a}(\boldsymbol{x}^*)$ is regular, i.e., $\operatorname{rank}(D\boldsymbol{a}(\boldsymbol{x}^*)) = m$. If every point $\boldsymbol{x} \in \mathcal{S}$ is regular, the surface $\mathcal{S}$ forms a submanifold of codimension $n - m$. Note further that the tangent space $T_{\boldsymbol{x}^*}\mathcal{S}$ at a regular point $\boldsymbol{x}^*$ is equivalent to the kernel $\ker(D\boldsymbol{a}(\boldsymbol{x}^*))$ (cf. Section 11.1 in [89]).

To reduce notational overhead, the argument of a function is omitted when it is clear from context. For instance, α is used in place of $\alpha(s)$. Alternatively, the shorthand notation $\alpha_s = \alpha(s)$ is used when clarification is needed. Differentiation with respect to a scalar variable, such as ${}^{\mathrm{d}\alpha}/_{\mathrm{d}s}$, is often abbreviated as $\dot{\alpha}$ or α'. The composition of two functions $a(x)$ and $b(x)$ is defined as $a(b(x)) = (a \circ b)(x) = a \circ b(x)$, where $\circ$ denotes the composition operator.

2.2 Numerical Continuation

In contrast to the general concept of tracing implicitly defined surfaces (known as continuation) as outlined in Section 1.2.2, this work focuses specifically on PCC methods for tracing one-dimensional paths (curves). The basic concepts of these PCC methods are outlined below, primarily based on the introductory book on numerical continuation methods by Allgower and Georg [6].

2.2.1 Predictor-Corrector Methods

Consider an implicit constraint $\boldsymbol{r}(\boldsymbol{\nu}) = \boldsymbol{0}$, where $\boldsymbol{r} : \mathbb{R}^{N+1} \to \mathbb{R}^N$ is a sufficiently differentiable function, i.e., $\boldsymbol{r} \in C^p$, with $N, p \in \mathbb{N}$. This constraint implicitly defines a surface of the form:

$$\mathcal{S} := \boldsymbol{r}^{-1}(\boldsymbol{0}) = \left\{ \boldsymbol{\nu} \in \mathbb{R}^{N+1} \mid \boldsymbol{r}(\boldsymbol{\nu}) = \boldsymbol{0} \right\}. \tag{2.1}$$

Further, assume the existence of a regular point $\boldsymbol{\nu}^* \in \mathcal{S}$. By the implicit function theorem, there exists a scalar $\varepsilon > 0$ and a neighborhood $\mathcal{V}$ of $\boldsymbol{\nu}^*$ such that a C^p function

$$\boldsymbol{c} : (-\varepsilon, \varepsilon) \to \mathcal{V} \subset \mathbb{R}^{N+1}, \tag{2.2}$$

satisfies $\boldsymbol{c}(0) = \boldsymbol{\nu}^*$ and remains on $\mathcal{S}$, i.e.,

$$\boldsymbol{r}\big(\boldsymbol{c}(s)\big) = \boldsymbol{0}, \quad \forall s \in (-\varepsilon, \varepsilon). \tag{2.3}$$

In other words, the zero set $\mathcal{S}$ of $\boldsymbol{r}$ near a regular point $\boldsymbol{\nu}^*$ forms a one-dimensional submanifold of $\mathbb{R}^{N+1}$, with $\boldsymbol{c}(s)$ providing a p-times differentiable parameterization of the curve in the neighborhood $\mathcal{V}$. At a regular

point $\boldsymbol{\nu}^*$, the tangent space $T_{\boldsymbol{\nu}^*}\mathcal{S}$ is equal to the kernel of the Jacobian $\boldsymbol{R}^* := D\boldsymbol{r}(\boldsymbol{\nu}^*)$. This follows from the fact that, for all $s \in (-\varepsilon, \varepsilon)$:

$$\boldsymbol{r}(\boldsymbol{c}(s)) = \boldsymbol{0} \quad \overset{\frac{\mathrm{d}}{\mathrm{d}s}}{\Rightarrow} \quad D\boldsymbol{r}(\boldsymbol{c}(s)) \cdot \dot{\boldsymbol{c}}(s) = \boldsymbol{0}, \tag{2.4}$$

which, in particular, implies for $s = 0$ that $\boldsymbol{R}^*\dot{\boldsymbol{\nu}}^* = \boldsymbol{0}$, where $\dot{\boldsymbol{\nu}}^* = \dot{\boldsymbol{c}}(0)$. To facilitate numerical exploration, this curve is parameterized with respect to the arclength parameter s such that $\|\dot{\boldsymbol{c}}(s)\|_2 = 1$. Additionally, Definition (2.1.7) from [6] is restated.

Definition (Tangent Vector)**.** *Let* $\boldsymbol{R} \in \mathbb{R}^{N \times N+1}$ *be a matrix of full rank. The unique tangent vector* $\boldsymbol{\tau}(\boldsymbol{R})$ *is said to be* induced by $\boldsymbol{R}$ *with*

$$\boldsymbol{\tau} := \left\{ \boldsymbol{\tau} \in \mathbb{R}^{N+1} \;\middle|\; \begin{array}{ll} \boldsymbol{R} \cdot \boldsymbol{\tau} & = \boldsymbol{0}, \\ \|\boldsymbol{\tau}\|_2 & = 1, \\ \det\left(\begin{bmatrix} \boldsymbol{R} \\ \boldsymbol{\tau}^{\mathrm{T}} \end{bmatrix}\right) & > 0. \end{array} \right. \tag{2.5}$$

With the third condition in (2.5), the vector $\boldsymbol{\tau}$ becomes uniquely defined for any regular point $\boldsymbol{c}(s)$. This condition on the determinant is essential for consistently defining the orientation of the curve $\boldsymbol{c}(s)$. Since a curve can be traced in either of two opposite directions, a scalar $d \in \{-1, 1\}$ is introduced to the resulting initial value problem:

$$\dot{\boldsymbol{c}}(s) = d \cdot \boldsymbol{\tau}\Big(D\boldsymbol{r}\big(\boldsymbol{c}(s)\big)\Big), \quad \boldsymbol{c}(0) = \boldsymbol{\nu}^*. \tag{2.6}$$

The predictor-corrector method begins with an initial predictor step, which typically approximates the ODE in (2.6) using a forward Euler scheme with a step size $\Delta s^i > 0$ for the i-th iteration:

$$\boldsymbol{\nu}^{i+1}_{\text{pred}} = \boldsymbol{\nu}^i + d \cdot \Delta s^i \cdot \boldsymbol{\tau}\Big(D\boldsymbol{r}(\boldsymbol{\nu}^i)\Big). \tag{2.7}$$

The step size Δs^i can be chosen adaptively to balance accuracy and computational efficiency when tracing $\boldsymbol{c}(s)$ (Chapter 6 [6]). Following the predictor step, the corrector step leverages the local contraction properties of Newton's method to solve $\boldsymbol{r}(\boldsymbol{\nu}) = \boldsymbol{0}$. Specifically, the corrector step approximately solves the following optimization problem:

$$\boldsymbol{\nu}^{i+1} := \boldsymbol{\nu}^{i+1}_{\text{corr}} \approx \underset{\boldsymbol{\nu} \in \mathcal{S}}{\operatorname{argmin}} \left\| \boldsymbol{\nu} - \boldsymbol{\nu}^{i+1}_{\text{pred}} \right\|_2. \tag{2.8}$$

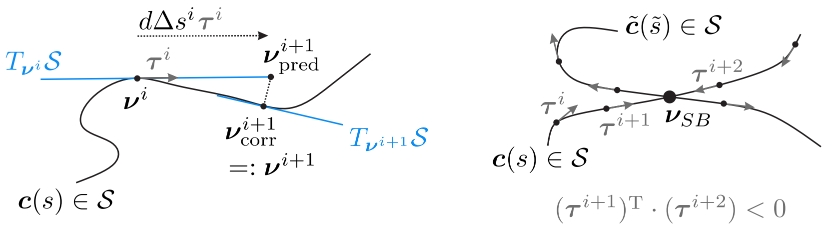

(a) (b)

Figure 2.1: (a) illustrates a predictor-corrector step as described by (2.7) and (2.8). (b) illustrates how a predictor-corrector step jumps over a simple bifurcation (SB) point $\boldsymbol{\nu}_{\mathrm{SB}}$ and the tangent vectors $\boldsymbol{\tau}$ flip direction. Both illustrations abbreviate tangent vectors by $\boldsymbol{\tau}^i := \boldsymbol{\tau}\big(D\boldsymbol{r}(\boldsymbol{\nu}^i)\big)$.

The predictor (2.7) and corrector (2.8) steps are illustrated in Fig. 2.1a. Various alternatives to (2.7) and (2.8) are outlined in Section 2.27 of the lecture notes by Keller [71]. These steps are executed repeatedly until the iterative process of tracing the curve $\boldsymbol{c}(s)$ is terminated, either by the user or upon encountering a so-called *simple bifurcation* (SB) point, indicating the presence of another curve in $\mathcal{S}$. Up to this point, it has been assumed that all points $\boldsymbol{c}(s)$ in (2.6) are regular. However, while tracing the curve $\boldsymbol{c}(s)$ in $\mathcal{S}$, the predictor-corrector method occasionally crosses over simple bifurcation points $\boldsymbol{\nu}_{\mathrm{SB}}$, where $\operatorname{rank}(D\boldsymbol{r}(\boldsymbol{\nu}_{\mathrm{SB}})) = N - 1$, resulting in $\det\left(\begin{bmatrix} D\boldsymbol{r}(\boldsymbol{\nu}_{\mathrm{SB}}) \\ \dot{\boldsymbol{\nu}}_{\mathrm{SB}}^{\mathrm{T}} \end{bmatrix}\right) = 0$. Hence, the point $\boldsymbol{\nu}_{\mathrm{SB}}$ is singular. As illustrated in Fig. 2.1b, a useful indicator for detecting SB points while tracing $\boldsymbol{c}(s)$ is the comparison of adjacent tangent vectors, which flip their orientation at such points (Section 8.1 [6]). To continue tracing the curve $\boldsymbol{c}(s) \in \mathcal{S}$ beyond an SB point, the orientation in the predictor (2.7) can be reversed by setting $d \leftarrow -d$. However, transitioning to a new curve $\tilde{\boldsymbol{c}}(\tilde{s}) \in \mathcal{S}$ requires further consideration.

2.2.2 Branching at Simple Bifurcations

To branch between the two curves $\boldsymbol{c}(s)$ and $\tilde{\boldsymbol{c}}(s)$ at a simple bifurcation point $\boldsymbol{\nu}_{\mathrm{SB}}$ (Fig. 2.1b), two methods are commonly employed: perturbation and Lyapunov-Schmidt reduction (Sections 8.2 and 8.3 of [6], respectively). This monograph adopts the latter, as it provides a systematic approach for computing the respective tangent vectors $\boldsymbol{\tau}_{\mathrm{SB}}$ and $\tilde{\boldsymbol{\tau}}_{\mathrm{SB}}$ at the SB point $\boldsymbol{\nu}_{\mathrm{SB}}$. The Lyapunov-Schmidt reduction begins with a factorization of the Jacobian $\boldsymbol{R}_{\mathrm{SB}} := D\boldsymbol{r}(\boldsymbol{\nu}_{\mathrm{SB}})$. For instance, applying the singular value decomposition (SVD) yields $\boldsymbol{R}_{\mathrm{SB}} = \boldsymbol{U}\boldsymbol{\Sigma}\boldsymbol{V}^{\mathrm{T}}$, where $\boldsymbol{U} \in \mathbb{R}^{N\times N}$ and $\boldsymbol{V} \in \mathbb{R}^{N+1\times N+1}$ are unitary matrices. This decomposition inherently provides an orthonormal basis for the two-dimensional kernel of $\boldsymbol{R}_{\mathrm{SB}}$. By choosing $\boldsymbol{U} = [\boldsymbol{U}_1\ \boldsymbol{U}_2]$, $\boldsymbol{V} = [\boldsymbol{V}_1\ \boldsymbol{V}_2]$ and arranging the singular values in $\boldsymbol{\Sigma} \in \mathbb{R}^{N\times N+1}$ in descending order, the following structure is obtained:

$$\begin{aligned}
\boldsymbol{U}_1 &= \boldsymbol{U}_2^{\perp}, & \operatorname{span}\{\boldsymbol{U}_2\} &= \ker(\boldsymbol{R}_{\mathrm{SB}}^{\mathrm{T}}), & \dim\big(\operatorname{span}\{\boldsymbol{U}_2\}\big) &= 1,\\
\boldsymbol{V}_1 &= \boldsymbol{V}_2^{\perp}, & \operatorname{span}\{\boldsymbol{V}_2\} &= \ker(\boldsymbol{R}_{\mathrm{SB}}), & \dim\big(\operatorname{span}\{\boldsymbol{V}_2\}\big) &= 2,
\end{aligned}$$

where $(\bullet)^{\perp}$ denotes the orthogonal complement of a vector space. Hence, with the two basis vectors in $\boldsymbol{V}_2 = [\boldsymbol{v}_\alpha\ \boldsymbol{v}_\beta]$, spanning the kernel of $\boldsymbol{R}_{\mathrm{SB}}$, the tangent $\dot{\boldsymbol{c}}(s)$ in (2.4) is defined by the linear combination

$$\dot{\boldsymbol{c}}(s_{\mathrm{SB}}) = \alpha\boldsymbol{v}_\alpha + \beta\boldsymbol{v}_\beta, \quad \alpha, \beta \in \mathbb{R}, \tag{2.9}$$

at the SB point $\boldsymbol{\nu}_{\mathrm{SB}} = \boldsymbol{c}(s_{\mathrm{SB}})$. To solve for α and β, we first need to differentiate (2.4) once more to obtain:

$$\begin{aligned}
& & D\boldsymbol{r}\big(\boldsymbol{c}(s)\big) \cdot \dot{\boldsymbol{c}}(s) &= \boldsymbol{0}, && \text{(2.10a)}\\
&\overset{\frac{\mathrm{d}}{\mathrm{d}s}}{\Longrightarrow} & D^2\boldsymbol{r}(\boldsymbol{c}(s))\big(\dot{\boldsymbol{c}}(s), \dot{\boldsymbol{c}}(s)\big) + D\boldsymbol{r}(\boldsymbol{c}(s)) \cdot \ddot{\boldsymbol{c}}(s) &= \boldsymbol{0}, && \text{(2.10b)}\\
&\overset{s = s_{\mathrm{SB}}}{\Longrightarrow} & D^2\boldsymbol{r}\big(\boldsymbol{c}(s_{\mathrm{SB}})\big)\big(\dot{\boldsymbol{c}}(s_{\mathrm{SB}}), \dot{\boldsymbol{c}}(s_{\mathrm{SB}})\big) + \boldsymbol{R}_{\mathrm{SB}} \cdot \ddot{\boldsymbol{c}}(s_{\mathrm{SB}}) &= \boldsymbol{0}, && \text{(2.10c)}\\
&\overset{\boldsymbol{U}_2^{\mathrm{T}} \cdot |}{\Longrightarrow} & \boldsymbol{U}_2^{\mathrm{T}} \cdot D^2\boldsymbol{r}\big(\boldsymbol{\nu}_{\mathrm{SB}}\big)\big(\dot{\boldsymbol{c}}(s_{\mathrm{SB}}), \dot{\boldsymbol{c}}(s_{\mathrm{SB}})\big) + \underbrace{\boldsymbol{U}_2^{\mathrm{T}} \cdot \boldsymbol{R}_{\mathrm{SB}}}_{=\boldsymbol{0}} \cdot \ddot{\boldsymbol{c}}(s_{\mathrm{SB}}) &= 0. && \text{(2.10d)}
\end{aligned}$$

where $(\bullet, \bullet)$ denotes the bilinear form of tensor products. Finally, plugging (2.9) into (2.10d) yields the problem

$$\begin{aligned}
\boldsymbol{0} &= \begin{bmatrix}\alpha & \beta\end{bmatrix} \boldsymbol{H}_{\mathrm{SB}} \begin{bmatrix}\alpha \\ \beta\end{bmatrix},\\
\boldsymbol{H}_{\mathrm{SB}} &= \begin{bmatrix} \boldsymbol{U}_2^{\mathrm{T}} \cdot D^2\boldsymbol{r}\big(\boldsymbol{\nu}_{\mathrm{SB}}\big)\big(\boldsymbol{v}_\alpha, \boldsymbol{v}_\alpha\big) & \boldsymbol{U}_2^{\mathrm{T}} \cdot D^2\boldsymbol{r}\big(\boldsymbol{\nu}_{\mathrm{SB}}\big)\big(\boldsymbol{v}_\alpha, \boldsymbol{v}_\beta\big)\\ \boldsymbol{U}_2^{\mathrm{T}} \cdot D^2\boldsymbol{r}\big(\boldsymbol{\nu}_{\mathrm{SB}}\big)\big(\boldsymbol{v}_\beta, \boldsymbol{v}_\alpha\big) & \boldsymbol{U}_2^{\mathrm{T}} \cdot D^2\boldsymbol{r}\big(\boldsymbol{\nu}_{\mathrm{SB}}\big)\big(\boldsymbol{v}_\beta, \boldsymbol{v}_\beta\big)\end{bmatrix},
\end{aligned} \tag{2.11}$$

where $\boldsymbol{H}_{\mathrm{SB}}$ is a symmetric 2-by-2 matrix. The quadratic (2.11) describes a degenerate conic section, as exactly two solutions are expected at a simple bifurcation. By exploiting an eigendecomposition of $\boldsymbol{H}_{\mathrm{SB}}$, the solution pairs (α, β) and $(\tilde{\alpha}, \tilde{\beta})$ are obtained, which then define the tangent vectors at $\boldsymbol{\nu}_{\mathrm{SB}}$ using (2.9):

$$\boldsymbol{\tau}_{\mathrm{SB}} = \alpha\boldsymbol{v}_\alpha + \beta\boldsymbol{v}_\beta, \quad \tilde{\boldsymbol{\tau}}_{\mathrm{SB}} = \tilde{\alpha}\boldsymbol{v}_\alpha + \tilde{\beta}\boldsymbol{v}_\beta. \tag{2.12}$$

It is important to note that in general a (simple) singular point does not necessarily imply the presence of a (simple) bifurcation, i.e., the emergence of additional linearly independent tangent vectors. Special care is therefore required when constructing tangent vectors at a singular point (Chapter 5 [71]).

2.3 Optimization

The following section highlights some fundamental concepts in optimization (minimization) that are crucial for its application to dynamical systems. For a concise mathematical derivation of optimality conditions using Lagrange multipliers, refer to Luenberger's books for the finite- [89] and infinite-dimensional cases [88]. This introduction to optimization tools concludes in Section 2.3.4 with a brief discussion on parameterized optimization and the use of continuation methods.

2.3.1 Unconstrained Optimization

Unconstrained optimization is introduced with a one-dimensional example, demonstrating how fundamental calculus concepts assess local optimality. These concepts are then extended to n dimensions, leading to the general necessary conditions for optimality.

1-D Example

Consider the problem of minimizing a function $f : \mathbb{R} \to \mathbb{R}$. In general, finding the global minimum of f can be challenging, as f is often not convex

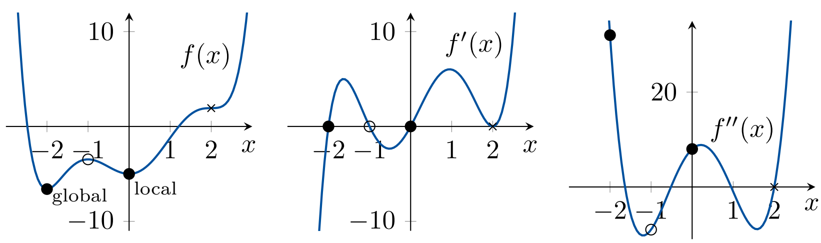

(a) (b) (c)

Figure 2.2: Graphs of the function f and its derivatives. The black dots ($\bullet$) indicate local minima, the black circle ($\circ$) marks a local maximum, and the black cross ($\times$) denotes a saddle point.

and may exhibit multiple local minima, as illustrated in the example in Fig. 2.2. The problem consists in minimizing the scalar function

$$f(x) = \frac{x^6}{6} - \frac{x^5}{5} - 6\frac{x^4}{4} + 4\frac{x^3}{3} + 8\frac{x^2}{2} - 5. \tag{2.13}$$

Minima correspond to stationary points x^* of the function $f(x)$, obtained by finding the roots of $f'(x) = (x+2)(x+1)x(x-2)^2$. In this example, the stationary points are $x^* = -2$, $x^* = 0$, $x^* = -1$, and $x^* = 2$. Among these, $x^* = -2$ and $x^* = 0$ correspond to minima, as shown by the positive curvature provided through the second derivatives $f''(-2) = 32 > 0$ and $f''(0) = 8 > 0$. The point $x^* = -1$ corresponds to a maximum ($f''(0) = -9 < 0$), while $x^* = 2$ is a saddle point ($f''(2) = 0$). Distinguishing global from local minima requires evaluating the function values at the minima, revealing the global optimum at $x^* = -2$, since $f(-2) < f(0)$.

Generalization to n-Dimensions

To formalize the previous observations and generalize the optimality conditions to the n-dimensional case, consider a scalar objective function $f : \mathbb{R}^n \to \mathbb{R}$. The geometric properties of f are analyzed by examining local perturbations around a stationary point $\boldsymbol{x}^*$, under the assumption that $f \in C^2$ in a neighborhood of $\boldsymbol{x}^*$. Using first-order ($\delta\boldsymbol{x} \in \mathbb{R}^n$) and second-order ($\delta^2\boldsymbol{x} \in \mathbb{R}^n$) variations within a Taylor expansion, the perturbed objective function is expressed as

$$\tilde{f}(\varepsilon) := f(\boldsymbol{x}^* + \varepsilon\delta\boldsymbol{x} + \varepsilon^2\delta^2\boldsymbol{x}), \quad \varepsilon \ll 1. \tag{2.14a}$$

Furthermore, the derivatives of (2.14a) at the stationary point ($\varepsilon = 0$) take the form

$$\tilde{f}'(0) = Df(x^*)\delta\boldsymbol{x}, \tag{2.14b}$$
$$\tilde{f}''(0) = \delta\boldsymbol{x}^{\mathrm{T}} D^2 f(x^*)\delta\boldsymbol{x} + Df(x^*)2\delta^2\boldsymbol{x}. \tag{2.14c}$$

This formulation leads to the general form of the optimality conditions for a *strict local minimum.*

1st-order necessary condition:

$$\tilde{f}'(0) = Df(\boldsymbol{x}^*)\delta\boldsymbol{x} \overset{!}{=} 0,\ \forall\delta\boldsymbol{x} \in \mathbb{R}^n, \quad \Rightarrow \quad Df(\boldsymbol{x}^*) = \boldsymbol{0}, \tag{2.15a}$$

2nd-order sufficient condition:

$$\tilde{f}''(0) = \delta\boldsymbol{x}^{\mathrm{T}} D^2 f(\boldsymbol{x}^*)\delta\boldsymbol{x} \overset{!}{>} 0,\ \forall\delta\boldsymbol{x} \in \mathbb{R}^n, \quad \Rightarrow \quad D^2 f(\boldsymbol{x}^*) \succ \boldsymbol{0}, \tag{2.15b}$$

where $\succ$ denotes positive-definiteness.

If f is convex, the conditions (2.15) ensure a strict global minimum.

2.3.2 Equality-Constrained Optimization

This dissertation frequently defines and solves equality-constrained optimization (ECO) problems of the form

$$\begin{aligned} \underset{\boldsymbol{x}}{\text{minimize}} \quad & f(\boldsymbol{x}) \\ \text{subject to} \quad & \boldsymbol{h}(\boldsymbol{x}) = \boldsymbol{0} \end{aligned}, \qquad \text{with} \begin{cases} f : \mathbb{R}^n \to \mathbb{R}, \\ \boldsymbol{h} : \mathbb{R}^n \to \mathbb{R}^m, \\ n > m. \end{cases} \tag{2.16}$$

As before, the existence of a stationary point $\boldsymbol{x}^*$ for problem (2.16) is assumed, with f and $\boldsymbol{h}$ being C^2 in a neighborhood of $\boldsymbol{x}^*$. Moreover, $\boldsymbol{x}^*$ is assumed to be a regular point of $\boldsymbol{h}(\boldsymbol{x}^*) = \boldsymbol{0}$, satisfying the linear independence constraint qualification (LICQ). Similar to the perturbation in the objective function (2.14a), a Taylor expansion is applied to the equality constraints:

$$\tilde{\boldsymbol{h}}(\varepsilon) := \boldsymbol{h}(\boldsymbol{x}^* + \varepsilon\delta\boldsymbol{x} + \varepsilon^2\delta^2\boldsymbol{x}), \quad \varepsilon \ll 1. \tag{2.17a}$$

Since the perturbations must remain on the constraint surface, the following holds:

$$\tilde{\boldsymbol{h}}(\varepsilon) = \boldsymbol{0}, \quad \forall\varepsilon \text{ in the neighborhood of } 0, \tag{2.17b}$$

$$\overset{\frac{\mathrm{d}}{\mathrm{d}\varepsilon}}{\Rightarrow} \tilde{\boldsymbol{h}}'(\varepsilon) = \boldsymbol{0}, \Rightarrow \tilde{\boldsymbol{h}}'(0) = D\boldsymbol{h}(\boldsymbol{x}^*)\delta\boldsymbol{x} = \boldsymbol{0}, \tag{2.17c}$$

$$\overset{\frac{\mathrm{d}}{\mathrm{d}\varepsilon}}{\Rightarrow} \tilde{\boldsymbol{h}}''(\varepsilon) = \boldsymbol{0}, \Rightarrow \tilde{\boldsymbol{h}}''(0) = D^2\boldsymbol{h}(\boldsymbol{x}^*)(\delta\boldsymbol{x}, \delta\boldsymbol{x}) + D\boldsymbol{h}(\boldsymbol{x}^*)2\delta^2\boldsymbol{x} = \boldsymbol{0}. \tag{2.17d}$$

Note that (2.17c) and (2.17d) are analogous to (2.10a) and (2.10b). From (2.17c) and the LICQ, it follows that all perturbations $\delta\boldsymbol{x}$ must lie within the tangent space $\ker(D\boldsymbol{h}(\boldsymbol{x}^*))$. Furthermore, as the constraint Jacobian $D\boldsymbol{h}(\boldsymbol{x}^*)$ is regular, a linearly independent basis for $\mathbb{R}^n$ can be constructed from $\mathrm{span}(D\boldsymbol{h}(\boldsymbol{x}^*))$ and its orthogonal complement $\mathrm{span}(\delta\boldsymbol{x})$. The stationarity condition $\tilde{f}'(0) = 0$ with (2.14b) implies that the objective gradient $Df(\boldsymbol{x}^*)$ can be expressed as a linear combination of the constraint Jacobian $D\boldsymbol{h}(\boldsymbol{x}^*)$:

$$\left.\begin{aligned} Df(\boldsymbol{x}^*)\delta\boldsymbol{x} &= 0 \\ D\boldsymbol{h}(\boldsymbol{x}^*)\delta\boldsymbol{x} &= \boldsymbol{0} \end{aligned}\right\} \overset{\text{LICQ}}{\Longrightarrow} \quad Df(\boldsymbol{x}^*) \in \mathrm{span}(D\boldsymbol{h}(\boldsymbol{x}^*)), \tag{2.18a}$$

$$\overset{\exists!\boldsymbol{\lambda}^* \in \mathbb{R}^m}{\Longleftrightarrow} \quad Df(\boldsymbol{x}^*) = -{\boldsymbol{\lambda}^*}^{\mathrm{T}} D\boldsymbol{h}(\boldsymbol{x}^*), \tag{2.18b}$$

where $\boldsymbol{\lambda}^* \in \mathbb{R}^m$ is the uniquely defined *Lagrange multiplier* corresponding to the stationary point $\boldsymbol{x}^*$. For notational convenience, the *Lagrangian* $\mathcal{L} : \mathbb{R}^n \times \mathbb{R}^m \to \mathbb{R}$ and its derivatives are defined as follows:

$$\mathcal{L}(\boldsymbol{x}, \boldsymbol{\lambda}) = f(\boldsymbol{x}) + \boldsymbol{\lambda}^{\mathrm{T}} \boldsymbol{h}(\boldsymbol{x}), \tag{2.19a}$$

$$D\mathcal{L}(\boldsymbol{x}, \boldsymbol{\lambda}) = \begin{bmatrix} Df(\boldsymbol{x}) + \boldsymbol{\lambda}^{\mathrm{T}} D\boldsymbol{h}(\boldsymbol{x}) & \boldsymbol{h}(\boldsymbol{x})^{\mathrm{T}} \end{bmatrix}, \tag{2.19b}$$

$$D^2\mathcal{L}(\boldsymbol{x}, \boldsymbol{\lambda}) = \begin{bmatrix} D^2 f(\boldsymbol{x}) + \boldsymbol{\lambda}^{\mathrm{T}} D^2\boldsymbol{h}(\boldsymbol{x}) & D\boldsymbol{h}(\boldsymbol{x})^{\mathrm{T}} \\ D\boldsymbol{h}(\boldsymbol{x}) & \boldsymbol{0} \end{bmatrix}. \tag{2.19c}$$

Setting $D_{\boldsymbol{x}}\mathcal{L}(\boldsymbol{x}^*, \boldsymbol{\lambda}^*) := Df(\boldsymbol{x}^*) + \boldsymbol{\lambda}^{*\mathrm{T}} D\boldsymbol{h}(\boldsymbol{x}^*)$ to zero is equivalent to the linear combination defined in (2.18b). Hence, the optimality conditions for a *strict local minimum* of the ECO problem (2.16) at a regular point $\boldsymbol{x}^*$ satisfying $\boldsymbol{h}(\boldsymbol{x}^*) = \boldsymbol{0}$ are stated as follows:
<u>1st-order necessary condition:</u>

$$\begin{aligned} &\tilde{f}'(0) = Df(x^*)\delta\boldsymbol{x} \overset{!}{=} 0, \ \forall \delta\boldsymbol{x} \in \ker(D\boldsymbol{h}(\boldsymbol{x}^*)), \\ &\Rightarrow \quad D_{\boldsymbol{x}}\mathcal{L}(\boldsymbol{x}^*, \boldsymbol{\lambda}^*) = \boldsymbol{0}, \end{aligned} \tag{2.20}$$

<u>2nd-order sufficient condition:</u>

$$\begin{aligned} &\tilde{f}''(0) = \delta\boldsymbol{x}^{\mathrm{T}} D^2_{\boldsymbol{x}}\mathcal{L}(\boldsymbol{x}^*, \boldsymbol{\lambda}^*)\delta\boldsymbol{x} \overset{!}{>} 0, \ \forall \delta\boldsymbol{x} \in \ker(D\boldsymbol{h}(\boldsymbol{x}^*)), \\ &\Rightarrow \quad \boldsymbol{\Delta}^{\mathrm{T}} D^2_{\boldsymbol{x}}\mathcal{L}(\boldsymbol{x}^*, \boldsymbol{\lambda}^*)\boldsymbol{\Delta} \succ \boldsymbol{0}, \end{aligned} \tag{2.21}$$

where $D^2_{\boldsymbol{x}}\mathcal{L}(\boldsymbol{x}, \boldsymbol{\lambda}) := D^2 f(\boldsymbol{x}) + \boldsymbol{\lambda}^{\mathrm{T}} D^2\boldsymbol{h}(\boldsymbol{x})$, and $\boldsymbol{\Delta}$ is an orthonormal matrix whose columns form a basis for the tangent space $\ker(D\boldsymbol{h}(\boldsymbol{x}^*))$. To derive the 2nd-order condition (2.21), (2.17d) is combined with the positive definiteness of $\tilde{f}''(0)$, as defined by (2.14b), yielding

$$\begin{aligned} &\tilde{f}''(0) + \boldsymbol{\lambda}^{\mathrm{T}} \tilde{\boldsymbol{h}}''(0) > 0, \\ \Leftrightarrow\ &\delta\boldsymbol{x}^{\mathrm{T}} D^2_{\boldsymbol{x}}\mathcal{L}(\boldsymbol{x}^*, \boldsymbol{\lambda}^*)\delta\boldsymbol{x} + \underbrace{D\mathcal{L}(\boldsymbol{x}^*, \boldsymbol{\lambda}^*)}_{=\boldsymbol{0}} 2\delta^2\boldsymbol{x} > 0. \end{aligned} \tag{2.22}$$

Remark 2.3.1. *The tuple* $(\boldsymbol{x}^*, \boldsymbol{\lambda}^*)$ *corresponding to a local minimum of* (2.16) *constitutes a saddle point of the Lagrangian* $\mathcal{L}$ *[70]. Consequently, finding a stationary point of* (2.16) *can be reformulated as solving the following unconstrained problem:*

$$\underset{\boldsymbol{x}, \boldsymbol{\lambda}}{\text{stationary}} \quad \mathcal{L}(\boldsymbol{x}, \boldsymbol{\lambda}). \tag{2.23a}$$

Analogous to (2.14a) *and* (2.15a)*, the perturbed Lagrangian*

$$\tilde{\mathcal{L}}(\varepsilon) := \mathcal{L}(\boldsymbol{x}^* + \varepsilon\delta\boldsymbol{x}, \boldsymbol{\lambda}^* + \varepsilon\delta\boldsymbol{\lambda}), \quad \varepsilon \ll 1, \tag{2.23b}$$

where $\delta\boldsymbol{x} \in \mathbb{R}^n$ *and* $\delta\boldsymbol{\lambda} \in \mathbb{R}^m$*, provides a tool to derive the first-order necessary condition* (2.20) *by imposing*

$$\tilde{\mathcal{L}}'(0) = 0 \quad \Rightarrow \quad D\mathcal{L}(\boldsymbol{x}^*, \boldsymbol{\lambda}^*) = \mathbf{0}. \tag{2.23c}$$

2.3.3 Extension to Infinite Dimensions

Trajectory optimization (TO) problems focus on finding the optimal trajectories $\boldsymbol{x}(\cdot)$ and $\boldsymbol{u}(\cdot)$ for a dynamical system defined by $\dot{\boldsymbol{x}} = \boldsymbol{f}(\boldsymbol{x}, \boldsymbol{u})$, where the vector field $\boldsymbol{f} : \mathbb{R}^{n_\mathrm{x}} \times \mathbb{R}^{n_\mathrm{u}} \to \mathbb{R}^{n_\mathrm{x}}$ governs the system's evolution. The system states $\boldsymbol{x}(t) \in \mathbb{R}^{n_\mathrm{x}}$ and control inputs $\boldsymbol{u}(t) \in \mathbb{R}^{n_\mathrm{u}}$ vary over time $t \in [0, T]$, leading to an infinite-dimensional search space for TO problems. For simplicity, consider the following structure for the objective function:

$$J(\boldsymbol{x}(\cdot), \boldsymbol{u}(\cdot)) = \int_0^T l\big(\boldsymbol{x}(t), \boldsymbol{u}(t)\big)\mathrm{d}t, \tag{2.24}$$

where $l : \mathbb{R}^{n_\mathrm{x}} \times \mathbb{R}^{n_\mathrm{u}} \to \mathbb{R}$. Extending (2.16), the infinite-dimensional constrained optimization problem can be formulated as

$$\begin{aligned} \underset{\boldsymbol{x}(\cdot), \boldsymbol{u}(\cdot)}{\text{minimize}} \quad & J\big(\boldsymbol{x}(\cdot), \boldsymbol{u}(\cdot)\big) \\ \text{subject to} \quad & \underbrace{\boldsymbol{f}\big(\boldsymbol{x}(t), \boldsymbol{u}(t)\big) - \dot{\boldsymbol{x}}(t)}_{=:\boldsymbol{h}(\boldsymbol{x}, \boldsymbol{u}, \dot{\boldsymbol{x}})} = \mathbf{0}, \quad \forall t \in [0, T] \ . \end{aligned} \tag{2.25}$$

The tools outlined in Section 2.3.2 extend naturally to this infinite-dimensional setting through the application of calculus of variations [83]. With the introduction of continuous-time Lagrange multipliers, referred to as costates $\boldsymbol{\lambda}(t) \in \mathbb{R}^{n_\mathrm{x}}$, the Lagrangian is expressed as

$$\mathcal{L}\big(\boldsymbol{x}(\cdot), \boldsymbol{u}(\cdot), \boldsymbol{\lambda}(\cdot)\big) = \int_0^T l\big(\boldsymbol{x}_t, \boldsymbol{u}_t\big) + \boldsymbol{\lambda}_t^\mathrm{T} \boldsymbol{h}\big(\boldsymbol{x}_t, \boldsymbol{u}_t, \dot{\boldsymbol{x}}_t\big)\mathrm{d}t, \tag{2.26a}$$

$$= \int_0^T \mathcal{H}\big(\boldsymbol{x}_t, \boldsymbol{u}_t, \boldsymbol{\lambda}_t\big) - \boldsymbol{\lambda}_t^\mathrm{T} \dot{\boldsymbol{x}}_t \mathrm{d}t, \tag{2.26b}$$

$$\mathcal{H}\big(\boldsymbol{x}_t, \boldsymbol{u}_t, \boldsymbol{\lambda}_t\big) = l\big(\boldsymbol{x}_t, \boldsymbol{u}_t\big) + \boldsymbol{\lambda}_t^\mathrm{T} \boldsymbol{f}\big(\boldsymbol{x}_t, \boldsymbol{u}_t\big), \tag{2.26c}$$

where $\mathcal{H}$ is referred to as the Hamiltonian of (2.25), as its value remains constant along stationary trajectories of $\mathcal{L}$. Assuming the existence of strict local minimizing functions $\boldsymbol{x}^*(\cdot)$, $\boldsymbol{u}^*(\cdot)$, and the corresponding costates $\boldsymbol{\lambda}^*(\cdot)$, the first-order optimality conditions are derived by perturbing the Lagrangian, analogous to Remark 2.3.1:

$$\tilde{\mathcal{L}}(\varepsilon) := \mathcal{L}\big(\boldsymbol{x}^*(\cdot) + \varepsilon\delta\boldsymbol{x}(\cdot), \boldsymbol{u}^*(\cdot) + \varepsilon\delta\boldsymbol{u}(\cdot), \boldsymbol{\lambda}^*(\cdot) + \varepsilon\delta\boldsymbol{\lambda}(\cdot)\big), \quad \varepsilon \ll 1, \tag{2.27}$$

where $\delta\boldsymbol{x}(\cdot)$, $\delta\boldsymbol{u}(\cdot)$ and $\delta\boldsymbol{\lambda}(\cdot)$ denote perturbation functions defined over the domain $t \in [0, T]$. Under standard assumptions, such as sufficient differentiability of $l(\cdot,\cdot)$ and $\boldsymbol{f}(\cdot,\cdot)$ [88], applying the fundamental lemma of the calculus of variations to the stationarity condition $\tilde{\mathcal{L}}'(0) = 0$ yields the following differential-algebraic equation (DAE) system:

$$\dot{\boldsymbol{x}} = \frac{\partial \mathcal{H}}{\partial \boldsymbol{\lambda}}^{\mathrm{T}}, \quad \dot{\boldsymbol{\lambda}} = -\frac{\partial \mathcal{H}}{\partial \boldsymbol{x}}^{\mathrm{T}}, \quad \boldsymbol{0} = \frac{\partial \mathcal{H}}{\partial \boldsymbol{u}}^{\mathrm{T}}. \tag{2.28}$$

A detailed derivation of this DAE, including boundary and transversality conditions, is provided in Chapter 6.2.1.

To further distinguish minima from maxima and saddle points, second-order variations must be applied to problem (2.25). However, this process is not straightforward and will therefore be omitted in this thesis.

2.3.4 Remarks on Parameterized Optimization

This section briefly examines how introducing a single parameter $\sigma \in \mathbb{R}$ influences the solution space of optimal points in the previously defined ECO problems (2.16) and (2.25). Additionally, it highlights how PCC methods from Section 2.2.1 can be leveraged for systematic exploration.

While parameterizing the optimization problem does not alter the derivation of optimality conditions, it introduces 1-D families of stationary points in the solution space, satisfying $\tilde{\mathcal{L}}'(\varepsilon;\sigma) = 0$. Within this first-order optimality condition, let the solution space variables be denoted by $\boldsymbol{\chi} \in \mathbb{R}^N$, leading to the parameterized root-finding problem $\boldsymbol{r}(\boldsymbol{\chi}, \sigma) = \boldsymbol{0}$, where $\boldsymbol{r} : \mathbb{R}^N \times \mathbb{R} \to \mathbb{R}^N$. Further, by defining $\boldsymbol{\nu}^{\mathrm{T}} = [\boldsymbol{\chi}^{\mathrm{T}}\ \sigma]$, the solution space $\mathcal{S}$ of stationary points can be formulated as in (2.1) and is therefore well-suited for exploration using the PCC method (2.6). When tracing the solution curve $\mathcal{S}$ along the arclength s, the evolution of the parameter $\sigma(s)$, particularly $\dot{\sigma}(s)$, provides valuable insights into second-order optimality. Specifically, for a curve of regular stationary points $\boldsymbol{c}(s) \in \mathcal{S}$ originating from a local minimizer $\boldsymbol{\chi}^*$, such that $\boldsymbol{c}(0)^{\mathrm{T}} = [\boldsymbol{\chi}^{*\mathrm{T}}\ \sigma^*]$, all points along the curve will correspond to local minima as long as $\sigma(s)$ varies monotonically. This conclusion follows from Theorem 11.8.2 in [6], which states that the eigenvalues of the Hessian $D^2\mathcal{L}$ retain their signs, provided the curve $\boldsymbol{c}(s) \in \mathcal{S}$ is monotonic in $\sigma(s)$.

This property is particularly useful, as directly verifying the second-order necessary condition at each point along $\boldsymbol{c}(s)$ may be computationally expensive or mathematically intricate, especially in infinite-dimensional TO problems.

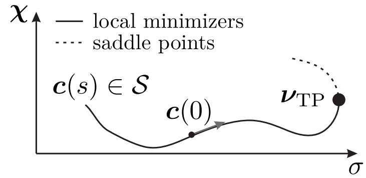

Conversely, a change in the sign of $\dot{p}(s)$ indicates that the curve $\boldsymbol{c}(s)$ is traversing a turning point $\boldsymbol{\nu}_{\mathrm{TP}}$, at which at least one eigenvalue of $D^2\mathcal{L}$ changes sign.[2] This signals a qualitative shift in the stationary point, where a local minimizer transitions into a saddle point within $\mathcal{S}$. Notably, a direct transition from a minimizer to a maximizer within $\mathcal{S}$ is highly unlikely for large N, as this would require all eigenvalues of $D^2\mathcal{L}$ to simultaneously change sign.

[2] A TP with a single vanishing eigenvalue of $D^2\mathcal{L}$ is referred to as a quadratic turning point in [53].

Chapter 3

Recurrent Hybrid Dynamical Systems

Since this dissertation investigates periodic motions in non-smooth dynamical systems, this chapter introduces the modeling framework and notation (Table 3.1) used to describe recurrent trajectories in a class of hybrid dynamical systems (HDSs). The discussion of recurrent HDSs and their trajectories (Section 3.1) remains general, laying the foundation for later chapters. The chapter concludes with a quantitative comparison of event-based and time-based shooting methods for determining the solution set of periodic orbits (Section 3.2). It further argues why time-based shooting is the preferred approach in this dissertation (Section 3.3).

A recurrent HDS consists of $m \in \mathbb{N}$ continuous phases and discrete transitions that switch between them. Following the notation in [52, 137], trajectories traverse these phases in a fixed recurring order, $1 \to 2 \to \cdots \to m \to 1$, with modulo notation $m+1 \equiv 1$. In each phase i, the system's state is denoted as $\boldsymbol{x}_i \in \mathcal{X}_i$, where $\mathcal{X}_i$ is an open connected subset of $\mathbb{R}^{n_{\mathrm{x},i}}$. The continuous evolution of $\boldsymbol{x}_i$ within phase i is governed by the phase dynamics $\dot{\boldsymbol{x}}_i(t) = \boldsymbol{f}_i(t, \boldsymbol{x}_i(t))$. The state evolution is generally influenced by control inputs $\boldsymbol{u}_i \in \mathcal{U}_i$, where $\mathcal{U}_i \subseteq \mathbb{R}^{n_{\mathrm{u},i}}$.

Remark 3.0.1. *This monograph focuses on open-loop control, where the function space of $\boldsymbol{u}_i(\cdot)$ is parameterized in time. This parameterization can be finite or infinite dimensional, as discussed further in the context of optimization in Chapter 6.*

Time dependence is captured in the continuously differentiable vector field $\boldsymbol{f}_i : \mathbb{R} \times \mathcal{X}_i \to T\mathcal{X}_i$.

Symbol	Brief description
$i \in \{1, \dots, m\}$	Index of a phase
$m \in \mathbb{N}$	Number of phases
$\Sigma = (\mathcal{X}, \mathcal{F}, \mathcal{E}, \mathcal{G})$	(Recurrent) HDSs
$\mathcal{X}_i \subseteq \mathbb{R}^{n_{\mathrm{x},i}}$	Phase domain
$n_{\mathrm{x},i} \in \mathbb{N}$	State dimension of a phase
$\boldsymbol{x}_i \in \mathcal{X}_i$	Phase state
$\boldsymbol{f}_i \in C^1,\ \boldsymbol{f}_i : \mathbb{R} \times \mathcal{X}_i \to T\mathcal{X}_i$	Phase vector field
$\mathcal{F}_i : \dot{\boldsymbol{x}}_i = \boldsymbol{f}_i(t, \boldsymbol{x}_i)$	Phase dynamics
$\boldsymbol{\varphi}_i(t, \bar{t}_i, \bar{\boldsymbol{x}}_i) =: \boldsymbol{x}_i(t)$	Phase flow
$t_i^{\max} \in \mathbb{R} \cup \{\infty\}$	Maximal flow time within a phase
$\mathcal{T}_i = [\bar{t}_i, \bar{t}_i + t_i^{\max})$	Maximal time interval of a phase
$\bar{\boldsymbol{x}}_i \in \mathcal{X}_i,\ \ \bar{\boldsymbol{x}}_1 = \boldsymbol{x}_0$	Initial conditions
$\bar{t}_i \in \mathbb{R},\ \ \bar{t}_1 = t_0$	Initial times
$e_i^{i+1} \in C^1,\ e_i^{i+1} : \mathbb{R} \times \mathcal{X}_i \to \mathbb{R}$	Event function
$\mathcal{E}_i^{i+1} \subset \mathbb{R} \times \mathcal{X}_i$	Event set / guard
$\underline{\mathcal{E}}_i^{i+1} \subset \mathcal{X}_i$	Projection of $\mathcal{E}_i^{i+1}$ onto $\mathcal{X}_i$.
$\boldsymbol{g}_i^{i+1} \in C^1,\ \boldsymbol{g}_i^{i+1} : \underline{\mathcal{E}}_i^{i+1} \to \mathcal{X}_{i+1}$	Reset map
$t^-,\ \boldsymbol{x}_i^-,\ \boldsymbol{f}_i^-$	Pre event quantitiy
$t^+,\ \boldsymbol{x}_i^+,\ \boldsymbol{f}_i^+$	Post event quantitiy
$t_i^{\mathcal{E}} : \mathcal{T}_i \times \mathcal{X}_i \to \mathbb{R} \cup \{\infty\}$	Time-to-event function (3.1)
$\Delta t_i = t_i^{\mathcal{E}} - \bar{t}_i$	Phase duration
$\boldsymbol{\varphi}(t, t_0, \boldsymbol{x}_0) =: \boldsymbol{x}(t)$	(Recurrent) hybrid flow (3.2)
$\mathcal{T} = \big[\bar{t}_{m+1}, \bar{t}_{m+1} + t_1^{\mathcal{E}}(\bar{t}_{m+1}, \bar{\boldsymbol{x}}_{m+1})\big)$	Final time interval in phase $m+1$

Table 3.1: These key symbols of a hybrid dynamical system (HDS) are used throughout this monograph.

The *phase flow* $\boldsymbol{\varphi}_i : \mathbb{R} \times \mathbb{R} \times \mathcal{X}_i \to \mathcal{X}_i$ describes the general solution to the phase dynamics. It characterizes the motion within phase i, starting from any initial condition $\bar{\boldsymbol{x}}_i \in \mathcal{X}_i$ at initial time $\bar{t}_i$ and continuing up to a maximal time $t_i^{\max} \in \mathbb{R} \cup \{\infty\}$. For each phase i, the phase flow $\boldsymbol{\varphi}_i(t, \bar{t}_i, \bar{\boldsymbol{x}}_i)$ is uniquely defined over the maximal time interval $\mathcal{T}_i = [\bar{t}_i, \bar{t}_i + t_i^{\max})$, ensuring $t \in \mathcal{T}_i$, due to the local Lipschitz continuity of the vector field $\boldsymbol{f}_i$ (cf. Theorem 1.1 [55], Theorem 3.1 [82]). To emphasize specific phase trajectories, the notation $\boldsymbol{x}_i(t) := \boldsymbol{\varphi}_i(t, \bar{t}_i, \bar{\boldsymbol{x}}_i)$ is used for brevity.

Additionally, a subset $\mathcal{E}_i^{i+1}$ in $\mathbb{R} \times \mathcal{X}_i$, referred to as event set or guard, determines a transition from phase i to phase $i+1$ via the continuously differentiable reset map $\boldsymbol{g}_i^{i+1} : \underline{\mathcal{E}}_i^{i+1} \to \mathcal{X}_{i+1}$, where $\underline{\mathcal{E}}_i^{i+1}$ denotes the

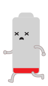

projection of $\mathcal{E}_i^{i+1}$ onto $\mathcal{X}_i$. This phase switch occurs whenever a continuously differentiable *event function* $e_i^{i+1} : \mathbb{R} \times \mathcal{X}_i \to \mathbb{R}$ becomes zero. Hence, the zeros of the scalar function $e_i^{i+1}(t, \boldsymbol{x}_i)$ define the event set as $\mathcal{E}_i^{i+1} = \left\{t \in \mathbb{R},\ \boldsymbol{x}_i \in \mathcal{X}_i \;\middle|\; e_i^{i+1}(t, \boldsymbol{x}_i) = 0\right\}$.

Adopting the notation from [52], the hybrid model takes the form:

Time-Variant Hybrid Dynamical System

$$\Sigma : \begin{cases} \mathcal{X} = \left\{\mathcal{X}_i\right\}_{i=1}^{m} & : \mathcal{X}_i \subset \mathbb{R}^{n_{\mathrm{x},i}} \\ \mathcal{F} = \left\{\mathcal{F}_i\right\}_{i=1}^{m} & : \mathcal{F}_i = \left\{\dot{\boldsymbol{x}}_i = \boldsymbol{f}_i(t, \boldsymbol{x}_i)\right\} \\ \mathcal{E} = \left\{\mathcal{E}_i^{i+1}\right\}_{i=1}^{m} & : \mathcal{E}_i^{i+1} = \left\{t \in \mathbb{R},\ \boldsymbol{x}_i \in \mathcal{X}_i \;\middle|\; e_i^{i+1}(t, \boldsymbol{x}_i) = 0\right\} \\ \mathcal{G} = \left\{\mathcal{G}_i^{i+1}\right\}_{i=1}^{m} & : \mathcal{G}_i^{i+1} = \left\{\boldsymbol{x}_{i+1}^{+} = \boldsymbol{g}_i^{i+1}(\boldsymbol{x}_i^{-})\right\} \end{cases} .$$

Here, the superscript $^-$ and $^+$ denote quantities immediately before and after a discrete transition, respectively. For compactness, the hybrid model is expressed as a tuple $\Sigma = (\mathcal{X}, \mathcal{F}, \mathcal{E}, \mathcal{G})$.

3.1 Hybrid Trajectories, Orbits and Flows

To construct a trajectory within Σ, the approach in [137] is extended to incorporate time-dependent events, leading to the definition of the phase-i *time-to-event function* $t_i^{\mathcal{E}} : \mathcal{T}_i \times \mathcal{X}_i \to \mathbb{R} \cup \{\infty\}$, by

$$t_i^{\mathcal{E}}(\bar{t}_i, \bar{\boldsymbol{x}}_i) := \inf \left\{t \geq \bar{t}_i \middle| \left(t, \boldsymbol{\varphi}_i(t, \bar{t}_i, \bar{\boldsymbol{x}}_i)\right) \in \mathcal{E}_i^{i+1}\right\}, \tag{3.1}$$

where, by convention, the infimum of an empty set is taken to be ∞.

Definition (Recurrent Hybrid Trajectory)**.** *A trajectory function $\boldsymbol{x} : \mathcal{T} \to \mathcal{X}_1$ that begins and ends within $\mathcal{X}_1$, while sequentially passing through all phases in the fixed order $1 \to 2 \to \cdots \to m \to 1$, is termed a recurrent hybrid trajectory. Given its initial time $t_0 \in \mathbb{R}$ and initial state $\boldsymbol{x}_0 \in \mathcal{X}_1$, the trajectory of a complete cycle is recursively defined as*

$$\boldsymbol{x}(t) = \boldsymbol{\varphi}_1\left(t, \bar{t}_{m+1}, \bar{\boldsymbol{x}}_{m+1}\right), \tag{3.2a}$$

$$\left\{\begin{aligned} \bar{t}_{i+1} &= t_i^{\mathcal{E}}(\bar{t}_i, \bar{\boldsymbol{x}}_i), \\ \bar{\boldsymbol{x}}_{i+1} &= \boldsymbol{g}_i^{i+1} \circ \boldsymbol{\varphi}_i\left(\bar{t}_{i+1}, \bar{t}_i, \bar{\boldsymbol{x}}_i\right), \end{aligned}\right\}_{i=1}^{m}, \tag{3.2b}$$

$$(\bar{t}_1, \bar{\boldsymbol{x}}_1) = (t_0, \boldsymbol{x}_0), \tag{3.2c}$$

where $t \in \mathcal{T}$, with $\mathcal{T} := \left[\bar{t}_{m+1}, \bar{t}_{m+1} + t_1^{\mathcal{E}}(\bar{t}_{m+1}, \bar{\boldsymbol{x}}_{m+1})\right)$, is a time value for which the system is in the last phase $m+1$ of a cycle.

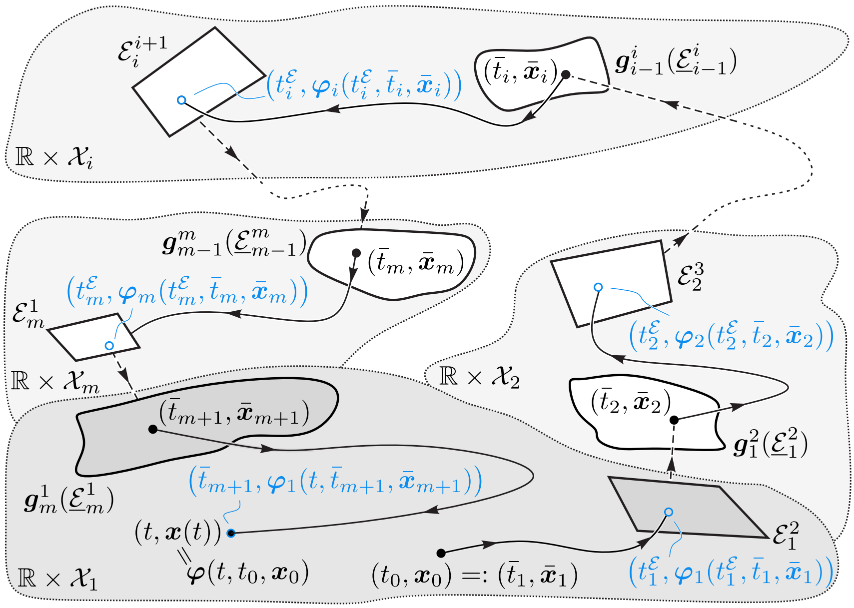

Figure 3.1: Graphical illustration of a recurrent hybrid trajectory of Σ that starts and ends in the same phase $\mathcal{X}_1$.

A graphical interpretation of (3.2) is illustrated in Fig. 3.1. All components of a HDS $\Sigma = (\mathcal{X}, \mathcal{F}, \mathcal{E}, \mathcal{G})$ are recurrent, meaning $\boldsymbol{f}_{m+1} = \boldsymbol{f}_1$ and $e_{m+1}^{m+2} = e_1^2$. However, the transition times $\bar{t}_i$ and states $\bar{\boldsymbol{x}}_i$ vary depending on the trajectory. As a result, the tuples $(\bar{t}_{m+1}, \bar{\boldsymbol{x}}_{m+1})$ and $(\bar{t}_1, \bar{\boldsymbol{x}}_1)$ generally represent different points. A recurrent trajectory is considered periodic when these points coincide.

Definition (Periodic Hybrid Trajectory)**.** *A recurrent hybrid trajectory $\boldsymbol{x}(t)$ is said to be periodic with period $T = \bar{t}_{m+1} - \bar{t}_1$ if $\bar{\boldsymbol{x}}_{m+1} = \bar{\boldsymbol{x}}_1$, and specifically, it holds*

$$\boldsymbol{f}_i\big(\tau_i, \boldsymbol{x}_i(\tau_i)\big) = \boldsymbol{f}_i\big(\tau_i + T, \boldsymbol{x}_i(\tau_i + T)\big), \quad \forall \tau_i \in \mathcal{T}_i,\ \forall i \in \{1, \dots m\}. \quad (3.3)$$

Such a periodic trajectory is also referred to as a (periodic) orbit.

The construction of recurrent hybrid trajectories and orbits focuses on the local properties of Σ, rather than the general existence and uniqueness of solutions, as discussed in [20, 47, 68]. This local perspective provides a sufficient foundation for the theoretical development in the following chapters but necessitates additional assumptions about the trajectory.

Assumption (Recurrent Hybrid Trajectory)**.** *A recurrent hybrid trajectory* $\boldsymbol{x}(t)$*, as defined by* (3.2)*, satisfies the following conditions:*

As1 *It is unique in forward time and yields finite time-to-event values, ensuring that* $t_i^{\mathcal{E}}(\bar{t}_i, \bar{\boldsymbol{x}}_i) < \bar{t}_i + t_i^{max}$ *holds within each phase* i*.*

As2 *It transversally intersects each event set* $\mathcal{E}_i^{i+1}$ *such that* $\dot{e}_i^{i+1} < 0$*.*

As3 *It satisfies* $\overline{\boldsymbol{g}_i^{i+1}(\mathcal{E}_i^{i+1})} \cap \mathcal{E}_{i+1}^{i+2} = \emptyset$ *in all phases, where* $\overline{\boldsymbol{g}_i^{i+1}(\cdot)}$ *denotes the closure of the set* $\boldsymbol{g}_i^{i+1}(\cdot)$*.*

Assumption *As1* ensures a unique mapping of the reset map $\boldsymbol{g}_i^{i+1}$, complementing the previously established uniqueness of the phase flows $\boldsymbol{\varphi}_i$ over their respective intervals $\mathcal{T}_i$. Additionally, the condition $t_i^{\mathcal{E}}(\bar{t}_i, \bar{\boldsymbol{x}}_i) - \bar{t}_i < t_i^{\max}$ guarantees that each event manifold is reached within finite time, thereby resulting in a finite duration $t \in \mathcal{T}$ for the recurrent hybrid trajectory $\boldsymbol{x}(t)$. Assumption *As2* imposes a transversality condition such that

$$\dot{e}_i^{i+1}(t^-, \boldsymbol{x}_i^-) = \left.\frac{\partial e_i^{i+1}}{\partial t}\right|_{(t^-, \boldsymbol{x}_i^-)} + \left.\frac{\partial e_i^{i+1}}{\partial \boldsymbol{x}_i}\right|_{(t^-, \boldsymbol{x}_i^-)} \boldsymbol{f}_i(t^-, \boldsymbol{x}_i^-) \neq 0, \tag{3.4}$$

for each $(t^-, \boldsymbol{x}_i^-) \in \mathcal{E}_i^{i+1}$. This condition guarantees that trajectories in phase i do not *graze* the event surface [47], thereby ensuring the well-posedness of the time-to-event function (3.1). Similar to hypotheses HSH5 in [137], Assumption *As3* ensures that the result of a reset does not immediately trigger another reset, thereby preventing simultaneous multi-events. This assumption further implies that the trajectory $\boldsymbol{x}(t)$ traverses all phases i with a strictly positive duration $\Delta t_i = t_i^{\mathcal{E}}(\bar{t}_i, \bar{\boldsymbol{x}}_i) - \bar{t}_i > 0$.

Under Assumptions *As1*-*As3*, the local behavior of a recurrent hybrid trajectory $\boldsymbol{x}(t)$ of Σ can be analyzed.

Definition (Recurrent Hybrid Flow)**.** *Given a recurrent hybrid trajectory* $\boldsymbol{x}(t)$ *and under Assumptions As1-As3, a recurrent hybrid flow is locally defined by* $\boldsymbol{\varphi} : \mathcal{T} \times \mathcal{T}_0 \times \mathcal{X}_0 \to \mathcal{X}_1$*. Specifically, within a neighborhood* $(\mathcal{T}_0 \times \mathcal{X}_0) \subset (\mathbb{R} \times \mathcal{X}_1)$ *of the initial conditions* $(t_0, \boldsymbol{x}_0)$*, the trajectory is given by* $\boldsymbol{x}(t) := \boldsymbol{\varphi}(t, t_0, \boldsymbol{x}_0)$*, where* $t \in \mathcal{T}$*.*

In general, phase flows $\boldsymbol{\varphi}_i$ and, consequently, hybrid trajectories $\boldsymbol{x}(t)$ cannot be described analytically, requiring the use of numerical integration methods to solve the phase ODEs $\mathcal{F}_i$.

3.2 Event-Based and Time-Based Shooting

This monograph employs variable-step size integrators (ODE solvers) to achieve accurate approximations of the hybrid flow $\boldsymbol{\varphi}(t, t_0, \boldsymbol{x}_0)$. Without loss of generality, the initial time is set to $t_0 = 0$. The problem of determining initial conditions $(t_0 = 0, \boldsymbol{x}_0)$ that correspond to periodic orbits falls within the class of shooting methods. As the name suggests, these methods adjust the initial state $\boldsymbol{x}_0$ to ensure the system reaches a final state $\boldsymbol{x}(T)$ after a period $T > 0$, satisfying the periodicity condition $\boldsymbol{x}(T) = \boldsymbol{x}(0)$.

The following discussion explores different formulations of this shooting problem by defining various root-finding problems of the form $\boldsymbol{r}^{\square}(\boldsymbol{\chi}) = \boldsymbol{0}$, where $\boldsymbol{r}^{\square} : \mathbb{R}^N \to \mathbb{R}^N$, and the superscript $^{\square}$ indicates that its Jacobian $\boldsymbol{R}^{\square} := D\boldsymbol{r}^{\square} \in \mathbb{R}^{N\times N}$ is a square matrix. When $\boldsymbol{r}^{\square}$ is parameterized by a scalar σ, the function is denoted as $\boldsymbol{r} : \mathbb{R}^{N+1} \to \mathbb{R}^N$, as defined in Chapter 2.

Remark 3.2.1. *For now, periodicty is defined on the set $\boldsymbol{g}_m^1(\underline{\mathcal{E}}_m^1)$ with $T = \bar{t}_{m+1}$, yielding $\boldsymbol{x}(T) = \bar{\boldsymbol{x}}_{m+1}$ in (3.2). For an autonomous HDS Σ, Chapter 4 will further explore the case where $T > \bar{t}_{m+1}$, meaning periodicty is not defined on the last hybrid event set.*

Given the definition of a hybrid flow and its recursive computation via (3.2), a straightforward implementation of this implicit function takes the form

$$\boldsymbol{r}^{\square}_{\text{eb,ss}}(\boldsymbol{\chi}_{\text{eb,ss}}) = \underbrace{\boldsymbol{g}_m^1 \circ \boldsymbol{\varphi}_m\left(t_m^{\mathcal{E}}, t_{m-1}^{\mathcal{E}}, \bar{\boldsymbol{x}}_m\right)}_{=\bar{\boldsymbol{x}}_{m+1}} - \bar{\boldsymbol{x}}_1, \tag{3.5a}$$

where the subscript $_{\text{eb,ss}}$ denotes event-based single shooting. The term *single shooting* reflects the fact that the decision variable influences only the initial state $\boldsymbol{\chi}_{\text{eb,ss}} = \bar{\boldsymbol{x}}_1 := \boldsymbol{x}_0$. Meanwhile, the term *event-based* highlights that numerical integrations of $\mathcal{F}_i$ within the hybrid trajectory (3.2) are terminated by events e_1^{i+1} rather than explicit time instances provided to the ODE solver. The problem dimension is $N_{\text{eb,ss}} = n_{\text{x},1}$.

By further introducing the initial states $\bar{\boldsymbol{x}}_i$ for each phase i as decision variables, the problem can be extended to event-based *multiple shooting*:

$$\boldsymbol{r}^{\square}_{\text{eb,ms}}(\boldsymbol{\chi}_{\text{eb,ms}}) = \begin{bmatrix} \boldsymbol{g}_m^1 \circ \boldsymbol{\varphi}_m\left(t_m^{\mathcal{E}}, t_{m-1}^{\mathcal{E}}, \bar{\boldsymbol{x}}_m\right) - \bar{\boldsymbol{x}}_1 \\ \boldsymbol{g}_{m-1}^m \circ \boldsymbol{\varphi}_{m-1}\left(t_{m-1}^{\mathcal{E}}, t_{m-2}^{\mathcal{E}}, \bar{\boldsymbol{x}}_{m-1}\right) - \bar{\boldsymbol{x}}_m \\ \vdots \\ \boldsymbol{g}_2^3 \circ \boldsymbol{\varphi}_2\left(t_2^{\mathcal{E}}, t_1^{\mathcal{E}}, \bar{\boldsymbol{x}}_2\right) - \bar{\boldsymbol{x}}_3 \\ \boldsymbol{g}_1^2 \circ \boldsymbol{\varphi}_1\left(t_1^{\mathcal{E}}, 0, \bar{\boldsymbol{x}}_1\right) - \bar{\boldsymbol{x}}_2 \end{bmatrix}, \tag{3.5b}$$

where the decision variable $\boldsymbol{\chi}_{\mathrm{eb,ms}}^{\mathrm{T}} = [\bar{\boldsymbol{x}}_m^{\mathrm{T}} \;\; \cdots \;\; \bar{\boldsymbol{x}}_1^{\mathrm{T}}]$ now includes all post-event states $\bar{\boldsymbol{x}}_i$. While multiple shooting increases the problem dimension to $N_{\mathrm{eb,ms}} = \sum_{i=1}^{m} n_{\mathrm{x},i}$, it facilitates the computation of sensitivity information within $\boldsymbol{r}_{\mathrm{eb,ms}}^{\square}$ and enables parallel solving of the ODEs $\mathcal{F}_i$.

An alternative to event-based ODE solvers used in (3.5) is the *time-based* approach, where the forward simulation of $\mathcal{F}_i$ is terminated by an explicitly defined time instance t_i. Unlike the state-based approach, this method decouples event detection from the integration process of $\mathcal{F}$ in (3.2b). As a result, the functional dependence of $\{t_i^{\mathcal{E}}\}_{i=1}^{m}$ on $\{(\bar{t}_i, \bar{\boldsymbol{x}}_i)\}_{i=1}^{m}$ is broken. Notably, the definition in (3.1) no longer holds, leading to a situation where the detection of an event is no longer unique. Instead, m independent variables t_i are introduced, along with an additional set of m constraints defined by the event conditions $e_i^{i+1} = 0$ to maintain an indirect coupling. Hence, the time-based single shooting approach is formulated as

$$\boldsymbol{r}_{\mathrm{tb,ss}}^{\square}(\boldsymbol{\chi}_{\mathrm{tb,ss}}) = \begin{bmatrix} \boldsymbol{g}_m^1 \circ \boldsymbol{\varphi}_m\left(t_m, t_{m-1}, \bar{\boldsymbol{x}}_m\right) - \bar{\boldsymbol{x}}_1 \\ e_m^1\big(t_m, \boldsymbol{\varphi}_m\left(t_m, t_{m-1}, \bar{\boldsymbol{x}}_m\right)\big) \\ \vdots \\ e_2^3\big(t_2, \boldsymbol{\varphi}_2\left(t_2, t_1, \bar{\boldsymbol{x}}_2\right)\big) \\ e_1^2\big(t_1, \boldsymbol{\varphi}_1\left(t_1, 0, \bar{\boldsymbol{x}}_1\right)\big) \end{bmatrix}, \tag{3.6a}$$

where the decision variable $\boldsymbol{\chi}_{\mathrm{tb,ss}}^{\mathrm{T}} = [t_m \;\; \cdots \;\; t_1 \;\; \bar{\boldsymbol{x}}_1^{\mathrm{T}}]$ includes the integration times, yielding a problem size of $N_{\mathrm{tb,ss}} = m + n_{\mathrm{x},1}$.

The time-based multiple shooting approach further decouples each phase i and is given by

$$\boldsymbol{r}_{\mathrm{tb,ms}}^{\square}(\boldsymbol{\chi}_{\mathrm{tb,ms}}) = \begin{bmatrix} \boldsymbol{g}_m^1 \circ \boldsymbol{\varphi}_m\left(t_m, t_{m-1}, \bar{\boldsymbol{x}}_m\right) - \bar{\boldsymbol{x}}_1 \\ e_m^1\big(t_m, \boldsymbol{\varphi}_m\left(t_m, t_{m-1}, \bar{\boldsymbol{x}}_m\right)\big) \\ \boldsymbol{g}_{m-1}^m \circ \boldsymbol{\varphi}_{m-1}\left(t_{m-1}, t_{m-2}, \bar{\boldsymbol{x}}_{m-1}\right) - \bar{\boldsymbol{x}}_m \\ e_{m-1}^m\big(t_{m-1}, \boldsymbol{\varphi}_{m-1}\left(t_{m-1}, t_{m-2}, \bar{\boldsymbol{x}}_{m-1}\right)\big) \\ \vdots \\ \boldsymbol{g}_1^2 \circ \boldsymbol{\varphi}_1\left(t_1, 0, \bar{\boldsymbol{x}}_1\right) - \bar{\boldsymbol{x}}_2 \\ e_1^2\big(t_1, \boldsymbol{\varphi}_1\left(t_1, 0, \bar{\boldsymbol{x}}_1\right)\big) \end{bmatrix}, \tag{3.6b}$$

where the decision variable $\boldsymbol{\chi}_{\mathrm{tb,ms}}^{\mathrm{T}} = [t_m \;\; \bar{\boldsymbol{x}}_m^{\mathrm{T}} \;\; \cdots \;\; t_1 \;\; \bar{\boldsymbol{x}}_1^{\mathrm{T}}]$ includes the integration times, leading to a problem size of $N_{\mathrm{tb,ms}} = m + \sum_{i=1}^{m} n_{\mathrm{x},i}$.

The advantage of event-based integration in (3.5) is that it keeps the root-finding problem low dimensional. Notably, the dimension of the single shooting implementation (3.5a) is independent of the number of hybrid phases m in Σ. This independence makes it particularly useful for finding close-to-periodic solutions, as even an approximate solution $\tilde{\boldsymbol{\chi}}_{\mathrm{eb,ss}}$ that yields $\boldsymbol{r}^{\square}_{\mathrm{eb,ss}}(\boldsymbol{\chi}_{\mathrm{eb,ss}}) \approx \mathbf{0}$ still represents (in most cases) a hybrid trajectory of Σ. However, event-based integration presents two major drawbacks when exploring the solution set

$$\mathcal{S}_{\mathrm{eb}} := \boldsymbol{r}_{\mathrm{eb}}^{-1}(\mathbf{0}) = \left\{\boldsymbol{\nu}_{\mathrm{eb}} \in \mathbb{R}^{N+1} \mid \boldsymbol{r}_{\mathrm{eb}}(\boldsymbol{\nu}_{\mathrm{eb}}) = \mathbf{0}\right\}. \tag{3.7}$$

In practice, solutions in $\mathcal{S}_{\mathrm{eb}}$ are often adjacent to points $\boldsymbol{\nu}^*_{\mathrm{eb}}$ [1, 3, 43, 116], where:

- *Grazing* occurs, i.e., $\dot{e}_i^{i+1} \to 0$, violating Assumption $As2$.
- *Phase durations vanish*, i.e., $\Delta t_i \to 0$, violating Assumption $As3$.

At grazing points $\boldsymbol{\nu}^*_{\mathrm{eb}}$, the sign of $\dot{e}_i^{i+1}$ changes within Σ, causing the solution set $\mathcal{S}_{\mathrm{eb}}$ in (3.5) to become disconnected at $\boldsymbol{\nu}^*_{\mathrm{eb}}$. Beyond this point, no local solutions exist that satisfy $\dot{e}_i^{i+1} < 0$. Moreover, the state-based maps (3.5) are non-differentiable at $\boldsymbol{\nu}^*_{\mathrm{eb}}$ because the implicit function theorem does not apply. This issue is explored further for autonomous HDS Σ in Section 4.3.1. The second issue arises from the vanishing local event time Δt_i, causing numerical inaccuracies within the respective ODE solver [125]. The ODE solver typically executes a first integration step to obtain $\dot{e}_i^{i+1}$ which becomes impractical for $\Delta t_i \to 0$.

In contrast, time-based integration (3.6) does not explicitly encode the event activation direction $\dot{e}_i^{i+1}$ or the minimum phase duration t_i, as defined in (3.1). As a result, the solution set

$$\mathcal{S}_{\mathrm{tb}} := \boldsymbol{r}_{\mathrm{tb}}^{-1}(\mathbf{0}) = \left\{\boldsymbol{\nu}_{\mathrm{tb}} \in \mathbb{R}^{N+1} \mid \boldsymbol{r}_{\mathrm{tb}}(\boldsymbol{\nu}_{\mathrm{tb}}) = \mathbf{0}\right\}. \tag{3.8}$$

for time-based integration is generally broader than $\mathcal{S}_{\mathrm{eb}}$ for event-based integration. Specifically, the phase trajectory $\boldsymbol{x}_i$ in (3.6) can also be computed in reverse, for $\Delta t_i < 0$. Consequently, time-based integration is unaffected by issues related to grazing and vanishing phase durations (i.e., violations of Assumptions *As2* and *As3*). However, a solution to (3.6) may correspond to an event activation with $\dot{e}_i^{i+1} \geq 0$ or may overlook prior activation instances where $\dot{e}_i^{i+1} < 0$, as t_i does not necessarily correspond to the minimum in (3.1).

A comparative overview of event-based and time-based integration is provided in Table 3.2.

	event-based	**time-based**
Termination of ODE solver	• at events $e_i^{i+1}(t, \boldsymbol{x}_i) = 0$ • $t_i(t, \boldsymbol{x}_i)$ is implicitly defined by (3.1)	• at specific time t_i • t_i is an independent variable
Assumptions	*As1*, *As2*, *As3*	*As1*
Restrictions	• no grazing points *As2* ($\dot{e}_i^{i+1} < 0$) • no vanishing phase durations *As3* ($\Delta t_i > 0$)	• t_i may not attain its infimum as defined in (3.1) • proper event activation, i.e., $e_i^{i+1} = 0$, is only guaranteed at zeros of $\boldsymbol{r}^\square$
Single shooting	$N = n_{\mathrm{x},1}$	$N = m + n_{\mathrm{x},1}$
Multiple shooting	$N = \sum_{i=1}^{m} n_{\mathrm{x},i}$	$N = m + \sum_{i=1}^{m} n_{\mathrm{x},i}$
Solution set $\mathcal{S}$	$\mathcal{S}_{\mathrm{eb}}$ may be disconnected because of its restrictions.	$\mathcal{S}_{\mathrm{tb}}$ is the larger solution set. It holds $\mathcal{S}_{\mathrm{eb}} \subseteq \mathcal{S}_{\mathrm{tb}}$.

Table 3.2: A comparison between event-based and time-based integration and their impact on the properties of $\boldsymbol{r}^\square$ and solution set $\mathcal{S} = \boldsymbol{r}^{-1}(\boldsymbol{0})$. Note that the solution sets become equivalent, i.e., $\mathcal{S}_{\mathrm{eb}} = \mathcal{S}_{\mathrm{tb}}$, under full compliance with all assumptions and restrictions.

3.3 Summary

The solution set $\mathcal{S}_{\mathrm{eb}}$ of the event-based (eb) implementation (3.5) is a subset of the solution set $\mathcal{S}_{\mathrm{tb}}$ of the time-based (tb) implementation (3.6). Moreover, under conditions of no grazing and strictly positive time durations, ensuring that the infimum is attained in accordance with (3.1), the two solution sets become equivalent.

Given the superior numerical robustness of ODE solvers and the stronger connectedness of periodic orbits, the time-based shooting approach is employed throughout this monograph for continuation and optimization problems.

Chapter 4

Conservative Hybrid Dynamical Systems

This chapter revisits the findings of [3], focusing on periodic orbits in conservative hybrid dynamical systems (cHDS). Section 4.1 begins by defining an autonomous hybrid dynamical system as a specific subclass of the time-variant dynamics introduced in Chapter 3. To accommodate this, the notation for time-variant dynamics (Table 3.1) is extended with additional symbols for autonomous HDS, as defined in Table 4.1. The following sections analyze the autonomous hybrid flow by first reviewing well-established properties of ODEs and then extending these concepts to HDSs. These fundamental properties are essential in establishing the groundwork for the discussion on the local existence and connectedness of periodic orbits in Section 4.2. The chapter concludes by exploring how numerical continuation techniques, particularly in combination with time-based shooting methods, facilitate the analysis of conservative orbits.

4.1 Autonomous Recurrent Hybrid Dynamics

An *autonomous hybrid model* $\Sigma = (\mathcal{X}, \mathcal{F}, \mathcal{E}, \mathcal{G})$ follows the structure defined in Chapter 3. Unlike time-variant dynamics, the phase dynamics $\mathcal{F}$ and event sets $\mathcal{E}$ are independent of time. This implies autonomous phase dynamics $\dot{\boldsymbol{x}}_i = \boldsymbol{f}_i(\boldsymbol{x}_i)$, with vector field $\boldsymbol{f}_i : \mathcal{X}_i \to T\mathcal{X}_i$, and a time-invariant event set $\mathcal{E}_i^{i+1}$, which coincides with $\underline{\mathcal{E}}_i^{i+1}$, projecting onto $\mathcal{X}_i$. Specifically, with the redefined event function $e_i^{i+1} : \mathcal{X}_i \to \mathbb{R}$, assuming $De_i^{i+1}(\boldsymbol{x}_i) \neq \boldsymbol{0}$ for all $\boldsymbol{x}_i \in \mathcal{E}_i^{i+1}$, the corresponding event set forms an embedded codimension-one submanifold defined by $\mathcal{E}_i^{i+1} = \left\{\boldsymbol{x}_i \in \mathcal{X}_i \;\middle|\; e_i^{i+1}(\boldsymbol{x}_i) = 0\right\}$.

Furthermore, the time-invariant $\mathcal{E}_i^{i+1}$ simplifies the definition of the phase-i time-to-event function $t_i^{\mathcal{E}}$, introducing the *local* time-to-event function $\Delta t_i^{\mathcal{E}} : \mathcal{X}_i \to \mathbb{R} \cup \{\infty\}$, which depends solely on the state:

$$\Delta t_i^{\mathcal{E}}(\bar{\boldsymbol{x}}_i) := \inf\{t \geq 0 | \boldsymbol{\varphi}_i(t, 0, \bar{\boldsymbol{x}}_i) \in \mathcal{E}_i^{i+1}\}. \tag{4.1}$$

For an autonomous ODE $\mathcal{F}_i$, the phase flow remains independent of the initial time $\bar{t}_i$, i.e., $\boldsymbol{\varphi}_i(t, \bar{t}_i, \bar{\boldsymbol{x}}_i) = \boldsymbol{\varphi}_i(t, 0, \bar{\boldsymbol{x}}_i)$ for all $\bar{t}_i \in \mathbb{R}$. Thus, in the autonomous case, the time spent in each hybrid phase is equivalently given by the phase duration $\Delta t_i = t_i^{\mathcal{E}}(\bar{t}_i, \bar{\boldsymbol{x}}_i) - \bar{t}_i$ or $\Delta t_i = \Delta t_i^{\mathcal{E}}(\bar{\boldsymbol{x}}_i)$.

Symbol	Brief description
$\boldsymbol{f}_i \in C^1$, $\boldsymbol{f}_i : \mathcal{X}_i \to T\mathcal{X}_i$	*Autonomous* phase vector field
$\mathcal{F}_i : \dot{\boldsymbol{x}}_i = \boldsymbol{f}_i(\boldsymbol{x}_i)$	*Autonomous* phase dynamics
$e_i^{i+1} \in C^1$, $e_i^{i+1} : \mathcal{X}_i \to \mathbb{R}$	*Autonomous* event function
$\mathcal{E}_i^{i+1} = \underline{\mathcal{E}}_i^{i+1} \subset \mathcal{X}_i$	Event manifold
$\mathcal{X}_0 \subset \mathcal{X}_1$	Neighborhood of $\boldsymbol{x}_0$
$\Delta t_i^{\mathcal{E}} : \mathcal{X}_i \to \mathbb{R} \cup \{\infty\}$	*Local* time-to-event function (4.1)
$\boldsymbol{\Phi}_i \widehat{=} \partial \boldsymbol{\varphi}_i / \partial \bar{\boldsymbol{x}}_i$	Fundamental matrix of phase i (4.4)
$\boldsymbol{S}_i^{i+1}$	Saltation matrix (4.7)
$\boldsymbol{\Phi} \widehat{=} \partial \boldsymbol{\varphi} / \partial \boldsymbol{x}_0$	Fundamental matrix of the hybrid flow (4.8)
$H_i : \mathcal{X}_i \to \mathbb{R}$	Phase first integral
$k_i \in \mathbb{N}$	Number of H_i
$\mathcal{H} := \{H_i\}_1^m$	Hybrid first integral
$k_{\mathcal{H}} \in \mathbb{N}$	Dimension of $\mathcal{H}$
$\Sigma^{\mathcal{H}}$	Conservative HDS
$\mathcal{A} \subset \mathcal{X}_1$	Poincaré section
$a : \mathcal{X}_1 \to \mathbb{R}$	Anchor function
$\Delta t_1^{\mathcal{A}} : \mathcal{X}_1 \to \mathbb{R}$	*Local* time-to-anchor function
$t^{\mathcal{A}} : \mathcal{X}_1 \to \mathbb{R}$	*Global* time-to-anchor function
$\mathcal{A}_0 = \mathcal{X}_0 \cap \mathcal{A}$	Initial subset of $\mathcal{A}$
$\boldsymbol{P} : \mathcal{A}_0 \to \mathcal{A}$	Poincaré map
$\boldsymbol{I}$	Identity matrix (4.13)
$T \in \mathbb{R}$	Period time (4.15)
$\boldsymbol{\Phi}_T := \boldsymbol{\Phi}(T, 0, \boldsymbol{x}_0)$	Monodromy matrix
$\bar{H} \in \mathbb{R}$	Level set of $\mathcal{H}$

Table 4.1: These additional symbols for (conservative) autonomous HDSs complement Table 3.1 and are used throughout this monograph.

In summary, the autonomous hybrid dynamical system takes the form:

Time-Invariant Hybrid Dynamical System

$$\Sigma : \begin{cases} \mathcal{X} = \left\{\mathcal{X}_i\right\}_{i=1}^{m} & : \mathcal{X}_i \subset \mathbb{R}^{n_{\mathrm{x},i}} \\ \mathcal{F} = \left\{\mathcal{F}_i\right\}_{i=1}^{m} & : \mathcal{F}_i = \left\{\dot{\boldsymbol{x}}_i = \boldsymbol{f}_i(\boldsymbol{x}_i)\right\} \\ \mathcal{E} = \left\{\mathcal{E}_i^{i+1}\right\}_{i=1}^{m} & : \mathcal{E}_i^{i+1} = \left\{\boldsymbol{x}_i \in \mathcal{X}_i \mid e_i^{i+1}(\boldsymbol{x}_i) = 0\right\} \\ \mathcal{G} = \left\{\mathcal{G}_i^{i+1}\right\}_{i=1}^{m} & : \mathcal{G}_i^{i+1} = \left\{\boldsymbol{x}_{i+1}^{+} = \boldsymbol{g}_i^{i+1}(\boldsymbol{x}_i^{-})\right\} \end{cases} .$$

For completeness, the recursive definition of a recurrent hybrid trajectory is restated for the autonomous case:

$$\boldsymbol{x}(t) = \boldsymbol{\varphi}_1\left(t, \bar{t}_{m+1}, \bar{\boldsymbol{x}}_{m+1}\right), \tag{4.2a}$$

$$\left\{ \begin{aligned} \bar{t}_{i+1} &= \bar{t}_i + \Delta t_i^{\mathcal{E}}(\bar{\boldsymbol{x}}_i), \\ \bar{\boldsymbol{x}}_{i+1} &= \boldsymbol{g}_i^{i+1} \circ \boldsymbol{\varphi}_i\left(\bar{t}_{i+1}, \bar{t}_i, \bar{\boldsymbol{x}}_i\right), \end{aligned} \right\}_{i=1}^{m}, \tag{4.2b}$$

$$(\bar{t}_1, \bar{\boldsymbol{x}}_1) = (0, \boldsymbol{x}_0), \tag{4.2c}$$

where $\bar{t}_1 = t_0$ is set to zero for simplicity and due to Σ's time invariance.

Remark 4.1.1. *Based on Assumptions As1-As3 from Chapter 3, the event times $\bar{t}_{i+1} = t_i^{\mathcal{E}}(\bar{t}_i, \bar{\boldsymbol{x}}_i) = \bar{t}_i + \Delta t_i^{\mathcal{E}}(\bar{\boldsymbol{x}}_i)$ are well-defined in all phases. Specifically, the no-grazing condition in Assumption As2 requires the vector field $\boldsymbol{f}_i$ to point outward from the event manifold $\mathcal{E}_i^{i+1}$, ensuring that*

$$\dot{e}_i^{i+1}(\boldsymbol{x}_i^-) = De_i^{i+1}(\boldsymbol{x}_i^-) \cdot \boldsymbol{f}_i(\boldsymbol{x}_i^-) < 0, \tag{4.3}$$

for each $\boldsymbol{x}_i^- \in \mathcal{E}_i^{i+1}$. By the implicit function theorem, each value of $\bar{t}_i$ is determined solely by the initial state $\boldsymbol{x}_0$ as it evolves through the hybrid trajectory $\boldsymbol{x}(t)$. This dependency is particularly evident in the recursive structure of (4.2b)*. Consequently, the initial state $\bar{\boldsymbol{x}}_i$ of each phase is influenced by the overall initial state $\boldsymbol{x}_0 \in \mathcal{X}_1$. To emphasize this relationship, the initial times are sometimes denoted as $\bar{t}_i(\boldsymbol{x}_0)$, and the initial state of a phase as $\bar{\boldsymbol{x}}_i(\boldsymbol{x}_0)$.*

4.1.1 Flow Derivatives

The following discusses the structure of phase and hybrid flow derivatives with respect to initial states $\bar{\boldsymbol{x}}_i$. Assumptions *As1*-*As3* indicate that the hybrid flow $\boldsymbol{\varphi}(t, 0, \boldsymbol{x}_0)$ is continuously differentiable in both time and state (Remark 5 [52]).

Given that $\boldsymbol{f}_i \in C^1$, the phase flow $\boldsymbol{\varphi}_i(t, \bar{t}_i, \bar{\boldsymbol{x}}_i)$ is continuously differentiable with respect to the initial state $\bar{\boldsymbol{x}}_i \in \mathcal{X}_i$ (§32.6 [11]). Consequently, the so-called fundamental matrix $\boldsymbol{\Phi}_i$ for a phase i is well-defined by

$$\boldsymbol{\Phi}_i\left(t, \bar{t}_i, \bar{\boldsymbol{x}}_i\right) = \left.\frac{\partial \boldsymbol{\varphi}_i\left(\tau, \tau_i, \boldsymbol{x}_i\right)}{\partial \boldsymbol{x}_i}\right|_{(t, \bar{t}_i, \bar{\boldsymbol{x}}_i)}, \quad t \in \mathcal{T}_i. \tag{4.4}$$

Notably, in an autonomous ODE, the phase flow $\boldsymbol{\varphi}_i$ and thus, the fundamental matrix $\boldsymbol{\Phi}_i$ are independent of the choice of initial time $\bar{t}_i$. Hence, the composition property[1] [33] for autonomous ODEs directly follows from a time shift $\bar{\tau}$, where $(\bar{\tau} \leq t) \in \mathcal{T}_i$, such that

$$\boldsymbol{\Phi}_i\left(t, \bar{t}_i, \bar{\boldsymbol{x}}_i\right) = \boldsymbol{\Phi}_i\left(t, \bar{\tau}, \boldsymbol{x}_i(\bar{\tau})\right) \cdot \boldsymbol{\Phi}_i\left(\bar{\tau}, \bar{t}_i, \bar{\boldsymbol{x}}_i\right). \tag{4.5}$$

A similar chained structure arises when computing state derivatives at time $t \in \mathcal{T}_{i+1}$ over a phase transition of Σ (see Appendix A.1 for a detailed derivation):

$$\begin{aligned} \left.\frac{\mathrm{d}}{\mathrm{d}\boldsymbol{x}_i} \boldsymbol{\varphi}_{i+1}\left(\tau, \tau_{i+1}, \boldsymbol{x}_{i+1}\right)\right|_{(t, \bar{t}_{i+1}, \bar{\boldsymbol{x}}_{i+1})} &= \boldsymbol{\Phi}_{i+1}\left(t, \bar{t}_{i+1}, \bar{\boldsymbol{x}}_{i+1}\right) \\ &\quad \cdot \boldsymbol{S}_i^{i+1} \cdot \boldsymbol{\Phi}_i\left(\bar{t}_{i+1}, \bar{t}_i, \bar{\boldsymbol{x}}_i\right), \end{aligned} \tag{4.6}$$

where $\boldsymbol{S}_i^{i+1}$ is the so-called saltation matrix [20, 76, 82], which describes how perturbations of a trajectory are carried over from phase i into $i+1$. With the shorthand notation

$$\begin{aligned} &\boldsymbol{x}_i^- := \boldsymbol{x}_i(t_i^{\mathcal{E}}(\bar{\boldsymbol{x}}_i)), \quad && \boldsymbol{x}_{i+1}^+ := \bar{\boldsymbol{x}}_{i+1} \overset{(4.2\mathrm{b})}{=} \boldsymbol{g}_i^{i+1}(\boldsymbol{x}_i^-), \quad && \boldsymbol{G}_i^{i+1} := \left.\frac{\partial \boldsymbol{g}_i^{i+1}(\boldsymbol{x}_i)}{\partial \boldsymbol{x}_i}\right|_{\boldsymbol{x}_i^-}, \\ &\boldsymbol{f}_i^- := \boldsymbol{f}_i(\boldsymbol{x}_i^-), && \boldsymbol{f}_{i+1}^+ := \boldsymbol{f}_{i+1}(\boldsymbol{x}_{i+1}^+), && De_i^{i+1} := \left.\frac{\partial e_i^{i+1}(\boldsymbol{x}_i)}{\partial \boldsymbol{x}_i}\right|_{\boldsymbol{x}_i^-}, \end{aligned}$$

the saltation matrix takes the form

$$\boldsymbol{S}_i^{i+1} = \boldsymbol{G}_i^{i+1} + \frac{\left(\boldsymbol{f}_{i+1}^+ - \boldsymbol{G}_i^{i+1} \boldsymbol{f}_i^-\right) De_i^{i+1}}{De_i^{i+1} \boldsymbol{f}_i^-}. \tag{4.7}$$

The saltation matrix (4.7) can be derived through calculus using the implicit function theorem or geometrically via first-order perturbations [76, 82, 96],

[1] (4.5) is referred to as transition property in (Chapter 7 [82]).

as detailed in Appendix A.1. Note that Assumptions *As1*-*As3* collectively ensure the well-defined nature of the saltation matrix $\boldsymbol{S}_i^{i+1}$ [15]. Specifically, Assumption *As2* ensures that $\dot{e}_i^{i+1} \neq 0$ in the denominator of (4.7). Hence, exploiting (4.5) and (4.6) in (4.2), the hybrid fundamental matrix $\boldsymbol{\Phi}$ is well-defined for any $t \in \mathcal{T}$ and $\boldsymbol{x}_0 \in \mathcal{X}_0$ (Section 7.1.4 [20]):

$$\boldsymbol{\Phi}(t, 0, \boldsymbol{x}_0) = \left.\frac{\partial \boldsymbol{\varphi}(\tau, \tau_0, \boldsymbol{x})}{\partial \boldsymbol{x}}\right|_{(t,0,\boldsymbol{x}_0)} \tag{4.8a}$$

$$= \boldsymbol{\Phi}_1(t, \bar{t}_{m+1}, \bar{\boldsymbol{x}}_{m+1})\bar{\boldsymbol{\Phi}}_{m+1}, \tag{4.8b}$$

$$\bar{\boldsymbol{\Phi}}_{i+1} = \boldsymbol{S}_i^{i+1}\boldsymbol{\Phi}_i(\bar{t}_{i+1}, \bar{t}_i, \bar{\boldsymbol{x}}_i), \quad i = 1, \ldots, m. \tag{4.8c}$$

Remark 4.1.2. *While the fundamental matrix $\boldsymbol{\Phi}_i(t, \bar{t}_i, \bar{\boldsymbol{x}}_i)$ of a single phase i is non-singular for all $t \in \mathcal{T}_i$ (Lemma 7.1 [82]), the hybrid fundamental matrix $\boldsymbol{\Phi}(t, 0, \boldsymbol{x}_0)$ can be singular depending on the projections of the saltation matrices $\boldsymbol{S}_i^{i+1}$ (Theorem 3.1 [15]). Hence, while hybrid flows $\boldsymbol{\varphi}(t, 0, \boldsymbol{x}_0)$ are unique in forward time (As1), a solution of Σ is in general not unique in the reverse time direction.*

4.1.2 First Integrals and Symmetries

This section examines the conservation properties of hybrid dynamical systems, starting again with a single phase. The dynamics $\mathcal{F}_i$ of a phase are considered conservative if there exists a non-trivial[2] first integral $H_i : \mathcal{X}_i \to \mathbb{R}$ of class C^1, such that H_i remains constant along solutions $\boldsymbol{x}_i(t)$ [11, 108, 124]. This leads to

$$\begin{aligned} H_i(\boldsymbol{x}_i(t)) &= \text{const.} \quad \forall t \in \mathcal{T}_i, \\ \overset{\frac{\mathrm{d}}{\mathrm{d}t}}{\Rightarrow} \dot{H}_i(\boldsymbol{x}_i(t)) &= DH_i(\boldsymbol{x}_i(t)) \cdot \boldsymbol{f}_i(\boldsymbol{x}_i(t)) = 0, \end{aligned} \tag{4.9}$$

where $DH_i(\boldsymbol{x}_i(t)) = {}^{\partial H_i(\boldsymbol{x})}/_{\partial \boldsymbol{x}}|_{\boldsymbol{x}_i(t)}$, and the initial condition $\bar{\boldsymbol{x}}_i$ is arbitrarily chosen within $\mathcal{X}_i$. A system with a conserved quantity H_i is often described as having a conservative vector field $\boldsymbol{f}_i$ and conservative dynamics $\mathcal{F}_i$.

Remark 4.1.3. *For a dynamical system and its solutions to be conservative,* (4.9) *must hold for all $\boldsymbol{x}_i \in \mathcal{X}_i$. On the other hand, for a non-conservative system, it is still possible to find local first integrals, for which particular solutions $\boldsymbol{x}_i(t)$ are conservative. In the context of periodic orbits, these solutions are typically isolated limit cycles [25, 27, 48].*

[2]A trivial first integral H_i is a constant function with a vanishing derivative, i.e., $DH_i \equiv \boldsymbol{0}$. For this reason, non-trivial H_i are commonly referred to as *non-constant* [11].

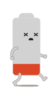

A first integral H_i of conservative dynamics $\mathcal{F}_i$ is generally not unique, since $\tilde{H}_i = \alpha H_i$ with $\alpha \in \mathbb{R}\backslash\{0\}$ is also a first integral. Only if there exists another first integral $\tilde{H}_i$, with $D\tilde{H}_i$ being pointwise linearly independent of DH_i, $\mathcal{F}_i$ is said to have more than one (functionally) *independent* first integral [97]. The presence of multiple independent first integrals in phase i is indicated with subscripts, i.e., $\{H_{i,j}\}_{j=1}^{k_i}$, where $H_{i,1} := H_i$, $H_{i,2} := \tilde{H}_i$, and so forth.

Remark 4.1.4. *The dimension $n_{\mathrm{x},i}$ of each phase domain $\mathcal{X}_i$ must be strictly greater than k_i as $n_{\mathrm{x},i} = k_i$ would fully define the phase dynamics, leading to a trivial vector field $\boldsymbol{f}_i \equiv \mathbf{0}$. This can be easily shown, since all $H_{i,j}$ are independent and $DH_{i,j}\boldsymbol{f}_i = 0$ holds for all $j \in \{1, \dots, k_i = n_{\mathrm{x},i}\}$ at any time t.*

Definition (Conservative Hybrid Dynamical System)**.** *An autonomous hybrid dynamical system Σ is classified as a conservative HDS (cHDS) with a hybrid first integral $\mathcal{H} := \{H_i\}_{i=1}^m$ if:*

Def1 *Each $H_i : \mathcal{X}_i \to \mathbb{R}$ is a continuously differentiable non-trivial first integral of $\mathcal{F}_i$.*

Def2 *The first integral is preserved across discrete transitions, i.e., $H_{i+1}(\boldsymbol{x}_{i+1}^+) = H_i(\boldsymbol{x}_i^-)$ for all reset maps $\boldsymbol{x}_{i+1}^+ = \boldsymbol{g}_i^{i+1}(\boldsymbol{x}_i^-)$ with $\boldsymbol{x}_i^- \in \mathcal{E}_i^{i+1}$.*

In analogy to the recurrent hybrid flow, where $\boldsymbol{f}_{m+1} = \boldsymbol{f}_1$, a conservative HDS satisfies $H_{m+1} = H_1$. The definition of a cHDS implies that for any $\boldsymbol{x}_0 \in \mathcal{X}_0$ its first integral H_1 in phase $i = 1$ is constant along the hybrid flow $\boldsymbol{\varphi}(t, 0, \boldsymbol{x}_0)$ for all times $t \in \mathcal{T}$. Furthermore, the hybrid first integral $\mathcal{H}$ only contains first integrals H_i that also fulfill Definition *Def2*. Hence, not all first integrals $\{H_{i,j}\}_{j=1}^{k_i}$ of phase i are also first integrals of the conservative HDS.

Lemma 4.1.1. *The number $k_{\mathcal{H}}$ of independent first integrals $\{H_{i,j}\}_{j=1}^{k_{\mathcal{H}}}$, satisfying definitions Def1 and Def2, remains constant across hybrid phases i. In particular, it holds $k_{\mathcal{H}} \leq \{k_i\}_{i=1}^m$.*

Proof. Under Assumption *As1*, recurrent hybrid flows are unique in forward time. Thus, two independent first integrals $H_{i,1}$ and $H_{i,2}$ in phase i cannot both map to a single first integral H_{i+1} via Definition *Def2*. Consequently, if phase i has $k_{\mathcal{H}}$ independent first integrals satisfying *Def2*, then phases $i-1$ and $i+1$ must also have exactly $k_{\mathcal{H}}$ independent first integrals. $\square$

A conservative hybrid dynamical system is denoted as $\Sigma^{\mathcal{H}}$ to emphasize the presence of a hybrid first integral $\mathcal{H}$.

Remark 4.1.5. *Determining first integrals for a given dynamical system is a challenging problem and an active area of research [50, 98]. One notable approach involves leveraging continuous symmetries $\boldsymbol{\theta} : \mathcal{X}_1 \to \mathcal{X}_1$ [81]. These symmetries obey to the equation $\boldsymbol{\theta} \circ \boldsymbol{\varphi}\big(t, 0, \boldsymbol{x}_0\big) = \boldsymbol{\varphi}\big(t, 0, \boldsymbol{\theta}(\boldsymbol{x}_0)\big)$ within Σ, and their existence implies the presence of a first integral, as indicated by Noether's theorem [49]. Of particular importance among these symmetries are so-called cyclic variables, which generate first integrals of generalized momenta in Hamiltonian systems [7, 8, 29].*

4.1.3 Transition Properties

The following restates well-known results from autonomous ODEs with first integrals [11, 33, 55, 82] and demonstrates that these results also apply to cHDSs $\Sigma^{\mathcal{H}}$.

Lemma 4.1.2. *For any conservative dynamics $\mathcal{F}_i$, with a first integral $H_i : \mathcal{X}_i \to \mathbb{R}$ and its phase trajectory $\boldsymbol{x}_i(t)$, originating from arbitrary $(\bar{t}_i, \bar{\boldsymbol{x}}_i) \in \mathbb{R} \times \mathcal{X}_i$, with $t \in \mathcal{T}_i$, it holds*

$$\boldsymbol{f}_i(\boldsymbol{x}_i(t)) = \boldsymbol{\Phi}_i(t, \bar{t}_i, \bar{\boldsymbol{x}}_i)\boldsymbol{f}_i(\bar{\boldsymbol{x}}_i), \tag{4.10a}$$

$$DH_i(\bar{\boldsymbol{x}}_i) = DH_i(\boldsymbol{x}_i(t))\boldsymbol{\Phi}_i(t, \bar{t}_i, \bar{\boldsymbol{x}}_i). \tag{4.10b}$$

Proof. For a fixed initial condition $(\bar{t}_i, \bar{\boldsymbol{x}}_i)$, the autonomous flow $\boldsymbol{\varphi}_i$ at any $t \in \mathcal{T}_i$ can be rewritten using a time shift $\bar{\tau}$ (§9.2 [11]) such that

$$\begin{aligned}
&\boldsymbol{x}_i(t) = \boldsymbol{\varphi}_i\big(t, \bar{\tau}, \boldsymbol{\varphi}_i(\bar{\tau}, \bar{t}_i, \bar{\boldsymbol{x}}_i)\big) \quad \forall \bar{\tau} \in [\bar{t}_i, t], \\
&\overset{\frac{\mathrm{d}}{\mathrm{d}\bar{\tau}}}{\Rightarrow} \mathbf{0} = \left.\frac{\partial \boldsymbol{\varphi}_i}{\partial \tau}\right|_{(t, \bar{\tau}, \bar{\boldsymbol{x}}_i)} \left.\frac{\partial (t-\tau)}{\partial \tau}\right|_{\bar{\tau}} + \left.\frac{\partial \boldsymbol{\varphi}_i}{\partial \boldsymbol{x}}\right|_{(t, \bar{\tau}, \bar{\boldsymbol{x}}_i)} \left.\frac{\partial \boldsymbol{\varphi}_i}{\partial \tau}\right|_{(\bar{\tau}, \bar{t}_i, \bar{\boldsymbol{x}}_i)}, \\
&\qquad \mathbf{0} = -\boldsymbol{f}_i(\boldsymbol{x}_i(t)) + \boldsymbol{\Phi}_i(t, \bar{\tau}, \bar{\boldsymbol{x}}_i)\boldsymbol{f}_i(\boldsymbol{x}_i(\bar{\tau})).
\end{aligned}$$

For $\bar{\tau} = \bar{t}_i$, this yields property (4.10a). The second property in (4.10b) is derived by considering neighboring phase flows of a first integral H_i and fixing the time t:

$$\begin{aligned}
&H_i(\boldsymbol{\varphi}_i(t, \bar{t}_i, \bar{\boldsymbol{x}}_i)) = H_i(\bar{\boldsymbol{x}}_i) \quad \forall \bar{\boldsymbol{x}}_i \in \mathcal{X}_i, \\
&\overset{\frac{\mathrm{d}}{\mathrm{d}\bar{\boldsymbol{x}}_i}}{\Rightarrow} \left.\frac{\partial H_i(\boldsymbol{x}_i)}{\partial \boldsymbol{x}_i}\right|_{\boldsymbol{x}_i(t)} \left.\frac{\partial \boldsymbol{\varphi}_i(\tau, \tau_i, \boldsymbol{x}_i)}{\partial \boldsymbol{x}_i}\right|_{(t, \bar{t}_i, \bar{\boldsymbol{x}}_i)} = \left.\frac{\partial H_i(\boldsymbol{x}_i)}{\partial \boldsymbol{x}_i}\right|_{\bar{\boldsymbol{x}}_i}.
\end{aligned}$$

$\square$

Lemma 4.1.3. *For a cHDS $\Sigma^{\mathcal{H}}$, with first integrals $H_i \in \mathcal{H}$, and its recurrent hybrid trajectory $\boldsymbol{x}(t)$, with $t \in \mathcal{T}$, it holds*

$$\boldsymbol{f}_1(\boldsymbol{x}(t)) = \boldsymbol{\Phi}(t, \bar{t}_i, \boldsymbol{x}_0)\boldsymbol{f}_1(\boldsymbol{x}_0), \tag{4.11a}$$

$$DH_1(\boldsymbol{x}_0) = DH_1(\boldsymbol{x}(t))\boldsymbol{\Phi}(t, \bar{t}_i, \boldsymbol{x}_0). \tag{4.11b}$$

Proof. Because of the chained structure of $\boldsymbol{\Phi}$ in (4.8c) and the properties from Lemma 4.1.2, it remains to be shown that

$$\boldsymbol{f}_{i+1}^{+} = \boldsymbol{S}_i^{i+1}\boldsymbol{f}_i^{-}, \qquad DH_i(\boldsymbol{x}_i^{-}) = DH_{i+1}(\boldsymbol{x}_{i+1}^{+})\boldsymbol{S}_i^{i+1},$$

holds for all $i \in \{1, \ldots, m\}$. The first condition is readily confirmed by simplifying the terms and fractions in (4.7). Similarly, employing (4.7) and (4.9) allows the second condition to be simplified as $DH_i(\boldsymbol{x}_i^{-}) = DH_{i+1}(\boldsymbol{x}_{i+1}^{+})\boldsymbol{G}_i^{i+1}$. This is demonstrated by computing the total derivative of Definition *Def2*:

$$H_{i+1} \circ \boldsymbol{g}_i^{i+1}(\boldsymbol{x}_i^{-}) = H_i(\boldsymbol{x}_i^{-}) \quad \forall \boldsymbol{x}_i^{-} \in \mathcal{E}_i^{i+1},$$

$$\overset{\frac{\mathrm{d}}{\mathrm{d}\bar{\boldsymbol{x}}_i}}{\Rightarrow} DH_{i+1}(\boldsymbol{x}_{i+1}^{+})\boldsymbol{G}_i^{i+1} = DH_i(\boldsymbol{x}_i^{-}).$$

□

4.1.4 First Recurrence Map

Note that (4.10a) and (4.11a) can be considered as transitions in time since a state always remains on the same flow when there is solely a change in time. The focus here, however, is on distinct recurrent hybrid flows, which result from local changes that are transversal to the flow. For this purpose, the well-known *Poincaré map* (Chapter 9.1 [82]) is introduced for recurrent hybrid flows.

Definition (Poincaré section). *Let a continuously differentiable function $a : \mathcal{X}_1 \to \mathbb{R}$ define the set $\mathcal{A} = \{\boldsymbol{x}_1 \in \mathcal{X}_1 | a(\boldsymbol{x}_1) = 0, \dot{a}(\boldsymbol{x}_1) < 0\}$. Within a recurrent hybrid trajectory $\boldsymbol{x}(t)$ of Σ, the Poincaré section $\mathcal{A}$ is locally defined at points where $\boldsymbol{x}(t) \in \mathcal{A}$.*

The implicit constraint $a(\boldsymbol{x}_1) = 0$ is referred to as the *anchor*. An illustration of the Poincaré section $\mathcal{A}$ is provided in Fig. 4.1.

Remark 4.1.6. *Without loss of generality, this chapter assumes that $\mathcal{A} \cap \mathcal{E}_m^1 = \emptyset$, meaning the* anchor *is not identical to an* event *of the HDS. This contrasts with the definitions in [52, 137], where $a := e_m^1$ is specifically used. The implications for the derivative of the hybrid flow are discussed in detail in Appendix A.2.*

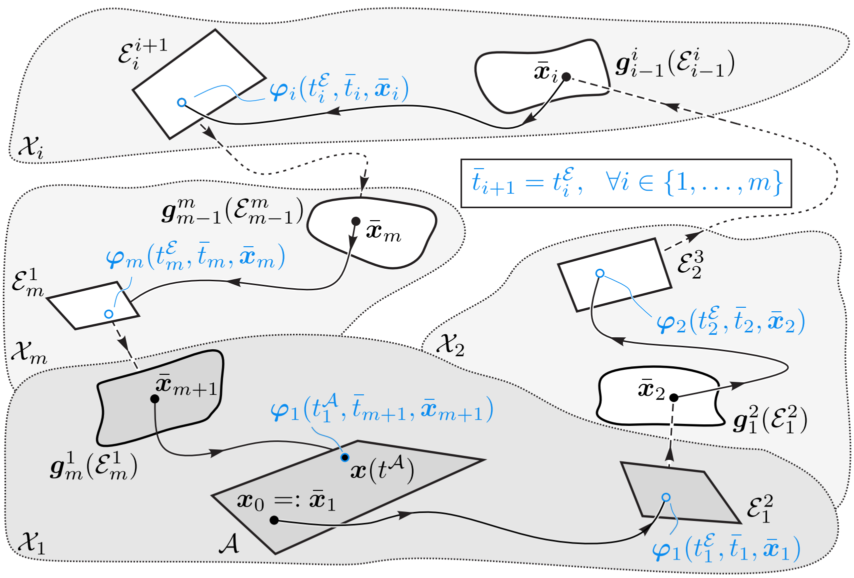

Figure 4.1: Graphical illustration of a recurrent hybrid trajectory of an autonomous HDS Σ that starts and ends on the Poincaré section $\mathcal{A}$ within $\mathcal{X}_1$.

With $\boldsymbol{\varphi}(t, 0, \boldsymbol{x}_0) \in \mathcal{A}$, the time $t \in \mathcal{T}$ is coupled to the initial state $\boldsymbol{x}_0$. This is easily seen by constructing *local* and *global time-to-anchor* functions

$$\Delta t_1^{\mathcal{A}}(\bar{\boldsymbol{x}}_{m+1}) := \inf\{t \geq 0 | \boldsymbol{\varphi}_1(t, 0, \bar{\boldsymbol{x}}_{m+1}) \in \mathcal{A}\}, \tag{4.12a}$$

$$t_1^{\mathcal{A}}(\bar{t}_{m+1}, \bar{\boldsymbol{x}}_{m+1}) := \inf\{t \geq \bar{t}_{m+1} | \boldsymbol{\varphi}_1(t, \bar{t}_{m+1}, \bar{\boldsymbol{x}}_{m+1}) \in \mathcal{A}\}, \tag{4.12b}$$

which are analogous to the time-to-event functions $\Delta t_i^{\mathcal{E}}$ and $t_i^{\mathcal{E}}$. Given the recursive structure of the hybrid trajectory (4.2b) and Remark 4.1.1, the overall time-to-anchor can also be stated as $t^{\mathcal{A}}(\boldsymbol{x}_0) := t_1^{\mathcal{A}}(\bar{t}_{m+1}, \bar{\boldsymbol{x}}_{m+1})$. Moreover, $t^{\mathcal{A}}(\boldsymbol{x}_0)$ is continuously differentiable due to the C^1 property of Σ and the anchor a.

In the following discussion, and without loss of generality, Poincaré sections $\mathcal{A}$ are considered for which $t^{\mathcal{A}}(\boldsymbol{x}_0)$ remains finite for any point $\boldsymbol{x}_0 \in \mathcal{A}_0$, where $\mathcal{A}_0 = \mathcal{A} \cap \mathcal{X}_0$.

Definition (Poincaré map)**.** *A state $\boldsymbol{x}_0$ from the subset $\mathcal{A}_0 = \mathcal{A} \cap \mathcal{X}_0$ is mapped back onto the Poincaré section $\mathcal{A}$ along the recurrent hybrid trajectory by the Poincaré map $\boldsymbol{P} : \mathcal{A}_0 \to \mathcal{A}$, where $\boldsymbol{P}(\boldsymbol{x}_0) = \boldsymbol{\varphi}\big(t^{\mathcal{A}}(\boldsymbol{x}_0), 0, \boldsymbol{x}_0\big)$, also known as the* first recurrence map.

Similar to the recurrent hybrid trajectory $\boldsymbol{x}(t)$, the Poincaré map $\boldsymbol{P} \in C^1$ is well defined on the set $\mathcal{A}_0$. However, since time t is eliminated by the introduction of the Poincaré section $\mathcal{A}$, no further transitions in time (4.11a) occur for the Jacobian of the Poincaré map $D\boldsymbol{P}(\boldsymbol{x}_0)$. Instead, the Jacobian takes the form

$$\begin{aligned} D\boldsymbol{P}(\boldsymbol{x}_0) &= \frac{\mathrm{d}}{\mathrm{d}\boldsymbol{x}_0} \boldsymbol{\varphi}\big(t^{\mathcal{A}}(\boldsymbol{x}_0), 0, \boldsymbol{x}_0\big) \\ &= \boldsymbol{f}_1\left(\boldsymbol{x}(t^{\mathcal{A}})\right) \frac{\partial t^{\mathcal{A}}}{\partial \boldsymbol{x}_0} + \boldsymbol{\Phi}\left(t^{\mathcal{A}}, 0, \boldsymbol{x}_0\right) \\ &= \left(\boldsymbol{I} - \frac{\boldsymbol{f}_1\left(\boldsymbol{x}(t^{\mathcal{A}})\right) Da\left(\boldsymbol{x}(t^{\mathcal{A}})\right)}{Da\left(\boldsymbol{x}(t^{\mathcal{A}})\right) \cdot \boldsymbol{f}_1\left(\boldsymbol{x}(t^{\mathcal{A}})\right)} \right) \boldsymbol{\Phi}\left(t^{\mathcal{A}}, 0, \boldsymbol{x}_0\right), \end{aligned} \tag{4.13}$$

where the implicit function theorem is used (cf. equation (A.5) in the appendix) to derive

$$\frac{\partial t^{\mathcal{A}}}{\partial \boldsymbol{x}_0} = -\frac{Da\left(\boldsymbol{x}(t^{\mathcal{A}})\right)}{Da\left(\boldsymbol{x}(t^{\mathcal{A}})\right) \cdot \boldsymbol{f}_1\left(\boldsymbol{x}(t^{\mathcal{A}})\right)} \boldsymbol{\Phi}\left(t^{\mathcal{A}}, 0, \boldsymbol{x}_0\right).$$

The absence of time-dependent transitions in the Jacobian $D\boldsymbol{P}(\boldsymbol{x}_0)$ is an expected outcome by introducing the Poincaré section, since the vector field $\boldsymbol{f}_1$ points outside of $\mathcal{A}$. Consequently, in the local search for neighboring trajectories $\boldsymbol{x}(t)$, perturbations along the vector field $\boldsymbol{f}_1$ are no longer admissible when using a Poincaré section $\mathcal{A}$.

4.2 Fixed Points & Periodic Orbits

This section focuses on the examination of fixed points denoted as $\boldsymbol{x}_0 \in \mathcal{A}_0$ of the Poincaré map $\boldsymbol{P}$, i.e., $\boldsymbol{x}_0 = \boldsymbol{P}(\boldsymbol{x}_0)$. The goal is to show that such a fixed point is not isolated for cHDSs (Theorem 4.2.1). To achieve this, admissible perturbations within $\mathcal{A}$ are explored, necessitating the utilization of the following Lemma.

Lemma 4.2.1. *Given a fixed point $\boldsymbol{x}_0$ of $\boldsymbol{P}$ (under Assumptions As1-As3), it holds that*

- *the phase vector field $\boldsymbol{f}_i$, and*
- *the derivative DH_i, with $H_i \in \mathcal{H}$,*

are nonzero in all phases i.

Proof. Due to the finite execution time $t_i^{\mathcal{E}}(\bar{\boldsymbol{x}}_i)$ of phase trajectories $\boldsymbol{x}_i(t)$ (*As1*), which are unique in forward and backward time, as well as the transversality condition (*As2*), it is ensured that $\boldsymbol{f}_i \neq \boldsymbol{0}$ holds for all phases $i \in \{1, \dots, m\}$. Furthermore, by applying the same line of reasoning, $\boldsymbol{f}_{m+1}$ is also nonzero due to the equality of vector fields $\boldsymbol{f}_{m+1}(\boldsymbol{x}(t^{\mathcal{A}})) = \boldsymbol{f}_1(\boldsymbol{x}_0)$ with the fixed point $\boldsymbol{x}_0 = \boldsymbol{x}(t^{\mathcal{A}})$. The property $DH_i \neq \boldsymbol{0}$ directly follows from $\boldsymbol{f}_i \neq \boldsymbol{0}$ and Theorem 1.1 in [78]. ☐

Theorem 4.2.1. *Given a cHDS $\Sigma^{\mathcal{H}}$, a fixed point of the Poincaré map $\boldsymbol{P}$ is never isolated.*

Proof. Assume a fixed point $\boldsymbol{x}_0 \in \mathcal{A}$ that satisfies $\boldsymbol{P}(\boldsymbol{x}_0) - \boldsymbol{x}_0 = \boldsymbol{0}$ is isolated. In other words, the kernel and cokernel of the square Jacobian $D\boldsymbol{P}(\boldsymbol{x}_0) - \boldsymbol{I}$ are assumed to be trivial and thus,

$$\dim(\ker(D\boldsymbol{P}(\boldsymbol{x}_0) - \boldsymbol{I})) = \dim(\ker(D\boldsymbol{P}(\boldsymbol{x}_0)^{\mathrm{T}} - \boldsymbol{I})) = 0.$$

However, using properties (4.9) and (4.11b), the row vector $DH_1(\boldsymbol{x}(t^{\mathcal{A}}))$ appears as a left eigenvector of the Poincaré map Jacobian (4.13), such that

$$DH_1(\boldsymbol{x}(t^{\mathcal{A}}))D\boldsymbol{P}(\boldsymbol{x}_0) = DH_1(\boldsymbol{x}_0) = DH_1(\boldsymbol{x}(t^{\mathcal{A}})), \tag{4.14}$$

where periodicity $\boldsymbol{x}(t^{\mathcal{A}}) = \boldsymbol{x}_0$ is used in the last equality of (4.14). From (4.14) and Lemma 4.2.1, $DH_1(\boldsymbol{x}(t^{\mathcal{A}}))^{\mathrm{T}} \neq \boldsymbol{0}$ lies in the kernel of $D\boldsymbol{P}(\boldsymbol{x}_0)^{\mathrm{T}} - \boldsymbol{I}$, contradicting the assumption of a trivial kernel. ☐

Note that every fixed point of the Poincaré map is directly related to a periodic orbit with period time $T = t^{\mathcal{A}}$, such that

$$\boldsymbol{\varphi}(T, 0, \boldsymbol{x}_0) = \boldsymbol{x}_0, \tag{4.15}$$

with its local linearization $\boldsymbol{\Phi}_T := \boldsymbol{\Phi}(T, 0, \boldsymbol{x}_0)$[3], called the monodromy matrix. With the well known *freedom of phase* property $\boldsymbol{\Phi}_T \boldsymbol{f}_1(\boldsymbol{x}_0) = \boldsymbol{f}_1(\boldsymbol{x}_0)$ of autonomous systems, due to (4.11a) and (4.15), $\boldsymbol{\Phi}_T$ has at least two eigenvalues of 1. Hence, Theorem 4.2.1 also implies that periodic orbits in a cHDS are non-isolated.

Remark 4.2.1. *Using an anchor a and introducing a Poincaré section $\mathcal{A}$, Theorem 4.2.1 provides a crucial step in numerically exploring periodic*

[3]The monodromy matrix $\boldsymbol{\Phi}_T$ is an essential tool for studying the stability and local existence of orbits (Chapter 7.1 [82]), with its eigenvalues known as Floquet multipliers.

orbits in HDSs. This approach differs from the original proof for ODEs (Theorem 4 [124]), which relies solely on the properties of the orbits (4.15) *and the monodromy matrix* $\boldsymbol{\Phi}_T$*. Establishing a Poincaré section is straightforward, as events are inherent to HDSs (Remark 4.1.6). This is crucial for numerically exploring periodic orbits, as described in Section 4.3.*

Due to the rank deficiency of the Jacobian $D\boldsymbol{P}(\boldsymbol{x}_0) - \boldsymbol{I}$, a periodic orbit of a conservative system is classified as degenerate (Definition 1 [124]). For the targeted exploration of neighboring periodic orbits, the focus is on the weakest form of degeneration. Specifically, distinct neighboring periodic orbits exist on adjacent level sets $\bar{H}_i$ of $H_i \in \mathcal{H}$.

Definition (Normal Conservative Orbit)**.** *A hybrid periodic trajectory of a cHDS* $\Sigma^{\mathcal{H}}$ *is* normal *if 1 is a simple eigenvalue of the Poincaré map Jacobian* $D\boldsymbol{P}(\boldsymbol{x}_0)$*, i.e.,* $\dim(\ker(D\boldsymbol{P}(\boldsymbol{x}_0) - \boldsymbol{I})) = 1$.

The definition is analogous to Definition 3 in [124], but generalizes to hybrid dynamical systems. It implies that a normal conservative orbit yields a monodromy matrix $\boldsymbol{\Phi}_T$ with exactly two eigenvalues of 1. Furthermore, only a single hybrid first integral $H_1 \in \mathcal{H}$ exists in $\mathcal{X}1$, meaning $k_1 = 1$. By Lemma 4.1.1, it follows that all $H_i \in \mathcal{H}$ are single hybrid first integrals, leading to $k_{\mathcal{H}} = 1$. Applying Theorem 4.2.1, a point $\boldsymbol{x}_0 \in \mathcal{A}$ corresponding to a normal conservative orbit lies on a locally defined one-dimensional submanifold (curve) parameterized by the level set $\bar{H}$. Any point on this curve is uniquely determined by the implicit equations

$$\begin{bmatrix} \boldsymbol{P}(\boldsymbol{x}_0) - \boldsymbol{x}_0 \\ H_1(\boldsymbol{x}_0) - \bar{H} \end{bmatrix} = \boldsymbol{0}. \tag{4.16}$$

A numerical construction of this curve and the detection of turning and bifurcation points for periodic orbits are discussed in Section 4.3.

Remark 4.2.2. *Theorem 4.2.1 focuses exclusively on the local existence of additional orbits. The general existence of periodic orbits is not addressed here, as it strongly depends on specific properties of* $\Sigma^{\mathcal{H}}$*. However, certain subclasses of* $\Sigma^{\mathcal{H}}$ *are noteworthy. As mentioned in Remark 4.1.4, for* $k_{\mathcal{H}} = n_1$*, the only solutions are equilibria, which violate Assumptions As1-As3. Moreover, symmetric periodic orbits exist in cHDS with* $m = 1$ *under a time-reversal symmetry* $\boldsymbol{\kappa} : \mathcal{X}_1 \to \mathcal{X}_1$*, satisfying* $\boldsymbol{\kappa} \circ \boldsymbol{\varphi}\big(t, 0, \boldsymbol{x}_0\big) = \boldsymbol{\varphi}\big(-t, 0, \boldsymbol{\kappa}(\boldsymbol{x}_0)\big)$, $\boldsymbol{\kappa} \circ \boldsymbol{\kappa} =$ *id. and* $\boldsymbol{g}_1^2 = \boldsymbol{\kappa}$ *[29, 66, 81].*[4]

[4]The concept of time-reversal symmetry is strongly connected to continuous symmetries (Remark 4.1.5). For more information, see [81].

4.3 Continuation of Periodic Orbits

This section explores the efficient computation of normal conservative orbits using the PCC methods introduced in Chapter 2. Since these methods cannot be directly applied to (4.16) due to the square Jacobian matrix of $\boldsymbol{P}(\boldsymbol{x}_0) - \boldsymbol{x}_0$, the Poincaré map $\boldsymbol{P}$ is modified by introducing a scalar parameter ξ in $\tilde{\boldsymbol{P}} : \mathcal{A} \times \mathbb{R} \to \mathcal{A}$. This modification embeds $\Sigma^{\mathcal{H}}$ in a one-parameter family of dissipative dynamics $\Sigma_\xi = \big(\mathcal{X}, \tilde{\mathcal{F}}, \mathcal{E}, \mathcal{G}\big)$, where

$$\tilde{\mathcal{F}} := \Big\{ \dot{\boldsymbol{x}} = \underbrace{\boldsymbol{f}_i(\boldsymbol{x}_i) + \xi \cdot DH_i(\boldsymbol{x}_i)^{\mathrm{T}}}_{=:\tilde{\boldsymbol{f}}_i(\boldsymbol{x}_i;\xi)} \Big\}_{i=1}^{m}, \tag{4.17}$$

with $H_i \in \mathcal{H}$. The idea of modifying an ODE with a first integral H_i in the form (4.17) originates from [124]. Introducing ξ in each phase dynamic (4.17) ensures a consistent influence on the overall hybrid flow $\boldsymbol{x}(t)$, even when the duration $\bar{t}_{i+1} - \bar{t}_i$ of a specific phase i approaches zero. Similar to other modifications of conservative ODEs [35, 97], this approach aims to resolve inherent state dependencies caused by first integrals. Note that for $\xi = 0$, the conservative dynamics $\Sigma^{\mathcal{H}} \equiv \Sigma_0$ are still within the one-parameter family Σ_ξ. In fact, the set of periodic orbits in Σ_ξ is shown to be equivalent to the periodic orbits of $\Sigma^{\mathcal{H}}$. The following theorem and proof build on (Theorem 1 [124]) and (Lemma 6 [97]).

Theorem 4.3.1. *The tuple $(\boldsymbol{x}_0, \xi)$ is a fixed point of $\tilde{\boldsymbol{P}}$ if and only if $\xi = 0$ and thus, $\boldsymbol{x}_0$ is a fixed point of $\boldsymbol{P}$.*

Proof. Assume that there exists an orbit of Σ_ξ such that $\tilde{\boldsymbol{P}}(\boldsymbol{x}_0, \xi) = \boldsymbol{x}_0$, implying $\boldsymbol{\varphi}(t^{\mathcal{A}}, 0, \boldsymbol{x}_0; \xi) = \boldsymbol{x}_0$. Consequently,

$$H_1(\boldsymbol{\varphi}(t^{\mathcal{A}}, 0, \boldsymbol{x}_0; \xi)) - H_1(\boldsymbol{x}_0) = 0. \tag{4.18a}$$

Furthermore, using the shorthand notation $\boldsymbol{x}_i(\tau) := \boldsymbol{\varphi}_i(\tau, \bar{t}_i, \bar{\boldsymbol{x}}_i; \xi)$, it holds

$$H_i(\boldsymbol{x}_i(\bar{t}_{i+1})) - H_i(\bar{\boldsymbol{x}}_i) = \underbrace{\int_{\bar{t}_i}^{\bar{t}_{i+1}} \frac{\mathrm{d}}{\mathrm{d}\tau} H_i(\boldsymbol{x}_i(\tau)) \mathrm{d}\tau}_{=:c_i}, \tag{4.18b}$$

for all $i \in \{1, \dots, m+1\}$, where $\bar{t}_{m+2} := t_1^{\mathcal{A}}$. Since the reset maps $\mathcal{G}$ in Σ_ξ remain independent of ξ, the integral $H_{i+1}(\boldsymbol{x}_{i+1}^{+}) = H_i(\boldsymbol{x}_i^{-})$ does not change across phase transitions (*Def2*). Hence, the left-hand side of (4.18a) takes the form

$$H_1\big(\varphi(t^{\mathcal{A}}, 0, \boldsymbol{x}_0; \xi)\big) - H_1\big(\boldsymbol{x}_0\big) = \sum_{i=1}^{m+1} c_i \overset{!}{=} 0. \tag{4.18c}$$

Herein, the constant c_i takes the particular form:

$$\begin{aligned} c_i &= \int_{\bar{t}_i}^{\bar{t}_{i+1}} \frac{\mathrm{d}}{\mathrm{d}\tau} H_i\big(\boldsymbol{x}_i(\tau)\big)\mathrm{d}\tau = \int_{\bar{t}_i}^{\bar{t}_{i+1}} DH_i\big(\boldsymbol{x}_i(\tau)\big)\tilde{\boldsymbol{f}}_i\big(\boldsymbol{x}_i(\tau);\xi\big)\mathrm{d}\tau \\ &= \int_{\bar{t}_i}^{\bar{t}_{i+1}} DH_i\big(\boldsymbol{x}_i(\tau)\big)\Big(\boldsymbol{f}_i\big(\boldsymbol{x}_i(\tau)\big) + \xi \cdot DH_i\big(\boldsymbol{x}_i(\tau)\big)^{\mathrm{T}}\Big)\mathrm{d}\tau \\ &= \xi \cdot \underbrace{\int_{\bar{t}_i}^{\bar{t}_{i+1}} \big\|DH_i\big(\boldsymbol{x}_i(\tau)\big)\big\|_2^2\,\mathrm{d}\tau}_{=:\tilde{c}_i}, \end{aligned} \tag{4.18d}$$

where the orthogonality condition $DH_i(\boldsymbol{x}_i)\boldsymbol{f}_i(\boldsymbol{x}_i) = 0$ in (4.9) also holds for any $\bar{\boldsymbol{x}}_i \in \mathcal{X}_i$ at initial time $\bar{t}_i$. Since $DH_i(\boldsymbol{x}_i) \neq \mathbf{0}$ (Lemma 4.2.1) and $\bar{t}_{i+1} > \bar{t}_i$ (*As3*), it follows that $\tilde{c}_i > 0$. Substituting (4.18d) into (4.18c) leads to $\xi = 0$, proving that periodic orbits in Σ_ξ can only occur when $\xi = 0$. □

Remark 4.3.1. *Following the approach in [97], additional scalars* $\{\xi_j\}_{j=1}^{N_{\mathcal{H}}}$ *can be introduced in* (4.17) *when* $\Sigma^{\mathcal{H}}$ *has* $N_{\mathcal{H}} > 1$ *functionally independent first integrals* $\{H_{i,j}\}_{j=1}^{N_{\mathcal{H}}} \in \mathcal{H}$*, yielding*

$$\tilde{\boldsymbol{f}}_i = \boldsymbol{f}_i(\boldsymbol{x}_i) + \sum_{j=1}^{N_{\mathcal{H}}} \xi_j \cdot DH_{i,j}(\boldsymbol{x}_i)^{\mathrm{T}}.$$

Based on Lemma 6 in [97], Theorem 4.3.1 extends naturally to show that $\xi_j = 0$ *for all* $j = 1, \ldots, N_{\mathcal{H}}$*. This approach is particularly useful for exploring a family of conservative orbits that are not normal. However, introducing multiple scalars leads to a multi-dimensional continuation problem, which is more challenging to handle numerically [57]. To mitigate this complexity, similar to the methods in [9, 10, 29], it is assumed that* $\Sigma^{\mathcal{H}}$ *can be equivalently reduced to a system with* $N_{\mathcal{H}} = 1$.

With Theorem 4.3.1 and the objective of parameterizing periodic orbits by level sets $\bar{H}$[5], the modification of (4.16) yields

$$\boldsymbol{r}_{\mathrm{eb,ss}}(\boldsymbol{\nu}_{\mathrm{eb,ss}}) := \begin{bmatrix} \tilde{\boldsymbol{P}}(\boldsymbol{x}_0, \xi) - \boldsymbol{x}_0 \\ H_1(\boldsymbol{x}_0) - \bar{H} \end{bmatrix} = \boldsymbol{0}, \tag{4.19}$$

where $\boldsymbol{\nu}_{\mathrm{eb,ss}}^{\mathrm{T}} := [\boldsymbol{x}_0^{\mathrm{T}}\ \xi\ \bar{H}]$ and $N_{\mathrm{eb,ss}} = n_1 + 1$. As discussed in Section 3.2, (4.19) is formulated as an event-based single shooting problem.

Remark 4.3.2. *The initial state $\boldsymbol{x}_0$ in* (4.19) *is not required to lie on the Poincaré section $\mathcal{A}$. In other words, any $\boldsymbol{x}_0 \in \mathcal{X}_1 \backslash \mathcal{A}$ in $\boldsymbol{\nu}_{\mathrm{eb,ss}}$ can still be used to evaluate $\boldsymbol{r}_{\mathrm{eb,ss}}(\boldsymbol{\nu}_{\mathrm{eb,ss}})$. However, at a solution $\boldsymbol{\nu}_{\mathrm{eb,ss}} \in \boldsymbol{r}_{\mathrm{eb,ss}}^{-1}(\boldsymbol{0})$, the periodicity condition $\boldsymbol{x}(t^{\mathcal{A}}) = \boldsymbol{x}_0$ ensures that $\boldsymbol{x}_0$ lies on $\mathcal{A}$. To systematically enforce this, a method involves projecting $\boldsymbol{x}_0$ into an $n_1 - 1$ dimensional coordinate system locally spanning $\mathcal{A}$. If the anchor function $a(\boldsymbol{x}_1)$ is linear, rendering the Poincaré section $\mathcal{A}$ a hyperplane, this coordinate projection is globally defined on $\mathcal{X}_1$ (Chapter 9.1 [82]).*

The modified map in (4.19) is now well suited for numerical continuation. The following theorem establishes the connection between normal conservative orbits and solutions of (4.19).

Theorem 4.3.2. *Given a normal conservative orbit where $\boldsymbol{x}_0$ is a fixed point of the Poincaré map $\boldsymbol{P}$, the point ${\boldsymbol{\nu}_{\mathrm{eb,ss}}^{*}}^{\mathrm{T}} = \left[\boldsymbol{x}_0^{\mathrm{T}}\ 0\ H_1(\boldsymbol{x}_0)\right]$ is a regular point of* (4.19).

Proof. For notational convenience, the subscript $_{\mathrm{eb,ss}}$ is omitted in this proof. To establish regularity, it must be shown that the Jacobian

$$D\boldsymbol{r}(\boldsymbol{\nu}^*) = \begin{bmatrix} \left.\dfrac{\partial \tilde{\boldsymbol{P}}}{\partial \boldsymbol{x}}\right|_{(\boldsymbol{x}_0,0)} - \boldsymbol{I} & \left.\dfrac{\partial \tilde{\boldsymbol{P}}}{\partial \xi}\right|_{(\boldsymbol{x}_0,0)} & 0 \\ DH_1(\boldsymbol{x}_0) & 0 & -1 \end{bmatrix}, \tag{4.20a}$$

has full rank. This is equivalent to showing that the tangent vector $\boldsymbol{\tau} \circ D\boldsymbol{r}(\boldsymbol{\nu}^*)$ is unique, or equivalently, $\dim(\ker(D\boldsymbol{r}(\boldsymbol{\nu}^*))) = 1$. Consider a tangent vector of the form

$$\boldsymbol{\tau}^* = \begin{bmatrix} \boldsymbol{\tau}_{x_0} \\ \tau_{\xi} \\ \tau_{\bar{H}} \end{bmatrix}, \quad \boldsymbol{\tau}_{x_0} \in \mathbb{R}^{n_1},\ \tau_{\xi} \in \mathbb{R},\ \tau_{\bar{H}} \in \mathbb{R}. \tag{4.20b}$$

[5] Adding the first integral constraint in (4.19) is, in a sense, redundant since the set of fixed points of $\tilde{\boldsymbol{P}}$ remains unchanged. However, it facilitates the search for periodic orbits at a specific level set $\bar{H}$.

Since ξ remains zero for normal conservative orbits of $\boldsymbol{r}^{-1}(\mathbf{0})$ (Theorem 4.3.1), it follows that $\tau_\xi = 0$. The remaining vector components, $\boldsymbol{\tau}_{x_0}$ and $\tau_{\bar{H}}$, are coupled through the last row of $D\boldsymbol{r}(\boldsymbol{\nu}^*)$, i.e., $DH_1(\boldsymbol{x}_0)\boldsymbol{\tau}_{x_0} = \tau_{\bar{H}}$. If $\boldsymbol{\tau}_{x_0} = \mathbf{0}$, then $\tau_{\bar{H}} = 0$, which results in the trivial tangent vector $\boldsymbol{\tau}^* = \mathbf{0}$. Thus, only nonzero $\boldsymbol{\tau}_{x_0}$ need to be considered in $D\boldsymbol{r}(\boldsymbol{\nu}^*)\boldsymbol{\tau}^* = \mathbf{0}$. Since $\boldsymbol{x}_0$ lies on a normal conservative orbit, the kernel of $D\boldsymbol{P}(\boldsymbol{x}_0) - \boldsymbol{I}$ has dimension one. For $\xi = 0$, the Jacobian $D\boldsymbol{P}(\boldsymbol{x}_0)$ is equivalent to ${\partial \tilde{\boldsymbol{P}}}/{\partial \boldsymbol{x}}|_{(\boldsymbol{x}_0,0)}$ in (4.20a). This implies that there only exists a single linearly independent vector $\boldsymbol{\tau}_{x_0} \neq \mathbf{0}$ in the kernel of ${\partial \tilde{\boldsymbol{P}}}/{\partial \boldsymbol{x}}|_{(\boldsymbol{x}_0,0)}$. Since $\boldsymbol{\tau}^*$ is the only linearly independent vector in the kernel of $D\boldsymbol{r}(\boldsymbol{\nu}^*)$, it follows that $\dim(\ker(D\boldsymbol{r}(\boldsymbol{\nu}^*)) = 1$. □

Note that the implication in Theorem 4.3.2 holds only in one direction. A regular point $\boldsymbol{\nu}^*_{\mathrm{eb,ss}}$ of (4.19) does not necessarily correspond to a normal conservative orbit. In this case, $\boldsymbol{\nu}^*_{\mathrm{eb,ss}}$ is a turning point with respect to the parameterization $\bar{H}$. That is, the last entry of the tangent vector $\boldsymbol{\tau} \circ D\boldsymbol{r}_{\mathrm{eb,ss}}(\boldsymbol{\nu}^*_{\mathrm{eb,ss}})$ vanishes, indicating no local change in the first integral's value.

4.3.1 Time-Based Shooting

As discussed in Section 3.2, the event-based implementation (4.19) has some limitations when numerically tracing the solution curve $\boldsymbol{r}^{-1}_{\mathrm{eb,ss}}(\mathbf{0})$, due to Assumptions *As2* and *As3*. In particular, the curve ends at limit points $\boldsymbol{\nu}^*_{\mathrm{eb,ss}}$, where:

- *Grazing* occurs, i.e., $De_i^{i+1}\boldsymbol{f}_i^- \to 0$, violating Assumption *As2*.
- *Phase durations vanish*, i.e., $\Delta t_i \to 0$, violating Assumption *As3*.

At grazing points, the saltation matrix S_i^{i+1} in (4.7) becomes undefined, making $\boldsymbol{r}_{\mathrm{eb,ss}}$ non-differentiable at $\boldsymbol{\nu}^*_{\mathrm{eb,ss}}$.

To mitigate these issues, the formulation in (4.19) is transformed into a time-based approach, detailed along with its practical implementation. This transformation decouples events from the integration of $\mathcal{F}$ in (4.2b), breaking the functional dependence of $\{t_i^{\mathcal{E}}\}_{i=1}^m$ and $t_1^{\mathcal{A}}$ on $\{\bar{\boldsymbol{x}}_i\}_{i=1}^m$ and $\bar{\boldsymbol{x}}_{m+1}$, respectively. Instead, a set of $m+1$ independent variables t_i is introduced, alongside $m+1$ additional constraints incorporating events $e_i^{i+1} = 0$ and an anchor condition $a = 0$ to maintain indirect coupling. The time-based multiple shooting problem takes the form:

$$
\boldsymbol{r}_{\mathrm{tb,ms}}(\boldsymbol{\nu}_{\mathrm{tb,ms}}) := \begin{bmatrix} \boldsymbol{\varphi}_1(t_{m+1}, t_m, \bar{\boldsymbol{x}}_{m+1}; \xi) - \bar{\boldsymbol{x}}_1 \\ a \circ \boldsymbol{\varphi}_1(t_{m+1}, t_m, \bar{\boldsymbol{x}}_{m+1}; \xi) \\ \begin{Bmatrix} \boldsymbol{g}_i^{i+1} \circ \boldsymbol{x}_i(t_i) - \bar{\boldsymbol{x}}_{i+1} \\ e_i^{i+1} \circ \boldsymbol{x}_i(t_i) \end{Bmatrix}_{i=1}^{m} \\ H_1(\bar{\boldsymbol{x}}_1) - \bar{H} \end{bmatrix}, \quad \begin{matrix} \text{(periodicity)} \\ \text{(anchor)} \\ \text{(shooting)} \\ \text{(event)} \\ \text{(first-integral)} \end{matrix} \tag{4.21}
$$

where $\boldsymbol{x}_i(t_i) := \boldsymbol{\varphi}_i(t_i, t_{i-1}, \bar{\boldsymbol{x}}_i; \xi)$, $\boldsymbol{\nu}_{\mathrm{tb,ms}}^{\mathrm{T}} := [t_{m+1} \ \bar{\boldsymbol{x}}_{m+1}^{\mathrm{T}} \ \cdots \ t_1 \ \bar{\boldsymbol{x}}_1^{\mathrm{T}} \ \xi \ \bar{H}]$ and thus, $N_{\mathrm{tb,ms}} = \sum_{i=1}^{m+1} n_i + m + 2$. The multiple shooting formulation in (4.21) is particularly advantageous for computing the Jacobian $D\boldsymbol{r}_{\mathrm{tb,ms}}$, where required sensitivities, denoted as $\boldsymbol{\Phi}_i(t) := {}^{\partial \boldsymbol{x}_i(t)}/_{\partial \bar{\boldsymbol{x}}_i}$ and $\boldsymbol{\Psi}_i(t) := {}^{\partial \boldsymbol{x}_i(t)}/_{\partial \xi}$, can be efficiently computed in parallel by solving matrix ODEs [32]:

$$
\begin{aligned}
\dot{\boldsymbol{\Phi}}_i(t) &= \left.\frac{\partial \tilde{\boldsymbol{f}}_i(\boldsymbol{x}_i; \xi)}{\partial \boldsymbol{x}_i}\right|_{(\boldsymbol{x}_i(t), \xi)} \boldsymbol{\Phi}_i(t), \\
\boldsymbol{\Phi}_i(0) &= \boldsymbol{I},
\end{aligned} \tag{4.22}
$$

$$
\begin{aligned}
\dot{\boldsymbol{\Psi}}_i(t) &= \left.\frac{\partial \tilde{\boldsymbol{f}}_i}{\partial \boldsymbol{x}_i}\right|_{(\boldsymbol{x}_i(t), \xi)} \boldsymbol{\Psi}_i(t) + \left.\frac{\partial \tilde{\boldsymbol{f}}_i}{\partial \xi}\right|_{(\boldsymbol{x}_i(t), \xi)}, \\
\boldsymbol{\Psi}_i(0) &= \boldsymbol{0}.
\end{aligned} \tag{4.23}
$$

For a large number of hybrid phases m, the Jacobian exhibits a sparse structure:

$$
D\boldsymbol{r}_{\mathrm{tb,ms}} = \begin{bmatrix}
\boldsymbol{R}_{m+1} & \boldsymbol{0} & \boldsymbol{0} & \dots & \boldsymbol{0} & \boldsymbol{0} & \boldsymbol{C} & \boldsymbol{\Xi}_{m+1} & \boldsymbol{0} \\
\boldsymbol{C} & \boldsymbol{R}_m & \boldsymbol{0} & \dots & \boldsymbol{0} & \boldsymbol{0} & \boldsymbol{0} & \boldsymbol{\Xi}_m & \boldsymbol{0} \\
\boldsymbol{0} & \boldsymbol{C} & \boldsymbol{R}_{m-1} & & \boldsymbol{0} & \boldsymbol{0} & \boldsymbol{0} & \boldsymbol{\Xi}_{m-1} & \boldsymbol{0} \\
\vdots & \ddots & \ddots & \ddots & \ddots & & & \vdots & \vdots \\
\boldsymbol{0} & \boldsymbol{0} & \boldsymbol{0} & & \boldsymbol{C} & \boldsymbol{R}_2 & \boldsymbol{0} & \boldsymbol{\Xi}_2 & \boldsymbol{0} \\
\boldsymbol{0} & \boldsymbol{0} & \boldsymbol{0} & \dots & \boldsymbol{0} & \boldsymbol{C} & \boldsymbol{R}_1 & \boldsymbol{\Xi}_1 & \boldsymbol{0} \\
\boldsymbol{0} & \boldsymbol{0} & \boldsymbol{0} & \dots & \boldsymbol{0} & \boldsymbol{0} & \boldsymbol{h}_1 & 0 & -1
\end{bmatrix}, \tag{4.24a}
$$

with

$$
\boldsymbol{R}_i = \begin{cases} \begin{bmatrix} \tilde{\boldsymbol{f}}_{m+1} & \boldsymbol{\Phi}_{m+1} \\ Da \cdot \tilde{\boldsymbol{f}}_{m+1} & Da \cdot \boldsymbol{\Phi}_{m+1} \end{bmatrix}, & i = m+1 \\ \begin{bmatrix} \boldsymbol{G}_i^{i+1} \cdot \tilde{\boldsymbol{f}}_i & \boldsymbol{G}_i^{i+1} \cdot \boldsymbol{\Phi}_i \\ De_i^{i+1} \cdot \tilde{\boldsymbol{f}}_i & De_i^{i+1} \cdot \boldsymbol{\Phi}_i \end{bmatrix}, & \text{otherwise,} \end{cases} \tag{4.24b}
$$

$$\boldsymbol{\Xi}_i = \begin{cases} \begin{bmatrix} \boldsymbol{\Psi}_{m+1} \\ Da \cdot \boldsymbol{\Psi}_{m+1} \end{bmatrix} & , \ i = m+1 \\ \begin{bmatrix} \boldsymbol{G}_i^{i+1} \cdot \boldsymbol{\Psi}_i \\ De_i^{i+1} \cdot \boldsymbol{\Psi}_i \end{bmatrix} & , \ \text{otherwise}, \end{cases} \tag{4.24c}$$

$$\boldsymbol{h}_1 = \begin{bmatrix} 0 & DH_1(\bar{\boldsymbol{x}}_1) \end{bmatrix}, \quad \boldsymbol{C} = \begin{bmatrix} \boldsymbol{0} & -\boldsymbol{I} \\ 0 & \boldsymbol{0} \end{bmatrix}. \tag{4.24d}$$

For compactness, function arguments are ommitted in (4.24b) and (4.24c). All functions are evaluated at their final phase duration t_i provided with the phase flows $\boldsymbol{\varphi}_i(t_i, t_{i-1}, \bar{\boldsymbol{x}}_i; \xi)$, which are computed simultaneously by the same numerical integration scheme. Also note that $\boldsymbol{R}_i$, $\boldsymbol{C}$ and $\boldsymbol{\Xi}_i$ are generally of different sizes, since the state dimension $n_{\mathrm{x},i}$ of a phase varies.

Remark 4.3.3. *A solution $\boldsymbol{\nu}^*_{\mathrm{tb,ms}}$ to* (4.21)*, satisfying the conditions of no grazing and strictly positive time durations (Assumptions As2, As3), such that it attains its infimum in accordance with* (4.1)*, corresponds to a solution $\boldsymbol{x}_0^* = \bar{\boldsymbol{x}}_1^*$ of the state-based problem* (4.19) *such that $\begin{bmatrix} \boldsymbol{x}_0^{*\mathrm{T}} & 0 & H_1(\boldsymbol{x}_0^*) \end{bmatrix} \in \boldsymbol{r}^{-1}_{\mathrm{eb,ss}}(\boldsymbol{0})$. This correspondence is established through the application of the implicit function theorem. Additionally, when $\boldsymbol{\nu}^*_{\mathrm{tb,ms}}$ is a regular solution of* (4.21)*, it follows that the corresponding solution $\boldsymbol{\nu}^*_{\mathrm{eb,ss}}$ for* (4.19) *is also regular. The same implication holds for turning points and thus, whether $\boldsymbol{x}_0^*$ corresponds to a normal conservative orbit or not.*

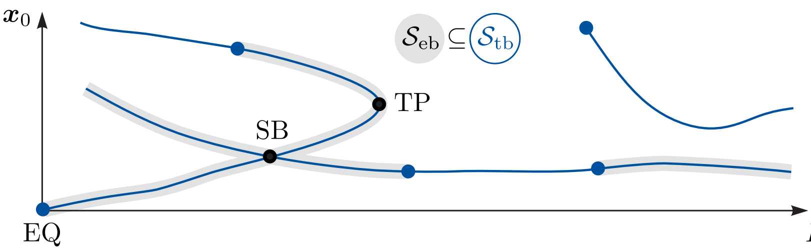

Figure 4.2: A schematic representation of the time-based solution space $\mathcal{S}_{\mathrm{tb}} = \boldsymbol{r}^{-1}_{\mathrm{tb}}(\boldsymbol{0})$, which includes equilibria (EQ), simple bifurcation (SB) points, and turning points (TP). The event-based solution space $\mathcal{S}_{\mathrm{eb}} = \boldsymbol{r}^{-1}_{\mathrm{eb}}(\boldsymbol{0})$ is entirely contained as a subset, excluding EQ and other points that violate Assumptions *As2* and *As3*, which are visualized as blue points.

4.3.2 Initial Periodic Orbits

To construct a curve within the set $\mathcal{S}_{\mathrm{tb}}$ using numerical continuation methods, as described in (2.6), it is essential to begin with an initial point $\boldsymbol{\nu}_{\mathrm{tb},0} \in \mathcal{S}_{\mathrm{tb}}$. When specific knowledge about the hybrid system $\Sigma^{\mathcal{H}}$ is unavailable, an initial point $\boldsymbol{\nu}_{\mathrm{tb},0}$ can be obtained by numerically solving $\boldsymbol{r}_{\mathrm{tb}}(\boldsymbol{\nu}_{\mathrm{tb}}) = \mathbf{0}$, starting from an arbitrary guess $\boldsymbol{u}_{\mathrm{tb,guess}} \in \mathbb{R}^{N+1}$. To improve tractability, the solution space can be reduced by fixing the level set $\bar{H}$. Since $\boldsymbol{\nu}_{\mathrm{tb,guess}}$ may be far from $\mathcal{S}_{\mathrm{tb}}$, expanding the region of convergence often becomes necessary. A common strategy involves modifying the original problem, such as minimizing the sum of squares [101] or embedding the problem into a global homotopy framework [6].

Alternatively, when specific knowledge about $\Sigma^{\mathcal{H}}$ is available, it can be leveraged to construct an initial $\boldsymbol{\nu}_{\mathrm{tb},0}$. Depending on the system's characteristics, local solutions may be derived analytically. For systems exhibiting time-reversal symmetry, a constructive approach to finding a starting point $\boldsymbol{\nu}_{\mathrm{tb},0}$ becomes available [29, 66].

For cases with limited insight into $\Sigma^{\mathcal{H}}$, the time-based implementation described in (4.21) provides an alternative method. This approach enables explicit exploitation of analytic grazing solutions, such as equilibria [115, 116], or hybrid dynamics that evolve with zero time duration ($\Delta t_i = 0$). Section 5.2 demonstrates the application of this method in constructing initial points for non-smooth mechanical systems that preserve energy in Section 5.2.

Chapter 5

Energetically Conservative Models

All models are wrong, but some are useful

—*George E. P. Box*

This chapter explores energetically conservative models (ECMs), where the system's energy serves as the first integral. This class of conservative HDSs is particularly relevant to impulsive (non-smooth) mechanical systems, such as legged robots. Section 5.1 derives the necessary conditions for energy conservation in rigid-body systems with contact and examines its implications for the well-posedness of phase vector fields $\boldsymbol{f}_i$. These insights are then applied to a spring-loaded monoped in Section 5.1.3. The chapter concludes in Section 5.2 with a numerical exploration of orbits in four ECMs using PCC methods.

5.1 Construction of Conservative Models

For the derivation of an ECM, consider a rigid-body system subject to contacts without sliding, which is commonly used to model legged robotic systems. Regardless of the active constraints, let the system's state be represented by the vector $\boldsymbol{x}^{\mathrm{T}} = [\boldsymbol{q}^{\mathrm{T}} \ \dot{\boldsymbol{q}}^{\mathrm{T}}] \in T\mathcal{Q} \subset \mathbb{R}^{2n_{\mathrm{q}}}$, where n_{q} denotes the number of degrees of freedom (DoF) and $T\mathcal{Q}$ is the tangent bundle of the configuration space $\mathcal{Q} \subset \mathbb{R}^{n_{\mathrm{q}}}$. This implies that the state dimension $n_{\mathrm{x},i} = n_{2\mathrm{q}}$ remains constant across all phases of an autnomous HDS Σ.[1] The system's total energy is given by $E(\boldsymbol{x}) = E_{\mathrm{kin}}(\boldsymbol{x}) + E_{\mathrm{pot}}(\boldsymbol{q})$, where $E_{\mathrm{kin}} : T\mathcal{Q} \to \mathbb{R}$ and $E_{\mathrm{pot}} : \mathcal{Q} \to \mathbb{R}$ are the kinetic and potential

[1] An alternative approach accounts for active constraints by defining a varying set of minimial coordinates $\boldsymbol{q}_i \in \mathcal{Q}_i$, leading to varying state dimensions $n_{\mathrm{x},i}$ in Σ (Section 5.2.4).

energy, respectively. In particular, the kinetic energy, expressed in terms of the system's mass matrix $\boldsymbol{M} : \mathcal{Q} \to \mathbb{R}^{n_\mathrm{q} \times n_\mathrm{q}}$ takes the form:

$$E_\mathrm{kin}(\boldsymbol{q}, \dot{\boldsymbol{q}}) = \frac{1}{2} \dot{\boldsymbol{q}}^\mathrm{T} \boldsymbol{M}(\boldsymbol{q}) \dot{\boldsymbol{q}}. \tag{5.1}$$

The system's active contacts are modeled as scleronomic equality constraints $\boldsymbol{j}_i : \mathcal{Q} \to \mathbb{R}^{n_{\mathrm{c},i}}$, where $n_{\mathrm{c},i} \in \mathbb{N} \cup \{0\}$ denotes the number of active constraints in phase i. If the active constraint set $\mathcal{J}_i := \{\boldsymbol{q} \in \mathcal{Q} \mid \boldsymbol{j}_i(\boldsymbol{q}) = 0\}$ is non-empty, i.e., $n_{\mathrm{c},i} > 0$, the constraints are assumend to be linearly independent, ensuring a regular contact Jacobian $\boldsymbol{J}_i(\boldsymbol{q}) := D\boldsymbol{j}_i(\boldsymbol{q})$.

Using Lagrange multipliers $\boldsymbol{\lambda}_i \in \mathbb{R}^{n_{\mathrm{c},i}}$ to represent constrained forces, the equations of motion are given by:

$$\boldsymbol{M}(\boldsymbol{q})\ddot{\boldsymbol{q}} = \boldsymbol{\eta}(\boldsymbol{q}, \dot{\boldsymbol{q}}) + \boldsymbol{J}_i(\boldsymbol{q})^\mathrm{T} \boldsymbol{\lambda}_i, \tag{5.2a}$$

$$\boldsymbol{j}_i(\boldsymbol{q}) = \boldsymbol{0}, \tag{5.2b}$$

where the conservative forces $\boldsymbol{\eta} : T\mathcal{Q} \to \mathbb{R}^{n_\mathrm{q}}$ arise from Lagrange's stationary-action principle:

$$\boldsymbol{\eta}(\boldsymbol{q}, \dot{\boldsymbol{q}})^\mathrm{T} = -\frac{1}{2} D\boldsymbol{M}(\boldsymbol{q})\big(\dot{\boldsymbol{q}}, \dot{\boldsymbol{q}}\big) - DE_\mathrm{pot}(\boldsymbol{q}). \tag{5.2c}$$

Obviously, no additional non-conservative forces, such as damping, friction, or actuation, are introduced in the process of constructing an ECM in (5.2).

5.1.1 Conditions for Energy Conservation

According to the definition in Chapter 4, for the energy function $E(\boldsymbol{x})$ to be a (hybrid) first-integral $\mathcal{H}$ of Σ, the following conditions must hold:

- All vector fields $\boldsymbol{f}_i$ are conservative (*Def1*).
- The energy remains constant across phase transitions (*Def2*).

Condition *Def1* can be readily verified by performing index reduction on the differential-algebraic equations (DAE) in (5.2), yielding the phase vector field:

$$\boldsymbol{f}_i(\boldsymbol{x}_i) = \begin{bmatrix} \dot{\boldsymbol{q}} \\ \boldsymbol{M}(\boldsymbol{q})^{-1}\Big(\boldsymbol{\eta}(\boldsymbol{q}, \dot{\boldsymbol{q}}) + \boldsymbol{J}_i(\boldsymbol{q})^\mathrm{T} \boldsymbol{\lambda}_i(\boldsymbol{q}, \dot{\boldsymbol{q}})\Big) \end{bmatrix}, \quad \boldsymbol{x}_i = \begin{bmatrix} \boldsymbol{q} \\ \dot{\boldsymbol{q}} \end{bmatrix}. \tag{5.3}$$

Here, the Lagrange multipliers are explicitly given by

$$\boldsymbol{\lambda}_i(\boldsymbol{x}_i) = -\widetilde{\boldsymbol{M}}_i(\boldsymbol{q})^{-1}\Big(\dot{\boldsymbol{J}}_i(\boldsymbol{q})\dot{\boldsymbol{q}} + \boldsymbol{J}_i(\boldsymbol{q})\boldsymbol{M}(\boldsymbol{q})^{-1}\boldsymbol{\eta}(\boldsymbol{x}_i)\Big), \tag{5.4}$$

$$\widetilde{\boldsymbol{M}}_i(\boldsymbol{q}) := \boldsymbol{J}_i(\boldsymbol{q})\boldsymbol{M}(\boldsymbol{q})^{-1}\boldsymbol{J}_i(\boldsymbol{q})^{\mathrm{T}}, \tag{5.5}$$

where $\widetilde{\boldsymbol{M}}_i$ denotes the Delassus matrix[2] for phase i. Hence, the derivative of the energy $DE(\boldsymbol{x}_i) = [-\boldsymbol{\eta}(\boldsymbol{x}_i)^{\mathrm{T}}\ \dot{\boldsymbol{q}}^{\mathrm{T}}\boldsymbol{M}(\boldsymbol{q})]$ is orthogonal to $\boldsymbol{f}_i(\boldsymbol{x}_i)$ in (5.3), using d'Alembert's principle such that $\dot{\boldsymbol{q}}^{\mathrm{T}}\boldsymbol{J}_i(\boldsymbol{q})^{\mathrm{T}}\boldsymbol{\lambda}_i = 0$.

The second condition *Def2* is more intrecate to verify as it assumes that four types of transitions can occur in a mechanical system:

1. Active constraints in phase i become inactive in phase $i+1$, i.e., $\mathcal{C}_{i+1} \subset \mathcal{C}_i$, implying $n_{\mathrm{c},i+1} < n_{\mathrm{c},i}$.

2. The constraint set remains unchanged, i.e., $\mathcal{C}_{i+1} = \mathcal{C}_i$.

3. Additional constraints become active in phase $i+1$, i.e., $\mathcal{C}_i \subset \mathcal{C}_{i+1}$, implying $n_{\mathrm{c},i} < n_{\mathrm{c},i+1}$.

4. A combination of transitions 1 and 3, in which previously active constraints become inactive and new constraints become active in phase $i+1$.

Transition 1 corresponds to rigid bodies breaking contact with their environment, indicated by an event $e_i^{i+1} = \lambda_{i,\mathrm{N}}(\boldsymbol{x}_i)$, where a normal force component $\lambda_{i,\mathrm{N}}$ of (5.4) crosses zero. Since no projection onto $\mathcal{C}_{i+1}$ is necessary, the discrete map is the identity, i.e., $\boldsymbol{g}_i^{i+1}(\boldsymbol{x}_i) = \boldsymbol{x}_i$, ensuring energy conservation: $E(\boldsymbol{x}_{i+1}) = E(\boldsymbol{x}_i)$.

Transitions 2 and 3 involve rigid bodies making contact with the environment. The collision process is modeled using Newton's coefficient of restitution $\epsilon_{\mathrm{CoR}} \in [0,1]$, which relates pre-collision relative velocities $\boldsymbol{\gamma}_{i+1}^-$ to post-collision relative velocities $\boldsymbol{\gamma}_i^+$:

$$\boldsymbol{\gamma}_{i+1}^+ = -\epsilon_{\mathrm{CoR}}\boldsymbol{\gamma}_i^-. \tag{5.6}$$

For $\epsilon_{\mathrm{CoR}} > 0$, transition 2 describes an elastic collision that does not create new persistent active constraints. A prominent example is the bouncing ball (Section 5.2.1), where $\boldsymbol{\gamma}_i^-$ and $\boldsymbol{\gamma}_{i+1}^+$ represent opposing velocities before and after the bounce. As required by *Def2*, energy remains constant only for a fully elastic collision, i.e., $\epsilon_{\mathrm{CoR}} = 1$.

[2]The Delassus matrix $\widetilde{\boldsymbol{M}}_i$ is named after Étienne Delassus [31].

In legged systems, a common assumption is fully plastic collisions ($\epsilon_{\mathrm{CoR}} = 0$), where a foot remains on the ground, enforcing $\boldsymbol{\gamma}_{i+1}^{+} = \mathbf{0}$, where $\boldsymbol{\gamma}_{i+1}^{+} := \boldsymbol{J}_{i+1}(\boldsymbol{q}^{+})\dot{\boldsymbol{q}}^{+}$. This (transition 3 and 4) corresponds to a projection onto $\mathcal{C}_{i+1}$. Since the system configuration $\boldsymbol{q}$ in mechanical systems remains constant across discrete transitions ($\boldsymbol{q} = \boldsymbol{q}^{+} = \boldsymbol{q}^{-}$), a projection within the map $\boldsymbol{g}_i^{i+1}(\boldsymbol{x}_i^{-})$ occurs on velocity level:

$$\dot{\boldsymbol{q}}^{+} = \left(\boldsymbol{I} - \boldsymbol{M}(\boldsymbol{q})^{-1}\boldsymbol{J}_{i+1}(\boldsymbol{q})^{\mathrm{T}}\widetilde{\boldsymbol{M}}_{i+1}(\boldsymbol{q})^{-1}\boldsymbol{J}_{i+1}(\boldsymbol{q})\right)\dot{\boldsymbol{q}}^{-}. \tag{5.7}$$

A constant configuration $\boldsymbol{q}$ also implies that the potential energy $E_{\mathrm{pot}}(\boldsymbol{q})$ remains unchanged across transitions. Consequently, to satisfy *Def2*, meaning that $E(\boldsymbol{x}_{i+1}^{+}) = E(\boldsymbol{x}_i^{-})$, the kinetic energy E_{kin} must also remain constant:

$$\frac{1}{2}\dot{\boldsymbol{q}}^{+\mathrm{T}}\boldsymbol{M}(\boldsymbol{q})\dot{\boldsymbol{q}}^{+} \overset{!}{=} \frac{1}{2}\dot{\boldsymbol{q}}^{-\mathrm{T}}\boldsymbol{M}(\boldsymbol{q})\dot{\boldsymbol{q}}^{-}, \quad \forall \boldsymbol{x}_i \in \mathcal{E}_i^{i+1}. \tag{5.8a}$$

Using (5.7), this condition can be expressed more compactly as:

$$\boldsymbol{\gamma}^{\mathrm{T}}\widetilde{\boldsymbol{M}}_{i+1}(\boldsymbol{q})^{-1}\boldsymbol{\gamma} \overset{!}{=} \mathbf{0}, \quad \forall \boldsymbol{\gamma} \in \mathrm{Im}(\boldsymbol{J}_{i+1}(\boldsymbol{q})\dot{\boldsymbol{q}}^{-}). \tag{5.8b}$$

Energy conservation is only possible if the inverse Delassus matrix $\widetilde{\boldsymbol{M}}_{i+1}^{-1}$ is zero. Intuitively, this means that inertia and mass involved in the projection must vanish to preserve energy. However, this leads to a problematic condition, as it results in singularities in the system's mass matrix $\boldsymbol{M}$.

5.1.2 Vanishing Masses & Inertias

Rather than enforcing vanishing masses and inertias directly, they are instead considered as a limiting case. To formalize this, introducing some abuse of notation, a parameterized mass matrix $\boldsymbol{M}(\boldsymbol{q};\varepsilon) = \boldsymbol{M}_{\varepsilon}$ is defined, where ε is a parameter that also affects the Delassus matrix, written as $\widetilde{\boldsymbol{M}}_{i+1}(\boldsymbol{q};\varepsilon)$. This parameterization must satisfy:

$$\lim_{\varepsilon\to 0}\widetilde{\boldsymbol{M}}_{i+1}(\boldsymbol{q};\varepsilon)^{-1} \overset{!}{=} \mathbf{0}. \tag{5.9}$$

From (5.8), it follows that the system is energetically conservative only in the limit $\varepsilon \to 0$. However, as noted in [68], massless appendages can create inconsistencies between accelerations and net forces in the dynamics (5.3). To ensure well-defined, finite-dimensional dynamics, rank deficiencies in the mass matrix $\boldsymbol{M}_{\varepsilon\to 0}$ must be addressed through constraints ($\boldsymbol{J}_i$, $\boldsymbol{\lambda}_i$).

By appropriately scaling $\boldsymbol{J}_i$, $\boldsymbol{h}$ and $\boldsymbol{\lambda}_i$ with ε, the singularities in $\boldsymbol{M}_\varepsilon^{-1}$ can be avoided, allowing (5.3) to be reformulated as:

$$\ddot{\boldsymbol{q}} = \boldsymbol{M}_\varepsilon^{-1}\big(\boldsymbol{\eta}(\boldsymbol{x};\varepsilon) + \boldsymbol{J}_i(\boldsymbol{q};\varepsilon)^{\mathrm{T}}\boldsymbol{\lambda}_i(\boldsymbol{x};\varepsilon)\big), \tag{5.10a}$$

$$= \boldsymbol{M}_\varepsilon^{-1}\big(\boldsymbol{\eta}_{\mathrm{mass}}(\boldsymbol{x};\varepsilon)\big) + \boldsymbol{M}_\varepsilon^{-1}\big(\boldsymbol{\eta}_{\mathrm{elast}}(\boldsymbol{q};\varepsilon) + \boldsymbol{J}_i(\boldsymbol{q};\varepsilon)^{\mathrm{T}}\boldsymbol{\lambda}_i(\boldsymbol{x};\varepsilon)\big). \tag{5.10b}$$

Since scaling masses also affect gravitational energy $E_{\mathrm{pot,grav}}$, the potential energy is further decomposed as $E_{\mathrm{pot}} = E_{\mathrm{pot,grav}} + E_{\mathrm{pot,elast}}$, yielding $\boldsymbol{\eta} = \boldsymbol{\eta}_{\mathrm{mass}} + \boldsymbol{\eta}_{\mathrm{elast}}$ in (5.2c). Here, the subscript $_{\mathrm{elast}}$ denotes the system's elastic components. The resulting conservative vector field, defined by equation (5.10), remains C^1 and well-posed in the analytic limit $\varepsilon \to 0$. In other words, while $\boldsymbol{M}_\varepsilon$ may become singular as $\varepsilon \to 0$, the products $\boldsymbol{M}^{-1}\boldsymbol{\eta}_{\mathrm{mass}}$, $\boldsymbol{M}^{-1}(\boldsymbol{\eta}_{\mathrm{elast}} + \boldsymbol{J}_i^{\mathrm{T}}\boldsymbol{\lambda}_i)$ remains finite.

Remark 5.1.1. *This approach aligns with Assumption A7 in [68]. However, unlike their formulation, the matrix* $\begin{bmatrix} \boldsymbol{M} & \boldsymbol{J}_i^{\mathrm{T}} \\ \boldsymbol{J}_i & \boldsymbol{0} \end{bmatrix}$ *does not need to be invertible in the limit. Additionally, the robot's topology does not require explicit modifications when a massless limb detaches from the ground (contrary to Assumption A6 in [68]). As noted in [68], massless limbs do not contribute to kinetic energy and thus evolve independently under their own decoupled dynamics.*

5.1.3 Example: The Spring-Loaded Hopper

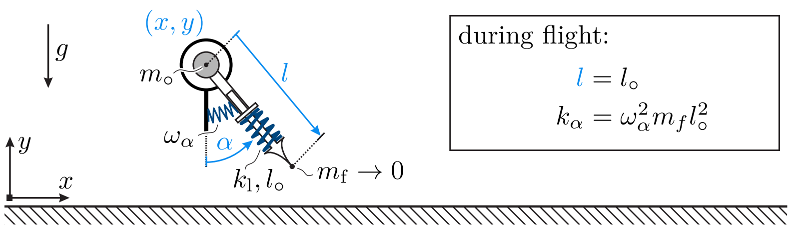

Figure 5.1: An energetically conservative one-legged hopper with a translational leg spring and a torsional hip spring. It's planar configuration is described by $\boldsymbol{q}^{\mathrm{T}} = [x\ y\ \alpha\ l]$.

The following applies the previously described methodology to derive an ECM for a SLIP-like one-legged hopper, as introduced in [43]. This model includes passive swing leg dynamics generated by a torsional hip spring (Fig. 5.1). Based on [1🎓], the systematic derivation of an ECM presented here addresses an unresolved issue in [43] concerning the spring leg dynamics during flight. This motion, which becomes singular when foot masses vanish, was previously ignored. Here, it is accounted for by incorporating additional holonomic constraints.

The model consists of a torso with mass $m_\circ$, constrained to purely linear motion (no rotation) as defined in [43]. Thus, the torso's configuration is given by the hip position (x, y). The leg is attached to the hip via a rotational joint with angle α and includes a torsional spring of stiffness k_α without damping. The legs are modeled as massless linear springs with length l, natural length $l_\circ$, stiffness k_l, no damping, and a point mass m_f at the foot. The total system mass is $m_\circ + m_\mathrm{f}$. The robot's configuration is represented by the generalized coordinates $\boldsymbol{q}^\mathrm{T} = [x \; y \; \alpha \; l]$, with $n_\mathrm{x} = 8$.

The model has two phases: *stance* S and *flight* F. The corresponding constraint forces in these phases are $\boldsymbol{\lambda}_\mathrm{S}^\mathrm{T} = [\lambda_\mathrm{T} \; \lambda_\mathrm{N}]$ and λ_F. These forces satisfy the constraints

$$j_\mathrm{F}(\boldsymbol{q}) = l - l_\circ = 0, \tag{5.11a}$$

$$\boldsymbol{j}_\mathrm{S}(\boldsymbol{q}) = \begin{bmatrix} x + l\sin(\alpha) - x_\mathrm{c} \\ y - l\cos(\alpha) \end{bmatrix} = 0, \tag{5.11b}$$

during *flight* and *stance*, respectively. The constraint (5.11a) fixes the leg length to $l_\circ$ during flight, whereas equation (5.11b) implements the assumption of no sliding during *stance* (with a horizontal contact point position x_c). For the continuous dynamics in (5.10), the elastic force vector is defined as

$$\boldsymbol{\eta}_\mathrm{elast}^\mathrm{T} := \begin{bmatrix} 0 & 0 & F_\alpha & F_\mathrm{l} \end{bmatrix}, \tag{5.12}$$

where $F_\alpha(\boldsymbol{q}) = -k_\alpha \alpha$ and $F_\mathrm{l}(\boldsymbol{q}) = k_\mathrm{l}(l_\circ - l)$ describe the hip and leg spring forces, respectively. The tangential and normal contact forces, λ_T and λ_N, are active only during *stance*. Similarly, $\lambda_\mathrm{F} \neq 0$ holds only during flight to constrain the leg length to its natural value, $l_\circ$. This results in impulsive forces and discontinuous changes in $\dot{l}$ whenever the foot leaves the ground with nonzero velocity. The touch-down event $e_\mathrm{F}^\mathrm{S}(\boldsymbol{q}) = [0 \; 1] \cdot \boldsymbol{j}_\mathrm{S}(\boldsymbol{q})$ is defined kinematically, while the lift-off event $e_\mathrm{S}^\mathrm{F}(\boldsymbol{q}, \dot{\boldsymbol{q}}) = \lambda_\mathrm{N}$ is triggered when λ_N changes sign from positive to negative.

To avoid kinetic energy losses during touchdown, the foot mass m_f is brought to zero, following an approach similar to that in [43, 44, 68, 100]. To satisfy *Def2* and ensure equation (5.9) holds, the foot mass is redefined as $m_\mathrm{f} = \varepsilon \hat{m}_\mathrm{f}$. Note, for $\varepsilon \to 0$, the condition in equation (5.9)remains valid for both the *stance* and *flight* transitions:

$$\lim_{\varepsilon \to 0} \widetilde{\boldsymbol{M}}_\mathrm{S}(\boldsymbol{q}; \varepsilon)^{-1} = \lim_{\varepsilon \to 0} \begin{bmatrix} \varepsilon \hat{m}_\mathrm{f} & 0 \\ 0 & \varepsilon \hat{m}_\mathrm{f} \end{bmatrix} = \boldsymbol{0}, \tag{5.13a}$$

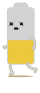

$$\lim_{\varepsilon\to 0} \widetilde{\boldsymbol{M}}_{\mathrm{F}}(\boldsymbol{q};\varepsilon)^{-1} = \lim_{\varepsilon\to 0} \frac{\varepsilon \hat{m}_{\mathrm{f}} m_{\circ}}{\varepsilon \hat{m}_{\mathrm{f}} + m_{\circ}} \quad = 0. \tag{5.13b}$$

To ensure finite continuous dynamics in the limit $\varepsilon \to 0$, the constraint forces are redefined as

$$\lambda_{\mathrm{F}} := -F_{\mathrm{l}} + \frac{\varepsilon \hat{m}_{\mathrm{f}}}{m_{\circ}} \hat{\lambda}_{\mathrm{F}}, \quad \boldsymbol{\lambda}_{\mathrm{S}} := -\begin{bmatrix} \sin(\alpha) \\ -\cos(\alpha) \end{bmatrix} F_{\mathrm{l}} + \frac{\varepsilon \hat{m}_{\mathrm{f}}}{m_{\circ}} \hat{\boldsymbol{\lambda}}_{\mathrm{S}}, \tag{5.14}$$

introducing new auxiliary forces $\hat{\lambda}_{\mathrm{F}}$, $\hat{\boldsymbol{\lambda}}_{\mathrm{S}}$. The core idea here is to decompose the constraint forces into two components: one that balances the elastic forces, represented by the known values of F_{l}, and another that counteracts inertial forces, computed when solving the DAE (5.2). The latter component is scaled with ε to ensure that $\hat{\lambda}_{\mathrm{F}}$ and $\hat{\boldsymbol{\lambda}}_{\mathrm{S}}$ remain finite even in the limit $\varepsilon \to 0$. Following [43], the leg swing frequency ω_α is prescribed by

$$k_\alpha = \omega_\alpha^2 \underbrace{m_{\mathrm{f}}}_{=\varepsilon \hat{m}_{\mathrm{f}}} l_\circ^2. \tag{5.15}$$

This ensures that ω remains finite as the foot mass approaches zero, leading to $k_\alpha \to 0$. With the modifications in (5.14) and (5.15), taking the limit $\varepsilon \to 0$ recovers the same finite-dimensional dynamics reported in [43].

5.2 Exploration of Periodic Orbits

To demonstrate the numerical computation and continuation of normal conservative orbits in cHDS, four examples from [3] are discussed: a bouncing ball, a rocking block, a bouncing rod (Fig. 5.2) and the previously derived SLIP-like hopper (Fig. 5.1). Each of these systems is based on an energetically conservative mechanical model with lossless collisions, where the hybrid first integral $\mathcal{H}$ consistently represents the total mechanical energy. To facilitate comparisons between them, the state variables and parameters of all systems are normalized with respect to total mass $m_\circ$, characteristic length $l_\circ$, and gravity g. The hybrid dynamics $\Sigma^{\mathcal{H}}$ of these systems are smooth in all components, ensuring that $\boldsymbol{r}_{\mathrm{tb}} \in C^\infty$. A particular emphasis is placed on the time-based (tb) multiple shooting (ms) implementation $\boldsymbol{r}_{\mathrm{tb,ms}}$ in (4.21), as it enables the exploration of non-physical behaviors that nonetheless connect smoothly to normal conservative orbits.

A higher-order variable step size integrator (explicit Runge–Kutta (4,5) with error tolerances 10^{-7}) is used to trade off accuracy and speed in the numerical computation of the root-finding problem $\boldsymbol{r}_{\mathrm{tb,ms}}(\boldsymbol{\nu}_{\mathrm{tb,ms}}) = \boldsymbol{0}$.

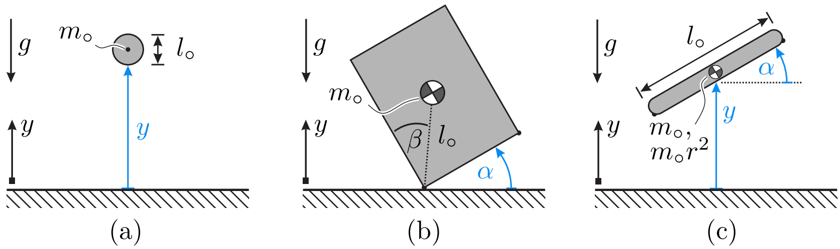

Figure 5.2: Shown are three conservative mechanical systems with impulsive dynamics due to fully elastic collisions with the ground ($\epsilon_{\mathrm{CoR}} = 1$): (a) bouncing ball, (b) rocking block and (c) bouncing rod. The system's configuration variables are shown in blue.

5.2.1 Example: The Bouncing Ball

The cHDS $\Sigma^{\mathcal{H}}$ of the bouncing ball (mass $m_\circ$, diameter $l_\circ$), shown in Fig. 5.2a, is represented as:

$$\mathcal{X}_1 = \left\{ \boldsymbol{x}_1 = \begin{bmatrix} y \\ \dot{y} \end{bmatrix} \;\middle|\; y \in \mathbb{R}, \dot{y} \in \mathbb{R} \right\}, \tag{5.16a}$$

$$\boldsymbol{f}_1 = \begin{bmatrix} \dot{y} & -g \end{bmatrix}^{\mathrm{T}}, \tag{5.16b}$$

$$\mathcal{E}_1^1 = \left\{ \boldsymbol{x}_1 = \begin{bmatrix} y \\ \dot{y} \end{bmatrix} \;\middle|\; e_1^1 = y = 0 \right\}, \tag{5.16c}$$

$$\boldsymbol{g}_1^1 = \begin{bmatrix} y & -\dot{y} \end{bmatrix}^{\mathrm{T}}, \tag{5.16d}$$

$$H_1 = \frac{1}{2} m_\circ \dot{y}^2 + m_\circ g y. \tag{5.16e}$$

These dynamics are limited to a single phase ($m = 1$) and represent a free-falling object traversing the phase sequence $1 \to 1$. The hybrid phase transition occurs when the ball touches the ground and the state returns to $\mathcal{X}_1$ via a fully elastic collision ($\epsilon_{\mathrm{CoR}} = 1$) to complete the recurrent motion as illustrated in Fig. 5.3. The total energy of the ball in (5.16e) serves as the hybrid first integral $\mathcal{H}$. Given the simplicity of the example, the hybrid flow $\boldsymbol{\varphi}$ of the cHDS $\Sigma^{\mathcal{H}}$ of (5.16) can be solved analytically according to the recursion in (4.2), which helps illustrate the concepts and symbols introduced in Chapters 3 and 4. The hybrid flow originates from

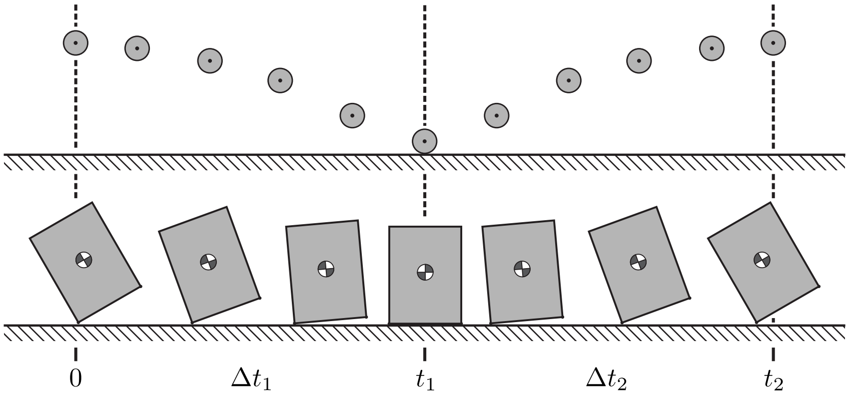

Figure 5.3: Key frames illustrating a normal conservative orbit of the bouncing ball and the rocking block. In the rocking block example, the system's symmetric motion is exploited, allowing us to compute only its pivoting motion about the left corner. An additional time symmetry is observed in both system's orbits, with $\Delta t_1 = \Delta t_2$.

an arbitrary initial point

$$\bar{\boldsymbol{x}}_1 = \boldsymbol{x}_0 = \begin{bmatrix} y_0 & \dot{y}_0 \end{bmatrix}^{\mathrm{T}} \in \mathcal{X}_1, \tag{5.17a}$$

$$\bar{t}_1 = t_0 = 0, \tag{5.17b}$$

where $\boldsymbol{x}_0 \in \mathcal{X}_0$ must be further constrained to produce physically realizable recurrent hybrid trajectories that satisfy Assumptions *As1*-*As3*. Specifically, the initial height must satisfy $y_0 \in \mathbb{R}_{>0}$ such that $e_1^1(\boldsymbol{x}_0) > 0$. Given this, the hybrid flow progresses through the first phase with

$$\boldsymbol{\varphi}_1\left(t_1, 0, \bar{\boldsymbol{x}}_1\right) = \begin{bmatrix} -\frac{1}{2} g t_1^2 + \dot{y}_0 t_1 + y_0 \\ -g t_1 + \dot{y}_0 \end{bmatrix}, \tag{5.17c}$$

until it reaches the event manifold $\mathcal{E}_1^1$ at time

$$\bar{t}_2 := t_1^{\mathcal{E}}(\bar{t}_1, \bar{\boldsymbol{x}}_1) = \frac{\dot{y}_0 + \sqrt{\dot{y}_0^2 + 2 y_0 g}}{g} + \underbrace{\bar{t}_1}_{=0}, \tag{5.17d}$$

with $e_1^1 \circ \boldsymbol{\varphi}_1(t_1^{\mathcal{E}}, 0, \bar{\boldsymbol{x}}_1) = 0$. The second part of the hybrid flow is initiated at the image of the reset map $\boldsymbol{g}_1^1$ with

$$\bar{\boldsymbol{x}}_2 = \boldsymbol{g}_1^1 \circ \boldsymbol{\varphi}_1\left(\bar{t}_2, 0, \bar{\boldsymbol{x}}_1\right) = \begin{bmatrix} -\frac{1}{2} g \bar{t}_2^2 + \dot{y}_0 \bar{t}_2 + y_0 \\ -\big(- g \bar{t}_2 + \dot{y}_0 \big) \end{bmatrix}, \tag{5.17e}$$

$$\overset{(5.17d)}{\Longrightarrow} \quad \bar{\boldsymbol{x}}_2 = \begin{bmatrix} \bar{y}_2 \\ \dot{\bar{y}}_2 \end{bmatrix} = \begin{bmatrix} 0 \\ \sqrt{\dot{y}_0^2 + 2y_0 g} \end{bmatrix}. \tag{5.17f}$$

Hence, with $\Delta t = t - \bar{t}_2$, the overall hybrid flow at time $t \in \mathcal{T}$ is defined as

$$\boldsymbol{\varphi}(t, 0, \boldsymbol{x}_0) = \boldsymbol{\varphi}_1\left(t, \bar{t}_2, \bar{\boldsymbol{x}}_2\right) = \begin{bmatrix} -\frac{1}{2} g \Delta t^2 + \dot{\bar{y}}_2 \Delta t \\ -g\Delta t + \dot{\bar{y}}_2 \end{bmatrix}. \tag{5.17g}$$

The time t can be chosen from the final time interval $\mathcal{T} = [\bar{t}_2, \bar{t}_3]$, where $\bar{t}_3 = \bar{t}_2 + \Delta t_1^{\mathcal{E}}(\bar{\boldsymbol{x}}_2)$ with

$$\Delta t_1^{\mathcal{E}}(\bar{\boldsymbol{x}}_2) = \frac{2}{g} \dot{\bar{y}}_2 \overset{(5.17f)}{=} \frac{2}{g}\sqrt{\dot{y}_0^2 + 2y_0 g} \tag{5.17h}$$

corresponds to the next ground collision. To eliminate time t and identify periodic orbits in (5.17g), the Poincaré section is defined as

$$\mathcal{A} = \left\{ \boldsymbol{x}_1 = \begin{bmatrix} y \\ \dot{y} \end{bmatrix} \;\middle|\; \begin{matrix} a = \dot{y} = 0, \\ \dot{a} = -g < 0 \end{matrix} \right\}, \tag{5.18}$$

which corresponds to the ball being instantaneously at rest. This implies the value of the local time-to-anchor function as $\Delta t_1^{\mathcal{A}}(\bar{\boldsymbol{x}}_2) = \dot{\bar{y}}_2/g$, leading to the overall time:

$$t^{\mathcal{A}}(\boldsymbol{x}_0) = \bar{t}_2 + \Delta t_1^{\mathcal{A}}(\bar{\boldsymbol{x}}_2) = \frac{\dot{y}_0 + 2\dot{\bar{y}}_2}{g} = \frac{\dot{y}_0 + 2\sqrt{\dot{y}_0^2 + 2y_0 g}}{g}. \tag{5.19a}$$

With that, the Poincaré map is given as

$$\boldsymbol{P}(\boldsymbol{x}_0) = \boldsymbol{x}(t^{\mathcal{A}}) = \begin{bmatrix} \frac{\dot{y}_0^2}{2g} + y_0 \\ 0 \end{bmatrix}, \quad \boldsymbol{x}_0 = \begin{bmatrix} y_0 \\ \dot{y}_0 \end{bmatrix}. \tag{5.19b}$$

Note, although $\boldsymbol{P}(\boldsymbol{x}_0) \in \mathcal{A}$, the initial state $\boldsymbol{x}_0$ still has to be chosen from the Poincaré section $\mathcal{A}$ (Remark 4.3.2). This requires $\dot{y}_0 = 0$ and simplifies (5.19) to

$$T = t^{\mathcal{A}}\left(\begin{bmatrix} y_0 & 0 \end{bmatrix}^{\mathrm{T}}\right) = 2\sqrt{2\frac{y_0}{g}}, \tag{5.20a}$$

$$\boldsymbol{P}\left(\begin{bmatrix} y_0 \\ 0 \end{bmatrix}\right) = \begin{bmatrix} y_0 \\ 0 \end{bmatrix}. \tag{5.20b}$$

Hence, any $\boldsymbol{x}_0 = [y_0\ 0]^{\mathrm{T}} \in \mathcal{A}$ with $y_0 > 0$ yields a fixed point of the Poincaré map $\boldsymbol{P}$ and a normal conservative orbit of (5.16), which also fulfills Assumption *As3*. That is, these fixed points are not isolated, as anticipated by Theorem 4.2.1 based on the existence of a hybrid first integral $\mathcal{H}$. A projection of this family of orbits is depicted by the solid blue line in Fig. 5.4a.

For the numerical exploration of periodic orbits, as discussed in Section 4.3, the time-based implementation in (4.21) is considered:

$$\boldsymbol{r}_{\mathrm{tb,ms}}(\boldsymbol{\nu}_{\mathrm{tb,ms}}) = \begin{bmatrix} \boldsymbol{\varphi}_1(t_2, t_1, \bar{\boldsymbol{x}}_2; \xi) - \bar{\boldsymbol{x}}_1 \\ a \circ \boldsymbol{\varphi}_1(t_2, t_1, \bar{\boldsymbol{x}}_2; \xi) \\ \boldsymbol{g}_1^1 \circ \boldsymbol{\varphi}_1(t_1, 0, \bar{\boldsymbol{x}}_1; \xi) - \bar{\boldsymbol{x}}_2 \\ e_1^1 \circ \boldsymbol{\varphi}_1(t_1, 0, \bar{\boldsymbol{x}}_1; \xi) \\ H_1(\bar{\boldsymbol{x}}_1) - \bar{H} \end{bmatrix}, \tag{5.21a}$$

$$\boldsymbol{\nu}_{\mathrm{tb,ms}} = \begin{bmatrix} t_2 & \bar{\boldsymbol{x}}_2^{\mathrm{T}} & t_1 & \bar{\boldsymbol{x}}_1^{\mathrm{T}} & \xi & \bar{H} \end{bmatrix}^{\mathrm{T}}, \tag{5.21b}$$

where the phase flows $\boldsymbol{\varphi}_1$ solve the modified ODE defined by the vector field in (4.17):

$$\tilde{\boldsymbol{f}}_1(\boldsymbol{x}_1, \xi) = \begin{bmatrix} \dot{y} + \xi m_\circ g \\ -g + \xi m_\circ \dot{y} \end{bmatrix}, \quad \boldsymbol{x}_1 = \begin{bmatrix} y \\ \dot{y} \end{bmatrix}. \tag{5.22}$$

Note that for $\xi = 0$, it holds $\tilde{\boldsymbol{f}}_1 = \boldsymbol{f}_1$, and in particular, with $\bar{H} > 0$, the solution spaces of periodic orbits of (5.21) and (5.20) are equivalent. With the map $\boldsymbol{r}_{\mathrm{tb,ms}}$ and its Jacobian $D\boldsymbol{r}_{\mathrm{tb,ms}}$, the solution space $\mathcal{S}_{\mathrm{tb,ms}} = \boldsymbol{r}_{\mathrm{tb,ms}}^{-1}(\boldsymbol{0})$ is explored utilizing a PCC method (Section 2.2.1).

The use of numerical continuation methods necessitates an initial point $\boldsymbol{\nu}_0 \in \mathcal{S}_{\mathrm{tb,ms}}$. With $m = 1$, an appropriate initial point for the continuation of periodic solutions is the equilibrium state of $\Sigma^{\mathcal{H}}$ at energy level $\bar{H} = 0\ m_\circ g l_\circ$ and thus, the trivial vector $\boldsymbol{\nu}_0 = \boldsymbol{0}$. Notably, this initial point does not fulfill Assumption *As3*, which, however, does not pose any issues for the time-based implementation (4.21). Upon closer inspection, one determines that this $\boldsymbol{\nu}_0$ marks a simple bifurcation (SB) point of $\boldsymbol{r}_{\mathrm{tb,ms}}$ with perpendicular tangent vectors $\boldsymbol{\tau}_1$ and $\boldsymbol{\tau}_2$, as they are depicted in Fig. 5.4a. These tangent vectors are constructed through a Lyapunov-Schmidt reduction (Section 2.2.2). Since the Jacobian $D\boldsymbol{r}(\boldsymbol{u}_0)$ exhibits a vanishing gradient with respect to ξ, the tangent vector $\boldsymbol{\tau}_1$ exclusively aligns with the direction of ξ. The corresponding projection of points from $\mathcal{S}_{\mathrm{tb,ms}}$ corresponds entirely to instances in which the ball is completely at rest (orange line in Fig. 5.4a). Such solutions exist for arbitrary values of ξ.

By following the tangent vector $\boldsymbol{\tau}_2$ in the direction of increasing phase durations Δt_1 and Δt_2, a normal conservative orbit arises, that corresponds to the fixed points of (5.20) (solid blue line). For negative phase durations $\Delta t_1 < 0$ and $\Delta t_2 < 0$ (illustrated by the dashed blue line), the phase dynamics traverse in reverse time. While this constitutes a non-physical solution, it is possible to solve the phase dynamics in (5.22) in reversed time, by modifying the vector field such that $\dot{\boldsymbol{x}}_1 = -\tilde{\boldsymbol{f}}_1(\boldsymbol{x}_1, \xi)$ and solving the corresponding ODE in forward time $t \in -[t_{i-1}, t_i]$ for $t_{i-1}, t_i < 0$. Note that only a point of the solid blue line corresponds to a normal conservative orbit and thus, to a solution of $\Sigma^{\mathcal{H}}$. Since the normal conservative orbits in this example can be computed analytically, the relationship between the period time and the first integral's values can be expressed in closed form as $T = \sqrt{\bar{H}\, {}^{8}/_{m_\circ g^2}}$. For the non-physical periodic orbits with reversed time (dashed blue line) this relationship is expressed by $T = -\sqrt{\bar{H}\, {}^{8}/_{m_\circ g^2}}$.

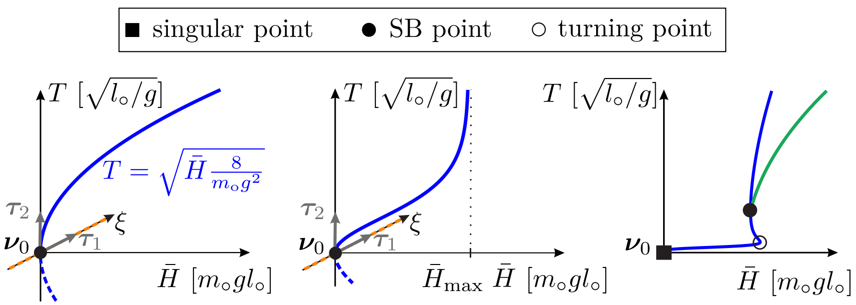

(a) (b) (c)

Figure 5.4: Projection of points from $\mathcal{S}_{\mathrm{tb,ms}}$ of (a) the bouncing ball, (b) the rocking block (b), and (c) the bouncing rod. Solid blue lines indicate normal conservative orbits originating from $\boldsymbol{\nu}_0 = \mathbf{0}$. The simplicity of the dynamics of the bouncing ball permits an analytic relationship between $\bar{H}$ and T. For the rocking block, $\bar{H}$ is bounded by a homoclinic orbit at $\bar{H}_{\max}$ as T tends to infinity. For the bouncing rod, $\boldsymbol{\nu}_0$ constitutes a non-simple bifurcation point. The family of conservative orbits further features turning points in $\bar{H}$ and a simple bifurcation (SB) point. Projections of the bifurcating solutions are shown by a solid green line, with further details provided in Fig. 5.5.

5.2.2 Example: The Rocking Block

Following the example in [24], a rectangular block of diagonal size $2l_\circ$, mass $m_\circ$ and so called block slenderness $\beta = 0.3$ rad is examined, as depicted in Fig. 5.2b. The block rocks back and forth between its left and right corners, experiencing lossless collisions ($\epsilon_{\text{CoR}} = 1$) during each movement. A detailed description of this motion can be found in [63]. Due to the block's inherent symmetry, its continuous dynamics during pivoting motion around either corner are equivalent. Key frames illustrating this symmetric motion are shown in Fig. 5.3. Consequently, with $m = 1$, the block's dynamics are defined as

$$\mathcal{X}_1 = \left\{ \boldsymbol{x}_1 = \begin{bmatrix} \alpha \\ \dot{\alpha} \end{bmatrix} \;\middle|\; \alpha \in \mathbb{R}, \dot{\alpha} \in \mathbb{R} \right\}, \tag{5.23a}$$

$$\boldsymbol{f}_1 = \begin{bmatrix} \dot{\alpha} \\ -\frac{3g}{4l_\circ} \sin(\beta - \alpha) \end{bmatrix}, \tag{5.23b}$$

$$\mathcal{E}_1^1 = \left\{ \boldsymbol{x}_1 = \begin{bmatrix} \alpha \\ \dot{\alpha} \end{bmatrix} \;\middle|\; e_1^1 = \alpha = 0 \right\}, \tag{5.23c}$$

$$\boldsymbol{g}_1^1 = \begin{bmatrix} \alpha & -\dot{\alpha} \end{bmatrix}^{\mathrm{T}}, \tag{5.23d}$$

$$H_1 = \frac{2}{3} m_\circ l_\circ^2 \dot{\alpha}^2 + \left(\cos(\alpha - \beta) - \cos(\beta)\right) m_\circ l_\circ g, \tag{5.23e}$$

where the angle α characterizes its rotation about the left corner and the total energy of the block in (5.23e) serves as the hybrid first integral $\mathcal{H}$. Note that, similar to the bouncing ball example, H_1 is defined such that its potential energy is bounded by the zero level set as $\alpha \to 0$. The condition $\alpha < \beta$ is further imposed, as the slenderness ratio β defines the upright unstable equilibrium of the block. As a result, to ensure that the recurrent hybrid trajectories $\boldsymbol{x}(t)$ are physically realizable and comply with Assumptions *As1*-*As3*, the initial state domain $\mathcal{X}_0$ must only include configurations where α lies within the range $(0, \beta)$. As before, this ensures $e_1^1(\boldsymbol{x}_0) > 0$.

The Poincaré section $\mathcal{A}$ is based on the anchor function

$$a(\boldsymbol{x}_1) = \dot{\alpha}, \quad \boldsymbol{x}_1 = \begin{bmatrix} \alpha & \dot{\alpha} \end{bmatrix}^{\mathrm{T}}, \tag{5.24}$$

which yields a time-based problem (4.21) of size $N = 7$, aligning with the structure of the preceding bouncing ball example. Utilizing the equilibrium state $\boldsymbol{\nu}_0 = \mathbf{0}$ of $\Sigma^{\mathcal{H}}$ as the starting point for the continuation process, the solid blue line in Fig. 5.4b once again depicts a family of normal conservative orbits. Similar to the bouncing ball example, any point $\boldsymbol{x}_0 = [\alpha_0 \ 0]^\mathrm{T} \in \mathcal{A}$ with $\alpha_0 \in (0, \beta)$ corresponds to a fixed point of $\boldsymbol{P}$. However, since $\boldsymbol{f}_1$ defines the dynamics of a conservative pendulum, the normal conservative orbits $\boldsymbol{x}(t)$ of $\Sigma^\mathcal{H}$ cannot be expressed in terms of elementary functions and instead require elliptic functions [24]. In this context, a noteworthy observation is the system's energy upper limit $\bar{H}_\mathrm{max}$ at $\alpha = \beta$ as the system approaches a homoclinic orbit for $T \to \infty$ [24]. Additional solution curves in $\mathcal{S}_\mathrm{tb,ms}$ with negative times and non-zero values of ξ exist analogous to the bouncing ball example.

5.2.3 Example: The Bouncing Rod

A rod of length $l_\circ$, mass $m_\circ$ and a radius of gyration $r = {}^{l_\circ}/_{100}$ is considered. The rod's rotation is described by the angle $\alpha \in (-\pi, \pi)$ and the distance of its center of mass to the ground by $y \in \mathbb{R}$. Hence, the configuration $\boldsymbol{q}^\mathrm{T} = [y \ \alpha]$ is defined in the configuration space $\mathcal{Q} = \mathbb{R} \times (-\pi, \pi)$. The cHDS $\Sigma^\mathcal{H}$ of the bouncing rod is of phase dimension $m = 2$ and is expressed as:

$$\mathcal{X}_1 = \mathcal{X}_2 = \left\{ \boldsymbol{x}_1 = \begin{bmatrix} y \\ \alpha \\ \dot{y} \\ \dot{\alpha} \end{bmatrix} \;\middle|\; \begin{matrix} [y \ \alpha]^\mathrm{T} \in \mathcal{Q}, \\ [\dot{y} \ \dot{\alpha}]^\mathrm{T} \in T_{\boldsymbol{q}}\mathcal{Q} \end{matrix} \right\}, \tag{5.25a}$$

$$\boldsymbol{f}_1 = \boldsymbol{f}_2 = \begin{bmatrix} \dot{y} & \dot{\alpha} & -g & 0 \end{bmatrix}^\mathrm{T}, \tag{5.25b}$$

$$e_1^2 = y - \frac{1}{2} l_\circ \sin(\alpha), \quad e_2^1 = y + \frac{1}{2} l_\circ \sin(\alpha), \tag{5.25c}$$

$$\boldsymbol{g}_1^2 = \boldsymbol{x}_1 - \frac{4}{l_\circ^2 \cos(\alpha)^2 + 4r^2} \begin{bmatrix} 0 \\ 0 \\ 2r^2\dot{y} - l_\circ r^2 \cos(\alpha)\dot{\alpha} \\ \frac{1}{2} l_\circ^2 \cos(\alpha)^2 \dot{\alpha} - l_\circ \cos(\alpha)\dot{y} \end{bmatrix}, \tag{5.25d}$$

$$\boldsymbol{g}_2^1 = \boldsymbol{x}_2 - \frac{4}{l_\circ^2 \cos(\alpha)^2 + 4r^2} \begin{bmatrix} 0 \\ 0 \\ 2r^2\dot{y} + l_\circ r^2 \cos(\alpha)\dot{\alpha} \\ \frac{1}{2} l_\circ^2 \cos(\alpha)^2 \dot{\alpha} + l_\circ \cos(\alpha)\dot{y} \end{bmatrix}, \tag{5.25e}$$

$$H_{1,1} = H_{2,1} = \frac{1}{2} m_\circ (\dot{y}^2 + r^2\dot{\alpha}^2) + m_\circ g y. \tag{5.25f}$$

The rod has fully elastic contact points ($\epsilon_{\mathrm{CoR}} = 1$) at its left and right corners, resulting in a flight phase between collisions. The event functions e_1^2 and e_2^1 denote when the left and right corners impact the ground, respectively. Therefore, the dynamics in (5.25) represent a left-right contact sequence with $1 \to 2 \to 1$. The total energy of the rod in both phases in (5.25f) serves as the hybrid first integral $\mathcal{H}$. It is notable that the angle α does not appear in (5.25f), indicating another first integral denoted as:

$$H_{1,2} = H_{2,2} = m_{\circ} r^2 \dot{\alpha}, \tag{5.26}$$

referred to as the angular momentum [49]. However, the discrete maps $\boldsymbol{g}_1^2$ and $\boldsymbol{g}_2^1$ instantaneously change the value of (5.26) for any $\alpha \in (-\pi, \pi)$ in the event sets $\mathcal{E}_1^2$ and $\mathcal{E}_2^1$, respectively. As $\{H_{i,2}\}_{i=1}^2$ does not meet Definition *Def2*[3], only the system's energy $\mathcal{H} = \{H_{1,1}, H_{2,1}\}$ is considered a hybrid first integral of the cHDS $\Sigma^{\mathcal{H}}$. As with the previous examples, trajectories originating from $\mathcal{X}_0$ must be physically realizable to satisfy Assumptions *As1*-*As3*. Hence, any $\boldsymbol{x}_0 \in \mathcal{X}_0$ must fulfill $e_1^2(\boldsymbol{x}_0) > 0$.

The anchor is positioned at apex transit such that

$$a(\boldsymbol{x}_1) = \dot{y}, \quad \boldsymbol{x}_1 = \begin{bmatrix} y & \alpha & \dot{y} & \dot{\alpha} \end{bmatrix}^{\mathrm{T}}. \tag{5.27}$$

Unlike the previous examples, not every point on the Poincaré section $\mathcal{A}$ corresponds to a periodic orbit. Additionally, while the system's equilibrium $\boldsymbol{\nu}_0 = \boldsymbol{0}$ remains a singular point of the time-based implementation (4.21), it does not constitute an SB point. Given $m = 2$ hybrid phases, the problem is of size $N = 17$ with the decision vector $\boldsymbol{\nu}_{\mathrm{tb,ms}}^{\mathrm{T}} = [t_3 \ \bar{\boldsymbol{x}}_3^{\mathrm{T}} \ t_2 \ \bar{\boldsymbol{x}}_2^{\mathrm{T}} \ t_1 \ \bar{\boldsymbol{x}}_1^{\mathrm{T}} \ \xi \ \bar{H}]$. Branching from $\boldsymbol{\nu}_0 = \boldsymbol{0}$ into a normal conservative orbit is initiated by constructing the tangent vector directing towards a symmetric orbit with $\Delta t_1 + \Delta t_3 = \Delta t_2$. Here, the phase durations are defined as $\Delta t_1 = t_1$, $\Delta t_2 = t_2 - t_1$ and $\Delta t_3 = t_3 - t_2$. The solid blue line in Fig. 5.4c illustrates this family of symmetric normal conservative orbits. These orbits cease to be normal at two turning and an SB point. At the SB point, the bifurcating orbits, depicted by solid green lines, break the previously mentioned symmetry. As a result, the SB point creates two additional 1D families of non-symmetric, normal conservative orbits. These orbits exhibit a phase duration Δt_2 that is either shorter or longer than $\Delta t_1 + \Delta t_3$, corresponding to different heights of the rod at the two apexes within a periodic orbit. Fig. 5.5 zooms in on the region of special orbits, revealing the two turning points and a projection of the bifurcating

[3] It can be shown that $\boldsymbol{f}_1$ in (5.25b) possesses three independent first integrals, yet only the energy in (5.25f) satisfies Definition *Def2*.

orbits. The key frames in Fig. 5.6 further illustrate the differences between symmetric and non-symmetric orbits. They also emphasize the system's stiff dynamics due to the low radius of gyration r. Consequently, while the vertical position y changes only slightly, the rod undergoes rapid rotation with high angular velocity $\dot{\alpha}$.

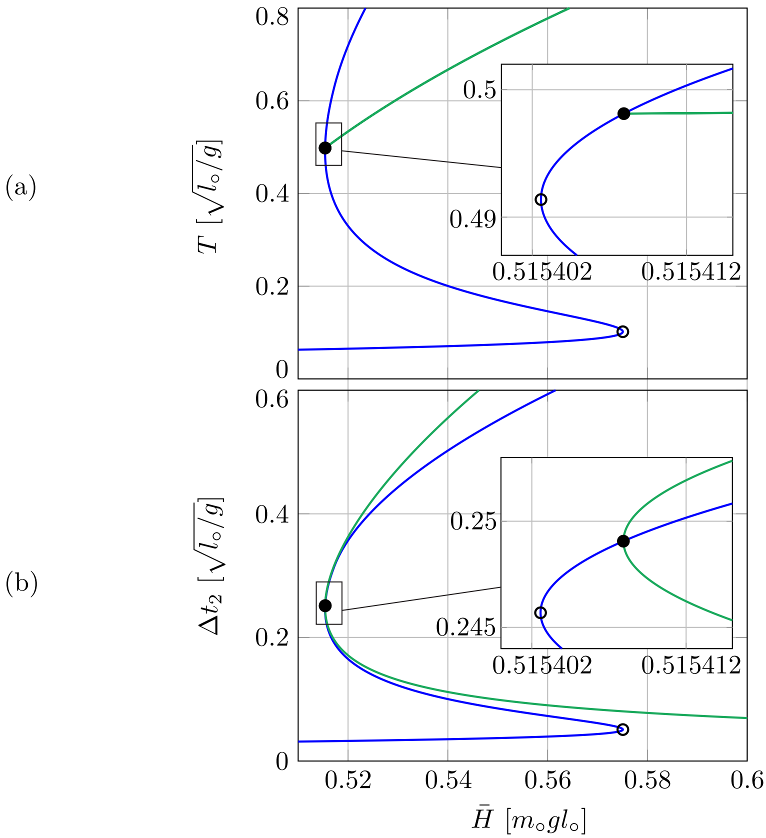

Figure 5.5: Projection of orbits of the bouncing rod system, highlighting turning points as circles and simple bifurcation (SB) points as dots. The solid blue line represents symmetric orbits with $\Delta t_1 + \Delta t_3 = \Delta t_2$, while the solid green line depicts a non-symmetric orbit that originates from an SB point. Shown in (a) is a detailed and rotated view of Fig. 5.4c, emphasizing the second turning point and SB point. An alternative projection is shown in (b), using the time duration Δt_2 of the second flight phase.

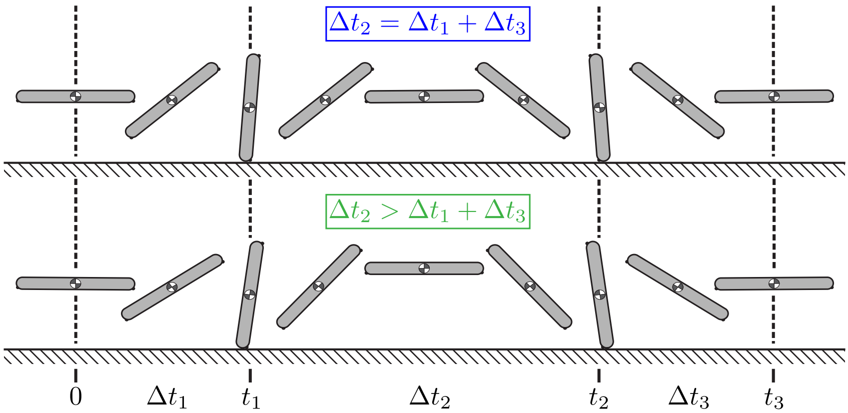

Figure 5.6: Key frames illustrating two normal conservative orbits of the bouncing rod at period $T = 0.8\,\sqrt{l_\circ/g}$. The frames compare a symmetric orbit ($\Delta t_2 = \Delta t_1 + \Delta t_3$) with a non-symmetric orbit ($\Delta t_2 > \Delta t_1 + \Delta t_3$). Only the symmetric orbit reaches the same maximum height twice.

5.2.4 Example: The Spring-Loaded Hopper (Continued)

The SLIP-like hopper with swing-leg dynamics (Fig. 5.1), introduced in Section 5.1.3, is revisited to analyze its periodic orbits. Using the parameter values reported in [43], the leg's stiffness is $k_\mathrm{l} = 40\, {}^{m_\circ g}/_{l_\circ}$ and its rotational frequency is $\omega_\alpha = \sqrt{5 g/l_\circ}$. As before, the alteration of ground contact is characterized by *stance* S and *flight* F, introducing $m = 2$ hybrid phases. However, now the system is described in minimal coordinates, eliminating the need to solve a DAE and the computation of constraint forces. As a result, the two phases have distinct domains of different sizes: $n_\mathrm{S} = 4$ and $n_\mathrm{F} = 5$. Accordingly, the cHDS $\Sigma^\mathcal{H}$ takes the form:

$$\mathcal{X}_\mathrm{S} = \left\{ \boldsymbol{x}_\mathrm{S} = \begin{bmatrix} \alpha \\ l \\ \dot\alpha \\ \dot l \end{bmatrix} \;\middle|\; \begin{matrix} [\alpha\ l]^\mathrm{T} \in \mathcal{Q}_\mathrm{S}, \\ [\dot\alpha\ \dot l]^\mathrm{T} \in T_{\boldsymbol{q}_\mathrm{S}}\mathcal{Q}_\mathrm{S} \end{matrix} \right\}, \tag{5.28a}$$

$$\mathcal{X}_\mathrm{F} = \left\{ \boldsymbol{x}_\mathrm{F} = \begin{bmatrix} y \\ \alpha \\ \dot x \\ \dot y \\ \dot\alpha \end{bmatrix} \;\middle|\; \begin{matrix} [y\ \alpha]^\mathrm{T} \in \mathcal{Q}_\mathrm{F}, \\ \dot x \in \mathbb{R}, \\ [\dot y\ \dot\alpha]^\mathrm{T} \in T_{\boldsymbol{q}_\mathrm{F}}\mathcal{Q}_\mathrm{F} \end{matrix} \right\}, \tag{5.28b}$$

$$\boldsymbol{f}_{\mathrm{S}} = \begin{bmatrix} \dot{\alpha} \\ \dot{l} \\ -2\frac{\dot{\alpha}\dot{l}}{l} + \frac{g}{l}\sin(\alpha) \\ l\dot{\alpha}^2 - g\cos(\alpha) - \frac{k_{\mathrm{l}}}{m_{\circ}}(l - l_{\circ}) \end{bmatrix}, \tag{5.28c}$$

$$\boldsymbol{f}_{\mathrm{F}} = \begin{bmatrix} \dot{y} & \dot{\alpha} & 0 & -g & -\alpha\omega_{\alpha}^2 \end{bmatrix}^{\mathrm{T}}, \tag{5.28d}$$

$$e_{\mathrm{S}}^{\mathrm{F}} = l_{\circ} - l, \tag{5.28e}$$

$$e_{\mathrm{F}}^{\mathrm{S}} = y - l_{\circ}\cos(\alpha), \tag{5.28f}$$

$$\boldsymbol{g}_{\mathrm{S}}^{\mathrm{F}} = \begin{bmatrix} l\cos(\alpha) \\ \alpha \\ -\dot{l}\sin(\alpha) - \dot{\alpha}l\cos(\alpha) \\ \dot{l}\cos(\alpha) - \dot{\alpha}l\sin(\alpha) \\ \dot{\alpha} \end{bmatrix}, \tag{5.28g}$$

$$\boldsymbol{g}_{\mathrm{F}}^{\mathrm{S}} = \begin{bmatrix} \alpha \\ l_{\circ} \\ -\frac{1}{l_{\circ}}\left(\cos(\alpha)\dot{x} + \sin(\alpha)\dot{y}\right) \\ \cos(\alpha)\dot{y} - \sin(\alpha)\dot{x} \end{bmatrix}, \tag{5.28h}$$

$$H_{\mathrm{S}} = \tfrac{1}{2}m_{\circ}(\dot{\alpha}^2 l^2 + \dot{l}^2) + m_{\circ}g\cos(\alpha)l + \tfrac{1}{2}k_{\mathrm{l}}(l - l_{\circ})^2 \tag{5.28i}$$

$$H_{\mathrm{F}} = \frac{1}{2}m_{\circ}(\dot{x}^2 + \dot{y}^2) + m_{\circ}gy, \tag{5.28j}$$

where the system's energy constitutes a hybrid first integral $\mathcal{H} = \{H_{\mathrm{S}}, H_{\mathrm{F}}\}$. $\Sigma^{\mathcal{H}}$ starts and ends its flow within the stance phase following the contact sequence $\mathrm{S} \to \mathrm{F} \to \mathrm{S}$. The configuration space during stance in (5.28a) is defined as $\mathcal{Q}_{\mathrm{S}} = \mathbb{S}^1 \times \mathbb{R}$, with the leg rotation $\alpha \in \mathbb{S}^1$ and the leg length $l \in \mathbb{R}$. Thus, $\boldsymbol{q}_{\mathrm{S}}^{\mathrm{T}} = [\alpha \ l]$. During flight, the configuration space in (5.28b) is defined as $\mathcal{Q}_{\mathrm{F}} = \mathbb{R} \times \mathbb{S}^1$, where $y \in \mathbb{R}$ denotes the vertical position of the point mass. Thus, $\boldsymbol{q}_{\mathrm{F}}^{\mathrm{T}} = [y \ \alpha]$. To ensure the physical realizability of the recurrent hybrid trajectory $\boldsymbol{x}(t)$ (*As1*-*As3*), the initial point $\boldsymbol{x}_0 \in \mathcal{X}_0$ must be selected such that $e_{\mathrm{S}}^{\mathrm{F}}(\boldsymbol{x}_0) > 0$.

The horizontal velocity $\dot{x}$ is constant during flight, as can be seen in the phase dynamics (5.28d). This implies another independent first integral of phase F by the linear momentum $H_{\mathrm{F},2} = m_{\circ}\dot{x}$. However, only H_{F} and H_{S} satisfy Definition *Def2*.

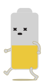

In this example, the Poincaré section is defined at nadir transit during stance, given the anchor function

$$a(\boldsymbol{x}_{\mathrm{S}}) = -\dot{l}, \quad \boldsymbol{x}_{\mathrm{S}} = \begin{bmatrix} \alpha & l & \dot{\alpha} & \dot{l} \end{bmatrix}^{\mathrm{T}}. \tag{5.29}$$

This framework allows us to derive an analytical starting point $\boldsymbol{\nu}_0$ for the time-based implementation (4.21), where $\boldsymbol{\nu}_{\mathrm{tb,ms}}^{\mathrm{T}} = [t_3 \; \bar{\boldsymbol{x}}_3^{\mathrm{T}} \; t_2 \; \bar{\boldsymbol{x}}_2^{\mathrm{T}} \; t_1 \; \bar{\boldsymbol{x}}_1^{\mathrm{T}} \; \xi \; \bar{H}]$. For an initial orbit involving purely vertical leg motion ($\alpha \equiv 0$) and a flight time of $\Delta t_2 = 0$, the resulting behavior manifests as a linear oscillation in l with a constant period:

$$T_\circ = \sum_{i=1}^{3} \Delta t_i = 2\pi\sqrt{m_\circ/k_{\mathrm{l}}}, \tag{5.30}$$

wherein $\Delta t_1 = \Delta t_3 = T_\circ/2$. Furthermore, with

$$\bar{\boldsymbol{x}}_3 = \begin{bmatrix} 0 \\ l_\circ \\ 0 \\ 0 \end{bmatrix}, \quad \bar{\boldsymbol{x}}_2 = \boldsymbol{g}_{\mathrm{S}}^{\mathrm{F}}(\bar{\boldsymbol{x}}_3), \quad \bar{\boldsymbol{x}}_1 = \begin{bmatrix} 0 \\ l_\circ - \frac{2m_\circ g}{k_{\mathrm{l}}} \\ 0 \\ 0 \end{bmatrix},$$

the starting point $\boldsymbol{\nu}_0$ defines an SB point at energy level $\bar{H} = 1 \; m_\circ g l_\circ$. In Fig. 5.7, various projections of the starting point and the bifurcating solutions, obtained via a Lyapunov-Schmidt reduction, are shown. The solid blue line represents a normal conservative orbit within $\Sigma^{\mathcal{H}}$, whereas the dashed orange curve depicts harmonic oscillations at higher energy levels $\bar{H}$ with a period of $T_\circ = \Delta t_1 + \Delta t_3$. Since the flight duration is zero ($\Delta t_2 = 0$), these oscillations are non-physical, violating Assumption *As3*. Note that the stance durations Δt_1 and Δt_3 are identical, aside from the harmonic oscillations. In the time-based implementation that generates a harmonic oscillation, the direction of event activation is irrelevant. This allows either t_1 or t_3 to define the timing of the first or second crossing of $l = l_\circ$ (Fig. 5.8b). Consequently, due to the symmetry between Δt_1 and Δt_3, they appear identical in the projection shown in Fig. 5.7b. Consistent with [43], Fig. 5.7a highlights two additional SB points. The introduction of further normal conservative orbits, represented by solid green lines, corresponds to forward and backward hopping motions with $\dot{x} \neq 0$. Fig. 5.8 illustrates key frames of individual orbits of the hopper, highlighting the main characteristics of the different orbit families shown in Fig. 5.7. Additional SB points emerge along the blue curve for larger period times and for $T < T_\circ$, depicted by the dashed blue line. A full identification and presentation of all bifurcation points in this model is beyond this section's scope.

Remark 5.2.1. *The horizontal position x is purposely neglected in the flight dynamics, since it is a cyclic coordinate that can be easily reconstructed by a solution $\boldsymbol{\varphi}(t, 0, \boldsymbol{x}_0)$ of the hybrid system $\Sigma^{\mathcal{H}}$. Unlike the SLIP model without swing dynamics ($\dot\alpha = 0$) during flight [16, 142], it is not possible to further reduce $\Sigma^{\mathcal{H}}$ to a model with $m = 1$, i.e., a single stance phase as in [29]. The reason for this is that there exists not a unique analytic solution for the flight duration $\Delta t_{\mathrm{F}}^{\mathcal{E}}$. In other words, a function that maps $\dot\alpha_{\mathrm{S}}^{+} \in \mathcal{E}_{\mathrm{S}}^{\mathrm{F}}$ to $\dot\alpha_{\mathrm{F}}^{+} \in \mathcal{E}_{\mathrm{F}}^{\mathrm{S}}$ is not unique, since there are known periodic orbits where $\dot\alpha_{\mathrm{S}}^{+} = \kappa$, with $\kappa \in \mathbb{R}$, yields either $\dot\alpha_{\mathrm{F}}^{+} = \kappa$ or $\dot\alpha_{\mathrm{F}}^{+} = -\kappa$ [43].*

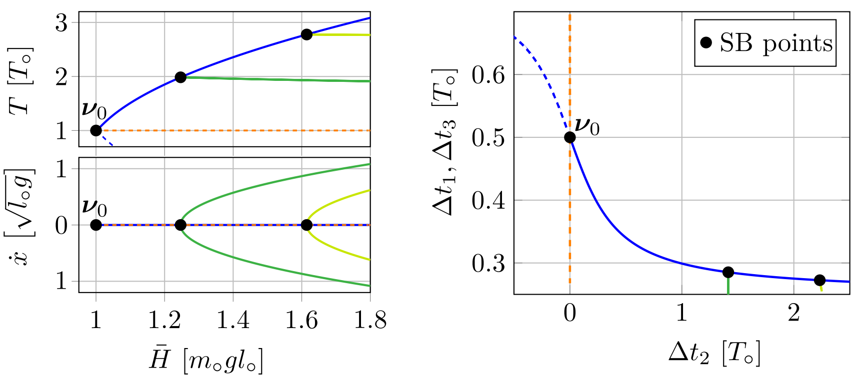

(a) (b)

Figure 5.7: Various projections of points from $\mathcal{S}_{\mathrm{tb,ms}}$ of the SLIP model. Shown in (a) are period time T and forward speed $\dot x$ during flight over energy level $\bar H$. (b) shows the stance durations, Δt_1 and Δt_3, relative to the flight duration Δt_2. The phase durations after and before the nadir transit, Δt_1 and Δt_3 respectively, appear identical in this projection. The period time $T_\circ = 2\pi\sqrt{m_\circ/k}$ illustrates a vertical harmonic oscillation with no flight duration ($\Delta t_2 = 0$), depicted by the dashed orange lines. For positive flight durations $\Delta t_2 > 0$, the solid blue line corresponds to hopping-in-place ($\dot x = 0$), while negative flight durations $\Delta t_2 < 0$ (dashed blue line) are non-physical. Simple bifurcations can be found at higher energy levels $\bar H$, depicting the bifurcating solutions of stationary hopping (solid blue line) into forward/backward hopping (solid green lines).

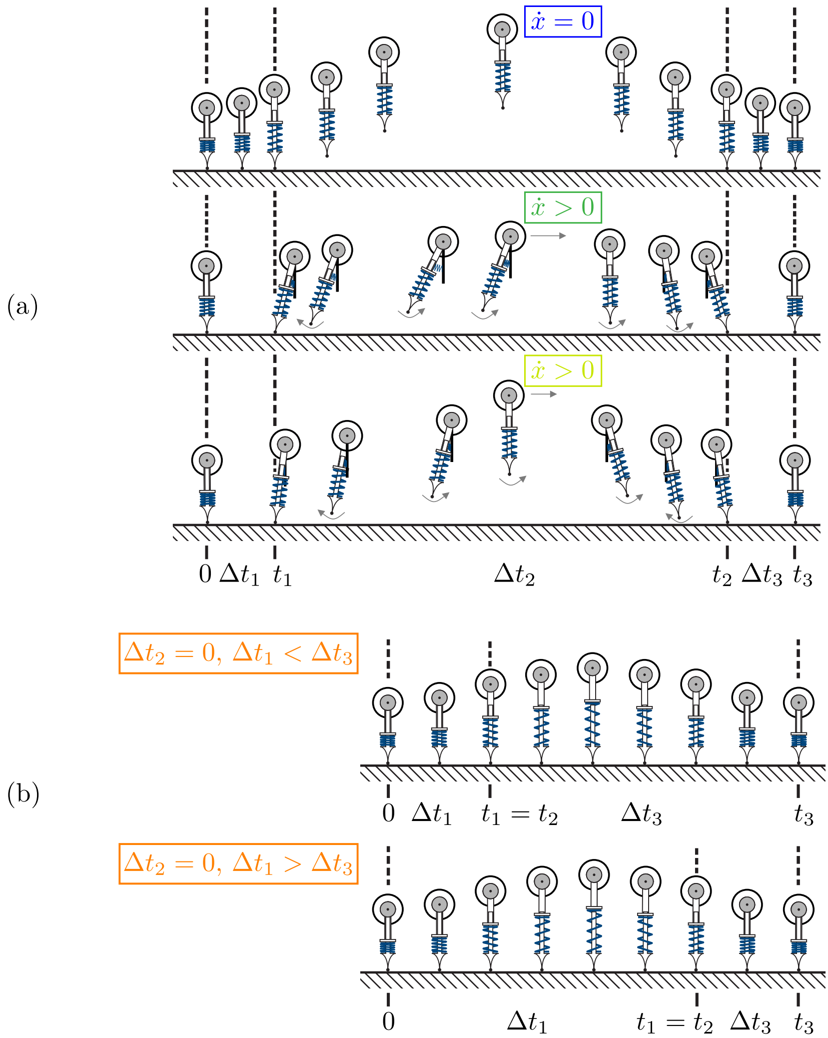

Figure 5.8: Key frames illustrating various periodic orbits of the hopper example. Shown in (a) are three distinct normal conservative orbits of the hopper at energy level $\bar{H} = 1.8\ m_\circ g l_\circ$. Additional arrows are provided to visualize linear and angular velocities within the motion. In contrast, (b) depicts harmonic in-place oscillations with vanishing flight duration $\Delta t_2 = 0$, which are considered non-physical as they violate Assumptions *As1*-*As3*.

5.3 Summary

With the theory and methodology presented in Chapter 4, ECMs can be systematically explored using PCC methods. This was demonstrated with the four examples in Section 5.2. Equilibria, specifically periodic orbits with zero phase duration ($\Delta t_i = 0$), prove to be particularly useful. These orbits require minimal domain knowledge about the system and can be used to seed normal conservative orbits (orbits parameterized by the energy level $\bar{E}$). This demonstrates that conservation is a strong property, enabling the targeted synthesis of recurrent dynamical systems.

On the other hand, constructing a well-defined HDS $\Sigma^{\mathcal{H}}$, according to Assumptions *As1*-*As3*, that admits a hybrid first integral $\mathcal{H}$ can be particularly challenging. Section 5.1 provided necessary conditions for energy conservation to facilitate the derivation of ECMs. To enforce these conditions, masses and inertias must be scaled with ε to handle plastic collisions, eventually bringing them to zero. This process requires careful handling to address the singularities that appear in the mass matrix $\boldsymbol{M}_{\varepsilon\to 0}$ and to ensure the completeness of the phase vector fields $\boldsymbol{f}_i$, as required by *As1*.

As demonstrated in the derivation of the SLIP-like hopper dynamics in Section 5.1.3, the various steps involved in deriving an ECM are often not straightforward and may require substantial domain knowledge.

Chapter 6

Optimization in Hybrid Dynamics

In contrast to the passive dynamics studied so far, this chapter reintroduces actuation into the system and presents periodic optimization problems as a tool for identifying economic gaits in legged systems. Section 6.1 defines a general periodic trajectory optimization (TO) problem within a recurrent hybrid dynamical system (HDS) and presents a selection of economic cost functions, along with the concept of passive-optimal solutions. Section 6.2 focuses on periodic optimization for an HDS Σ with a single phase ($m = 1$). The optimality conditions for such problems are derived using both indirect and direct methods (Section 6.2.1). When passive gaits are present, Section 6.2.2 further explores the reconstruction of Lagrange multipliers for each method. The chapter concludes (Section 6.3) with remarks on conservation in the indirect method and an extension of the direct method to HDSs with multiple phases ($m \geq 1$).

Before proceeding, the continuous dynamics of Σ, as outlined in Chapter 3, are revisited. Within each phase i, the state evolution $\boldsymbol{x}_i : \mathcal{T}_i \to \mathcal{X}_i$ is influenced by the time-dependent actuation $\boldsymbol{u}_i : \mathcal{T}_i \to \mathcal{U}_i$. Since this monograph considers both finite- and infinite-dimensional parameterizations of $\boldsymbol{u}_i(\cdot)$ (Remark 3.0.1), the phase dynamics are generally expressed as $\mathcal{F}_i : \dot{\boldsymbol{x}}_i(t) = \boldsymbol{f}_i(\boldsymbol{x}_i(t), \boldsymbol{u}_i(t))$, where $\boldsymbol{f}_i : \mathcal{X}_i \times \mathcal{U}_i \to T\mathcal{X}_i$.

6.1 Periodic Trajectory Optimization

Central to any optimization problem is an objective function to be minimized and a decision space where the minimum can be attained. Given the flexibility of a time-based implementation of Σ (Section 3.3), the decision variables include the event times t_i, phase trajectories $\boldsymbol{x}_i(\cdot)$, and inputs $\boldsymbol{u}_i(\cdot)$.

Consequently, the scalar objective function $c\big(\{t_i, \boldsymbol{x}_i(\cdot), \boldsymbol{u}_i(\cdot)\}_{i=1}^m\big)$, also referred to as the cost function, depends on these variables, leading to the following periodic TO problem:

Periodic Trajectory Optimization Problem

$$
\mathcal{P}^m : \left\{
\begin{array}{lll}
\underset{\left\{\begin{array}{c} t_i, \\ \boldsymbol{x}_i(\cdot), \\ \boldsymbol{u}_i(\cdot) \end{array}\right\}_{i=1}^{m}}{\text{minimize}} & \underbrace{\kappa\big(\{t_i, \boldsymbol{x}_i(t_i)\}_{i=0}^m\big) \cdot \sum_{i=1}^{m} \int_{t_{i-1}}^{t_i} l_i\big(\boldsymbol{x}_i(t), \boldsymbol{u}_i(t)\big)\mathrm{d}t}_{=\,c(\cdot)} & \\
\text{subject to} & \left\{\dot{\boldsymbol{x}}_i(t) = \boldsymbol{f}_i\big(\boldsymbol{x}_i(t), \boldsymbol{u}_i(t)\big), \quad t \in [t_{i-1}, t_i]\right\}_{i=1}^{m}, & \\
 & \left\{e_i^{i+1}\big(t_i, \boldsymbol{x}_i(t_i)\big) = 0\right\}_{i=1}^{m}, & \\
 & \left\{\boldsymbol{x}_{i+1}(t_i) = \boldsymbol{g}_i^{i+1}\big(\boldsymbol{x}_i(t_i)\big)\right\}_{i=1}^{m-1}, & \\
 & \boldsymbol{x}_1(t_0) = \boldsymbol{g}_m^1\big(\boldsymbol{x}_m(t_m)\big), & \text{(periodicity)} \\
 & t_0 := 0, & \text{(initial time)} \\
 & \boldsymbol{x}_0(t_0) := \boldsymbol{x}_1(0), & \text{(initial state)} \\
 & t_m = T, & \text{(period time)} \\
 & \boldsymbol{\omega}\big(\{t_i, \boldsymbol{x}_i(t_i)\}_{i=0}^m\big) = \mathbf{0}, & \text{(operating point)}
\end{array}\right.
$$

where $\kappa \in \mathbb{R}_{\geq 0}$ is a scaling factor within c and the stage cost of each phase is defined as $l_i : \mathbb{R}^{n_{\mathrm{x},i}} \times \mathbb{R}^{n_{\mathrm{u},i}} \to \mathbb{R}$. The final set of equality constraints in problem $\mathcal{P}^m$ defines an operating point $\boldsymbol{\omega} \in \mathbb{R}^{n_\omega}$, imposing $n_\omega > 1$ operating conditions. The operating point typically specifies desired amplitudes and frequencies, or metrics such as average system energy and velocities. Introducing an operating point is essential for generating motions with user-defined characteristics, especially when optimizing for energetic efficiency. It actively avoids trivial optimal solutions that correspond to either no motion (equilibria) or zero phase duration ($\Delta t_i = 0$).

Note that the decision variables are assumed to be unconstrained such that its domains are simplified to $\mathcal{T}_i = \mathbb{R}$, $\mathcal{X}_i = \mathbb{R}^{n_{\mathrm{x},i}}$ and $\mathcal{U}_i = \mathbb{R}^{n_{\mathrm{u},i}}$.

Assumption (Existence of Local Extrema)**.** *The optimization problem $\mathcal{P}^m$ admits at least one strict local minimizer $\big(\{t_i^*, \boldsymbol{x}_i^*(\cdot), \boldsymbol{u}_i^*(\cdot)\}_{i=1}^m\big)$ with phase durations $\Delta t_i^* > 0$.*

Assumption (Differentiability)**.** *The control inputs are continuous, i.e., $\boldsymbol{u}_i \in C^0$, and unconstrained. The functions $c(\cdot)$, $\boldsymbol{f}_i(\cdot,\cdot)$, $l_i(\cdot,\cdot)$, $\boldsymbol{g}_i^{i+1}(\cdot)$, $e_i^{i+1}(\cdot,\cdot)$ and $\boldsymbol{\omega}(\cdot)$ are of class C^∞ with respect to all arguments.*

Although the continuity assumption on the inputs $\boldsymbol{u}_i$ can be relaxed [83, 129] using Pontryagin's maximum principle [107], this consideration is not relevant to the problems addressed in this monograph. This is because the focus is on effort-based cost functions without input constraints, rather than on time-optimal formulations that yield bang-bang control behavior.

Remark 6.1.1. *The problem $\mathcal{P}^m$ is formulated within a time-based framework, where the anchor is defined by the last event, i.e., $a := e_m^1$ (Remark 4.1.6), and phase times t_i are treated independently from events e_i^{i+1}. In contrast, a state-based approach eliminates t_i as decision variables by introducing implicit time-to-event functions $t_i^{\mathcal{E}}$. This requires Assumptions As2 and As3, which restrict the search space and complicate gradient computation in the TO solver. Consequently, the time-based formulation of $\mathcal{P}^m$ offers greater flexibility, allowing for grazing conditions ($\dot{e}_i^{i+1} = 0$) and vanishing phase durations ($\Delta t = 0$) in the optimization process.*

6.1.1 Economic Cost Functions

Economic cost functions in mechatronic systems model energy expenditure during periodic operations. These functions depend on the system's design and purpose, such as periodic flight [119] or pick and place tasks [38], as well as its actuation and energy source, e.g., gas tanks or batteries. The following economic cost functions are primarily based on [112]. They are especially relevant to legged systems powered by electric motors and batteries, as this is currently the dominant design in legged robotics [21, 75].

By denoting the actuator torques and forces as $\boldsymbol{u}_i \in \mathbb{R}^{n_{\mathrm{u}_i}}$ and the actuators velocity as ${}_{\mathrm{u}}\dot{\boldsymbol{q}}_i \in \mathbb{R}^{n_{\mathrm{u}_i}} \subset \mathcal{X}$, common stage costs within $c(\cdot)$ are:

$$l_i = {\boldsymbol{u}_i}^{\mathrm{T}} \boldsymbol{K} \boldsymbol{u}_i, \qquad \text{(copper losses/input squared)} \quad (6.1\text{a})$$

$$l_i = {}_{\mathrm{u}}\dot{\boldsymbol{q}}_i^{\mathrm{T}} \boldsymbol{u}_i, \qquad \text{(mechanical power)} \quad (6.1\text{b})$$

$$l_i = \max\left(0, {}_{\mathrm{u}}\dot{\boldsymbol{q}}_i^{\mathrm{T}} \boldsymbol{u}_i\right), \qquad \text{(positive mechanical power)} \quad (6.1\text{c})$$

$$l_i = |{}_{\mathrm{u}}\dot{\boldsymbol{q}}_i^{\mathrm{T}} \boldsymbol{u}_i|, \qquad \text{(absolute mechanical power)} \quad (6.1\text{d})$$

$$l_i = {}_{\mathrm{u}}\dot{\boldsymbol{q}}_i^{\mathrm{T}} \boldsymbol{u}_i + {\boldsymbol{u}_i}^{\mathrm{T}} \boldsymbol{K} \boldsymbol{u}_i, \qquad \text{(electrical power)} \quad (6.1\text{e})$$

$$l_i = \max\left(0, {}_{\mathrm{u}}\dot{\boldsymbol{q}}_i^{\mathrm{T}} \boldsymbol{u}_i + {\boldsymbol{u}_i}^{\mathrm{T}} \boldsymbol{K} \boldsymbol{u}_i\right), \qquad \text{(positive electrical power)} \quad (6.1\text{f})$$

where the positive-definite diagonal matrix $\boldsymbol{K}$ relates to the speed-torque gradient of a DC-motor. Note that the stage costs in (6.1c), (6.1d) and (6.1f) are not differentiable at $l_i = 0$, requiring either smoothing or a reformulation using slack variables [14] to satisfy the differentiability assumption. To enable a comparison of energy economy across different legged systems, actuator work is typically normalized as

$$\kappa = \frac{1}{m_\circ g \Delta x\big(\{\boldsymbol{x}_i(t_i)\}_{i=0}^m\big)}, \tag{6.2}$$

where $m_\circ$ is the total mass, g is gravity, and Δx represents the distance traveled within a periodic gait as a function of the states $\boldsymbol{x}_i$. This normalization renders the cost c dimensionless, a metric commonly referred to as the cost of transport.

Note that all cost functions that are defined through the stages costs in (6.1) yield zero cost ($c = 0$) if the input remains constantly zero ($\boldsymbol{u}_i \equiv \mathbf{0}$).

Definition (Economic Cost Function)**.** *A cost function $c(\cdot)$ belongs to the class of economic cost functions $\mathcal{C}$ if it satisfies $c = 0$ whenever $\boldsymbol{u}_i \equiv \mathbf{0}$ for all $i \in \{1, \ldots, m\}$.*

Thus, if a system is capable of purely passive locomotion ($\boldsymbol{u}_i \equiv \mathbf{0}$), an economic cost will reflect this by indicating zero energy expenditure.

6.1.2 Passive-Optimal Solutions

This dissertation places a particular emphasis on passive gaits. In actuated systems, passive gaits correspond to periodic orbits with zero actuation ($\boldsymbol{u}_i \equiv \mathbf{0}$). Since a primary objective of legged systems and other periodically operating systems is to minimize energy dissipation[1], passive gaits appear to be globally optimal from an economic perspective. Specifically, for a certain subclass $\mathcal{C}_0 \subset \mathcal{C}$ of economic cost functions within the TO problem $\mathcal{P}^m$, passive orbits with zero energy supply constitute globally optimal solutions to $\mathcal{P}^m$.

Definition (Passive-Optimal Solution)**.** *A global minimizer $\big(\{t_i^*, \boldsymbol{x}_i^*(\cdot), \boldsymbol{u}_i^*(\cdot)\}_{i=1}^m\big)$ of $\mathcal{P}^m$, where $\boldsymbol{u}_i^* \equiv \mathbf{0}$ for all $i \in \{1, \ldots, m\}$, is referred to as a passive-optimal solution, or in the context of legged locomotion, a passive-optimal gait. Furthermore, if the minimizer is strict, meaning it is isolated from other minimizers, it is referred to as strictly passive-optimal.*

[1] In contrast, airborne wind energy systems are designed to harvest energy from their environment [26].

Passive optimal gaits inherently solve an inverse optimization problem. That is, given a passive gait with an operating condition $\boldsymbol{\omega}(\cdot) = \mathbf{0}$, a corresponding class of optimization problems $\mathcal{P}^m$ with cost functions $\mathcal{C}_0$ can be constructed to ensure that passive gaits emerge as globally optimal solutions.

6.1.3 Solution Strategies: Direct and Indirect Methods

For practical applications, a dynamical system must operate under a range of conditions $\boldsymbol{\omega}$. Since passive-optimal solutions alone cannot cover this entire range, a general solution strategy for $\mathcal{P}^m$ is required. Solution strategies for the TO problem $\mathcal{P}^m$ can generally be divided into two categories: the direct and indirect approaches. This distinction arises because $\mathcal{P}^m$ is an infinite-dimensional optimization problem, given that the function space of $\boldsymbol{u}_i$ is infinite-dimensional.

Direct Method

The direct method approximates $\mathcal{P}^m$ with a finite-dimensional problem $\hat{\mathcal{P}}^m$ by introducing a time discretization, often referred to as transcription [34, 72, 135]. The resulting nonlinear program (NLP) $\hat{\mathcal{P}}^m$, specifically an ECO problem as discussed in Section 2.3.2, is then solved by satisfying its optimality conditions. When using shooting methods for transcription, the inputs $\boldsymbol{u}_i(\cdot)$ are parameterized by control parameters $\boldsymbol{\xi}_i \in \mathbb{R}^{n_{\xi,i}}$. Note that $n_{\xi,i} \in \mathbb{N}_{>n_\omega}$, as the number of decision variables must exceed the number of independent equality constraints for optimization. This leads to parameterized control functions of the form $\hat{\boldsymbol{u}}_i : \mathbb{R} \times \mathbb{R}^{n_{\xi,i}} \to \mathbb{R}^{n_{\mathrm{u},i}}$.

Assumption (Input Parameterization)**.** *The parameterization of the input functions satisfies the following conditions:*

$$\hat{\boldsymbol{u}}_i \in C^2, \tag{6.3a}$$

$$\hat{\boldsymbol{u}}_i(t, \mathbf{0}) \equiv \mathbf{0}, \tag{6.3b}$$

$$\hat{\boldsymbol{u}}_i(t, \boldsymbol{\xi}_i^*) = \hat{\boldsymbol{u}}_i(t, \boldsymbol{\xi}_i^{**}) \Rightarrow \boldsymbol{\xi}_i^* = \boldsymbol{\xi}_i^{**}, \tag{6.3c}$$

for all $t \in \mathbb{R}$ and $\boldsymbol{\xi}_i \in \mathbb{R}^{n_{\xi,i}}$.

Remark 6.1.2. *Equation* (6.3c) *ensures that the basis functions used in $\hat{\boldsymbol{u}}_i(\cdot,\cdot)$ are linearly independent. This property is commonly satisfied by Bézier curves, B-Splines [105], and Fourier series. Additionally, these basis functions naturally satisfy condition* (6.3b)*.*

Indirect Method

The indirect method approaches the problem differently by first deriving the first-order optimality conditions using variational calculus [83]. This involves considering the entire function space of $\boldsymbol{u}_i$ to derive the stationary conditions of $\mathcal{P}^m$, which take the form of a boundary-value problem (BVP). While the indirect method can yield analytical solutions in rare cases where the BVP remains simple, solving such problems generally requires time transcription, similar to the direct approach.

Both approaches in this dissertation rely on shooting methods for time transcription. In summary, the direct method follows a "discretize first, then optimize" approach, whereas the indirect method first derives optimality conditions and applies discretization afterward.

6.2 Single Hybrid Phase Optimization

This section applies the previously discussed solution strategies, direct and indirect approaches, to single-phase models Σ with $m = 1$. Such systems are often referred to as simple hybrid systems [10]. For notational simplicity, the phase index i is omitted when considering simple hybrid systems. Additionally, an auxiliary state $y(\cdot)$ is introduced for the stage cost, where $y(t) \in \mathbb{R}$, allowing the problem $\mathcal{P}^m$ to be rewritten in the so-called Mayer form:

$$
\mathcal{P}^1 : \begin{cases}
\underset{T,\boldsymbol{x}(\cdot),\boldsymbol{u}(\cdot)}{\text{minimize}} \quad c(T, \boldsymbol{x}(T), y(T)) & \text{(6.4a)} \\
\text{subject to} \quad \dot{\boldsymbol{x}}(t) = \boldsymbol{f}\big(\boldsymbol{x}(t), \boldsymbol{u}(t)\big), \quad t \in [0, T], & \text{(6.4b)} \\
\qquad \boldsymbol{x}(0) = \boldsymbol{g}(\boldsymbol{x}(T)), & \text{(6.4c)} \\
\qquad \dot{y}(t) = l\big(\boldsymbol{x}(t), \boldsymbol{u}(t)\big), \quad t \in [0, T], & \text{(6.4d)} \\
\qquad y(0) = 0, & \text{(6.4e)} \\
\qquad \underbrace{\begin{bmatrix} e\big(T, \boldsymbol{x}(T)\big) \\ \boldsymbol{\omega}\big(T, \boldsymbol{x}(T), \boldsymbol{x}(0)\big) \end{bmatrix}}_{=\boldsymbol{h}\left(T, \boldsymbol{x}(T), \boldsymbol{x}(0)\right)} = \boldsymbol{0}, & \text{(6.4f)}
\end{cases}
$$

where $c : \mathbb{R} \times \mathbb{R}^{n_x} \times \mathbb{R} \to \mathbb{R}$ denotes the terminal cost function and the equality constraint $\boldsymbol{h} : \mathbb{R} \times \mathbb{R}^{n_x} \times \mathbb{R}^{n_x} \to \mathbb{R}^{1+n_\omega}$ in (6.4f) encompasses both the event constraint e and an operating point constraint $\boldsymbol{\omega} : \mathbb{R} \times \mathbb{R}^{n_x} \times \mathbb{R}^{n_x} \to \mathbb{R}^{n_\omega}$.

6.2.1 Optimality Conditions

The following subsections derive the optimality conditions for $\mathcal{P}^1$ using both the direct and indirect approaches.

Direct Method

The problem $\mathcal{P}^1$ is approximated using the input parameterization $\hat{\boldsymbol{u}}(t, \boldsymbol{\xi})$ from (6.3) and a single shooting approach, yielding the NLP:

$$\hat{\mathcal{P}}^1 : \begin{cases} \min\limits_{T, \boldsymbol{x}_0, \boldsymbol{\xi}} & c(T, \hat{\boldsymbol{x}}(T), \hat{y}(T)) \\ \text{s.t.} & \underbrace{\begin{bmatrix} \boldsymbol{g}(\hat{\boldsymbol{x}}(T)) - \boldsymbol{x}_0 \\ e\big(T, \hat{\boldsymbol{x}}(T)\big) \\ \boldsymbol{\omega}\big(T, \hat{\boldsymbol{x}}(T), \boldsymbol{x}_0\big) \end{bmatrix}}_{=\hat{\boldsymbol{h}}\left(T, \boldsymbol{x}_0, \boldsymbol{\xi}\right)} = \boldsymbol{0}, \end{cases} \iff \begin{cases} \min\limits_{\hat{\boldsymbol{\varkappa}}} & \hat{c}(\hat{\boldsymbol{\varkappa}}) \\ \text{s.t.} & \hat{\boldsymbol{h}}(\hat{\boldsymbol{\varkappa}}) = \boldsymbol{0}, \\ & \hat{\boldsymbol{\varkappa}} = \begin{bmatrix} T \\ \boldsymbol{x}_0 \\ \boldsymbol{\xi} \end{bmatrix}, \end{cases}$$

where $\hat{\boldsymbol{x}}(t) = \boldsymbol{\varphi}(t, 0, \boldsymbol{x}_0, \boldsymbol{\xi})$ and $\hat{y}(t) = \int_0^t l\big(\hat{\boldsymbol{x}}(\tau), \hat{\boldsymbol{u}}(\tau, \boldsymbol{\xi})\big)\mathrm{d}\tau$ result from numerically integrating (6.4b) and (6.4d), respectively. Furthermore, the dependence on the initial condition $\boldsymbol{x}(0) = \boldsymbol{x}_0$ and input parameters $\boldsymbol{\xi}$ is explicitly incorporated by defining the approximate cost function $\hat{c} : \mathbb{R} \times \mathbb{R}^{n_\mathrm{x}} \times \mathbb{R}^{n_\xi} \to \mathbb{R}$, where $\hat{c}(T, \boldsymbol{x}_0, \boldsymbol{\xi}) := c(T, \hat{\boldsymbol{x}}(T), \hat{y}(T))$. The periodicity, event and operating conditions are combined into a single equality constraint $\hat{\boldsymbol{h}} : \mathbb{R} \times \mathbb{R}^{n_\mathrm{x}} \times \mathbb{R}^{n_\xi} \to \mathbb{R}^{n_{\hat{\lambda}}}$, where $n_{\hat{\lambda}} = n_\mathrm{x} + 1 + n_\omega$. According to Section 2.3.2, introducing the decision vector $\hat{\boldsymbol{\varkappa}}^\mathrm{T} = [T \ \boldsymbol{x}_0^\mathrm{T} \ \boldsymbol{\xi}^\mathrm{T}]$ and Lagrange mulipliers $\hat{\boldsymbol{\lambda}} \in \mathbb{R}^{n_{\hat{\lambda}}}$, the optimality conditions for a strict local minimizer $\hat{\boldsymbol{\varkappa}}^*$ (satisfying the LICQ) take the form:

First- and Second-Order Optimality Conditions for $\hat{\mathcal{P}}^1$

1st-order necessary condition:

$$\begin{aligned} \hat{\boldsymbol{h}}(\hat{\boldsymbol{\varkappa}}^*) &\overset{!}{=} \boldsymbol{0}, \\ D\hat{c}(\hat{\boldsymbol{\varkappa}}^*)^\mathrm{T} + D\hat{\boldsymbol{h}}(\hat{\boldsymbol{\varkappa}}^*)^\mathrm{T}\hat{\boldsymbol{\lambda}} &\overset{!}{=} \boldsymbol{0}, \end{aligned} \tag{6.5a}$$

2nd-order sufficient condition:

$$\delta\mathbf{w}^\mathrm{T}\big(D^2\hat{c}(\hat{\boldsymbol{\varkappa}}^*) + D^2\hat{\boldsymbol{h}}(\hat{\boldsymbol{\varkappa}}^*)^\mathrm{T}\hat{\boldsymbol{\lambda}}\big)\delta\mathbf{w} \overset{!}{>} 0, \ \ \forall \delta\mathbf{w} \in \ker(D\hat{\boldsymbol{h}}(\hat{\boldsymbol{\varkappa}}^*)). \tag{6.5b}$$

Indirect Method

In contrast to the direct approach, the indirect method formalizes the first-order necessary conditions of the original problem $\mathcal{P}^1$. This is achieved using Lagrange's multiplier method for the so-called non-integral (6.4b), (6.4d) and integral constraint equations (6.4c), (6.4e), (6.4f) [83]. The non-integral equality constraints (6.4b) and (6.4d) must hold pointwise in time for all $t \in [0, T]$. They introduce continuous time Lagrange multipliers, referred to as the costates $\boldsymbol{p} \in \mathbb{R}^{n_\mathrm{x}}$ and $q \in \mathbb{R}$ of $\boldsymbol{x}$ and y, respectively. The integral equality constraints (6.4f) also introduce Lagrange multipliers $\boldsymbol{\lambda}^\mathrm{T} = [\lambda_\mathrm{e}\ \boldsymbol{\lambda}_\omega^\mathrm{T}] \in \mathbb{R}^{1+n_\omega}$. However, these multipliers are discrete in time, as they act at constraints that depend only on the states at the boundary of the trajectory. Similarly, for the integral equality constraints (6.4c) and (6.4e), additional Lagrange multipliers ${}_\mathrm{z}\boldsymbol{\lambda}^\mathrm{T} = [{}_\mathrm{x}\boldsymbol{\lambda}^\mathrm{T}\ {}_\mathrm{y}\lambda]$ are introduced, where ${}_\mathrm{x}\boldsymbol{\lambda} \in \mathbb{R}^{n_\mathrm{x}}$ and ${}_\mathrm{y}\lambda \in \mathbb{R}$.

For notational convenience, the continuous and discrete time variables are grouped as

$$\boldsymbol{z}(\cdot)^\mathrm{T} = \begin{bmatrix} \boldsymbol{x}(\cdot)^\mathrm{T} & y(\cdot) \end{bmatrix}, \tag{6.6a}$$

$$\boldsymbol{\rho}(\cdot)^\mathrm{T} = \begin{bmatrix} \boldsymbol{p}(\cdot)^\mathrm{T} & q(\cdot) \end{bmatrix}, \tag{6.6b}$$

$$\boldsymbol{w}(\cdot)^\mathrm{T} = \begin{bmatrix} \boldsymbol{z}(\cdot)^\mathrm{T} & \boldsymbol{\rho}(\cdot)^\mathrm{T} & \boldsymbol{u}(\cdot)^\mathrm{T} \end{bmatrix}, \tag{6.6c}$$

$$\boldsymbol{v}^\mathrm{T} = \begin{bmatrix} T & \boldsymbol{\lambda}^\mathrm{T} \end{bmatrix}, \tag{6.6d}$$

and the Hamiltonian defined as

$$\mathcal{H}(\underbrace{\boldsymbol{x}, y, \boldsymbol{p}, q, \boldsymbol{u}}_{=\boldsymbol{w}}) = \boldsymbol{p}^\mathrm{T} \boldsymbol{f}(\boldsymbol{x}, \boldsymbol{u}) + q \cdot l(\boldsymbol{x}, \boldsymbol{u}). \tag{6.7}$$

With the introduction of these Lagrange multipliers, the Lagrangian is defined as

$$\mathcal{L}\big({}_\mathrm{z}\boldsymbol{\lambda}, \boldsymbol{v}, \boldsymbol{w}(\cdot)\big) = \mathcal{L}_1(\boldsymbol{v}, \boldsymbol{w}) + \mathcal{L}_2({}_\mathrm{z}\boldsymbol{\lambda}, \boldsymbol{w}) + \mathcal{L}_3(\boldsymbol{v}, \boldsymbol{w}), \tag{6.8a}$$

where

$$\mathcal{L}_1 = c\big(T, \boldsymbol{z}(T)\big) + \boldsymbol{\lambda}^\mathrm{T} \boldsymbol{h}\big(T, \boldsymbol{x}(T), \boldsymbol{x}(0)\big), \tag{6.8b}$$

$$\mathcal{L}_2 = {}_\mathrm{x}\boldsymbol{\lambda}^\mathrm{T} \big(\boldsymbol{g}(\boldsymbol{x}(T)) - \boldsymbol{x}(0)\big) + {}_\mathrm{y}\lambda y(0), \tag{6.8c}$$

$$\mathcal{L}_3 = \int\limits_0^T \mathcal{H}(\boldsymbol{w}) - \boldsymbol{\rho}^\mathrm{T} \dot{\boldsymbol{z}} \mathrm{d}t, \tag{6.8d}$$

With the Lagrangian, the stationarity condition within the constrained optimization problem $\mathcal{P}^1$ can be equivalently written as an unconstrained problem [70]:

$$\underset{{}_{\mathrm{z}}\boldsymbol{\lambda},\boldsymbol{v},\boldsymbol{w}(\cdot)}{\text{stationary}} \quad \mathcal{L}\big({}_{\mathrm{z}}\boldsymbol{\lambda},\boldsymbol{v},\boldsymbol{w}(\cdot)\big). \tag{6.9}$$

To derive the stationary condition of the new problem (6.9), its solution $\big({}_{\mathrm{z}}\boldsymbol{\lambda}^*,\boldsymbol{v}^*,\boldsymbol{w}^*(\cdot)\big)$ is perturbed by introducing variations:

$$\begin{aligned} \delta_{\mathrm{z}}\boldsymbol{\lambda}^{\mathrm{T}} &= \begin{bmatrix}\delta_{\mathrm{x}}\boldsymbol{\lambda}^{\mathrm{T}} & \delta_{\mathrm{y}}\lambda\end{bmatrix}, \\ \delta\boldsymbol{v}^{\mathrm{T}} &= \begin{bmatrix}\delta T & \delta\boldsymbol{\lambda}^{\mathrm{T}}\end{bmatrix}, \\ \delta\boldsymbol{w}(\cdot)^{\mathrm{T}} &= \begin{bmatrix}\delta\boldsymbol{z}(\cdot)^{\mathrm{T}} & \delta\boldsymbol{u}(\cdot)^{\mathrm{T}} & \delta\boldsymbol{\rho}(\cdot)^{\mathrm{T}}\end{bmatrix}. \end{aligned} \tag{6.10a}$$

The perturbed variables are then expressed as:

$$\begin{aligned} {}_{\mathrm{z}}\tilde{\boldsymbol{\lambda}} &= {}_{\mathrm{z}}\boldsymbol{\lambda}^* + \varepsilon\delta_{\mathrm{z}}\boldsymbol{\lambda}, \\ \tilde{\boldsymbol{v}} &= \boldsymbol{v}^* + \varepsilon\delta\boldsymbol{v}, \\ \tilde{\boldsymbol{w}}(\cdot) &= \boldsymbol{w}^*(\cdot) + \varepsilon\delta\boldsymbol{w}(\cdot), \end{aligned} \tag{6.10b}$$

where ε is infinitesimally small. Note that $\boldsymbol{w}(t)$ is a function of time and is thus, coupled to the variation of the period time T in $\boldsymbol{v}$ at the end of the trajectory:

$$\begin{aligned} \tilde{\boldsymbol{w}}(\tilde{T}) &= \boldsymbol{w}^*(\tilde{T}) + \varepsilon\delta\boldsymbol{w}(\tilde{T}) \\ &= \boldsymbol{w}^*(T^* + \varepsilon\delta T) + \varepsilon\delta\boldsymbol{w}(T^* + \varepsilon\delta T). \end{aligned} \tag{6.10c}$$

At a locally optimal point of problem $\mathcal{P}$, the first variation $\delta\mathcal{L}|_*$ of the Lagrangian (6.8) must vanish. With $\tilde{\mathcal{L}}(\varepsilon) := \mathcal{L}({}_{\mathrm{z}}\tilde{\boldsymbol{\lambda}},\tilde{\boldsymbol{v}},\tilde{\boldsymbol{w}}(\cdot))$, the stationary condition takes the form

$$\delta\mathcal{L}|_* := \left.\frac{\partial\tilde{\mathcal{L}}(\varepsilon)}{\partial\varepsilon}\right|_{\varepsilon=0} = 0. \tag{6.11}$$

Remark 6.2.1. *Formulating the unconstrained problem* (6.9) *using Lagrange multipliers requires certain regularity conditions on the equality constraints. The notion of regularity is not introduced here, as it involves technical details specific to the infinite-dimensional vector spaces under consideration. For a thorough discussion on the required regularity conditions, please refer to Chapter 9.2 of Luenberger [88].*

The first-order variation defined in equation (6.11) is executed in its three components (6.8):

$$
\begin{aligned}
\delta\mathcal{L}_1|_* &= \left.\frac{\mathrm{d}\mathcal{L}_1}{\mathrm{d}\varepsilon}\right|_{\varepsilon=0} \qquad (6.12)\\
&= \left.\left[\frac{\mathrm{d}}{\mathrm{d}\varepsilon}C\big(\tilde{T}, \boldsymbol{z}^*(\tilde{T}) + \varepsilon\cdot\delta\boldsymbol{z}(\tilde{T})\big)\right]\right|_{\varepsilon=0}\\
&\quad + \left.\frac{\mathrm{d}}{\mathrm{d}\varepsilon}\Big(\tilde{\boldsymbol{\lambda}}^{\mathrm{T}}\boldsymbol{h}\big(\tilde{T},\ \boldsymbol{x}^*(\tilde{T}) + \varepsilon\delta\boldsymbol{x}(\tilde{T}),\ \boldsymbol{x}^*(0) + \varepsilon\delta\boldsymbol{x}(0)\big)\Big)\right|_{\varepsilon=0}\\
&= \left[\left.\frac{\partial C}{\partial T}\right|_* + \left.\frac{\partial C}{\partial \boldsymbol{z}_T}\right|_* \dot{\boldsymbol{z}}^*(T^*) + \boldsymbol{\lambda}^{*\mathrm{T}}\left(\left.\frac{\partial \boldsymbol{h}}{\partial T}\right|_* + \left.\frac{\partial \boldsymbol{h}}{\partial \boldsymbol{x}_T}\right|_* \dot{\boldsymbol{x}}^*(T^*)\right)\right]\delta T + \delta\boldsymbol{\lambda}^{\mathrm{T}}\boldsymbol{h}|_*\\
&\quad + \left.\frac{\partial C}{\partial y_T}\right|_* \delta y(T^*) + \left[\left.\frac{\partial C}{\partial \boldsymbol{x}_T}\right|_* + \boldsymbol{\lambda}^{*\mathrm{T}}\left.\frac{\partial \boldsymbol{h}}{\partial \boldsymbol{x}_T}\right|_*\right]\delta\boldsymbol{x}(T^*) + \boldsymbol{\lambda}^{*\mathrm{T}}\left.\frac{\partial \boldsymbol{h}}{\partial \boldsymbol{x}_0}\right|_*\delta\boldsymbol{x}(0),
\end{aligned}
$$

$$
\begin{aligned}
\delta\mathcal{L}_2|_* &= \left.\frac{\mathrm{d}\mathcal{L}_2}{\mathrm{d}\varepsilon}\right|_{\varepsilon=0} \qquad (6.13)\\
&= \frac{\mathrm{d}}{\mathrm{d}\varepsilon}\Big({}_{\mathrm{x}}\tilde{\boldsymbol{\lambda}}^{\mathrm{T}}\boldsymbol{g}\big(\boldsymbol{x}^*(\tilde{T}) + \varepsilon\delta\boldsymbol{x}(\tilde{T})\big)\\
&\qquad \left.- {}_{\mathrm{x}}\tilde{\boldsymbol{\lambda}}^{\mathrm{T}}\big(\boldsymbol{x}^*(0) + \varepsilon\delta\boldsymbol{x}(0)\big) + {}_{\mathrm{y}}\tilde{\lambda}\big(y^*(0) + \varepsilon\delta y(0)\big)\Big)\right|_{\varepsilon=0}\\
&= {}_{\mathrm{x}}\boldsymbol{\lambda}^{*\mathrm{T}}\left.\frac{\partial \boldsymbol{g}}{\partial \boldsymbol{x}_T}\right|_* \dot{\boldsymbol{x}}^*(T^*)\delta T + {}_{\mathrm{x}}\boldsymbol{\lambda}^{*\mathrm{T}}\left.\frac{\partial \boldsymbol{g}}{\partial \boldsymbol{x}_T}\right|_*\delta\boldsymbol{x}(T^*) - {}_{\mathrm{x}}\boldsymbol{\lambda}^{*\mathrm{T}}\delta\boldsymbol{x}(0) + {}_{\mathrm{y}}\lambda^*\delta\boldsymbol{y}(0)\\
&\quad + \delta_{\mathrm{x}}\boldsymbol{\lambda}^{\mathrm{T}}\big(\boldsymbol{g}(\boldsymbol{x}^*(T^*)) - \boldsymbol{x}^*(0)\big) + \delta_{\mathrm{y}}\lambda y^*(0),
\end{aligned}
$$

$$
\begin{aligned}
\delta\mathcal{L}_3|_* &= \left.\frac{\mathrm{d}\mathcal{L}_3}{\mathrm{d}\varepsilon}\right|_{\varepsilon=0} \qquad (6.14a)\\
&= \left.\frac{\mathrm{d}}{\mathrm{d}\varepsilon}\left(\int_0^{T^*+\varepsilon\delta T} \mathcal{H}(\boldsymbol{w}^* + \varepsilon\delta\boldsymbol{w}) - (\boldsymbol{\rho}^* + \varepsilon\delta\boldsymbol{\rho})^{\mathrm{T}}(\dot{\boldsymbol{z}}^* + \varepsilon\delta\dot{\boldsymbol{z}})\,\mathrm{d}t\right)\right|_{\varepsilon=0}\\
&= \left.\int_0^{T^*+\varepsilon\delta T}\frac{\mathrm{d}}{\mathrm{d}\varepsilon}\Big(\mathcal{H}(\boldsymbol{w}^* + \varepsilon\delta\boldsymbol{w}) - (\boldsymbol{\rho}^* + \varepsilon\delta\boldsymbol{\rho})^{\mathrm{T}}(\dot{\boldsymbol{z}}^* + \varepsilon\delta\dot{\boldsymbol{z}})\Big)\mathrm{d}t\,\right|_{\varepsilon=0} \qquad (6.14b)\\
&\quad + \left[\mathcal{H}\big(\boldsymbol{w}^*_{T^*}\big) - \boldsymbol{\rho}^{*\,\mathrm{T}}_{T^*}\dot{\boldsymbol{z}}^*_{T^*}\right]\delta T\\
&= \int_0^{T^*}\left(\left.\frac{\partial\mathcal{H}}{\partial\boldsymbol{w}}\right|_*\delta\boldsymbol{w} - \delta\boldsymbol{\rho}^{\mathrm{T}}\dot{\boldsymbol{z}}^* - \boldsymbol{\rho}^{*\mathrm{T}}\delta\dot{\boldsymbol{z}}\right)\mathrm{d}t + \left[\mathcal{H}\big(\boldsymbol{w}^*_{T^*}\big) - \boldsymbol{\rho}^{*\,\mathrm{T}}_{T^*}\dot{\boldsymbol{z}}^*_{T^*}\right]\delta T
\end{aligned}
$$

$$
\begin{aligned}
&= \Big[-\boldsymbol{\rho}^{*\mathrm{T}}\delta\boldsymbol{z}\Big]_0^{T^*} + \int_0^{T^*}\left(\frac{\partial\mathcal{H}}{\partial\boldsymbol{w}}\bigg|_*\delta\boldsymbol{w} - \delta\boldsymbol{\rho}^{\mathrm{T}}\dot{\boldsymbol{z}}^* + \dot{\boldsymbol{\rho}}^{*\,\mathrm{T}}\delta\boldsymbol{z}\right)\mathrm{d}t \qquad (6.14c)\\
&\quad + \Big[\mathcal{H}\big(\boldsymbol{w}^*_{T^*}\big) - \boldsymbol{\rho}^{*\ \mathrm{T}}_{T^*}\dot{\boldsymbol{z}}^*_{T^*}\Big]\delta T\\
&= \boldsymbol{\rho}_0^{*\mathrm{T}}\delta\boldsymbol{z}(0) - \boldsymbol{\rho}^{*\ \mathrm{T}}_{T^*}\delta\boldsymbol{z}(T^*) + \Big[\mathcal{H}\big(\boldsymbol{w}^*_{T^*}\big) - \boldsymbol{\rho}^{*\ \mathrm{T}}_{T^*}\dot{\boldsymbol{z}}^*_{T^*}\Big]\delta T\\
&\quad + \int_0^{T^*}\left(\left[\frac{\partial\mathcal{H}}{\partial\boldsymbol{z}}\bigg|_* + \dot{\boldsymbol{\rho}}^{*\mathrm{T}}\right]\delta\boldsymbol{z} + \frac{\partial\mathcal{H}}{\partial\boldsymbol{u}}\bigg|_*\delta\boldsymbol{u} + \left[\frac{\partial\mathcal{H}}{\partial\boldsymbol{\rho}}\bigg|_* - \dot{\boldsymbol{z}}^{*\mathrm{T}}\right]\delta\boldsymbol{\rho}\right)\mathrm{d}t,
\end{aligned}
$$

where the Leibniz integral rule is applied in (6.14b), and integration by parts is used in (6.14c). By summing equations (6.12)–(6.14), grouping the terms accordingly, and omitting the superscript *, the following expression is obtained:

$$
\begin{aligned}
0 &= \delta\mathcal{L}\\
&= \int_0^{T}\left(\left[\frac{\partial\mathcal{H}}{\partial\boldsymbol{z}} + \dot{\boldsymbol{\rho}}^{\mathrm{T}}\right]\delta\boldsymbol{x} + \left[\frac{\partial\mathcal{H}}{\partial\boldsymbol{\rho}} - \dot{\boldsymbol{z}}^{\mathrm{T}}\right]\delta y + \left[\frac{\partial\mathcal{H}}{\partial\boldsymbol{u}}\right]\delta\boldsymbol{u}\right)\mathrm{d}t \qquad (6.15a)\\
&\quad + \Big[\delta\boldsymbol{z}_0^{\mathrm{T}} \quad \delta\boldsymbol{z}_T^{\mathrm{T}} \quad \delta T \quad \delta\boldsymbol{\lambda}^{\mathrm{T}} \quad \delta_{\mathrm{z}}\boldsymbol{\lambda}^{\mathrm{T}}\Big]\cdot{}_{\delta}\tilde{\boldsymbol{r}},
\end{aligned}
$$

where

$$
\begin{aligned}
{}_{\delta}\tilde{\boldsymbol{r}}^{\mathrm{T}} &= \Big[{}_{\boldsymbol{z}_0}\tilde{\boldsymbol{r}}^{\mathrm{T}} \quad {}_{\boldsymbol{z}_T}\tilde{\boldsymbol{r}}^{\mathrm{T}} \quad {}_{T}\tilde{r} \quad \boldsymbol{h}^{\mathrm{T}} \quad {}_{\mathrm{z}}\boldsymbol{h}^{\mathrm{T}}\Big], && (6.15b)\\
{}_{\boldsymbol{z}_0}\tilde{\boldsymbol{r}}^{\mathrm{T}} &= \Big[{}_{\boldsymbol{x}_0}\tilde{\boldsymbol{r}}^{\mathrm{T}} \quad {}_{y_0}\tilde{r}\Big] && (6.15c)\\
{}_{\boldsymbol{z}_T}\tilde{\boldsymbol{r}}^{\mathrm{T}} &= \Big[{}_{\boldsymbol{x}_T}\tilde{\boldsymbol{r}}^{\mathrm{T}} \quad {}_{y_T}\tilde{r}\Big] && (6.15d)\\
{}_{\mathrm{z}}\boldsymbol{h}^{\mathrm{T}} &= \Big[\big(\boldsymbol{g}(\boldsymbol{x}_T) - \boldsymbol{x}_0\big)^{\mathrm{T}} \quad y_0\Big], && (6.15e)
\end{aligned}
$$

with

$$
\begin{aligned}
{}_{\boldsymbol{x}_0}\tilde{\boldsymbol{r}} &= \frac{\partial\boldsymbol{h}}{\partial\boldsymbol{x}_0}^{\mathrm{T}}\boldsymbol{\lambda} + \boldsymbol{p}_0 - {}_{\mathrm{x}}\boldsymbol{\lambda}, && (6.15f)\\
{}_{y_0}\tilde{r} &= q_0 + {}_{\mathrm{y}}\lambda, && (6.15g)\\
{}_{\boldsymbol{x}_T}\tilde{\boldsymbol{r}} &= \frac{\partial\boldsymbol{g}}{\partial\boldsymbol{x}_T}^{\mathrm{T}}{}_{\mathrm{x}}\boldsymbol{\lambda} - \boldsymbol{p}_T + \frac{\partial c}{\partial\boldsymbol{x}_T}^{\mathrm{T}} + \frac{\partial\boldsymbol{h}}{\partial\boldsymbol{x}_T}^{\mathrm{T}}\boldsymbol{\lambda}, && (6.15h)\\
{}_{y_T}\tilde{r} &= \frac{\partial c}{\partial y_T} - q_T, && (6.15i)
\end{aligned}
$$

$$
\begin{aligned}
{}_{T}\tilde{r} &= \mathcal{H}(\boldsymbol{w}_T) + \frac{\partial c}{\partial T} + \boldsymbol{\lambda}^{\mathrm{T}} \frac{\partial \boldsymbol{h}}{\partial T} && \text{(6.15j)}\\
&\quad + {}_{\boldsymbol{x}_T}\tilde{\boldsymbol{r}}^{\mathrm{T}} \cdot \dot{\boldsymbol{x}}_T + {}_{y_T}\tilde{r} \cdot \dot{y}_T . && \text{(6.15k)}
\end{aligned}
$$

Since the problem (6.9) is unconstrained, the first-order variation (6.15a) must hold for arbitrary perturbations $\delta_{\mathrm{z}}\boldsymbol{\lambda}$, $\delta\boldsymbol{v}$ and $\delta\boldsymbol{w}(\cdot)$. Thus, applying the fundamental lemma of the calculus of variations yields

$$
\begin{aligned}
\dot{\boldsymbol{\rho}}(t) &= -\left.\frac{\partial \mathcal{H}}{\partial \boldsymbol{z}}\right|_{\boldsymbol{w}(t)}^{\mathrm{T}}, && \text{(6.16a)}\\
\dot{\boldsymbol{z}}(t) &= \left.\frac{\partial \mathcal{H}}{\partial \boldsymbol{\rho}}\right|_{\boldsymbol{w}(t)}^{\mathrm{T}}, && \text{(6.16b)}\\
\boldsymbol{0} &= \left.\frac{\partial \mathcal{H}}{\partial \boldsymbol{u}}\right|_{\boldsymbol{w}(t)}^{\mathrm{T}}, && \text{(6.16c)}
\end{aligned}
$$

for all $t \in [0, T]$ and requires the residual equations (6.15b) to vanish:

$$
\begin{bmatrix} {}_{\boldsymbol{x}_0}\tilde{\boldsymbol{r}}^{\mathrm{T}} & {}_{y_0}\tilde{r} & {}_{\boldsymbol{x}_T}\tilde{\boldsymbol{r}}^{\mathrm{T}} & {}_{y_T}\tilde{r} & {}_{T}\tilde{r} & \boldsymbol{h}^{\mathrm{T}} & {}_{\mathrm{z}}\boldsymbol{h}^{\mathrm{T}} \end{bmatrix} = \boldsymbol{0}. \tag{6.17}
$$

While the DAE (6.16) constitute the first part of the necessary conditions, (6.17) contains so-called transversality (${}_{j}\tilde{\boldsymbol{r}}$) and boundary ($\boldsymbol{h}$, ${}_{\mathrm{z}}\boldsymbol{h}$) conditions. Notably, from (6.16a) follows: $\dot{q} = -{}^{\partial\mathcal{H}}/_{\partial y} = 0$. This results in a constant Lagrange multiplier q which is derived from the transversality condition (6.15i) as $q(t) \equiv q_0 = q_T = {}^{\partial c}/_{\partial y_T}$. Likewise, the transversality conditions (6.15f) and (6.15g) can be rewritten as

$$
{}_{\mathrm{x}}\boldsymbol{\lambda} = \frac{\partial \boldsymbol{h}}{\partial \boldsymbol{x}_0}^{\mathrm{T}} \boldsymbol{\lambda} + \boldsymbol{p}_0, \tag{6.18}
$$

$$
{}_{\mathrm{y}}\lambda = -q\,. \tag{6.19}
$$

Hence, ${}_{\mathrm{x}}\boldsymbol{\lambda}$ can be eliminated from the transversality condition (6.15h). Finally, under the fulfillment of the residuals ${}_{\boldsymbol{x}_T}\tilde{\boldsymbol{r}} = \boldsymbol{0}$ and ${}_{y_T}\tilde{r} = 0$, the last transversality condition (6.15j) simplifies as its additive terms (6.15k) vanish. With these simplifications, equations (6.16) and (6.17) lead to the first-order necessary conditions, which are presented in the compact form in the following box.

First-Order Necessary Condition for $\mathcal{P}^1$

The first-order optimality takes the form of a DAE:

$$\dot{\boldsymbol{x}} = \frac{\partial \mathcal{H}}{\partial \boldsymbol{p}}^{\mathrm{T}} = \boldsymbol{f}(\boldsymbol{x}, \boldsymbol{u}), \tag{6.20a}$$

$$\dot{y} = \frac{\partial \mathcal{H}}{\partial q} = l(\boldsymbol{x}, \boldsymbol{u}), \tag{6.20b}$$

$$\dot{\boldsymbol{p}} = -\frac{\partial \mathcal{H}}{\partial \boldsymbol{x}}^{\mathrm{T}} = -\frac{\partial \boldsymbol{f}}{\partial \boldsymbol{x}}^{\mathrm{T}} \boldsymbol{p} - \frac{\partial l}{\partial \boldsymbol{x}}^{\mathrm{T}} q, \tag{6.20c}$$

$$q \equiv \frac{\partial c}{\partial y_T}, \tag{6.20d}$$

$$\boldsymbol{0} = \frac{\partial \mathcal{H}}{\partial \boldsymbol{u}}^{\mathrm{T}} = \frac{\partial \boldsymbol{f}}{\partial \boldsymbol{u}}^{\mathrm{T}} \boldsymbol{p} + \frac{\partial l}{\partial \boldsymbol{u}}^{\mathrm{T}} q, \tag{6.20e}$$

with associated boundary and transversality constraints:

$$\boldsymbol{g}\left(\boldsymbol{x}(T)\right) - \boldsymbol{x}(0) = \boldsymbol{0}, \tag{6.21a}$$

$$y(0) = 0, \tag{6.21b}$$

$$\boldsymbol{h}\big(T, \boldsymbol{x}(T), \boldsymbol{x}(0)\big) = \boldsymbol{0}, \tag{6.21c}$$

$$\mathcal{H}\big(\boldsymbol{w}(T)\big) + \frac{\partial c}{\partial T} + \boldsymbol{\lambda}^{\mathrm{T}} \frac{\partial \boldsymbol{h}}{\partial T} = 0, \tag{6.21d}$$

$$\frac{\partial \boldsymbol{g}}{\partial \boldsymbol{x}_T}^{\mathrm{T}} \cdot \left(\boldsymbol{p}(0) + \frac{\partial \boldsymbol{h}}{\partial \boldsymbol{x}_0}^{\mathrm{T}} \boldsymbol{\lambda} \right) - \boldsymbol{p}(T) + \frac{\partial c}{\partial \boldsymbol{x}_T}^{\mathrm{T}} + \frac{\partial \boldsymbol{h}}{\partial \boldsymbol{x}_T}^{\mathrm{T}} \boldsymbol{\lambda} = \boldsymbol{0}, \tag{6.21e}$$

where the Hamiltonian is defined as

$$\mathcal{H}(\underbrace{\boldsymbol{x}, y, \boldsymbol{p}, q, \boldsymbol{u}}_{=\boldsymbol{w}}) = \boldsymbol{p}^{\mathrm{T}} \boldsymbol{f}(\boldsymbol{x}, \boldsymbol{u}) + q \cdot l(\boldsymbol{x}, \boldsymbol{u}). \tag{6.22}$$

As the next step in the indirect method, shooting can be applied to solve the BVP defined by the DAE (6.20) with boundary conditions (6.21).

Remark 6.2.2. *This monograph does not explore sufficient conditions for the indirect approach, including second-order variations as discussed by Speyer (1984). Deriving such a second-order variational theory is cumbersome, even for small subclasses of periodic optimization problems in $\mathcal{P}^1$. Among other requirements, this involves showing the existence of particular solutions to Riccati differential equations and analyzing properties of the Monodromy matrix for the underlying DAE/ODE.*

6.2.2 Lagrange Multipliers for Passive Orbits

As previously shown, Lagrange's multiplier method is a crucial tool in both direct and indirect approaches for incorporating nonlinear constraints into the cost function when seeking a local minimum. By introducing Lagrange multipliers, it eliminates the need to explicitly construct the constraint tangent space, though it expands the space of decision variables to satisfy the stationarity conditions. For a strictly passive-optimal solution $(T^*, \boldsymbol{x}^*(\cdot), \boldsymbol{u}^*(\cdot) \equiv \mathbf{0})$, the Lagrange multipliers can be directly reconstructed for both the direct $\hat{\mathcal{P}}^1$ and indirect $\mathcal{P}^1$ problems.

Direct Method

In the direct approach, a passive-optimal solution corresponds to the point $\hat{\boldsymbol{\varkappa}}^{*\mathrm{T}} = [T^* \; \boldsymbol{x}_0^{*\mathrm{T}} \; \boldsymbol{\xi}^{*\mathrm{T}}]$, where $\boldsymbol{\xi}^* = \mathbf{0}$ holds independently of the choice of input parameterization (Remark 6.1.2). Assuming strict passive-optimality with respect to an economic cost function c, such that $\hat{\boldsymbol{\varkappa}}^*$ constitutes a regular point, the Langrange multiplier in (6.5a) is given by

$$\hat{\boldsymbol{\lambda}} = -\big(D\hat{\boldsymbol{h}}(\hat{\boldsymbol{\varkappa}}^*)^{\mathrm{T}}\big)^{\dagger} \; D\hat{c}(\hat{\boldsymbol{\varkappa}}^*)^{\mathrm{T}}, \tag{6.23}$$

where $\dagger$ denotes the Moore–Penrose inverse. Since the Jacobian $D\hat{\boldsymbol{h}}(\hat{\boldsymbol{\varkappa}}^*)$ has full rank (satisfying the LICQ), the Moore–Penrose inverse uniquely defines $\hat{\boldsymbol{\lambda}}$.

Indirect Method

Provided a strictly passive-optimal solution, the multipliers $\boldsymbol{\lambda}$ and $\boldsymbol{\rho}(\cdot)$ can be reconstructed via the necessary conditions (6.20) and (6.21). In particular, with the condition (6.20d), the first Lagrange multiplier can be readily reconstructed:

$$q = \left.\frac{\partial c}{\partial y_T}\right|_{\left(T^*, \boldsymbol{x}^*(T^*), y(T^*)\right)}, \tag{6.24}$$

where $y(T^*) = \int_0^{T^*} l\big(\boldsymbol{x}^*(t), \mathbf{0}\big)\mathrm{d}t$. For the reconstruction of the costate trajectory $\boldsymbol{p}(\cdot)$, the necessary conditions (6.20) are reformulated to

$$\dot{\boldsymbol{w}} = \boldsymbol{F}(\boldsymbol{w}), \tag{6.25a}$$

$$\mathbf{0} = \mathcal{H}_u(\boldsymbol{w}), \tag{6.25b}$$

where

$$\boldsymbol{F} := \begin{bmatrix} \boldsymbol{f}(\boldsymbol{x}, \boldsymbol{u}) \\ l(\boldsymbol{x}, \boldsymbol{u}) \\ -\dfrac{\partial \boldsymbol{f}}{\partial \boldsymbol{x}}\bigg|_{(\boldsymbol{x},\boldsymbol{u})}^{\mathrm{T}} \cdot \boldsymbol{p} - \dfrac{\partial l}{\partial \boldsymbol{x}}\bigg|_{(\boldsymbol{x},\boldsymbol{u})}^{\mathrm{T}} \cdot q \\ 0 \\ \mathbf{0} \end{bmatrix}, \tag{6.26a}$$

$$\mathcal{H}_u := \frac{\partial \boldsymbol{f}}{\partial \boldsymbol{u}}\bigg|_{(\boldsymbol{x},\boldsymbol{u})}^{\mathrm{T}} \cdot \boldsymbol{p} + \frac{\partial l}{\partial \boldsymbol{u}}\bigg|_{(\boldsymbol{x},\boldsymbol{u})}^{\mathrm{T}} \cdot q. \tag{6.26b}$$

Note that the dynamics $\dot{\boldsymbol{u}} = \mathbf{0}$ in (6.26a) result from the passive inputs $\boldsymbol{u}^* \equiv \mathbf{0}$.

Since the costates $\boldsymbol{p}(\cdot)$ are uniquely associated to a strict optimizer with $\boldsymbol{x}^*$ and $\boldsymbol{u}^*$ by (6.25), they are locally observable within (6.25b) (Section 1.9 [67]). Exploiting the affine dependence of $\boldsymbol{p}$ and q on the vector field $\boldsymbol{F}$ and the function $\mathcal{H}_u$, the Lie derivative L is utilized to define

$$\left.\begin{bmatrix} \mathcal{H}_u \\ L_{\boldsymbol{F}}\mathcal{H}_u \\ L_{\boldsymbol{F}}L_{\boldsymbol{F}}\mathcal{H}_u \\ \vdots \end{bmatrix}\right|_{\left(\boldsymbol{x}^*,\boldsymbol{p},\boldsymbol{u}^*\right)} = \tilde{\boldsymbol{A}}\boldsymbol{p} + \tilde{\boldsymbol{b}}q \stackrel{!}{=} \mathbf{0}, \tag{6.27a}$$

where

$$\tilde{\boldsymbol{A}} = \begin{bmatrix} \frac{\partial \boldsymbol{f}}{\partial \boldsymbol{u}}^{\mathrm{T}} \\ \left(\sum_{i=1}^{n_{\mathrm{x}}} f_i \frac{\partial}{\partial x_i} \frac{\partial \boldsymbol{f}}{\partial \boldsymbol{u}}\right)^{\mathrm{T}} - \left(\frac{\partial \boldsymbol{f}}{\partial \boldsymbol{x}} \frac{\partial \boldsymbol{f}}{\partial \boldsymbol{u}}\right)^{\mathrm{T}} \\ \vdots \end{bmatrix}, \tag{6.27b}$$

$$\tilde{\boldsymbol{b}} = \begin{bmatrix} \frac{\partial l}{\partial \boldsymbol{u}}^{\mathrm{T}} \\ \left(\sum_{i=1}^{n_{\mathrm{x}}} f_i \frac{\partial}{\partial x_i} \frac{\partial l}{\partial \boldsymbol{u}}\right)^{\mathrm{T}} - \left(\frac{\partial l}{\partial \boldsymbol{x}} \frac{\partial \boldsymbol{f}}{\partial \boldsymbol{u}}\right)^{\mathrm{T}} \\ \vdots \end{bmatrix}, \tag{6.27c}$$

are evaluated at the point $(\boldsymbol{x}^*, \boldsymbol{u}^*)$. Due to the local observability of $\boldsymbol{p}$, the matrix $\tilde{\boldsymbol{A}}$ has full (column) rank for all $\left(\boldsymbol{x}^*(t), \boldsymbol{u}^*(t) = \mathbf{0}\right)$ and $t \in [0, T^*]$. Speciaficially, it holds $\mathrm{span}(\tilde{\boldsymbol{A}}^{\mathrm{T}}) = \mathrm{span}(\boldsymbol{A}^{\mathrm{T}})$[2]. Thus, for each time instant,

[2]According to the terminology of Isidori [67], $\mathrm{span}(\tilde{\boldsymbol{A}}^{\mathrm{T}})$ is referred to as a distribution.

a square matrix $\boldsymbol{A}(t) \in \mathbb{R}^{n_\mathrm{x} \times n_\mathrm{x}}$ can be reconstructed from n_x rows of $\tilde{\boldsymbol{A}}$ such that $\det(\boldsymbol{A}(t)) \neq 0$. Furthermore, selecting the same n_x rows from $\tilde{\boldsymbol{b}}$ constitutes the vector $\boldsymbol{b}(t) \in \mathbb{R}^{n_\mathrm{x}}$. Finally, the costate can be reconstructed by

$$\boldsymbol{p}(t) = \boldsymbol{A}(t)^{-1}\boldsymbol{b}(t)q, \tag{6.28}$$

for any time $t \in [0, T^*]$. With the computed costates $\boldsymbol{p}(0)$ and $\boldsymbol{p}(T^*)$ at the boundary, the remaining Lagrange multipliers $\boldsymbol{\lambda}$ are reconstructed from (6.21e):

$$\boldsymbol{\lambda} = \boldsymbol{H}^\dagger\left(\boldsymbol{p}(T^*) - \left.\frac{\partial \boldsymbol{g}}{\partial \boldsymbol{x}_T}\right|^\mathrm{T}_{\left(\boldsymbol{x}^*(T^*)\right)} \boldsymbol{p}(0) - \left.\frac{\partial c}{\partial \boldsymbol{x}_T}\right|^\mathrm{T}_{\left(T^*, \boldsymbol{x}^*(T^*), y(T^*)\right)}\right), \tag{6.29a}$$

$$\boldsymbol{H} = \left.\left(\frac{\partial \boldsymbol{g}}{\partial \boldsymbol{x}_T}^\mathrm{T} \frac{\partial \boldsymbol{h}}{\partial \boldsymbol{x}_0}^\mathrm{T} + \frac{\partial \boldsymbol{h}}{\partial \boldsymbol{x}_T}^\mathrm{T}\right)\right|_{\left(T^*, \boldsymbol{x}^*(T^*), \boldsymbol{x}^*(0)\right)}. \tag{6.29b}$$

Similar the direct approach and (6.23), assuming the matrix $\boldsymbol{H}$ has full rank (satisfying the LICQ), the multiplier $\boldsymbol{\lambda}$ is uniquely reconstructed by (6.29a).

6.3 Remarks and Extensions

The following extends the discussion of solving a TO problem of a hybrid system Σ.

6.3.1 Indirect Method: Conservation in Optimization

In Section 6.2.1, the Hamiltonian $\mathcal{H} = \boldsymbol{p}^\mathrm{T}\boldsymbol{f} + ql$ was introduced in (6.7) for the TO problem $\mathcal{P}^1$ of a simple hybrid system Σ with $m = 1$. While Chapter 4 generally refers to $\mathcal{H}$ as a hybrid first integral, characterizing a conservative HDS, it can indeed be regarded as a hybrid first integral $\tilde{\mathcal{H}}$ of a higher-dimensional cHDS $\tilde{\Sigma}^{\tilde{\mathcal{H}}}$. That is, the first-order optimality conditions (6.20), (6.21) can be understood as a time-based approach to identifying conservative orbits in $\tilde{\Sigma}^{\tilde{\mathcal{H}}}$. Since cHDSs are treated as autonomous in this monograph, constructing $\tilde{\Sigma}^{\tilde{\mathcal{H}}}$ requires:

- A DAE index reduction for (6.20e) to derive a closed-form expression for the input: $\tilde{\boldsymbol{u}}(\boldsymbol{x}, \boldsymbol{p})$.
- Augmenting the state with $\tau \in \mathbb{R}$ and defining its dynamics as $\dot{\tau} = 1$ to eliminate time dependence in the event function: $\tilde{e}_1^1(\tau, \boldsymbol{x})$.

By introducing the state variables $\tilde{\boldsymbol{x}}_1^{\mathrm{T}} = [\boldsymbol{z}^{\mathrm{T}}\ \boldsymbol{\rho}^{\mathrm{T}}\ \tau]$ for $\tilde{\Sigma}^{\tilde{\mathcal{H}}}$, the hybrid first integral takes the form:

$$\tilde{H}_1(\tilde{\boldsymbol{x}}_1) = \boldsymbol{p}^{\mathrm{T}} \boldsymbol{f}(\boldsymbol{x}, \tilde{\boldsymbol{u}}(\boldsymbol{x}, \boldsymbol{p})) + q \cdot l(\boldsymbol{x}, \tilde{\boldsymbol{u}}(\boldsymbol{x}, \boldsymbol{p})). \tag{6.30}$$

While the first condition for a hybrid first integral (*Def1*), i.e., ${}^{\mathrm{d}}/_{\mathrm{d}t}\tilde{H}_1 = 0$, is straightforward to verify, the second condition (*Def2*) requires the preservation of the discrete map $\tilde{\boldsymbol{g}}_1^1(\tilde{\boldsymbol{x}}_1)$ in $\tilde{\Sigma}^{\tilde{\mathcal{H}}}$. This aspect is not further explored here, as enforcing the periodicity condition $\tilde{\boldsymbol{g}}_1^1(\tilde{\boldsymbol{x}}_1(T)) = \tilde{\boldsymbol{x}}_1(0)$, and consequently constructing $\tilde{\boldsymbol{g}}_1^1$, introduces the challenge that the initial state $\tilde{\boldsymbol{x}}_1(0)$ and the final state $\tilde{\boldsymbol{x}}_1(T)$ are nonlinearly coupled in (6.21e). One possible approach to address this issue involves modifying the time coordinate so that the costate dynamics in (6.16a) are integrated backward in time.

In contrast to the root-finding problems discussed in Chapter 4, where orbits had to be constrained to a level set of $\mathcal{H}$ to ensure their isolation, this condition is inherently satisfied here through the transversality constraint (6.21d), which defines the constant value of $\tilde{\mathcal{H}} = \{\tilde{H}_1\}$.

6.3.2 Direct Method: Multiple Hybrid Phases

The indirect method for multiple hybrid phases ($m > 1$), including events dependent on the input $\boldsymbol{u}_i$ (such as detecting vanishing normal forces when breaking contact), is not discussed in this monograph. However, the direct method can be seamlessly applied to $\mathcal{P}^m$ with $m > 1$.

Parameterizing the inputs $\boldsymbol{u}_i(\cdot)$ with parameters $\boldsymbol{\xi}_i \in \mathbb{R}^{n_{\xi,i}}$ enables the numerical integration of $\dot{\boldsymbol{x}}_i = \boldsymbol{f}_i\big(\boldsymbol{x}_i, \hat{\boldsymbol{u}}(t, \boldsymbol{\xi}_i)\big)$ to obtain the phase flows

$$\hat{\boldsymbol{x}}_i(t_i) = \boldsymbol{\varphi}_i(t_i, t_{i-1}, \bar{\boldsymbol{x}}_i, \boldsymbol{\xi}_i), \tag{6.31}$$

where the initial time is $t_0 = 0$. Additionally, the stage costs in $c(\cdot)$ are numerically integrated and expressed as

$$\hat{y}_i(t_i) = \int_{t_{i-1}}^{t_i} l_i\big(\hat{\boldsymbol{x}}_i(t), \hat{\boldsymbol{u}}(t, \boldsymbol{\xi}_i)\big)\mathrm{d}t. \tag{6.32}$$

Hence, approximating $\mathcal{P}^m$ using a time-based (tb) multiple shooting (ms) approach yields the following NLP:

$$\hat{\mathcal{P}}^m : \begin{cases} \underset{\left\{\begin{smallmatrix} t_i, \\ \bar{\boldsymbol{x}}_i, \\ \boldsymbol{\xi}_i \end{smallmatrix}\right\}_{i=1}^{m}}{\text{minimize}} & \underbrace{\kappa\big(\{t_i, \hat{\boldsymbol{x}}_i(t_i)\}_{i=0}^{m}\big) \cdot \sum_{i=1}^{m} \hat{y}_i(t_i)}_{=\hat{c}_{\text{tb,ms}}(\cdot)} \\ \text{subject to} & \underbrace{\begin{bmatrix} \boldsymbol{g}_m^1 \circ \hat{\boldsymbol{x}}_m(t_m) - \bar{\boldsymbol{x}}_1 \\ e_m^1\big(t_m, \hat{\boldsymbol{x}}_m(t_m)\big) \\ \boldsymbol{g}_{m-1}^m \circ \hat{\boldsymbol{x}}_{m-1}(t_{m-1}) - \bar{\boldsymbol{x}}_m \\ e_{m-1}^m\big(t_{m-1}, \hat{\boldsymbol{x}}_{m-1}(t_{m-1})\big) \\ \vdots \\ \boldsymbol{g}_1^2 \circ \hat{\boldsymbol{x}}_1(t_1) - \bar{\boldsymbol{x}}_2 \\ e_1^2\big(t_1, \hat{\boldsymbol{x}}_1(t_1)\big) \\ \boldsymbol{\omega}\big(\{t_i, \hat{\boldsymbol{x}}_i(t_i)\}_{i=0}^{m}\big) \end{bmatrix}}_{=\hat{\boldsymbol{h}}_{\text{tb,ms}}(\cdot)} = \mathbf{0}. \end{cases}$$

With the decision variables $\hat{\boldsymbol{\varkappa}}_{\text{tb,ms}}^{\text{T}} = [t_m\ \bar{\boldsymbol{x}}_m^{\text{T}}\ \boldsymbol{\xi}_m^{\text{T}}\ \cdots\ t_1\ \bar{\boldsymbol{x}}_1^{\text{T}}\ \boldsymbol{\xi}_1^{\text{T}}] \in \mathbb{R}^{n_{\text{tb,ms}}}$, where $n_{\text{tb,ms}} = m + \sum_{i=1}^{m} n_{\text{x},i} + n_{\xi,i}$, the approximated cost is defined as $\hat{c}_{\text{tb,ms}} : \mathbb{R}^{n_{\text{tb,ms}}} \to \mathbb{R}$. Furthermore, the equality constraint $\hat{h}_{\text{tb,ms}} : \mathbb{R}^{n_{\text{tb,ms}}} \to \mathbb{R}^{N_{\text{tb,ms}}+n_\omega}$ extends the time-based multiple shooting equation (3.6b) in Chapter 3 by incorporating the parameterization $\boldsymbol{\xi}_i$ and the operating condition $\boldsymbol{\omega}(\cdot)$. Here, $N_{\text{tb,ms}} = m + \sum_{i=1}^{m} n_{\text{x},i}$ was defined in the same chapter.

Similarly, the time-based (tb) single shooting (ss) equation (3.6a) can be extended to approximate the constraint space of the TO problem $\mathcal{P}^m$ as

$$\hat{\boldsymbol{h}}_{\text{tb,ss}} = \begin{bmatrix} \boldsymbol{g}_m^1 \circ \hat{\boldsymbol{x}}_m(t_m) - \boldsymbol{x}_0 \\ e_m^1\big(t_m, \hat{\boldsymbol{x}}_m(t_m)\big) \\ e_{m-1}^m\big(t_{m-1}, \hat{\boldsymbol{x}}_{m-1}(t_{m-1})\big) \\ \vdots \\ e_1^2\big(t_1, \hat{\boldsymbol{x}}_1(t_1)\big) \\ \boldsymbol{\omega}\big(\{t_i, \hat{\boldsymbol{x}}_i(t_i)\}_{i=0}^{m}\big) \end{bmatrix}, \tag{6.33}$$

where the intermediate grid points for the initial states $\{\bar{\boldsymbol{x}}_i\}_{i=2}^{m}$ are removed. With only the initial state $\boldsymbol{x}_0 = \bar{\boldsymbol{x}}_1 =: \hat{\boldsymbol{x}}_0(t_0)$, the decision variables are defined as $\hat{\boldsymbol{\varkappa}}_{\text{tb,ss}}^{\text{T}} = [t_m\ \boldsymbol{\xi}_m^{\text{T}}\ \cdots\ t_1\ \boldsymbol{\xi}_1^{\text{T}}\ \boldsymbol{x}_0^{\text{T}}] \in \mathbb{R}^{n_{\text{tb,ss}}}$, where $n_{\text{tb,ss}} = m + n_{\text{x},1} + \sum_{i=1}^{m} n_{\xi,i}$. Accordingly, the equality constraint is defined as $\hat{h}_{\mathrm{tb,ss}} : \mathbb{R}^{n_{\mathrm{tb,ss}}} \to \mathbb{R}^{N_{\mathrm{tb,ss}}+n_\omega}$, where $N_{\mathrm{tb,ms}} = m + n_{\mathrm{x},1}$, and the approximated cost is defined as $\hat{c}_{\mathrm{tb,ss}} : \mathbb{R}^{n_{\mathrm{tb,ss}}} \to \mathbb{R}$.

For both implementations of $\hat{\mathcal{P}}^m$, the optimality conditions are of the form (6.5).

Chapter 7

Parameterized Periodic Trajectory Optimization

> If we observe similar structural features possessed by the solutions of a sequence of models, then we may feel that we have an approximation to what is called a "law of nature".[1]
>
> —*Richard Bellman*

This chapter explores the generation and analysis of continuous 1-D families of optimally actuated orbits by introducing a parameter into previously defined TO problems.

Section 7.1 presents parameterized zero-functions that encode first-order optimality conditions for parameterized TO problems, using both direct and indirect methods. It also demonstrates how PCC methods can be applied to trace and construct 1-D families of optimal gaits.

Section 7.2 introduces the model homotopy approach from [2], which systematically connects passive-optimal orbits of a lossless model (ECM) to locally optimal orbits of a desired actuated system with dissipation. This methodology is illustrated using a monopedal robot.

Section 7.3 showcases how optimal gait libraries can be systematically expanded from passive-optimal gaits for the compass-gait walker using both direct and indirect methods. Based on [4], the example further highlights the advantages of indirect shooting over direct shooting.

Finally, Section 7.4 provides a comparative summary, highlighting the main differences of Sections 7.2 and 7.3.

[1]This quote is from the preface of the book by Bellman [13].

With some abuse of notation, the parameter $\sigma \in \mathbb{R}$ is introduced in the TO problem:

Parameterizted Periodic Trajectory Optimization Problem

$$
\mathcal{P}_\sigma^m : \begin{cases}
\underset{\left\{ \substack{t_i,\\ \boldsymbol{x}_i(\cdot),\\ \boldsymbol{u}_i(\cdot)} \right\}_{i=1}^{m}}{\text{minimize}} & \underbrace{\kappa\Big(\cdot\,;\sigma\Big) \cdot \sum_{i=1}^{m} \int_{t_{i-1}}^{t_i} l_i\big(\boldsymbol{x}_i(t), \boldsymbol{u}_i(t); \sigma\big)\mathrm{d}t}_{=\, c(\cdot\,;\sigma)} \\
\text{subject to} & \Big\{ \dot{\boldsymbol{x}}_i(t) = \boldsymbol{f}_i\big(\boldsymbol{x}_i(t), \boldsymbol{u}_i(t); \sigma\big),\ t \in [t_{i-1}, t_i] \Big\}_{i=1}^{m}, \\
& \Big\{ e_i^{i+1}\big(t_i, \boldsymbol{x}_i(t_i); \sigma\big) = 0 \Big\}_{i=1}^{m}, \\
& \Big\{ \boldsymbol{x}_{i+1}(t_i) = \boldsymbol{g}_i^{i+1}\big(\boldsymbol{x}_i(t_i); \sigma\big) \Big\}_{i=1}^{m-1}, \\
& \boldsymbol{x}_1(t_0) = \boldsymbol{g}_m^1\big(\boldsymbol{x}_m(t_m); \sigma\big), \quad \text{(periodicity)} \\
& t_0 := 0, \quad \text{(initial time)} \\
& \boldsymbol{x}_0(t_0) := \boldsymbol{x}_1(0), \quad \text{(initial state)} \\
& t_m = T, \quad \text{(period time)} \\
& \boldsymbol{\omega}\big(\cdot\,;\sigma\big) = \boldsymbol{0}, \quad \text{(operating point)}
\end{cases}
$$

Accordingly, the previously defined TO problems $\mathcal{P}^1$, $\hat{\mathcal{P}}^1$, and $\hat{\mathcal{P}}^m$ are also modified by introducing the parameter σ, resulting in the parameterized problems $\mathcal{P}_\sigma^1$, $\hat{\mathcal{P}}_\sigma^1$, and $\hat{\mathcal{P}}_\sigma^m$. Throughout this section, these problems are assumed to be sufficiently differentiable with respect to σ. This is a crucial assumption for succuessfully appling direct and indirect shooting.

Assumption (Existence and Differentiability of Trajectories)**.**

Direct method: For any $\bar{\boldsymbol{x}}_i$, $\boldsymbol{\xi}_i$, and σ, the trajectory functions $\hat{\boldsymbol{x}}_i(t)$ exist locally for all $t \in [t_{i\text{-}1}, t_i]$ and are differentiable in these variables.

Indirect method: For any $\boldsymbol{x}(0)$, $\boldsymbol{p}(0)$, and σ, the trajectory functions $\boldsymbol{x}(t)$, $\boldsymbol{p}(t)$, and specificially $\boldsymbol{u}\big(\boldsymbol{x}(t), \boldsymbol{p}(t)\big)$ exist locally for all $t \in [0, T]$ and are differentiable in these variables.

In particular, the functions c, $\boldsymbol{f}_i$, l_i, $\boldsymbol{g}_i^{i+1}$, e_i^{i+1}, and $\boldsymbol{\omega}$ are assumed to be continuously differentiable in σ.

7.1 Parameterized First-Order Optimality

The introduction of σ also parmeterizes the optimality conditions derived in Section 6.2.1 for both the direct and indirect methods. Using the shooting approach, the first-order necessary conditions are formulated as parameterized root-finding problems: $\hat{\boldsymbol{r}} : \mathbb{R}^{\hat{N}+1} \to \mathbb{R}^{\hat{N}}$ for the direct method, and $\boldsymbol{r} : \mathbb{R}^{N+1} \to \mathbb{R}^{N}$ for the indirect method.

Direct Shooting

The first-order necessary conditions in (6.5a) can be compactly expressed as the following parameterized root-finding problem:

$$\hat{\boldsymbol{r}}(\underbrace{\hat{\boldsymbol{\chi}}, \sigma}_{=\hat{\boldsymbol{\nu}}}) := \begin{bmatrix} \left.\dfrac{\partial \hat{c}(\boldsymbol{\varkappa}; \sigma)}{\partial \boldsymbol{\varkappa}}\right|_{(\hat{\boldsymbol{\varkappa}};\sigma)}^{\mathrm{T}} + \left.\dfrac{\partial \hat{\boldsymbol{h}}(\boldsymbol{\varkappa}; \sigma)}{\partial \boldsymbol{\varkappa}}\right|_{(\hat{\boldsymbol{\varkappa}};\sigma)}^{\mathrm{T}} \hat{\boldsymbol{\lambda}} \\ \hat{\boldsymbol{h}}(\hat{\boldsymbol{\varkappa}}; \sigma) \end{bmatrix} = \boldsymbol{0}, \tag{7.1}$$

where the decision variable is defined as $\hat{\boldsymbol{\chi}}^{\mathrm{T}} = [\hat{\boldsymbol{\varkappa}}^{\mathrm{T}} \; \hat{\boldsymbol{\lambda}}^{\mathrm{T}}]$. The dimension $\hat{N}$ of $\hat{\boldsymbol{\chi}}$ depends on the number of hybrid phases m and the implementation (single shooting or multiple shooting), as discussed in Section 6.3.2.

In addition to the numerical integration of $\hat{\boldsymbol{x}}_i(t_i)$ within the equality constraints $\hat{\boldsymbol{h}} = 0$, the evaluation of $\hat{\boldsymbol{r}}$ depends on sensitivity information based on $\hat{\boldsymbol{\varkappa}}$. There are three numerical approaches for computing the sensitivities $\partial \hat{c}/\partial \hat{\boldsymbol{\varkappa}}$ and $\partial \hat{\boldsymbol{h}}/\partial \hat{\boldsymbol{\varkappa}}$: finite differences, forward sensitivities and adjoint techniques [123].

Generally, finite difference methods require extensive manual tuning of step sizes to achieve the desired accuracy in gradient information. In contrast, when using variable step-size solvers, this accuracy is automatically maintained within the solver's tolerances for both forward sensitivities and adjoint techniques.

As in Section 4.3.1, the examples in this chapter also use forward sensitivities, which compute the sensitivity of the flow $\partial \hat{\boldsymbol{z}}_i/\partial \hat{\boldsymbol{\varkappa}}$ by simultaneously integrating the dynamics $\dot{\boldsymbol{z}}_i^{\mathrm{T}} = [\boldsymbol{f}_i^{\mathrm{T}} \; l_i]$ and their derivatives. While forward sensitivities are straightforward to implement, their complexity scales for each hybrid phase as $\mathcal{O}(n_{\mathrm{x},i} \cdot n_{\xi,i})$, which can become computationally expensive when the input parameterization is large ($n_{\xi,i} \gg n_{\mathrm{x},i}$).

In such cases, the adjoint method is more efficient, with a complexity of $\mathcal{O}(n_{\mathrm{x},i} + n_{\xi,i})$, as it only provides sensitivity information at the final times t_i. Since only the sensitivities at the final times t_i are needed to compute $\hat{\boldsymbol{r}}$, the adjoint method avoids the overhead of forward sensitivity methods, which return sensitivities at all times $t \in [t_{i-1}, t_i]$.

Indirect Shooting

Similiarly for the indirect approach, a parameterized root-finding problem is derived for a simple hybrid system ($m = 1$) by applying the shooting approach to the boundary value problem arising from the first-order optimality conditions (6.20)-(6.21). In this formulation, the unknown initial conditions and parameters are combined into a single decision variable

$$\boldsymbol{\chi}^{\mathrm{T}} = \begin{bmatrix} T & \boldsymbol{x}_0^{\mathrm{T}} & \boldsymbol{p}_0^{\mathrm{T}} & q & \boldsymbol{u}_0^{\mathrm{T}} & \boldsymbol{\lambda}^{\mathrm{T}} \end{bmatrix}, \tag{7.2}$$

where the initial input $\boldsymbol{u}_0$ is included as an additional variable, since the DAE (6.20) is expressed in semi-explicit form. Starting from the initial condition $\boldsymbol{w}_0^{\mathrm{T}} = [\boldsymbol{x}_0^{\mathrm{T}}\ 0\ \boldsymbol{p}_0^{\mathrm{T}}\ q\ \boldsymbol{u}_0^{\mathrm{T}}]$, , the trajectory $\boldsymbol{w}(t)$ for $t \in [0, T]$ is computed numerically by solving the DAE system (6.20) using established DAE solvers [17, 54]. Note that solving DAEs numerically is more complex than integrating ODEs, as in the direct shooting approach. In addition to assuming smooth dynamics, the solution quality and choice of solver heavily depend on the index-reduction techniques applied to $\partial\mathcal{H}/\partial\boldsymbol{u}$.

Assuming the existence and differentiability of trajectories, the parameterized root-finding problem is defined as $\boldsymbol{r} : \mathbb{R}^{N+1} \to \mathbb{R}^{N}$, with $N = 2n_{\mathrm{x}} + n_{\mathrm{u}} + 4$, encompassing the necessary conditions (6.20)-(6.21) of the indirect approach as:

$$\boldsymbol{r}(\underbrace{\boldsymbol{\chi}, \sigma}_{=\boldsymbol{\nu}}) := \begin{bmatrix} \boldsymbol{r}_T(\boldsymbol{\chi}; \sigma) \\ \boldsymbol{r}_{\boldsymbol{x}_T}(\boldsymbol{\chi}; \sigma) \\ q - \left.\dfrac{\partial c}{\partial y_T}\right|_{\left(T, \boldsymbol{x}(T), y(T); \sigma\right)} \\ \left.\dfrac{\partial \mathcal{H}}{\partial \boldsymbol{u}}\right|_{\left(\boldsymbol{w}(0); \sigma\right)} \\ \boldsymbol{g}(\boldsymbol{x}(T); \sigma) - \boldsymbol{x}_0 \\ \boldsymbol{h}\big(T, \boldsymbol{x}(T), \boldsymbol{x}_0; \sigma\big) \end{bmatrix} = \boldsymbol{0}, \tag{7.3a}$$

where

$$r_T(\boldsymbol{\nu}) = \mathcal{H}(\boldsymbol{w}(T); \sigma) + \left.\frac{\partial c}{\partial T}\right|_{\left(T, \boldsymbol{x}(T), y(T); \sigma\right)} + \boldsymbol{\lambda}^{\mathrm{T}} \left.\frac{\partial \boldsymbol{h}}{\partial T}\right|_{\left(T, \boldsymbol{x}(T), \boldsymbol{x}_0; \sigma\right)}, \tag{7.3b}$$

$$\begin{aligned} \boldsymbol{r}_{\boldsymbol{x}_T}(\boldsymbol{\nu}) = {} & \left.\frac{\partial \boldsymbol{g}}{\partial \boldsymbol{x}_T}\right|_{\left(\boldsymbol{x}(T); \sigma\right)}^{\mathrm{T}} \cdot \left(\boldsymbol{p}_0 + \left.\frac{\partial \boldsymbol{h}}{\partial \boldsymbol{x}_0}\right|_{\left(T, \boldsymbol{x}(T), \boldsymbol{x}_0; \sigma\right)}^{\mathrm{T}} \boldsymbol{\lambda} \right) \\ & - \boldsymbol{p}(T) + \left.\frac{\partial c}{\partial \boldsymbol{x}_T}\right|_{\left(T, \boldsymbol{x}(T), y(T); \sigma\right)}^{\mathrm{T}} + \left.\frac{\partial \boldsymbol{h}}{\partial \boldsymbol{x}_T}\right|_{\left(T, \boldsymbol{x}(T), y(T); \sigma\right)}^{\mathrm{T}} \boldsymbol{\lambda}. \end{aligned} \tag{7.3c}$$

7.1.1 Tracing Optimal Orbits

The parameterized root-finding problems $\hat{\boldsymbol{r}} : \mathbb{R}^{\hat{N}+1} \to \mathbb{R}^{\hat{N}}$ in the direct approach and $\boldsymbol{r} : \mathbb{R}^{N+1} \to \mathbb{R}^{N}$ in the indirect approach implicitly define a curve of stationary periodic orbits. Imposing the differentiability assumption, this curve can be efficiently traced using PCC methods. Since both direct and indirect shooting approaches are implemented within PCC, the functions $\hat{\boldsymbol{r}}$ and $\boldsymbol{r}$ are used interchangeably in this discussion about continuation. As outlined in Chapter 2, a PCC method, specificially the pseudo-arclength constinuation, consists of predictor and corrector steps (Algorithm 1), both of which require Jacobian computations:

$$\boldsymbol{R}(\boldsymbol{\nu}) := \begin{bmatrix} \frac{\partial \boldsymbol{r}}{\partial \boldsymbol{\chi}} & \frac{\partial \boldsymbol{r}}{\partial \sigma} \end{bmatrix} = D\boldsymbol{r}(\boldsymbol{\nu}), \quad \boldsymbol{R}(\boldsymbol{\nu}) \in \mathbb{R}^{N \times N+1}, \tag{7.4a}$$

$$\boldsymbol{R}^{\square}(\boldsymbol{\chi}) := \frac{\partial \boldsymbol{r}}{\partial \boldsymbol{\chi}}, \qquad \boldsymbol{R}^{\square}(\boldsymbol{\chi}) \in \mathbb{R}^{N \times N}. \tag{7.4b}$$

Algorithm 1: Continuation to create 1-D orbit family

Input: Stationary point $\boldsymbol{\chi}_{\text{start}}$ with parameter σ_{start} and desired range $[\sigma_{\text{start}}, \sigma_{\text{end}}]$; Step size $\Delta s > 0$

Output: Curve of stationary orbits of $\mathcal{P}^m_\sigma$ in the range $[\sigma_{\text{start}}, \sigma_{\text{end}}]$

$\boldsymbol{\nu}_{\text{start}} = (\boldsymbol{\chi}_{\text{start}}, \sigma_{\text{start}})$

compute initial tangent vector $\boldsymbol{\tau}_{\text{start}}$ `/* eq. (2.5) */`

$d \in \{-1, 1\}$ `/* eq. (7.5) */`

$\boldsymbol{\nu} \leftarrow \boldsymbol{\nu}_{\text{start}}, \ \boldsymbol{\tau} \leftarrow \boldsymbol{\tau}_{\text{start}}, \ \sigma \leftarrow \sigma_{\text{start}}$

while $\sigma \neq \sigma_{end}$ **do**

`/* predictor */`

$\boldsymbol{\nu}_{\text{pred}} \leftarrow \boldsymbol{\nu} + d\Delta s \boldsymbol{\tau}$ `/* eq. (2.7) */`

compute $\boldsymbol{\tau}_{\text{pred}}$ at $\boldsymbol{\nu}_{\text{pred}}$ `/* eq. (2.5) */`

`/* corrector */`

Newton's Method $(\boldsymbol{\nu}_{\text{pred}}, \boldsymbol{\tau}_{\text{pred}})$**:**

$$\boldsymbol{\nu} \leftarrow \boldsymbol{\nu} - \begin{bmatrix} \boldsymbol{R}(\boldsymbol{\nu}) \\ \boldsymbol{\tau}^{\mathrm{T}} \end{bmatrix}^{-1} \cdot \begin{bmatrix} \boldsymbol{r}(\boldsymbol{\nu}) \\ 0 \end{bmatrix}$$

until convergence `/* loop */`

return $\{\boldsymbol{\nu}_{\text{corr}} = (\chi_{\text{corr}}, \sigma_{\text{corr}}); \ \boldsymbol{\tau}_{\text{corr}}\}$

$\boldsymbol{\nu} \leftarrow \boldsymbol{\nu}_{\text{corr}}, \ \boldsymbol{\tau} \leftarrow \boldsymbol{\tau}_{\text{corr}}, \ \sigma \leftarrow \sigma_{\text{corr}}$

These steps, repeated iteratively, construct the desired family of stationary orbits over a specified parameter range $[\sigma_{\text{start}}, \sigma_{\text{end}}]$. The process requires an initial solution $\boldsymbol{\chi}_{\text{start}}$ at σ_{start}, satisfying $\boldsymbol{r}(\boldsymbol{\chi}_{\text{start}}, \sigma_{\text{start}}) = \boldsymbol{0}$, which can be derived from a passive-optimal solution (Section 6.2.2). Assuming that σ_{start} corresponds to a regular point $\boldsymbol{\nu}_{\text{start}}$, the tangent vector $\boldsymbol{\tau}_{\text{start}} = \boldsymbol{\tau} \circ \boldsymbol{R}(\boldsymbol{\nu}_{\text{start}})$ is uniquely defined via (2.5). Since the curve $\boldsymbol{r}^{-1}(\boldsymbol{0})$ passing through $\boldsymbol{\nu}_{\text{start}}$ can be traced in opposite directions, the continuation process proceeds towards σ_{end}, where the initial direction is determined as

$$d = \operatorname{sign}\big(\sigma_{\text{end}} - \sigma_{\text{start}}\big) \cdot \operatorname{sign}\big(\begin{bmatrix} 0 & \cdots & 0 & 1 \end{bmatrix} \cdot \boldsymbol{\tau}_{\text{start}}\big). \tag{7.5}$$

Algorithm 1 assumes monotonicity of the solution curve $\boldsymbol{r}^{-1}(\boldsymbol{0})$ in the parameter $\sigma \in [\sigma_{\text{start}}, \sigma_{\text{end}}]$ to define the direction d of the curve as in equation (7.5). However, in general, a curve traced via the presented PCC method may include turning points in σ or bifurcation points. Consequently, there is no guarantee that an initial stationary point $\boldsymbol{\chi}_{\text{start}}$ can be locally continued to $\boldsymbol{\chi}_{\text{end}}$, which corresponds to σ_{end}.

Second-Order Optimality

A particular challenge arises at turning points ($\det(\boldsymbol{R}^{\square}) = 0$), where the curve transitions from local minimizers to saddle points, or vice versa, as discussed in Section 2.3.4. In the case of the direct approach, a stationary point can be readily classified as either a saddle point or a local minimizer. By simply reusing the Jacobian $\hat{\boldsymbol{R}}$ from the continuation process, the second-order optimality conditions from (6.5b) can be expressed in terms of the projected Hessian:

$$\begin{aligned} \hat{\boldsymbol{H}} &= \left(\begin{bmatrix} \boldsymbol{I} \\ \boldsymbol{0} \end{bmatrix} \hat{\boldsymbol{\Delta}}\right)^{\mathrm{T}} \hat{\boldsymbol{R}}^{\square} \left(\begin{bmatrix} \boldsymbol{I} \\ \boldsymbol{0} \end{bmatrix} \hat{\boldsymbol{\Delta}}\right) = \hat{\boldsymbol{\Delta}} \left(D^2 \hat{c}(\hat{\boldsymbol{\varkappa}}; \sigma) + D^2 \hat{\boldsymbol{h}}(\hat{\boldsymbol{\varkappa}}; \sigma)^{\mathrm{T}} \hat{\boldsymbol{\lambda}}\right) \hat{\boldsymbol{\Delta}}, \\ \hat{\boldsymbol{H}} &\succ \boldsymbol{0}, \end{aligned} \tag{7.6a}$$

where $\hat{\boldsymbol{\Delta}}$ represents an orthonormal basis of the tangent space, satisfying $\operatorname{span}(\hat{\boldsymbol{\Delta}}) = \operatorname{null}(D\hat{\boldsymbol{h}})$. In practice, the matrix $\hat{\boldsymbol{\Delta}}$ can be constructed using the singular value decomposition (SVD) of $D\hat{\boldsymbol{h}}$. Hence, for a zero $\hat{\chi} \in \hat{\boldsymbol{r}}^{-1}(\boldsymbol{0})$, checking the sign of the smallest eigenvalue of $\hat{\boldsymbol{H}}$ is sufficient to distinguish between a local minimum and a saddle point. This classification can be summarized compactly as:

$$\min\big(\operatorname{eig}(\hat{\boldsymbol{H}})\big) \quad \begin{cases} < 0, & \text{saddle point}, \\ = 0, & \text{local minimum}, \\ > 0, & \text{strict local minimum}. \end{cases} \tag{7.6b}$$

7.2 Model Homotopy

This section introduces an approach from [2] that leverages the ease of finding conservative orbits for ECMs, as demonstrated in Chapter 5, along with the fact that these gaits require no actuation to maintain. Consequently, these orbits serve as passive-optimal gaits to a parameterized TO problem $\mathcal{P}_{\varepsilon}^{m}$, establishing a connection between an ECM and a more realistic (dissipative) robot model via a homotopy parameter $\varepsilon =: \sigma$. Through this homotopic approach, passive-optimal gaits can be continuously transformed into optimal gaits of the target system. This so-called *model homotopy* provides a continuous mapping in ε from realistic models ($\varepsilon = 1$) to their corresponding ECMs ($\varepsilon = 0$) and then traces optimal gaits of the ECM back to optimal gaits of the realistic model (Fig. 7.1).

The transition between models is achieved by appropriately scaling inertial, damping, and frictional terms with ε to ensure no energy is lost during continuous motions or collisions. As discussed for ECMs in Chapter 5, singularities in the dynamics are avoided by introducing kinematic constraints when necessary.

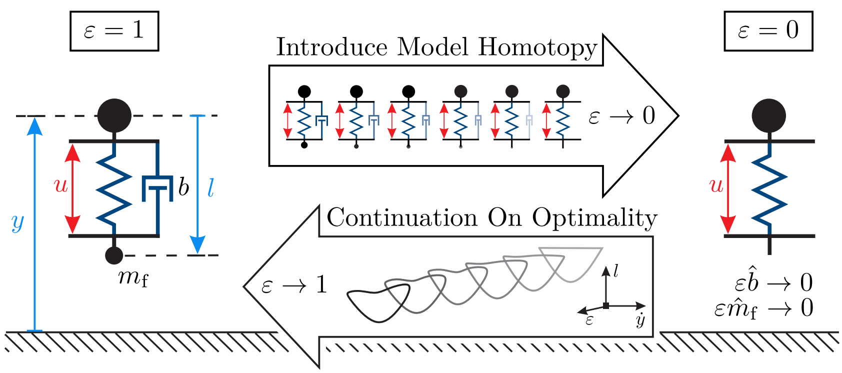

Figure 7.1: Illustration of the methodology applied to a 1-D hopper. A model homotopy is introduced by scaling the damping coefficient b and the foot mass m_{f} with the parameter $\sigma := \varepsilon$. When $\varepsilon = 1$, the fully dissipative (open) model is obtained, as shown on the left, while $\varepsilon = 0$ represents the lossless (closed), but actuated model, shown on the right. The passive-optimal hopping gaits ($u^* \equiv 0$) identified in the lossless model are then traced using PCC methods (Algorithm 1), into optimal trajectories of the dissipative model. This process enables the continuous transition of optimal gaits from a simple model to a more complex, realistic system.

7.2.1 Dissipation (Homotopy) Parameter

The first step in this methodology is to introduce the parameter $\varepsilon \in \mathbb{R}$ into the hybrid dynamics of an actuated system. In the special case where $\boldsymbol{u}_i \equiv \boldsymbol{0}$, ε behaves similarly to ξ from Section 4.3, as it embeds an ECM into a one-parameter family of dissipative dynamics Σ_ε. Thus, ε is also termed *dissipation parameter*, as it continuously switches dissipation on and off. Although ε can take any real value, it is particularly useful in connecting an actuated, lossless HDS Σ_0 to an actuated, dissipative HDS Σ_1, where $\varepsilon \in [0, 1]$ establishes a model homotopy.

Homotopy in Dynamics

With the ε-scaling introduced in Chapter 5 and by augmenting (5.10) with inputs, the actuated dynamical system is defined as

$$\ddot{\boldsymbol{q}} = \boldsymbol{M}_\varepsilon^{-1}\Big(\boldsymbol{n}(\boldsymbol{x};\varepsilon) + \boldsymbol{J}_i(\boldsymbol{q};\varepsilon)^{\mathrm{T}}\boldsymbol{\lambda}_i(\boldsymbol{x};\varepsilon) + \boldsymbol{B}_i(\boldsymbol{x};\varepsilon)\boldsymbol{u}_i\Big), \tag{7.7a}$$

where the parameterized input matrix $\boldsymbol{B}_i(\boldsymbol{x};\varepsilon) \in \mathbb{R}^{n_\mathrm{x} \times n_\mathrm{u}}$ maps the inputs $\boldsymbol{u}_i$ into the generalized torques. Furthermore, assuming the system undergoes plastic collisions, the velocity jumps defined by (5.7) are also parameterized as

$$\dot{\boldsymbol{q}}^+ = \Big(\boldsymbol{I} - \boldsymbol{M}_\varepsilon^{-1}\boldsymbol{J}_{i+1}(\boldsymbol{q};\varepsilon)^{\mathrm{T}}\widetilde{\boldsymbol{M}}_{i+1}(\boldsymbol{q};\varepsilon)^{-1}\boldsymbol{J}_{i+1}(\boldsymbol{q};\varepsilon)\Big)\dot{\boldsymbol{q}}^-, \tag{7.7b}$$

where the Delassus' matrix $\widetilde{\boldsymbol{M}}_{i+1}(\boldsymbol{q};\varepsilon)^{-1}$ vanishes at $\varepsilon = 0$ to conserve energy. Using the same set of coordinates for all phases, yields the state $\boldsymbol{x}_i^{\mathrm{T}} = \boldsymbol{x}^{\mathrm{T}} = [\boldsymbol{q}^{\mathrm{T}}\ \dot{\boldsymbol{q}}^{\mathrm{T}}]$. Leaving the state space $\mathcal{X}$ unaffected by the model homotopy, the parameterized continuous dynamics, discrete dynamics and event sets of Σ_ε take the following form:

$$\mathcal{F}_\varepsilon = \left\{\dot{\boldsymbol{x}}_i = \boldsymbol{f}_i(\boldsymbol{x}_i, \boldsymbol{u}_i;\varepsilon) = \begin{bmatrix}\dot{\boldsymbol{q}}\\ \ddot{\boldsymbol{q}}\end{bmatrix}\right\}_{i=1}^{m}, \tag{7.7c}$$

$$\mathcal{G}_\varepsilon = \left\{\boldsymbol{g}_i^{i+1}(\boldsymbol{x}_i;\varepsilon) = \begin{bmatrix}\boldsymbol{q}^+\\ \dot{\boldsymbol{q}}^+\end{bmatrix}\right\}_{i=1}^{m}, \tag{7.7d}$$

$$\mathcal{E}_\varepsilon = \Big\{\{t \in \mathbb{R},\ \boldsymbol{x}_i \in \mathcal{X}_i \mid e_i^{i+1}(t, \boldsymbol{x}_i;\varepsilon) = 0\}\Big\}_{i=1}^{m}. \tag{7.7e}$$

Finally, based on the previously stated assumptions of existence and differentiability, the vector field $\boldsymbol{f}_i$ is complete for all $\varepsilon \in [0, 1]$ and at least twice differentiable with respect to ε.

7.2.2 Homotopy Continuation via the Direct Method

Introducing a model homotopy into the dynamics Σ_ε prameterizes the equality constraints in the TO problem $\mathcal{P}_\varepsilon^m$. To numerically solve $\mathcal{P}_\varepsilon^m$ and trace stationary gaits within the model homotopy, the problem is transcribed into $\hat{\mathcal{P}}_\varepsilon^m$ using the direct shooting approach. By implementing the input parameterization $\hat{\boldsymbol{u}}_i$ as defined in (6.3), the first-order necessary conditions of $\hat{\mathcal{P}}_\varepsilon^m$ define the parameterized root-finding problem $\hat{\boldsymbol{r}}(\hat{\boldsymbol{\chi}}, \varepsilon) = \mathbf{0}$ in (7.1).

Using Algorithm 1, a curve of stationary gaits is generated, connecting a strictly passive-optimal gait $\hat{\boldsymbol{\chi}}_{\text{start}}$ at $\varepsilon_{\text{start}} = 0$ (corresponding to an ECM) to a locally optimal gait $\hat{\boldsymbol{\chi}}_{\text{end}}$ at $\varepsilon_{\text{end}} = 1$.

To ensure that an initial gait with zero actuation ($\hat{\boldsymbol{u}}_i = \mathbf{0}$) is strictly passive-optimal, the starting point $\hat{\boldsymbol{\chi}}_{\text{start}}$ must correspond to a normal conservative orbit of the ECM Σ_0, where zero actuation implies $\boldsymbol{\xi}_i = \mathbf{0}$. Only if this regularity condition holds for $\hat{\mathcal{P}}_0^m$, the curve $\hat{\boldsymbol{r}}^{-1}(\mathbf{0})$ can be uniquely extended into $\varepsilon > 0$ from the initial point $\hat{\boldsymbol{\nu}}_{\text{start}}^{\mathrm{T}} = [\hat{\boldsymbol{\chi}}_{\text{start}}^{\mathrm{T}}\ 0]$. Additionally, the cost function of $\hat{\mathcal{P}}_\varepsilon^m$ must belong to a specific subclass $\mathcal{C}_0 \subset \mathcal{C}$ of economic cost functions.

Definition (Economic Cost Functions for Lossless Systems)**.** *By applying direct shooting, the subclass of economic cost functions* $\hat{\mathcal{C}}_0$ *includes functions* $\hat{c}(\hat{\boldsymbol{\varkappa}}; \varepsilon)$ *that are:*

C1 at least twice differentiable in all variables, i.e., $\hat{c} \in C^2$*,*

C2 of zero value when $\boldsymbol{u}_i(\cdot) \equiv \mathbf{0}$ *and* $\varepsilon = 0$*, i.e.,* $\hat{c}(\hat{\boldsymbol{\varkappa}}_0, 0) = 0$*, and*

C3 locally positive-definite in $\frac{\partial^2 \hat{c}}{\partial \boldsymbol{\xi}^2}(\hat{\boldsymbol{\varkappa}}, \varepsilon)\big|_{(\hat{\boldsymbol{\varkappa}} = \hat{\boldsymbol{\varkappa}}_0, \varepsilon = 0)}$*,*

where the decision vector $\hat{\boldsymbol{\varkappa}}_0$ *denotes* $\hat{\boldsymbol{\varkappa}}$ *with input parameters* $\boldsymbol{\xi}_i = \mathbf{0}$*.*

While conditions *C1* and *C2* align with the general definition of economic cost functions, *C3* ensures that a normal conservative orbit constitues a strict local minimimizer.

Remark 7.2.1. *The properties C1–C3 hold for a broad class of economic cost functions, as discussed in Section 6.1.1, though some functions may require smoothing to satisfy C1. An exception within the list of economic cost functions* (6.1) *is mechanical power* (6.1b)*, which fails to meet C3. Specifically, the function* $\hat{c}$ *remains zero in the neighborhood of a passive gait where nonzero actuation* ($\hat{\boldsymbol{u}}_i \neq \mathbf{0}$) *injects and removes equal amounts of energy.*

7.2.3 Example: Monoped

To demonstrate the effectiveness of the homotopic approach, optimally actuated gaits are generated for a 2D one-legged hopping robot with parallel elastic actuation (Fig. 7.2). This system has been extensively studied in previous works [112, 113, 139, 140]. To achieve this, a model homotopy parameterized by ε is developed, and a COP $\hat{\mathcal{P}}_{\varepsilon}^{2}$, where $m = 2$, is defined by selecting an appropriate economic cost function, input parameterization, and set of operating points.

The hopper consists of a torso with mass m_t and inertia Θ_t, an upper leg segment $(m_\mathrm{l}, \Theta_\mathrm{l})$, and a lower leg segment $(m_\mathrm{f}, \Theta_\mathrm{f})$ with a spherical foot (radius r_f). The torso's configuration is given by its orientation φ and the hip position (x, y). The upper leg segment is connected to the hip via a rotational joint with an angle α, while the lower leg is attached through a prismatic joint, defining an overall leg length l. Thus, the generalized coordinates are given by $\boldsymbol{q}^\mathrm{T} = [x\ y\ \varphi\ \alpha\ l]$, with $n_\mathrm{x} = 10$. Both the hip and leg joints incorporate linear elastic springs with stiffnesses k_α and k_l, along with damping ratios b_α and b_l. These springs operate in parallel with actuators that generate torques $\boldsymbol{u}^\mathrm{T} = [\tau_\mathrm{mot}\ f_\mathrm{mot}]$. The remaining model parameters are defined in Fig. 7.2 and Table 7.1. All values are normalized with respect to total mass $m_\circ$, leg length $l_\circ$ and gravity g. The hopper has two phases: *stance* S and *flight* F. During *stance*, the foot stays on the ground and is constrained to a pure rolling motion $\boldsymbol{j}_\mathrm{S}(\boldsymbol{q}) = 0$ with the associated constraint forces $\boldsymbol{\lambda}_\mathrm{S}^\mathrm{T} = [\lambda_\mathrm{T}\ \lambda_\mathrm{N}]$.

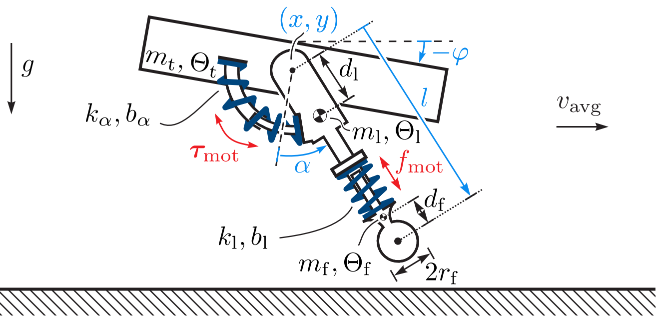

Figure 7.2: A one-legged hopper with parallel elastic actuation at the leg and hip ($\boldsymbol{u}^\mathrm{T} = [\tau_\mathrm{mot}\ f_\mathrm{mot}]$). Its configuration is given by $\boldsymbol{q}^\mathrm{T} = [x\ y\ \varphi\ \alpha\ l]$.

$m_\mathrm{f} = 0.1\, m_\circ$	$\Theta_\mathrm{f} = 0.04\, m_\mathrm{f} l_\circ^2$	$r_\mathrm{f} = 0.05\, l_\circ$	$k_\mathrm{l} = 20\ m_\circ g/l_\circ$
$m_\mathrm{l} = 0.2\, m_\circ$	$\Theta_\mathrm{l} = 0.02\, m_\mathrm{l} l_\circ^2$	$d_\mathrm{f} = 0.25\, l_\circ$	$k_\alpha = 100\ m_\mathrm{f} g l_\circ/\mathrm{rad}$
$m_\mathrm{t} = 0.7\, m_\circ$	$\Theta_\mathrm{t} = 0.40\, m_\mathrm{t} l_\circ^2$	$d_\mathrm{l} = 0.25\, l_\circ$	$b_\mathrm{l} = 0.4\sqrt{2}\, m_\circ \sqrt{g/l_\circ}$
			$b_\alpha = 3.5\, m_\mathrm{f} l_\circ \sqrt{g l_\circ}/\mathrm{rad}$

Table 7.1: All model parameters are adapted from [113] and normalized with respect to total mass $m_\circ$, leg length $l_\circ$ and gravity g.

Model Homotopy

To construct the model homotopy, the process begins with a standard multibody dynamic model of the hopper, representing the dynamics for $\varepsilon = 1$. Since this model includes damping and collision losses, a similar approach to the one outlined in Section 5.1 is used to derive a lossless model for $\varepsilon = 0$. To ensure that $\lim_{\varepsilon \to 0} \widetilde{\boldsymbol{M}}_\mathrm{S}(\boldsymbol{q};\varepsilon)^{-1}$ approaches zero, the masses and inertias m_f, m_l, Θ_f, and Θ_l involved in the projection $\widetilde{\boldsymbol{M}}_\mathrm{S}$ are appropriately scaled. This is achieved by redefining the foot and leg masses as $m_\mathrm{f} = \varepsilon \hat{m}_\mathrm{f}$ and $m_\mathrm{l} = \varepsilon \hat{m}_\mathrm{l}$, respectively. Due to this scaling, the inertial torques generated by the leg vanish as ε approaches zero. To maintain meaningful pitch dynamics, the torso inertia is also scaled, given by $\Theta_\mathrm{t} = \varepsilon \hat{\Theta}_\mathrm{t}$. The DoF associated with the massless limbs must be constrained in all phases (Remark 5.1.1). Consequently, the *flight* constraint $j_\mathrm{F}(\boldsymbol{q}) = l - l_\circ$ is introduced, accompanied by the constraint force λ_F. Similar to the hopper model in Section 5.1.3, auxiliary forces $\hat{\lambda}_\mathrm{F}$ and $\hat{\boldsymbol{\lambda}}_\mathrm{S}$, leading to the constraint force formulations $\lambda_\mathrm{F}(\varepsilon) = \varepsilon \hat{\lambda}_\mathrm{F}$ and $\boldsymbol{\lambda}_\mathrm{S}(\varepsilon) = \varepsilon \hat{\boldsymbol{\lambda}}_\mathrm{S}$, respectively. Since the constraint $j_\mathrm{F}(\boldsymbol{q}) = 0$ is only required for $\varepsilon = 0$, the resulting constraint force λ_F is multiplied by $(1-\varepsilon)$ when incorporated into (7.7a). To achieve a finite leg swing frequency as $\varepsilon \to 0$, the spring stiffness in the hip is scaled as $k_\alpha = \varepsilon \hat{k}_\alpha$, analogous to (5.15). Since the damping force $b_\alpha \dot{\alpha}$ and the actuation $\boldsymbol{u}$ would similarly exhibit singularities, additional scaling is introduced:

$$\boldsymbol{J}_i = \begin{bmatrix} 0 & 0 & 0 & \varepsilon & 0 \\ J_i^{21} & J_i^{22} & 0 & 0 & \varepsilon \end{bmatrix}, \qquad b_\alpha = \varepsilon^2 \hat{b}_\alpha, \tag{7.8}$$

where $J_\mathrm{F}^{21} = J_\mathrm{F}^{22} = 0$, $J_\mathrm{S}^{21} = -\sin(\alpha+\varphi)(1-\varepsilon)$ and $J_i^{22} = \cos(\alpha+\varphi)(1-\varepsilon)$. The repeated multiplication of the damping coefficient $\hat{b}_\alpha$ by ε follows from the final scaling law: to eliminate damping losses in (7.7a) for $\varepsilon \to 0$, the damping coefficients are scaled by ε. Similarly, we set $b_\mathrm{l} = \varepsilon \hat{b}_\mathrm{l}$.

Results

Optimal gaits were generated using the phase sequence S $\rightarrow$ F, where $m = 2$ and $T := t_{\mathrm{F}}$, at different average speeds v_{avg} through time-based single shooting:

$$\hat{\boldsymbol{h}} = \begin{bmatrix} \boldsymbol{g}_{\mathrm{F}}^{\mathrm{S}} \circ \hat{\boldsymbol{x}}_{\mathrm{F}}(t_{\mathrm{F}}) - \boldsymbol{x}_0 \\ e_{\mathrm{F}}^{\mathrm{S}}\big(t_{\mathrm{F}}, \hat{\boldsymbol{x}}_{\mathrm{F}}(t_{\mathrm{F}})\big) \\ e_{\mathrm{S}}^{\mathrm{F}}\big(t_{\mathrm{S}}, \hat{\boldsymbol{x}}_{\mathrm{S}}(t_{\mathrm{S}})\big) \\ \omega\big(\{t_i, \hat{\boldsymbol{x}}_i(t_i)\}_{i=0}^{2}\big) \end{bmatrix}. \tag{7.9}$$

A single operating condition ($n_\omega = 1$) defines the monoped's average speed:

$$\omega(t_{\mathrm{F}}, \hat{\boldsymbol{x}}_{\mathrm{F}}(t_{\mathrm{F}}), t_{\mathrm{S}}, \hat{\boldsymbol{x}}_{\mathrm{S}}(t_{\mathrm{S}}), \boldsymbol{x}_0) := \hat{x}(T) - x(0) - v_{\mathrm{avg}} T, \tag{7.10}$$

where the horizontal positions $x(0)$ and $\hat{x}(T)$ are the first entries in the vectors $\boldsymbol{x}_0$ and $\hat{\boldsymbol{x}}_{\mathrm{F}}(t_{\mathrm{F}})$, respectively. To enable horizontal forward motion during the periodic gait, the first entry in $\boldsymbol{g}_{\mathrm{F}}^{\mathrm{S}}$ is set to zero, yielding the initial horizontal position $x(0) = 0$ in the periodicity condition of (7.9).

While touch-down $e_{\mathrm{F}}^{\mathrm{S}}(\boldsymbol{q})$ is kinematic, the lift-off $e_{\mathrm{S}}^{\mathrm{F}}(\boldsymbol{x}, \varepsilon) = \lambda_{\mathrm{N}}$ occurs when λ_{N} transitions from a positive to a negative value. In this example, the input space is discretized using a single 3-term Fourier series ($n_{\xi,i} = 14$):

$$\underbrace{\hat{\boldsymbol{u}}_{\mathrm{S}}(t, \boldsymbol{\xi}_{\mathrm{S}})}_{=\hat{\boldsymbol{u}}(t,\boldsymbol{\xi})} = \xi_{\mathrm{S}}^{1} + \sum_{k=1}^{3} \left(\xi_{\mathrm{S}}^{2k} \cos\left(\frac{2\pi}{T} kt\right) + \xi_{\mathrm{S}}^{2k+1} \sin\left(\frac{2\pi}{T} kt\right) \right), \tag{7.11a}$$

$$\underbrace{\hat{\boldsymbol{u}}_{\mathrm{F}}(t, \boldsymbol{\xi}_{\mathrm{F}})}_{=\hat{\boldsymbol{u}}(t,\boldsymbol{\xi})} = \xi_{\mathrm{F}}^{1} + \sum_{k=1}^{3} \left(\xi_{\mathrm{F}}^{2k} \cos\left(\frac{2\pi}{T} kt\right) + \xi_{\mathrm{F}}^{2k+1} \sin\left(\frac{2\pi}{T} kt\right) \right), \tag{7.11b}$$

$$\boldsymbol{\xi}_{\mathrm{S}} = \boldsymbol{\xi}_{\mathrm{F}} =: \boldsymbol{\xi}, \tag{7.11c}$$

Copper losses in the motor are used as the economic cost function:

$$\hat{c} := \int_0^{t_{\mathrm{S}}} \hat{\boldsymbol{u}}_{\mathrm{S}}(t, \boldsymbol{\xi}_{\mathrm{S}})^{\mathrm{T}} \boldsymbol{K} \hat{\boldsymbol{u}}_{\mathrm{S}}(t, \boldsymbol{\xi}_{\mathrm{S}}) \mathrm{d}t + \int_{t_{\mathrm{S}}}^{t_{\mathrm{F}}} \hat{\boldsymbol{u}}_{\mathrm{F}}(t, \boldsymbol{\xi}_{\mathrm{F}})^{\mathrm{T}} \boldsymbol{K} \hat{\boldsymbol{u}}_{\mathrm{F}}(t, \boldsymbol{\xi}_{\mathrm{F}}) \mathrm{d}t \tag{7.12a}$$

$$\overset{(7.11c)}{=} \int_0^{T} \hat{\boldsymbol{u}}(t, \boldsymbol{\xi})^{\mathrm{T}} \boldsymbol{K} \hat{\boldsymbol{u}}(t, \boldsymbol{\xi}) \mathrm{d}t, \tag{7.12b}$$

where the motor's speed-torque gradient is $\boldsymbol{K} = \mathrm{diag}\big(m_\circ \sqrt{g l_\circ^3}, m_\circ \sqrt{g/l_\circ}\big)^{-1}$. Note that the properties *C1*-*C3* are easy to confirm for (7.12). With the simplification (7.11c), the decision variable of the problem $\hat{\mathcal{P}}^2_\varepsilon$ is defined as $\hat{\boldsymbol{\varkappa}}^{\mathrm{T}} = [t_{\mathrm{F}}\ t_{\mathrm{S}}\ \boldsymbol{\xi}^{\mathrm{T}}\ \boldsymbol{x}_0^{\mathrm{T}}] \in \mathbb{R}^{26}$.

Using the methods for tracing orbits in ECMs as described in Chapters 4 and 5, the connected space of passive gaits was systematically explored. The search was initialized with a simple hopping-in-place motion derived analytically. Due to different parameter choices, the lossless model exhibited a significantly higher leg swing frequency compared to the ECM of a spring-loaded hopper in Section 5.2.4. As a result, the first simple bifurcation connecting the hopping-in-place branch with forward and backward hopping motions was identified at a notably smaller *flight* duration of $\Delta t_{\mathrm{F}} \approx 0.1658\ \sqrt{g/l_\circ}$. The branch of passive forward hopping motions was subsequently traced for average speeds of up to $v_{\mathrm{avg}} = 1.4\ \sqrt{gl_\circ}$.

Algorithm 1 was initialized with these motions, successfully tracing the first-order optimality from the passive gaits of the lossless model ($\varepsilon = 0$) to the optimally actuated gaits of the model at $\varepsilon = 1$. This process is illustrated in Figure 7.3 for $v_{\mathrm{avg}} = 1\ \sqrt{gl_\circ}$. As ε increased from 0 to 1, the cost $\hat{c}$ monotonically rose from 0 to $0.737 m_\circ g l_\circ$. The gait remained optimal, satisfying both the first- and second-order optimality. Specifically, the smallest eigenvalue $\mu_{\min}$ of $\hat{\boldsymbol{H}}$ had to remain positive to meet the sufficient condition (7.6b), as depicted in Figure 7.3.

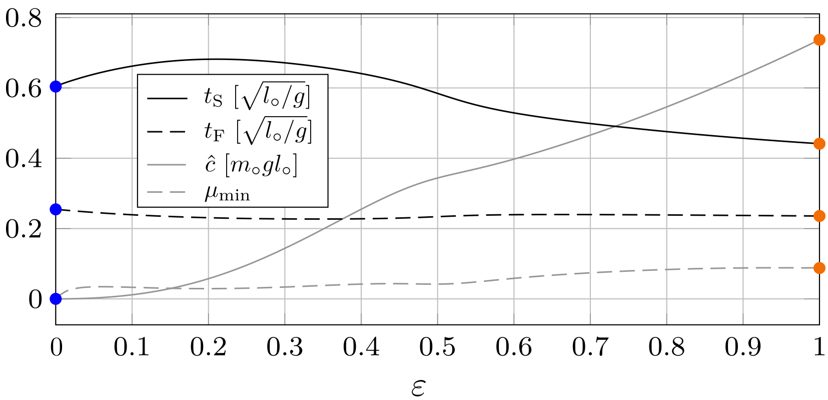

Figure 7.3: Shown is the evolution of stance duration Δt_{S}, flight duration Δt_{F}, cost value $\hat{c}$, and $\mu_{\min}$ during the transition from the lossless model ($\varepsilon = 0$, blue) to the full model ($\varepsilon = 1$, orange). The smallest eigenvalue of the Hessian $\hat{\boldsymbol{H}}$, denoted $\mu_{\min}$, is $\mu_{\min}(0) = 0.005$ at $\varepsilon = 0$ and remains positive, ensuring strict optimality throughout the homotopy. This data is from a forward hopping motion with $v_{\mathrm{avg}} = 1\ \sqrt{gl_\circ}$.

The process was repeated for a range of forward speeds v_{avg} from 0 to 1.4 $\sqrt{gl_\circ}$, consistently starting from passive gaits. The process reliably converged for speeds greater than $v^*_{\text{avg}} \approx 0.12\ \sqrt{gl_\circ}$. Figure 7.4 visualizes the results for selected speeds, showing passive gaits (blue line) emerging from in-place hopping motions (dashed blue), while active gaits appear as orange dots. The connecting black lines illustrate how $\boldsymbol{x}_0$ evolves throughout the homotopy.

To investigate why the process failed for speeds below $v^*_{\text{avg}} \approx 0.12\ \sqrt{gl_\circ}$, a continuation was performed on stationary points of $\hat{\mathcal{P}}^2_{v_{\text{avg}}}$, where $\sigma := v_{\text{avg}}$. Instead of fixing v_{avg} and varying ε, this approach held ε constant while adjusting v_{avg} (orange line in Figure 7.4). This method was more efficient for analyzing optimal gaits across speeds and revealed additional structure. In particular, the smallest eigenvalue $\mu_{\min}$ of $\hat{\boldsymbol{H}}$ showed a turning point at v^*_{avg}, beyond which stationary points became saddle points (dashed line) and ceased to be optimal.

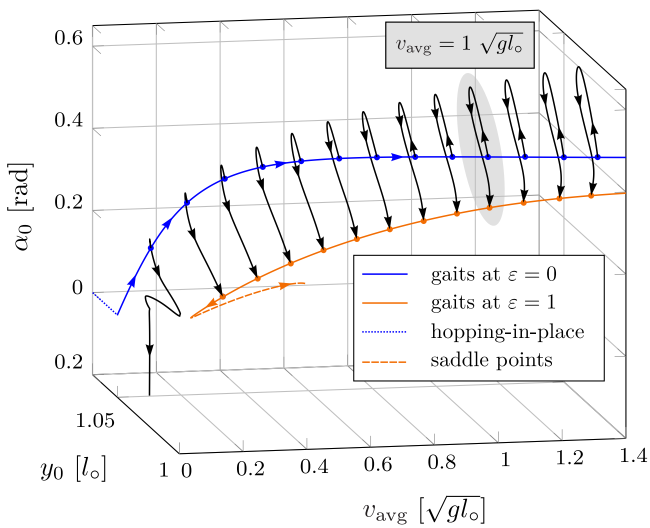

Figure 7.4: Projection of the initial state space (α_0, y_0) showing passive gaits (blue) with $\hat{c} = 0$, $\hat{\boldsymbol{u}} \equiv \boldsymbol{0}$, identified via numerical continuation from a passive hopping-in-place motion. A model homotopy traces these gaits from $\varepsilon = 0$ to locally optimal solutions at $\varepsilon = 1$ (orange). A separate continuation at fixed $\varepsilon = 1$ (orange line) reveals a turning point at $v^*_{\text{avg}} \approx 0.12\ \sqrt{gl_\circ}$, where stationary points become saddle points, losing optimality.

7.3 Example: Compass-Gait Walker

Based on [4], this section further explores the generation of optimal gait libraries, expanding on passive-optimal gaits for the compass-gait walker (Fig. 7.5), a simple hybrid system with $m = 1$. Special emphasis is placed on the application and comparison of both direct and indirect shooting methods for $\mathcal{P}^1_\sigma$. The analysis focuses on both computational efficiency and the numerical sensitivity of the different formulations. Since the indirect method does not rely on a finite parameterization of the control inputs, it serves as a reliable benchmark for assessing various input parameterizations used in direct methods. Despite the simplicity of the compass-gait walker, which has only four state variables ($n_\mathrm{x} = 4$), it remains a widely adopted model for studying bipedal locomotion [12, 51, 90, 115, 117, 131, 137]. Its characteristics—underactuation, non-smooth dynamics, limit cycle behavior, and the need for optimizing energy efficiency—are representative of the challenges encountered in more complex legged robots.

Furthermore, the compass-gait walker can passively walk down a slope, driven solely by gravity g. This capability will be utilized to generate families of gaits parameterized by the slope's incline γ and the robot's average speed v_avg.

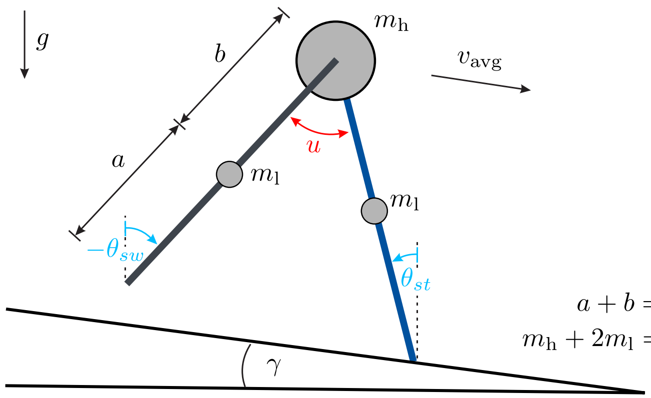

$a + b = l_\circ$

$m_\mathrm{h} + 2m_\mathrm{l} = m_\circ$

Figure 7.5: The compass-gait walker on a slope (γ). The robot's parameters are normalized by total mass $m_\circ$, gravity g and leg length $l_\circ$. Its proportions are defined as $a/b = 1$ and $m_\mathrm{h}/m_\mathrm{l} = 2$.

7.3.1 Model and Problem Description

The model consists of a stance leg (with angle θ_{st} relative to vertical) that remains on the ground without sliding and a swing leg (with angle θ_{sw} relative to vertical) that swings freely. During forward motion, the swing leg strikes the ground ahead of the stance leg, triggering an instantaneous role reversal between the two. Hence, the swing leg becomes the stance leg and vice versa. Both legs, of length $l_\circ = a + b$, have a point mass m_{l} and are connected at the hip, where the point mass m_{h} constitutes the main body of the biped. A single motor ($n_{\mathrm{u}} = 1$) at the hip applies torque u between the legs. Figure 7.5 provides the robot's specific proportions, normalized by total mass $m_\circ$, gravity g, and leg length $l_\circ$. Given its configuration $\boldsymbol{q} = [\theta_{\mathrm{sw}}\ \theta_{\mathrm{st}}]^{\mathrm{T}} \in \mathcal{Q}$ with configuration space $\mathcal{Q} = \mathbb{S}^1 \times \mathbb{S}^1$ and the slope γ, its parameterized hybrid dynamics Σ_γ are as follows:

$$\mathcal{X} = \mathcal{X}_1 = \left\{ \boldsymbol{x}^{\mathrm{T}} = \boldsymbol{x}_1^{\mathrm{T}} = \begin{bmatrix} \boldsymbol{q}^{\mathrm{T}} & \dot{\boldsymbol{q}}^{\mathrm{T}} \end{bmatrix} \ :\ \boldsymbol{q} \in \mathcal{Q},\ \dot{\boldsymbol{q}} \in T_{\boldsymbol{q}}\mathcal{Q} \right\}, \tag{7.13a}$$

$$\boldsymbol{f} = \boldsymbol{f}_1 = \begin{bmatrix} \dot{\boldsymbol{q}} \\ \boldsymbol{M}(\boldsymbol{q})^{-1}\left(\boldsymbol{\eta}(\boldsymbol{q}, \dot{\boldsymbol{q}}) + \boldsymbol{B}u\right) \end{bmatrix}, \tag{7.13b}$$

$$\mathcal{E}_\gamma = \mathcal{E}_1^1 = \left\{ \boldsymbol{x}_1 \in \mathcal{X}_1 \ :\ e = e_1^2 = \theta_{\mathrm{sw}} + \theta_{\mathrm{st}} + 2\gamma \right\}, \tag{7.13c}$$

$$\boldsymbol{g} = \boldsymbol{g}_1^1 = \begin{bmatrix} \begin{bmatrix} 0 & 1 \\ 1 & 0 \end{bmatrix} \boldsymbol{q} \\ \boldsymbol{Q}^{+}(\boldsymbol{q})^{-1}\boldsymbol{Q}^{-}(\boldsymbol{q})\dot{\boldsymbol{q}} \end{bmatrix}, \tag{7.13d}$$

where, with the auxilary angle $\alpha(\boldsymbol{q}) = \theta_{\mathrm{st}} - \theta_{\mathrm{sw}}$,

$$\boldsymbol{M} = \begin{bmatrix} m_{\mathrm{h}} b^2 & -m_{\mathrm{l}} l_\circ b \cos(\alpha) \\ -m_{\mathrm{l}} l_\circ b \cos(\alpha) & (m_{\mathrm{h}} + m_{\mathrm{l}}) l_\circ^2 + m_\circ a^2 \end{bmatrix}, \tag{7.13e}$$

$$\boldsymbol{\eta} = \begin{bmatrix} -m_{\mathrm{l}} l_\circ b \sin(\alpha) \dot{\theta}_{\mathrm{st}}^2 \\ m_{\mathrm{l}} l_\circ b \sin(\alpha) \dot{\theta}_{\mathrm{sw}}^2 \end{bmatrix} + \begin{bmatrix} -m_{\mathrm{l}} b g \sin(\theta_{\mathrm{sw}}) \\ (m_{\mathrm{h}} l_\circ + m_{\mathrm{l}} a + m_{\mathrm{l}} l_\circ) g \sin(\theta_{\mathrm{st}}) \end{bmatrix}, \tag{7.13f}$$

$$\boldsymbol{B} = \begin{bmatrix} -1 \\ 1 \end{bmatrix}, \tag{7.13g}$$

$$\boldsymbol{Q}^{-} = \begin{bmatrix} 0 & (m_{\mathrm{h}} l_\circ^2 + 2 m_{\mathrm{l}} a l_\circ) \cos(\alpha) \\ 0 & 0 \end{bmatrix} - m_{\mathrm{l}} a b \begin{bmatrix} 1 & 1 \\ 0 & 1 \end{bmatrix}, \tag{7.13h}$$

$$\boldsymbol{Q}^{+} = \begin{bmatrix} m_{\mathrm{l}} b^2 & m_{\mathrm{l}} l_\circ^2 + m_{\mathrm{l}} a^2 + m_{\mathrm{h}} l_\circ^2 \\ m_{\mathrm{l}} b^2 & 0 \end{bmatrix} - m_{\mathrm{l}} b l_\circ \cos(\alpha) \begin{bmatrix} 1 & 1 \\ 0 & 1 \end{bmatrix}. \tag{7.13i}$$

Note that the relabeling of coordinates $[\theta_{\mathrm{sw}}\ \theta_{\mathrm{st}}] \rightarrow [\theta_{\mathrm{st}}\ \theta_{\mathrm{sw}}]$ in (7.13d) extends the half stride to a complete periodic motion. In addition to periodicity, we require the robot to walk with a given average speed v_{avg}, which is specified within a single operating condition ($n_\omega = 1$):

$$\omega = 2\sin\big(\theta_{\mathrm{sw}}(T) + \gamma\big) - v_{\mathrm{avg}}T. \tag{7.14}$$

(7.13c) and (7.14) constitute the equality constraint $\boldsymbol{h}\big(T, \boldsymbol{x}(T), \boldsymbol{x}(0); \sigma\big) = \mathbf{0}$ within the parameterized optimization problem $\mathcal{P}^1_\sigma$, where the parameter σ is set to either the slope γ or the averge speed v_{avg}. The objective in this example is to minimize the cost of transport, defined as

$$c = \frac{y(T)}{m_\circ g \Delta x}, \quad \text{where} \quad y(T) = \int_0^T \underbrace{\frac{k}{2}\, u(t)^2}_{=l(\boldsymbol{x},u)} \mathrm{d}t,\ \Delta x = v_{\mathrm{avg}}T, \tag{7.15}$$

and the constant $k = (m\sqrt{g l_\circ^3})^{-1}$ relates to the speed-torque gradient of a DC-motor. Note that the traveled distance Δx is typically strictly positive and bounded to ensure meaningful gaits with forward motion. As a result, the cost reaches its minimum value of zero only at passive optimal gaits, where $u \equiv 0$.

Remark 7.3.1. *With the stage cost defined as $l = {}^k\!/_2\, u^2$, the reconstruction of Lagrange multipliers at passive-optimal gaits (Section 6.2.2) becomes straightforward, as the vector $\tilde{\boldsymbol{b}}$ from* (6.27c) *vanishes. Consequently, from* (6.28)*, the costate $\boldsymbol{p}$ is zero at all times ($\boldsymbol{p} \equiv \mathbf{0}$). By inspection of* (6.29a)*, the Lagrange multiplier $\boldsymbol{\lambda}$ is also zero ($\boldsymbol{\lambda} = 0$). The remaining scalar costate q is reconstructed using* (6.24)*, yielding $q = (m_\circ g v_{\mathrm{avg}} T^*)^{-1}$.*

In the following, the passive optimal gaits of the compass-gait walker are leveraged to initialize Algorithm 1, generating optimal families of gaits within the parameterized TO problem $\mathcal{P}^1_\sigma$ (Section 7.3.2). Additionally, this workflow allows for a performance and accuracy comparison between the indirect and direct methods (Section 7.3.3). This comparison is extended to gait families that do not include passive gaits (Section 7.3.4).

Algorithm 1 is implemented in MATLAB with a tolerance of 10^{-8} for evaluating $\tilde{\boldsymbol{r}} = \mathbf{0}$. MATLAB's variable step-size integrator `ode15s` is used to solve the DAEs within $\boldsymbol{r}$, with relative and absolute tolerances of 10^{-9} and 10^{-10}, respectively. To ensure a fair comparison, the same settings are applied for solving the ODEs in the direct method. For simplicity, the Jacobians $\boldsymbol{R}$ are approximated using forward finite differences with a step size of 10^{-9}.

7.3.2 Passive to Active Walking via the Indirect Method

To demonstrate the exploratory potential of the indirect approach combined with numerical continuation, an initial library of gaits is generated based on the passive gaits of the compass-gait walker, similar to the work in Rosa et al. [117]. As detailed in Rosa and Lynch [115], passive gaits can be systematically derived from standing still (equilibrium) using PCC methods, with the slope γ varied as well. As shown in Fig. 7.6a, two distinct curves of passive gaits emerge from the standstill: one with a shorter period (T_{short}) and another with a longer period (T_{long}), corresponding to the swing leg taking a shorter or longer time to strike the ground, respectively. To generate a 1-D family of optimal gaits on a varying slope, the scalar continuation parameter is defined as $\sigma := \gamma$, while constraining the average speed to $v_{\mathrm{avg}} = 0.1\sqrt{gl_{\circ}}$. The Algorithm 1 is initialized with a passive gait at slope $\gamma_{\mathrm{l.}}$, which corresponds to the longer period (T_{long}) at $v_{\mathrm{avg}} = 0.1\sqrt{gl_{\circ}}$. This passive gait serves as the optimal passive solution, represented by the tuple $(T^*_{\mathrm{l.}}, \boldsymbol{x}^*_{\mathrm{l.}}(\cdot), u^*_{\mathrm{l.}}(\cdot))$, with zero input $u^*_{\mathrm{l.}} \equiv 0$ and cost $c = 0$ for the parameterized optimization problem $\mathcal{P}^1_{\gamma}$.

As noted in Remark 7.3.1, the reconstruction of the costates and Lagrange multipliers is straightforward. Thus, Algorithm 1 is initialized with

$$\boldsymbol{\chi}_{\mathrm{start}} = \begin{bmatrix} T_{\mathrm{start}} \\ \boldsymbol{x}_{0,\mathrm{start}} \\ \boldsymbol{p}_{0,\mathrm{start}} \\ q_{\mathrm{start}} \\ u_{0,\mathrm{start}} \\ \boldsymbol{\lambda}_{\mathrm{start}} \end{bmatrix} = \begin{bmatrix} T^*_{\mathrm{l.}} \\ \boldsymbol{x}^*_{\mathrm{l.}}(0) \\ \mathbf{0} \\ (m_{\circ} g v_{\mathrm{avg}} T^*_{\mathrm{l.}})^{-1} \\ 0 \\ \mathbf{0} \end{bmatrix}, \tag{7.16a}$$

$$\sigma_{\mathrm{start}} = \gamma_{\mathrm{l.}}, \tag{7.16b}$$

where $v_{\mathrm{avg}} = 0.1\sqrt{gl_{\circ}}$ is fixed throughout the algorithm. To generate a gait family that includes level-ground walking, the desired range of the slope parameter is set to $[\sigma_{\mathrm{start}}, \sigma_{\mathrm{end}}] = [\gamma_{\mathrm{l.}}, 0°]$. Figure 7.6a shows a projection of the gait family curve $\boldsymbol{r}^{-1}(\mathbf{0})$, depicted in orange, as the output of Algorithm 1. The orange curve also indicates an intersection with the other passive gait family, characterized by a shorter period (T_{short}). Figure 7.6b further illustrates how the initial costates $\boldsymbol{p}_0$ and input u_0 vanish at those slopes γ where a passive gait exists, corresponding to an average speed of $v_{\mathrm{avg}} = 0.1\sqrt{gl_{\circ}}$.

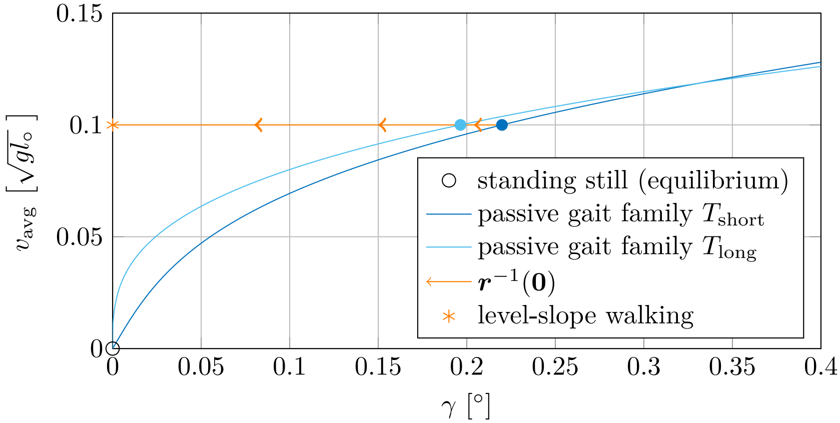

(a) The continuation towards level-ground walking, crossing two passive gaits.

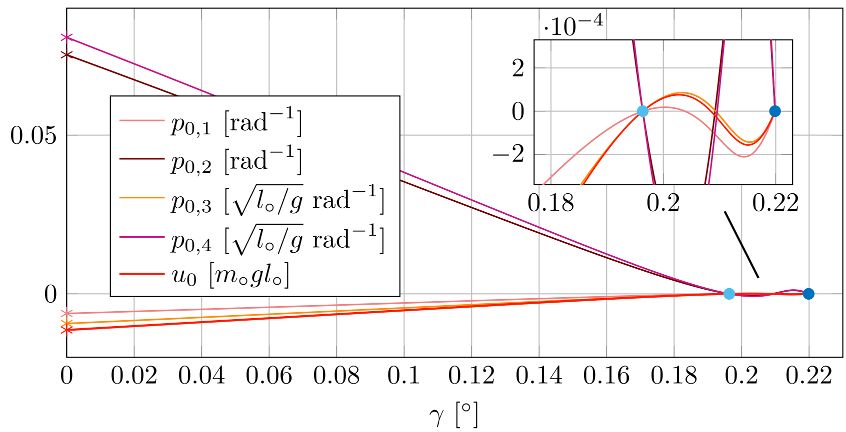

(b) The evolution of initial costates $\boldsymbol{p}_0$ and input u_0 within the implicit curve $\boldsymbol{r}^{-1}(\mathbf{0})$. At passive gaits ($u \equiv 0$), the costates vanish ($\boldsymbol{p} \equiv \mathbf{0}$).

Figure 7.6: Projections of the implicit curve $\boldsymbol{r}^{-1}(\mathbf{0})$, computed via Algorithm 1 with continuation parameter $\sigma := \gamma$. The curve corresponds to a fixed average speed of $v_{\text{avg}} = 0.1\sqrt{gl_\circ}$ and originates from the passive gait family with the shorter period time T_{short}. As the curve progresses towards level slope at $\gamma = 0°$ (marked by $*$), it intersects the passive gait family with the longer period time T_{long}. The filled circles indicate points where the passive and optimal gaits coincide.

7.3.3 Direct vs. Indirect Shooting

Building on the gait family $\boldsymbol{r}^{-1}(\mathbf{0})$ from the previous section, this section compares indirect and direct methods. The direct method uses a variable step-size shooting approach (MATLAB's `ode15s`), where the control input is defined as $\boldsymbol{u} := \hat{\boldsymbol{u}}(t, \boldsymbol{\xi})$. For comparison, a cubic B-spline and a Bézier curve are evaluated for varying n_ξ, as these parameterizations achieve high accuracy with relatively few parameters [84].

Input Parameterization

While the Bézier polynomial is implemented in its explicit form:

$$\hat{\boldsymbol{u}}(t, \boldsymbol{\xi}) = \sum_{j=1}^{n_\xi} \binom{n_\xi - 1}{j-1} (1-t)^{n_\xi - j} t^{j-1} \xi_j, \tag{7.17}$$

the cubic B-spline is defined by the recursion formula from deBoor, Cox, and Mansfield [Chapter 2.2 in [105]]:

$$\hat{\boldsymbol{u}}(t, \boldsymbol{\xi}) = \sum_{j=1}^{n_\xi} \mathcal{B}_{j-1, n_{\text{poly}}}(t) \xi_j, \tag{7.18a}$$

$$\mathcal{B}_{i,k}(t) = \frac{t - \tau_i}{\tau_{i+k} - \tau_i} \mathcal{B}_{i,k-1}(t) + \frac{\tau_{i+k+1} - t}{\tau_{i+k+1} - \tau_{i+1}} \mathcal{B}_{i+1,k-1}(t), \tag{7.18b}$$

$$\mathcal{B}_{i,0}(t) = \begin{cases} 1 & \text{if } \tau_i \leq t < \tau_{i+1}, \\ 0 & \text{otherwise,} \end{cases} \tag{7.18c}$$

where the polynomial degree $n_{\text{poly}} = 3$ corresponds to the cubic spline. Knot points τ_i are uniformly spaced with

$$\tau_i = (i - n_{\text{poly}}) \Delta t, \quad \forall i \in \{0, 1, \ldots, n_\tau - 1\}, \tag{7.18d}$$

where $\Delta t = {}^{T}\!/\!{}_{n_{\text{seg}}}$, $n_{\text{seg}} = n_\xi - n_{\text{poly}}$, and $n_\tau = 2n_{\text{poly}} + n_{\text{seg}}$.

Transcribing $\mathcal{P}_\sigma^1$ with $\boldsymbol{u} := \hat{\boldsymbol{u}}(t, \boldsymbol{\xi})$ yields first-order necessary conditions within $\hat{\boldsymbol{r}} : \mathbb{R}^{\hat{N}+1} \to \mathbb{R}^{\hat{N}}$, where $\hat{N} = 2n_{\text{x}} + n_\xi + 3$, as defined by (7.1).

Comparison: $\hat{\boldsymbol{r}}$ vs. $\boldsymbol{r}$

In accordance with [117], direct shooting with Algorithm 1 generates a family of gaits $\hat{\boldsymbol{r}}^{-1}(\mathbf{0})$, which includes both passive gaits and a level-ground walking gait in the parameter range $[\sigma_{\text{start}}, \sigma_{\text{end}}] = [\gamma_{1.}, 0°]$. As in implicit shooting (Section 7.3.2), the scalar continuation parameter is defined as $\sigma := \gamma$, while the average speed is constrained to $v_{\text{avg}} = 0.1\sqrt{g l_\circ}$.

Figures 7.7 and 7.8 compare direct ($\hat{\boldsymbol{r}}^{\square}$) and indirect ($\boldsymbol{r}^{\square}$) shooting for a locally optimal gait at level slope ($\gamma = 0°$) with $v_{\text{avg}} = 0.1\sqrt{g l_\circ}$.

To analyze and contrast the region of convergence, the condition numbers of $\boldsymbol{R}^{\square}$ and $\hat{\boldsymbol{R}}^{\square}$ are computed for varying input parameters n_ξ (Fig. 7.8a). While the condition number of the indirect method remains constant, as it is independent of the input parameterization, the condition number of $\hat{\boldsymbol{R}}^{\square}$ varies with n_ξ. The Bézier-based parameterization becomes highly sensitive to parameter variations as n_ξ increases. This sensitivity arises from the global nature of this parameterization, where adjusting a single parameter ξ_i in the vector $\boldsymbol{\xi}$ affects the entire shape of the input curve $\hat{\boldsymbol{u}}(t, \boldsymbol{\xi})$. As a result, for $n_\xi > 7$, Algorithm 1 stalled at certain points in traversing $\hat{\boldsymbol{r}}^{-1}(\mathbf{0})$, where Newton's method failed to converge due to the high sensitivities and the use of forward finite differences in computing $\hat{\boldsymbol{R}}$.

In contrast, cubic B-splines introduce $n_\xi - 3$ locally decoupled segments, so varying a single ξ_i only locally affects the input curve $\hat{\boldsymbol{u}}(t, \boldsymbol{\xi})$. This allows for arbitrarily large parameterizations without a blow-up in the condition number (Fig. 7.8a). Therefore, as the accuracy of approximating the control input space increases, cubic B-splines are much better suited. This is also evident in Fig.7.8b, where the relative cost error of direct shooting($^{\hat{c}-c}/_{c}$) decreases as n_ξ increases, with $\hat{c}$ approaching but remaining above the indirect cost c. Notably, Bézier polynomials and cubic B-splines yield the same cost at $n_\xi = 4$ since both describe a cubic curve. It is also worth noting that Bézier polynomials and cubic B-splines yield the same cost value at $n_\xi = 4$ since both describe a cubic curve. However, cubic B-splines are more computationally efficient due to their recursive formulation in (7.18). This plot of CPU times also highlights that indirect shooting can be significantly faster than direct shooting for large n_ξ.

Improvements

There is considerable room for improving efficiency, as the current implementation is in MATLAB. Beyond optimizing runtime by switching to a more efficient language like Julia or C++, both direct and indirect shooting approaches can be accelerated. For the direct method, alternative approaches exist for computing $\hat{\boldsymbol{r}}$ as discussed in Section 7.1. The indirect method can be significantly sped up by eliminating the input variable u_0 from $\boldsymbol{\chi}$. Often, the control input u can be explicitly expressed as a function of $\boldsymbol{x}$, $\boldsymbol{p}$, and q via $^{\partial \mathcal{H}}/_{\partial u} = 0$. With a stage cost $l = {}^{k}/_{2} u^2$ and the input-affine dynamics of the compass-gait walker, the input takes the form: $u = -\frac{1}{kq} \frac{\partial \boldsymbol{f}}{\partial u}^{\mathrm{T}} \boldsymbol{p}$. By eliminating the variable u_0, this step transforms the DAE into an ODE in $\boldsymbol{x}$ and $\boldsymbol{p}$, which can generally be solved more quickly.

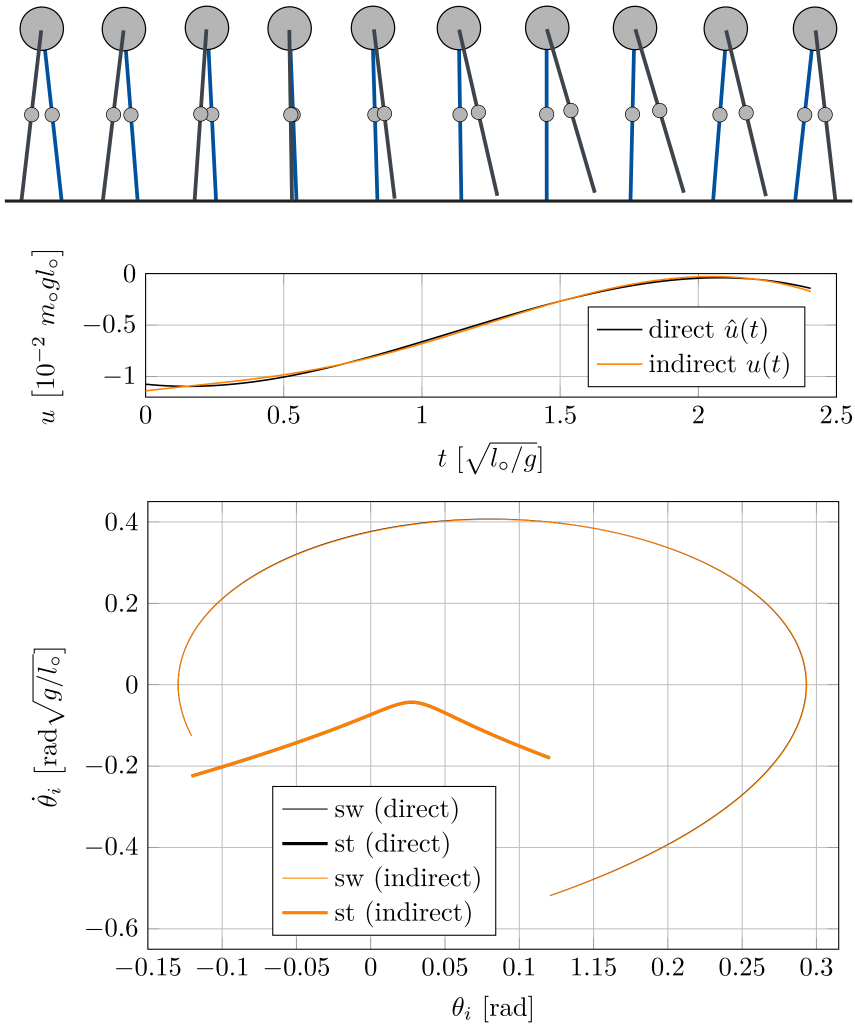

Figure 7.7: Visualization of an optimal walking gait at an average velocity of $v_{\text{avg}} = 0.1\sqrt{gl_\circ}$ on a level slope ($\gamma = 0°$). The keyframes depict the compass-gait walker, while the input and state trajectories (swing leg "sw" and stance leg "st") are shown for both the indirect (orange) and direct (black) shooting methods. The direct method uses a single cubic B-spline ($n_\xi = 4$).

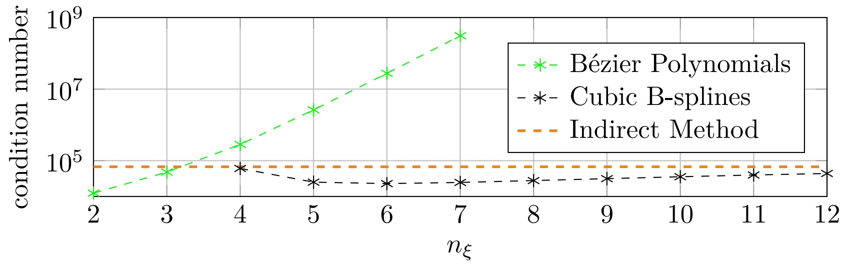

(a) Condition numbers of the indirect Jacobian ($\boldsymbol{R}^\square$) and direct Jacobian ($\hat{\boldsymbol{R}}^\square$). The direct method using Bézier polynomials fails to converge for $n_\xi > 7$ due to high sensitivity in $\boldsymbol{\xi}$ within the shooting problem.

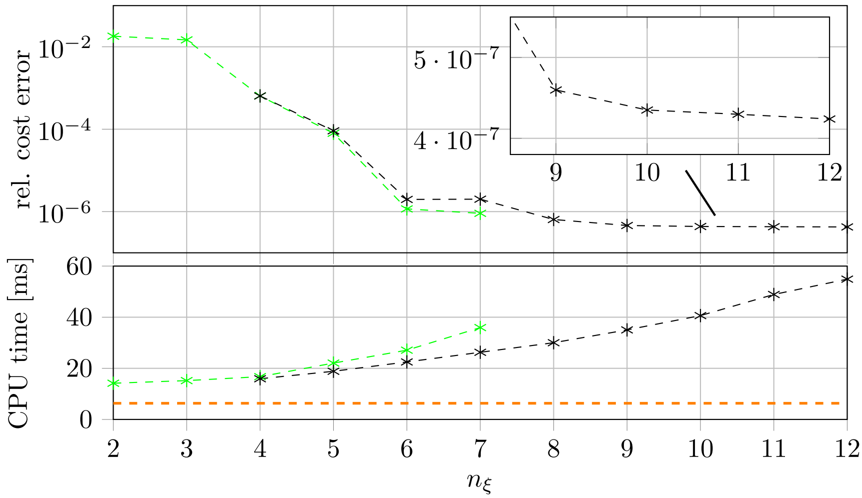

(b) Relative error $\frac{\hat{c}-c}{c}$ in the optimal cost between the direct method ($\hat{c}$) and the indirect method (c), along with the average CPU time over 1000 evaluations of the indirect function $\boldsymbol{r}^\square$ and the direct function $\hat{\boldsymbol{r}}^\square$.

Figure 7.8: Comparison of the direct ($\hat{\boldsymbol{r}}^\square$) and indirect ($\boldsymbol{r}^\square$) approaches in a MATLAB implementation on an Intel Core i5-8500 CPU @ 3.00GHz with 8GB RAM. The direct method parameterizes the input space with Bézier polynomials or cubic B-splines, introducing n_ξ variables. The data in a) and b) corresponds to level walking ($\gamma = 0°$) at an average speed of $v_{\text{avg}} = 0.1\sqrt{gl_\circ}$. The correspondig (locally) optimal gaits were generated via continuation from a passive gait using Algorithm 1, as shown in Fig. 7.6.

7.3.4 Generation of Additional Gait Families

In addition to the previous sections, the versatility and practical applicability of the proposed methods in legged locomotion are further demonstrated by generating a new family of optimal gaits that does not directly arise from passive dynamics. Specifically, the previously computed locally optimal gait at a level slope ($\gamma = 0°$) and average speed $v_{\text{avg}} = 0.1\sqrt{gl_\circ}$ initializes Algorithm 1 for the generation of a family of level walking gaits $\boldsymbol{r}^{-1}(\boldsymbol{0})$. Unlike before where the slope was varied, the slope is now fixed at $\gamma = 0°$, and speed is varied, acting as the continuation parameter $\sigma := v_{\text{avg}}$. This approach highlights the method's ability to adapt to different operating conditions, thus extending its relevance to practical robotic systems.

As shown in Fig. 7.9, the gait family (orange curve) is generated by running Algorithm 1 twice, with $\sigma_{\text{end}} = 0.01\sqrt{gl_\circ}$ and $\sigma_{\text{end}} = 0.4\sqrt{gl_\circ}$. In the latter case, tracing $\boldsymbol{r}^{-1}(\boldsymbol{0})$ involves four turning points in v_{avg}, resulting in multiple stationary gaits for certain ranges of v_{avg}. Without second-order conditions, the indirect method cannot distinguish between locally optimal points and saddle points in such cases, where $\mathcal{P}^1$ is non-convex.

While deriving second-order conditions for $\mathcal{P}^1$ is not covered here (Remark 6.2.2), the direct method provides a useful comparison, as sufficient conditions can be verified through the positive-definiteness of the Hessian $\hat{\boldsymbol{H}}$. The black curve in Fig. 7.9 shows projections from the direct shooting approach (points in $\hat{\boldsymbol{r}}^{-1}$) using a single cubic B-spline ($n_\xi = 4$). Solid lines indicate strict local minimizers, while dashed lines correspond to families of saddle points. When traversing the curve $\hat{\boldsymbol{r}}^{-1}$, the switch between minimizer and saddle point always occurs at turning points in v_{avg}.

Furthermore, the cost plot in Fig. 7.9 distinguishes good from bad local minima. Notably, similar to Fig. 7.8b, the indirect method consistently yields a lower cost value. This is due to the input space parametrization in the direct method, which can only approximate the true optimal solution, whereas the indirect method is more flexible, utilizing an adaptive step-size DAE solver.

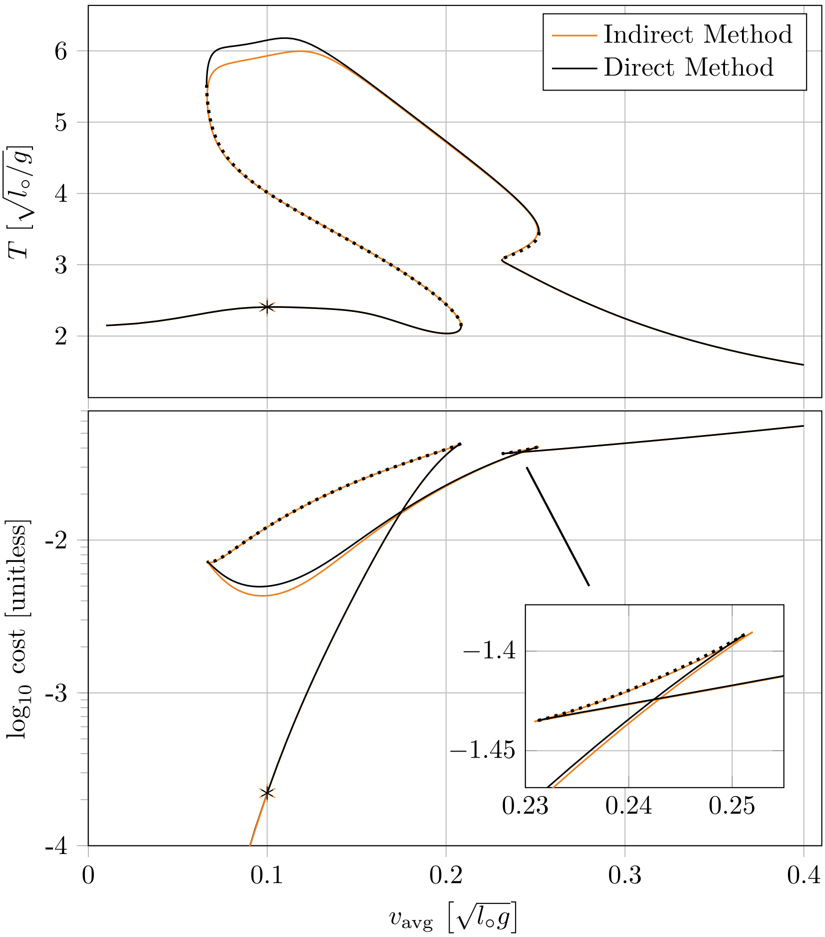

Figure 7.9: Projections of the implicit curves derived from the indirect method $\boldsymbol{r}^{-1}(\mathbf{0})$ and the direct method $\hat{\boldsymbol{r}}^{-1}(\mathbf{0})$, both computed using Algorithm 1 with the continuation parameter $\sigma := v_{\text{avg}}$. These curves represent level-slope walking ($\gamma = 0°$) and originate from an optimal gait at $v_{\text{avg}} = 0.1\sqrt{gl_\circ}$ (denoted by $*$). The indirect method consistently yields gaits with lower costs, whereas the direct method (utilizing cubic B-splines with $n_\xi = 4$) can distinguish local minima (solid black line) from saddle points (dotted black line) by applying second-order optimality conditions.

7.4 Summary

This section introduced a scalar ($\sigma \in \mathbb{R}$) parameterization of the TO problem, yielding $\mathcal{P}_\sigma^m$, which encodes a 1-D solution space of optimal periodic orbits. To numerically explore this space, both direct and indirect shooting methods were applied, implementing the first-order necessary conditions through parameterized root-finding problems of the form $\hat{\boldsymbol{r}}(\hat{\boldsymbol{\nu}}) = \mathbf{0}$ and $\boldsymbol{r}(\boldsymbol{\nu}) = \mathbf{0}$, respectively. Algorithm 1 facilitates the targeted generation of a continuous library of optimal trajectories within the range $\sigma \in [\sigma_{\text{start}}, \sigma_{\text{end}}]$ using PCC methods.

When applied to legged systems, different parameterizations of $\mathcal{P}_\sigma^m$ may include the robot's average speed $\sigma := v_{\text{avg}}$, the incline of a slope $\sigma := \gamma$, or modifications in the robot's dynamics, such as the dissipation parameter $\sigma := \varepsilon$ used for the model homotopy (Section 7.2). A key strategy in generating these optimal gait families is to start from known passive-optimal gaits at σ_{start}. This approach is particularly advantageous because libraries of passive-optimal gaits can be systematically generated from trivial solutions, such as a system's equilibria. According to the classification in Figure 1.1, Sections 7.2 and 7.3 examined two classes of passive dynamics:

1. Passive-*closed* dynamics ($\varepsilon = 0$), exemplified by a model homotopy of the planar monoped (Section 7.2).

2. Passive-*open* dynamics (γ_{passive}), exemplified by a compass-gait walker traversing down a slope (Section 7.3).

The model homotopy has the great potential to offer valuable insights into how the robot's morphology (e.g., value and distribution of spring stiffnesses) affects gait efficiency. This is achieved by continuously transitioning from passive-optimal gaits ($\sigma_{\text{start}} := \varepsilon_{\text{start}} = 0$) to optimal dissipative gaits ($\sigma_{\text{end}} := \varepsilon_{\text{end}} = 1$). However, while only the gaits at σ_{start} and σ_{end} are typically relevant for real legged robots in a model homotopy, the compass-gait walker example illustrates how passive-optimal gaits can be leveraged without modifying the system dynamics. Consequently, all generated gaits for $\sigma := \gamma$ are valuable and could potentially be implemented in a real legged system.

Beyond these two classes of passive dynamics, which provide passive-optimal gaits, Section 7.3.3 compared the direct ($\hat{\boldsymbol{r}}$) and indirect ($\boldsymbol{r}$) optimization methods. By evaluating both approaches on the compass-gait walker, the analysis demonstrated that indirect shooting achieves superior accuracy in generating optimal solutions while effectively addressing the inherent challenges of input space parameterization.

Chapter 8

Conclusions and Outlook

This dissertation has developed a theoretical and computational framework for analyzing and generating periodic orbits in hybrid dynamical systems (HDSs), with a focus on energy-optimal gaits in legged systems. Motivated by the observation that passive, unactuated motions are inherently optimal from an energy perspective, the work develops mathematical tools to uncover and extend families of such gaits. The monograph begins with foundational mathematical tools and introduces a general framework for recurrent time-variant and conservative HDSs, establishing conditions for the existence of periodic orbits via first integrals and Poincaré maps. Building on this, energetically conservative models (ECMs) are constructed, enabling the use of continuation methods to explore passive gait families. These insights are then embedded in a trajectory optimization framework, defining passive-optimal solutions and extending necessary conditions for both direct and indirect shooting methods. Finally, the dissertation formulates parameterized trajectory optimization problems and introduces a model homotopy approach that bridges passive and actuated dynamics.

While these contributions represent a coherent progression from theoretical foundations to practical algorithmic tools, there remains substantial opportunity for further advancement in understanding, generating, and optimizing economical locomotion patterns and other non-smooth periodic orbits. The following sections synthesize the implications of the presented work, outline its limitations, and discuss promising directions for future research.

8.1 Discussion

The exemplary models within this monograph to which the proposed methodologies were applied are summarized in Figure 8.1, organized according to the system classification introduced in Figure 1.1. A central insight linking these four system classes is the concept of defining passive gaits as globally optimal actuated gaits, referred to as *passive-optimal*.

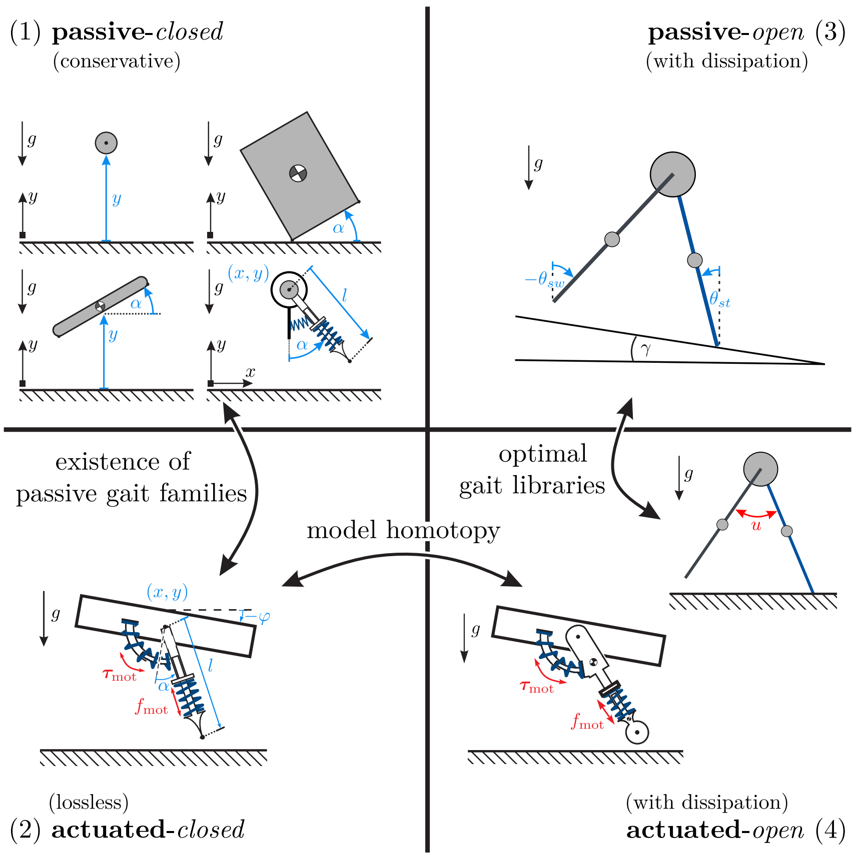

Figure 8.1: Classification of the models discussed in this monograph into the four categories introduced in Figure 1.1, based on energy transfer through the environment (closed or open) and actuator work (passive or actuated).

8.1.1 Extending the Idea of Passive-Optimality

This monograph has formally defined a class of economic cost functions for passive-optimal gaits in *lossless* systems (Section 7.2.2). In these systems, most economic cost functions associated with a passive gait define a strict global optimum: an isolated orbit corresponding to zero cost. The main exception is the mechanical actuator work cost function, where the passive-optimal gait represents only a weak minimizer (Remark 7.2.1).

An important consideration is how this class of economic cost functions applies to more general passive-open systems, such as passive dynamic walkers. Although not explicitly addressed until now, it is clear in the case of input-squared costs (copper losses) that any actuation is penalized, making passive gaits globally optimal across all types of systems. This was demonstrated for the compass-gait walker in Section 7.3, where optimally actuated gait families were derived from passive gaits. For other cost functions, however, global optimality is less straightforward to define. Passive dynamic walkers, in particular, harvest energy from gravity to compensate for losses and achieve limit cycles. In such systems, minimizing mechanical actuator work no longer favors passive gaits. In fact, the optimal cost becomes negative, as the ideal actuation policy would exploit the gravitational energy injection to produce as much negative actuator work as possible.

Complexity of Passive Models

Beyond exploring various economic costs in passive-open dynamics, the system class itself can be generalized to enable a deeper investigation of natural dynamics. Inspired by the periodic motion concept of Krack [79], one could imagine replacing the incline (slope) with alternative forms of artificial or environmental energy input to enable passive gaits. This strategy offers the potential to extend systematic studies of passive dynamics to more complex, higher-dimensional models.

The methods presented in this monograph, particularly the PCC framework, are largely applicable to more complex dynamics, as demonstrated by Rosa and Lynch [116]. Nevertheless, a more generalized approach could overcome some of the limitations, particularly those associated with ECMs.

One notable limitation is the derivation of ECMs, which often involves a cumbersome scaling procedure (see Chapter 5) and does not scale well for systems with a large number of DoFs. Although this monograph highlights the explanatory power of ECMs, especially their ability to intrinsically form families of passive gaits, their simplicity also creates a significant gap between these models and realistic legged systems.

The Importance of Dissipation

Throughout this monograph, energy losses such as damping, friction, and collisions have primarily been considered undesirable, as they dissipate the system's energy and must be counteracted by energy-consuming (and therefore inefficient) actuation. While engineers typically aim to minimize dissipation in robotic systems, it cannot be entirely eliminated due to the second law of thermodynamics.

However, dissipation can also be beneficial. When strategically exploited, it contributes to the stabilization of locomotion, as seen in the limit cycles of passive dynamic walkers. In this way, dissipation serves as a passive energy exchange mechanism that supports robustness in locomotion [56].

Moreover, dissipation can simplify the dynamics of legged robots by damping out high-frequency internal oscillations, which would otherwise complicate the search for periodic orbits. Consider, for example, a hopper with a spring-loaded leg: if fast leg oscillations are not damped, determining the precise moment of foot touch-down becomes significantly more difficult. Hence, simplified models such as the SLIP model assume a constant leg length. This property was explored in this monograph as an outcome of reducing the foot mass to zero. From another perspective, this property can also be justified by considering strong damping in the leg during flight, effectively reducing the system's dynamics onto a slow manifold [87].

8.1.2 Toward Global Gait Libraries

In the generation of parameterized families of optimal gaits, passive-optimal orbits provide ideal starting points. However, due to the non-convex nature of the optimization problem, a passive-optimal gait is often not unique for a given operating point. This means that multiple equally optimal gaits may exist to initialize the generation of a user-defined gait library.

An important open question therefore arises: how should the best seed for the gait library be selected, and does this choice guarantee global optimality for all actuated gaits within the library? Once the gait family moves beyond the passive regime, it becomes unclear how actuation influences the associated cost. This challenge is particularly evident in Algorithm 1, where it remains uncertain whether a passive gait at σ_{start} can be smoothly continued to the desired optimally actuated gait at σ_{end}.

In general, there is no guarantee that a globally optimal orbit is continuously connected to a passive gait or equilibrium. Understanding the conditions under which such a connection can be established remains an open research question.

Discontinuous Gait Families

The issue of disjoint solution sets already appears within the space of passive gaits. One reason for such discontinuities is a change in the contact sequence, or footfall pattern. The Delassus matrix provides the tool to study this behavior. In general, the order of contacts is not commutative due to inertial coupling within the system's contact space [20, 103].

In the case of ECMs, scaling the system's masses and inertias causes the inverse Delassus matrix to vanish (Chapter 5). This condition permits the commutation of contact order. As a result, gaits with different footfall patterns (such as walking and running) may connect continuously through bifurcation points, as demonstrated by the SLIP-like biped in [43].

Another cause of disjoint orbit sets is the activation of inequality constraints intended to prevent grazing events and zero phase durations, as defined in Assumptions *As2* and *As3*. In this monograph, the issue was resolved by adopting a time-based approach, which allowed for the continuous connection of solution sets, even in the presence of grazing or vanishing phase durations.

This approach may be seen as a general strategy for connecting otherwise disjoint solution sets caused by the activation of inequality constraints. The same strategy can be extended to stationary and optimal gait families, particularly when additional path constraints or second-order optimality conditions are imposed. In this work, the inequality constraint associated with second-order optimality was not enforced. This allowed locally optimal orbits to connect continuously through saddle points as shown in the compass-gait walker example (Figure 7.9).

Nevertheless, this strategy may not be sufficient to connect all disjoint solution sets. In such cases, an alternative is to explicitly allow discontinuities or "jumps" when using PCC methods. Guddat et al. [53] propose a *jump* algorithm to overcome turning points. They also describe how PCC methods can be adapted to handle changes in the active constraint set. This is particularly relevant when using inequality constraints on the system dynamics. In this modified approach, the predictor anticipates changes in the active set, while the corrector step is performed by a standard NLP solver. This implementation has proven highly effective in tracing optimal gaits using direct methods [118].

While inequalities can be readily incorporated into the direct method, for example to represent path constraints or enforce second-order optimality, extending the indirect approach to handle these cases remains an open area of research.

Extending the Indirect Approach

Incorporating inequality constraints, such as joint limits or actuator torque bounds, into the indirect method requires dividing the time domain into subarcs. Within each subarc, constraints are either active or inactive, as described by [14]. This could also be addressed by introducing a multiple shooting scheme. A major challenge in this context is the unknown number and order of subarcs, which complicates the application of variable step-size shooting methods. Developing strategies to handle this complexity would significantly enhance the versatility of the indirect method and broaden its applicability to more complex, real-world systems where inequality constraints are critical.

Furthermore, the first-order necessary conditions derived in this work are currently tailored to TO problems of simple hybrid systems ($\mathcal{P}^1$), characterized by a single continuous and a single discrete dynamic map. A critical direction for future research involves extending these conditions to address more complex locomotion patterns, such as running or walking with a double support phase, where foot lift-off and touch-down do not occur simultaneously. Such extensions would require incorporating kinetic events (such as a foot leaving the ground when ground reaction forces reach zero) into the event definitions. Currently, our event functions are solely defined kinematically or by time, but this extension would necessitate incorporating actuation inputs ($\boldsymbol{u}$) into the definition of the event function. Moreover, the introduction of multiple hybrid phases would convert the current two-point boundary problem into a multi-point boundary problem. This transformation could be effectively addressed using a multiple shooting approach, where the initial shooting conditions align with the image of the discrete (reset) maps.

8.1.3 Other Promising Methodologies

In addition to the presented approaches that use PCC methods to generate gait families and solve TO problems for energy-efficient locomotion, several other promising directions remain to be explored.

One fundamentally different approach to exploiting natural dynamics in legged systems, without relying on optimization, is based on *nonlinear normal modes* (NNMs). NNMs extend the concept of invariant linear modes to general nonlinear dynamics [2, 73]. In this framework, controllers are designed to constrain the system to move along invariant manifolds, which are derived from the system's underlying conservative (lossless) dynamics [120, 121].

Although the extension of NNMs to non-smooth (hybrid) dynamics is challenging, it offers an optimization-free approach of leveraging a system's natural dynamics. In particular, it does not depend on the choice of economic cost functions as in the TO problem. Furthermore, by design the NNM approach inherently provides a stabilizing feedback control law.

Stability of Economic Gaits

This monograph focused exclusively on energy-optimal open-loop trajectories. However, implementing these periodic orbits on real legged systems requires feedback control to ensure robust locomotion in the presence of environmental disturbances and model uncertainties.

In general, energy optimality and robustness are competing objectives, especially in inherently unstable bipedal systems [80]. Nonetheless, selecting passive-optimal gaits with larger stability margins can reduce the efforts of an active feedback controller. To assess the region of convergence around a limit cycle, the method introduced by Manchester et al. [90] may be particularly useful.

Beyond the straightforward approach of adding an asymptotic feedback controller to open-loop trajectories, *differential dynamic programming* (DDP) offers a more compact and potentially more insightful alternative [133]. DDP not only computes an optimal trajectory but also produces a locally linear feedback control law. Since DDP has already been successfully applied to generate optimal gait libraries [86], it appears to be a promising methodology for further exploration of natural dynamics in legged systems.

8.2 Conclusion

The central theme of this dissertation is the development of systematic approaches for generating energetically optimal gaits in legged systems, with a strong emphasis on exploring their natural dynamics. Together, these contributions form a coherent progression from theory to algorithmic tools. They offer a unified methodology for understanding, generating, and optimizing economical locomotion patterns and other non-smooth periodic orbits in both conservative and dissipative HDSs.

While much remains to be understood, this work offers an initial step toward uncovering the connection between morphology and motion. It is hoped that the ideas and methods developed here may serve as a useful foundation for future efforts in designing and controlling efficient legged systems.

Appendix **A**

The Saltation Matrix in Autonomous Hybrid Dynamics

The saltation matrix describes how changes in the trajectory are propagated from phase i into $i+1$. In autonomous HDS, satisfying Assumptions *As2* and *As3*, the saltation matrix takes the form

$$\boldsymbol{S}_i^{i+1} = \boldsymbol{G}_i^{i+1} + \frac{\left(\boldsymbol{f}_{i+1}^{+} - \boldsymbol{G}_i^{i+1}\boldsymbol{f}_i^{-}\right) De_i^{i+1}}{De_i^{i+1}\boldsymbol{f}_i^{-}}, \tag{A.1}$$

where the following shorthand notation is used:

$$\boldsymbol{x}_i^{-} := \boldsymbol{x}_i(t_i^{\mathcal{E}}(\bar{\boldsymbol{x}}_i)), \quad \boldsymbol{x}_{i+1}^{+} := \bar{\boldsymbol{x}}_{i+1} \overset{(4.2\text{b})}{=} \boldsymbol{g}_i^{i+1}(\boldsymbol{x}_i^{-}), \quad \boldsymbol{G}_i^{i+1} := \left.\frac{\partial \boldsymbol{g}_i^{i+1}(\boldsymbol{x}_i)}{\partial \boldsymbol{x}_i}\right|_{\boldsymbol{x}_i^{-}},$$

$$\boldsymbol{f}_i^{-} := \boldsymbol{f}_i(\boldsymbol{x}_i^{-}), \qquad \boldsymbol{f}_{i+1}^{+} := \boldsymbol{f}_{i+1}(\boldsymbol{x}_{i+1}^{+}), \qquad De_i^{i+1} := \left.\frac{\partial e_i^{i+1}(\boldsymbol{x}_i)}{\partial \boldsymbol{x}_i}\right|_{\boldsymbol{x}_i^{-}}.$$

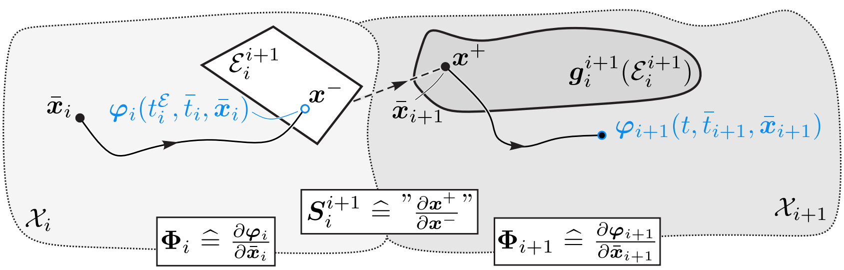

Figure A.1: A nominal trajectory propagating from phase i into $i+1$.

A.1 Construction of the Saltation Matrix

In the following, the saltation matrix $\boldsymbol{S}_i^{i+1}$ is constructed through calculus via the implicit function theorem (Section A.1.1) and from a geometric perspective using first-order perturbations (Section A.1.2). These derivations build on the work of [76, 82, 96]. While the presented $\boldsymbol{S}_i^{i+1}$ applies to autonomous Σ, its extension to time-variant Σ is straightforward.

A.1.1 Applying the Implicit Function Theorem

This approach derives (A.1) using local derivatives of the hybrid flow in phases i and $i+1$. Specifically, the total derivative of the phase flow $\boldsymbol{x}_{i+1}(t) = \boldsymbol{\varphi}_{i+1}(t, \bar{t}_{i+1}, \bar{\boldsymbol{x}}_{i+1})$ with respect to $\bar{\boldsymbol{x}}_i$ is computed. For the time $t \in [\bar{t}_{i+1}, \bar{t}_{i+1} + t_{i+1}^{\mathcal{E}})$ in phase $i+1$, where $\bar{t}_{i+1} = t_i^{\mathcal{E}}(\bar{\boldsymbol{x}}_i)$ is well-defined under Assumption *As2* (Remark 4.1.1) and strictly greater than $\bar{t}_i$ (Assumption *As3*), this derivative takes the form:

$$
\begin{aligned}
\frac{\mathrm{d}}{\mathrm{d}\bar{\boldsymbol{x}}_i}\boldsymbol{x}_{i+1}(t) = {} & \frac{\mathrm{d}}{\mathrm{d}\bar{\boldsymbol{x}}_i}\boldsymbol{\varphi}_{i+1}\left(t, t_i^{\mathcal{E}}(\bar{\boldsymbol{x}}_i), \boldsymbol{g}_i^{i+1} \circ \boldsymbol{\varphi}_i\left(t_i^{\mathcal{E}}(\bar{\boldsymbol{x}}_i), \bar{t}_i, \bar{\boldsymbol{x}}_i\right)\right) \\
\overset{\text{c.r.}}{=} {} & \left.\frac{\partial \boldsymbol{\varphi}_{i+1}}{\partial t}\right|_{(t, \bar{t}_{i+1}, \boldsymbol{x}_{i+1}^{+})} \left.\frac{\partial(t-\tau)}{\tau}\right|_{t_i^{\mathcal{E}}} \frac{\partial t_i^{\mathcal{E}}(\bar{\boldsymbol{x}}_i)}{\partial \bar{\boldsymbol{x}}_i} \\
& + \left.\frac{\partial \boldsymbol{\varphi}_{i+1}}{\partial \boldsymbol{x}}\right|_{(t, \bar{t}_{i+1}, \boldsymbol{x}_{i+1}^{+})} \left.\frac{\partial \boldsymbol{g}_i^{i+1}}{\partial \boldsymbol{x}}\right|_{\boldsymbol{x}_i^{-}} \frac{\mathrm{d}\boldsymbol{\varphi}_i\left(t_i^{\mathcal{E}}(\bar{\boldsymbol{x}}_i), \bar{t}_i, \bar{\boldsymbol{x}}_i\right)}{\mathrm{d}\bar{\boldsymbol{x}}_i} \\
\overset{(4.10\text{a})}{=} {} & -\boldsymbol{\Phi}_{i+1}(t, \bar{t}_{i+1}, \boldsymbol{x}_{i+1}^{+}) \boldsymbol{f}_{i+1}^{+} \frac{\partial t_i^{\mathcal{E}}(\bar{\boldsymbol{x}}_i)}{\partial \bar{\boldsymbol{x}}_i} \\
& + \boldsymbol{\Phi}_{i+1}(t, \bar{t}_{i+1}, \boldsymbol{x}_{i+1}^{+}) \boldsymbol{G}_i^{i+1} \frac{\mathrm{d}}{\mathrm{d}\bar{\boldsymbol{x}}_i}\boldsymbol{x}_i(\bar{t}_{i+1}),
\end{aligned}
\tag{A.2}
$$

where the chain rule is applied at c.r., and Lemma 4.1.2 is used along with the flow property $\boldsymbol{f}_{i+1}(\boldsymbol{x}_{i+1}(t)) = \boldsymbol{\Phi}_{i+1}(t, \bar{t}_{i+1}, \boldsymbol{x}_{i+1}^{+})\boldsymbol{f}_{i+1}(\boldsymbol{x}_{i+1}^{+})$. The remaining total derivative in (A.2) takes the form

$$
\begin{aligned}
\frac{\mathrm{d}}{\mathrm{d}\bar{\boldsymbol{x}}_i}\boldsymbol{x}_i(\bar{t}_{i+1}) &= \frac{\mathrm{d}}{\mathrm{d}\bar{\boldsymbol{x}}_i}\boldsymbol{\varphi}_i\left(t_i^{\mathcal{E}}(\bar{\boldsymbol{x}}_i), \bar{t}_i, \bar{\boldsymbol{x}}_i\right) \\
&\overset{\text{c.r.}}{=} \left.\frac{\partial \boldsymbol{\varphi}_i}{\partial t}\right|_{(\bar{t}_{i+1}, \bar{t}_i, \bar{\boldsymbol{x}}_i)} \frac{\partial t_i^{\mathcal{E}}(\bar{\boldsymbol{x}}_i)}{\partial \bar{\boldsymbol{x}}_i} + \left.\frac{\partial \boldsymbol{\varphi}_i}{\partial \boldsymbol{x}}\right|_{(t_i^{\mathcal{E}}, \bar{t}_i, \bar{\boldsymbol{x}}_i)} \\
&= \boldsymbol{f}_i^{-} \frac{\partial t_i^{\mathcal{E}}(\bar{\boldsymbol{x}}_i)}{\partial \bar{\boldsymbol{x}}_i} + \boldsymbol{\Phi}_i(t_i^{\mathcal{E}}, \bar{t}_i, \bar{\boldsymbol{x}}_i).
\end{aligned}
\tag{A.3}
$$

Introducing additional shorthand notation

$$\boldsymbol{\Phi}_{i+1} := \boldsymbol{\Phi}_{i+1}(t, \bar{t}_{i+1}, \boldsymbol{x}_{i+1}^{+}), \quad \boldsymbol{\Phi}_{i} := \boldsymbol{\Phi}_{i}(\bar{t}_{i+1}, \bar{t}_{i}, \bar{\boldsymbol{x}}_{i}), \quad Dt_i^{\mathcal{E}} := \frac{\partial t_i^{\mathcal{E}}(\bar{\boldsymbol{x}}_i)}{\partial \bar{\boldsymbol{x}}_i},$$

and plugging (A.3) into (A.2), yields

$$\frac{\mathrm{d}}{\mathrm{d}\bar{\boldsymbol{x}}_i}\boldsymbol{\varphi}_{i+1} = \boldsymbol{\Phi}_{i+1}\Big(\left(\boldsymbol{G}_i^{i+1}\boldsymbol{f}_i^{-} - \boldsymbol{f}_{i+1}^{+}\right) Dt_i^{\mathcal{E}} + \boldsymbol{G}_i^{i+1}\boldsymbol{\Phi}_i \Big). \tag{A.4}$$

The switching time derivative $Dt_i^{\mathcal{E}}$ in (A.4) is well-defined due to Assumption *As2* and the implicit function theorem. Hence, the total derivative of the event function e_i^{i+1} yields

$$\begin{aligned} & e_i^{i+1}\Big(\boldsymbol{\varphi}_i\left(t_i^{\mathcal{E}}(\bar{\boldsymbol{x}}_i), \bar{t}_i, \bar{\boldsymbol{x}}_i\right)\Big) = 0 \quad \forall \bar{\boldsymbol{x}}_i \in \tilde{\mathcal{X}}_i, \\ \Rightarrow\ & \frac{\mathrm{d}}{\mathrm{d}\bar{\boldsymbol{x}}_i} e_i^{i+1} \circ \boldsymbol{\varphi}_i\left(t_i^{\mathcal{E}}(\bar{\boldsymbol{x}}_i), \bar{t}_i, \bar{\boldsymbol{x}}_i\right) = 0, \\ \Leftrightarrow\ & De_i^{i+1} \cdot \underbrace{\left(\boldsymbol{f}_i^{-} Dt_i^{\mathcal{E}} + \boldsymbol{\Phi}_i\right)}_{(\text{A.3})} = 0, \\ \Rightarrow\ & Dt_i^{\mathcal{E}} = -\frac{De_i^{i+1}}{De_i^{i+1}\boldsymbol{f}_i^{-}}\boldsymbol{\Phi}_i, \end{aligned} \tag{A.5}$$

where $\tilde{\mathcal{X}}_i \subset \mathcal{X}_i$, since $\tilde{\mathcal{X}}_i = \mathcal{X}_0$ when $i = 1$ and otherwise $\tilde{\mathcal{X}}_i = \boldsymbol{g}_{i-1}^{i}(\mathcal{E}_{i-1}^{i})$. Finally, plugging the switching time derivative (A.5) into (A.4), yields the desired structure

$$\frac{\mathrm{d}}{\mathrm{d}\bar{\boldsymbol{x}}_i}\boldsymbol{x}_{i+1}(t) = \boldsymbol{\Phi}_{i+1}\boldsymbol{S}_i^{i+1}\boldsymbol{\Phi}_i,$$

where the saltation matrix $\boldsymbol{S}_i^{i+1}$ takes the form reported in (A.1).

A.1.2 Using First-Order Perturbations

To obtain first-order sensitivity information with respect to $\bar{\boldsymbol{x}}_i$, an initial perturbation $\delta\bar{\boldsymbol{x}}_i \in \mathbb{R}^{n_{\mathrm{x},i}}$, with $\varepsilon \ll 1$ is introduced, defining the perturbed initial state as $\tilde{\bar{\boldsymbol{x}}}_i := \bar{\boldsymbol{x}}_i + \varepsilon\delta\bar{\boldsymbol{x}}_i$. This infinitesimal perturbation alters the event activation time, resulting in $\tilde{\bar{t}}_{i+1} := t_i^{\mathcal{E}}(\tilde{\boldsymbol{x}}_i)$. With the nominal activation time $\bar{t}_{i+1} := t_i^{\mathcal{E}}(\bar{\boldsymbol{x}}_i)$, the resulting time variation $\varepsilon\delta t := \tilde{\bar{t}}_{i+1} - \bar{t}_{i+1}$ can be either positive or negative, leading to two distinct cases illustrated in Figures A.2 and A.3. In both scenarios, the saltation matrix is constructed through $\boldsymbol{S}_i^{i+1} = {}^{\delta\boldsymbol{x}_{i+1}^{+}}/_{\delta\boldsymbol{x}_i^{-}}$, where $\delta\boldsymbol{x}_i^{-}$ and $\delta\boldsymbol{x}_{i+1}^{+}$ represent the state differences before and after the event, respectively, as a result of the initial state perturbation $\delta\bar{\boldsymbol{x}}_i$.

Positive Time Variation ($\delta t > 0$)

As shown in Figure A.2, the infinitesimal state differences before and after the event are defined as follows:

$$\varepsilon\delta\boldsymbol{x}_i^- = \tilde{\boldsymbol{x}}_i(\bar{t}_{i+1}) - \boldsymbol{x}_i^-, \tag{A.6a}$$
$$\varepsilon\delta\boldsymbol{x}_{i+1}^+ = \tilde{\boldsymbol{x}}_{i+1}(\bar{t}_{i+1}+\varepsilon\delta t) - \boldsymbol{x}_{i+1}(\bar{t}_{i+1}+\varepsilon\delta t). \tag{A.6b}$$

To locally construct $\boldsymbol{S}_i^{i+1}$, all terms involving δt are expanded to their first-order approximation in the vicinity of the event:

$$\begin{aligned}
\tilde{\boldsymbol{x}}_i(\bar{t}_{i+1}+\varepsilon\delta t) &= \tilde{\boldsymbol{x}}_i(\bar{t}_{i+1}) + \boldsymbol{f}_i\big(\tilde{\boldsymbol{x}}_i(\bar{t}_{i+1})\big)\varepsilon\delta t + \mathcal{O}(\varepsilon^2) \qquad \text{(A.7a)}\\
&\overset{\text{(A.6a)}}{=} \boldsymbol{x}_i^- + \varepsilon\delta\boldsymbol{x}_i^- + \boldsymbol{f}_i\big(\boldsymbol{x}_i^- + \varepsilon\delta\boldsymbol{x}_i^-\big)\varepsilon\delta t + \mathcal{O}(\varepsilon^2)\\
&= \boldsymbol{x}_i^- + \varepsilon\delta\boldsymbol{x}_i^- + \underbrace{\boldsymbol{f}_i\big(\boldsymbol{x}_i^-\big)}_{=\boldsymbol{f}_i^-}\varepsilon\delta t + \mathcal{O}(\varepsilon^2),\\
e_i^{i+1}\big(\tilde{\boldsymbol{x}}_i(\bar{t}_{i+1}+\varepsilon\delta t)\big) &\overset{\text{(A.7a)}}{=} e_i^{i+1}\big(\boldsymbol{x}_i^- + \varepsilon\delta\boldsymbol{x}_i^- + \boldsymbol{f}_i^-\varepsilon\delta t\big) + \mathcal{O}(\varepsilon^2) \qquad \text{(A.7b)}\\
&= \underbrace{e_i^{i+1}(\boldsymbol{x}_i^-)}_{=0} + De_i^{i+1}\cdot\big(\varepsilon\delta\boldsymbol{x}_i^- + \boldsymbol{f}_i^-\varepsilon\delta t\big) + \mathcal{O}(\varepsilon^2),\\
\tilde{\boldsymbol{x}}_{i+1}(\bar{t}_{i+1}+\varepsilon\delta t) &= \boldsymbol{g}_i^{i+1}\big(\tilde{\boldsymbol{x}}_i(\bar{t}_{i+1}+\varepsilon\delta t)\big) \qquad \text{(A.7c)}\\
&\overset{\text{(A.7a)}}{=} \boldsymbol{g}_i^{i+1}\big(\boldsymbol{x}_i^- + \varepsilon\delta\boldsymbol{x}_i^- + \boldsymbol{f}_i^-\varepsilon\delta t\big) + \mathcal{O}(\varepsilon^2)\\
&= \underbrace{\boldsymbol{g}_i^{i+1}(\boldsymbol{x}_i^-)}_{=\boldsymbol{x}_{i+1}^+} + \boldsymbol{G}_i^{i+1}\big(\varepsilon\delta\boldsymbol{x}_i^- + \boldsymbol{f}_i^-\varepsilon\delta t\big), + \mathcal{O}(\varepsilon^2)\\
\boldsymbol{x}_{i+1}(\bar{t}_{i+1}+\varepsilon\delta t) &= \boldsymbol{x}_{i+1}^+ + \boldsymbol{f}_{i+1}^+\varepsilon\delta t + \mathcal{O}(\varepsilon^2). \qquad \text{(A.7d)}
\end{aligned}$$

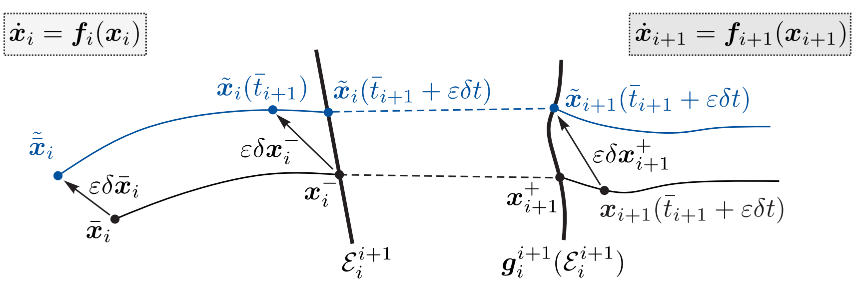

Figure A.2: Illustration of a perturbed flow reaching the event manifold $\mathcal{E}_i^{i+1}$ at time $\tilde{\bar{t}}_{i+1}$ later than the nominal flow, resulting in $\varepsilon\delta t := \tilde{\bar{t}}_{i+1} - \bar{t}_{i+1} > 0$.

With (A.7c) and (A.7d), taking $\varepsilon \to 0$, the post-event state difference (A.6b) can be expanded to its first-order as

$$\delta \boldsymbol{x}_{i+1}^{+} = \boldsymbol{G}_i^{i+1}\delta \boldsymbol{x}_i^{-} + \left(\boldsymbol{G}_i^{i+1}\boldsymbol{f}_i^{-} - \boldsymbol{f}_{i+1}^{+}\right)\delta t. \tag{A.8}$$

When the perturbed flow reaches the event manifold, it satisfies, $e_i^{i+1}\left(\tilde{\boldsymbol{x}}_i(\bar{t}_{i+1} + \delta t)\right) = 0$, allowing the time variation δt to be computed from (A.7b):

$$\delta t = -\frac{De_i^{i+1}\delta \boldsymbol{x}_i^{-}}{De_i^{i+1}\boldsymbol{f}_i^{-}}, \tag{A.9}$$

where $\varepsilon \to 0$. Geometrically, setting (A.7b) to zero implies that the vector $\tilde{\boldsymbol{x}}_i(\bar{t}_{i+1} + \varepsilon\delta t) - \boldsymbol{x}_i^{-}$ is locally tangent to $\mathcal{E}_i^{i+1}$ and thus orthogonal to De_i^{i+1}. Plugging (A.9) into (A.8) yields the saltation matrix $\boldsymbol{S}_i^{i+1} = {}^{\delta \boldsymbol{x}_{i+1}^{+}}/_{\delta \boldsymbol{x}_i^{-}}$ reported in (A.1).

Negative Time Variation ($\delta t < 0$)

Similar to the previous case, the infinitesimal state differences before and after the event (Figure A.3) are defined as follows:

$$\varepsilon\delta \boldsymbol{x}_i^{-} = \tilde{\boldsymbol{x}}_i(\bar{t}_{i+1} + \varepsilon\delta t) - \boldsymbol{x}_i(\bar{t}_{i+1} + \varepsilon\delta t), \tag{A.10a}$$

$$\varepsilon\delta \boldsymbol{x}_{i+1}^{+} = \tilde{\boldsymbol{x}}_{i+1}(\bar{t}_{i+1}) - \boldsymbol{x}_{i+1}^{+}. \tag{A.10b}$$

To locally construct $\boldsymbol{S}_i^{i+1}$, all terms involving δt are expanded to their first-order approximation in the vicinity of the event:

$$\boldsymbol{x}_i(\bar{t}_{i+1} + \varepsilon\delta t) = \underbrace{\boldsymbol{x}_i(\bar{t}_{i+1})}_{=\boldsymbol{x}_i^{-}} + \boldsymbol{f}_i^{-}\varepsilon\delta t + \mathcal{O}(\varepsilon^2), \tag{A.11a}$$

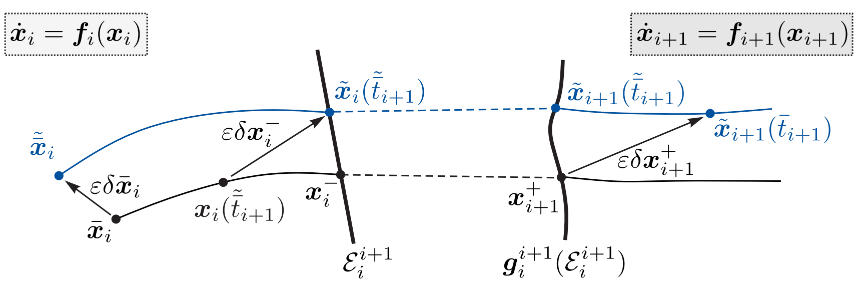

Figure A.3: Illustration of a perturbed flow reaching the event manifold $\mathcal{E}_i^{i+1}$ at time $\tilde{\bar{t}}_{i+1}$ earlier than the nominal flow, resulting in $\varepsilon\delta t := \tilde{\bar{t}}_{i+1} - \bar{t}_{i+1} < 0$.

$$\begin{aligned} e_i^{i+1}\big(\tilde{\boldsymbol{x}}_i(\bar{t}_{i+1}+\varepsilon\delta t)\big) &\overset{\text{(A.10a)}}{=} e_i^{i+1}\big(\boldsymbol{x}_i(\bar{t}_{i+1}+\varepsilon\delta t)+\varepsilon\delta\boldsymbol{x}_i^-\big) \\ &\overset{\text{(A.11a)}}{=} e_i^{i+1}\big(\boldsymbol{x}_i^- +\varepsilon\delta\boldsymbol{x}_i^- +\boldsymbol{f}_i^-\varepsilon\delta t\big)+\mathcal{O}(\varepsilon^2) \\ &= \underbrace{e_i^{i+1}(\boldsymbol{x}_i^-)}_{=0} + De_i^{i+1}\cdot\big(\varepsilon\delta\boldsymbol{x}_i^- +\boldsymbol{f}_i^-\varepsilon\delta t\big)+\mathcal{O}(\varepsilon^2), \end{aligned} \tag{A.11b}$$

$$\begin{aligned} \tilde{\boldsymbol{x}}_{i+1}(\bar{t}_{i+1}+\varepsilon\delta t) &= \tilde{\boldsymbol{x}}_{i+1}(\bar{t}_{i+1})+\boldsymbol{f}_{i+1}\big(\tilde{\boldsymbol{x}}_{i+1}(\bar{t}_{i+1})\big)\varepsilon\delta t+\mathcal{O}(\varepsilon^2) \\ &\overset{\text{(A.10b)}}{=} \boldsymbol{x}_{i+1}^+ +\varepsilon\delta\boldsymbol{x}_{i+1}^+ +\boldsymbol{f}_{i+1}\big(\boldsymbol{x}_{i+1}^+ +\varepsilon\delta\boldsymbol{x}_{i+1}^+\big)\varepsilon\delta t+\mathcal{O}(\varepsilon^2) \\ &= \boldsymbol{x}_{i+1}^+ +\varepsilon\delta\boldsymbol{x}_{i+1}^+ \underbrace{\boldsymbol{f}_{i+1}\big(\boldsymbol{x}_{i+1}^+\big)}_{=\boldsymbol{f}_{i+1}^+}\varepsilon\delta t+\mathcal{O}(\varepsilon^2), \end{aligned} \tag{A.11c}$$

$$\begin{aligned} \tilde{\boldsymbol{x}}_{i+1}(\bar{t}_{i+1}+\varepsilon\delta t) &= \boldsymbol{g}_i^{i+1}\big(\tilde{\boldsymbol{x}}_i(\bar{t}_{i+1}+\varepsilon\delta t)\big) \\ &\overset{\text{(A.10a)}}{=} \boldsymbol{g}_i^{i+1}\big(\boldsymbol{x}_i(\bar{t}_{i+1}+\varepsilon\delta t)+\varepsilon\delta\boldsymbol{x}_i^-\big) \\ &\overset{\text{(A.11a)}}{=} \boldsymbol{g}_i^{i+1}\big(\boldsymbol{x}_i^- +\varepsilon\delta\boldsymbol{x}_i^- +\boldsymbol{f}_i^-\varepsilon\delta t\big)+\mathcal{O}(\varepsilon^2) \\ &= \underbrace{\boldsymbol{g}_i^{i+1}(\boldsymbol{x}_i^-)}_{=\boldsymbol{x}_{i+1}^+} + \boldsymbol{G}_i^{i+1}\big(\varepsilon\delta\boldsymbol{x}_i^- +\boldsymbol{f}_i^-\varepsilon\delta t\big), +\mathcal{O}(\varepsilon^2). \end{aligned} \tag{A.11d}$$

Combining (A.11c) and (A.11d) and taking the limit as $\varepsilon \to 0$, the post-event state difference (A.10b) can be expanded to first order, as previously shown in (A.8). When the perturbed flow reaches the event manifold, it satisfies $e_i^{i+1}\big(\tilde{\boldsymbol{x}}_i(\bar{t}_{i+1}+\delta t)\big) = 0$, resulting in a time variation δt of the same form as in (A.8). Consequently, the remaining steps for constructing the saltation matrix $\boldsymbol{S}_i^{i+1} = {}^{\delta\boldsymbol{x}_{i+1}^+}/_{\delta\boldsymbol{x}_i^-}$ follow the same procedure as in the previous case.

A.2 Poincaré Section

In Chapter 4, the Poincaré section was defined within the returning phase $m+1 = 1$. However, the anchor can also be assigned to the last event $a := e_m^1$ as in Chapters 6 and 7, assuming that the event manifolds $\mathcal{E}_i^{i+1}$ share the same transversality to the flow (Assumption *As2*) as the Poincaré section $\mathcal{A}$. With this choice, a hybrid trajectory $\boldsymbol{x}(t_{m+1}^{\mathcal{A}})$ terminates immediately after the discrete transition $\boldsymbol{g}_m^1$, returning to the first phase such that $t_{m+1}^{\mathcal{A}} = t_m^{\mathcal{E}}$. Consequently, the initial state $\boldsymbol{x}_0$ must lie within $\boldsymbol{g}_m^1(\mathcal{E}_m^1) \subseteq \mathcal{X}_0$. This also modifies the structure of the Poincaré map's Jacobian, as defined in (4.13). While the fundamental matrix in phase m keeps its chained structure in (4.8), the last saltation matrix $\boldsymbol{S}_m^{m+1}$ drops the term $\boldsymbol{f}_{m+1}^{+}$ in (4.7), resulting in

$$\tilde{\boldsymbol{S}}_m^{m+1} = \tilde{\boldsymbol{S}}_m^{1} = \boldsymbol{G}_m^{1} \left(\boldsymbol{I} - \frac{\boldsymbol{f}_m^{-} D e_m^{1}}{D e_m^{1} \boldsymbol{f}_m^{-}} \right). \tag{A.12}$$

Hence, with the choice $a := e_m^1$, the Poincaré map's Jacobian takes the form

$$\begin{aligned} D\boldsymbol{P}(\boldsymbol{x}_0) = \tilde{\boldsymbol{S}}_m^{1} \cdot \boldsymbol{\Phi}_m(\underbrace{t_m^{\mathcal{E}}(\bar{\boldsymbol{x}}_m)}_{=\bar{t}_{m+1}}, \bar{t}_m, \bar{\boldsymbol{x}}_m) \\ \cdot \prod_{i=1}^{m-1} \boldsymbol{S}_i^{i+1} \cdot \boldsymbol{\Phi}_i(\bar{t}_{i+1}, \bar{t}_i, \bar{\boldsymbol{x}}_i). \end{aligned} \tag{A.13}$$

The qualitative results reported in Chapters 4 and 5 remain unaffected by this modified Poincaré map and its Jacobian.

PhD Publications

[1] Maximilian Raff, Nelson Rosa, and C. David Remy. Connecting gaits in energetically conservative legged systems. *IEEE Robotics and Automation Letters*, 7(3):8407–8414, 2022. doi: 10.1109/LRA.2022.3186500.

[2] Maximilian Raff, Nelson Rosa, and C. David Remy. Generating families of optimally actuated gaits from a legged system's energetically conservative dynamics. In *2022 IEEE/RSJ International Conference on Intelligent Robots and Systems (IROS)*. IEEE, October 2022. doi: 10.1109/iros47612.2022.9981693.

[3] Maximilian Raff and C. David Remy. Continuation of periodic orbits in conservative hybrid dynamical systems and its application to mechanical systems with impulsive dynamics. *Nonlinear Dynamics*, January 2025. ISSN 1573-269X. doi: 10.1007/s11071-024-10565-3.

[4] Maximilian Raff, Kathrin Flaßkamp, and C. David Remy. The indirect method for generating libraries of optimal periodic trajectories and its application to economical bipedal walking, 2024. `https://doi.org/10.48550/arXiv.2410.09512`.

Bibliography

[1] M. Abou-Taleb, M. Raff, K. Flaßkamp, and C. D. Remy. Koopman based trajectory optimization with mixed boundaries. In *Proceedings of the 7th Annual Learning for Dynamics & Control Conference (L4DC)*, volume 283 of *Proceedings of Machine Learning Research*, pages 1565–1577. PMLR, 04–06 Jun 2025. URL `https://proceedings.mlr.press/v283/abou-taleb25a.html`.

[2] A. Albu-Schäffer and C. D. Santina. A review on nonlinear modes in conservative mechanical systems. *Annual Reviews in Control*, 50:49–71, 2020. doi: 10.1016/j.arcontrol.2020.10.002.

[3] R. Alexander and A. Jayes. Fourier analysis of forces exerted in walking and running. *Journal of Biomechanics*, 13(4):383–390, Jan. 1980. ISSN 0021-9290. doi: 10.1016/0021-9290(80)90019-6.

[4] R. M. Alexander. Optimum walking techniques for quadrupeds and bipeds. *Journal of Zoology*, 192(1):97–117, Sept. 1980. ISSN 1469-7998. doi: 10.1111/j.1469-7998.1980.tb04222.x.

[5] R. M. Alexander. Simple models of human movement. *Applied Mechanics Reviews*, 48(8):461–470, Aug. 1995. ISSN 2379-0407. doi: 10.1115/1.3005107.

[6] E. L. Allgower and K. Georg. *Introduction to numerical continuation methods*. Society for Industrial and Applied Mathematics, Jan. 2003. doi: 10.1137/1.9780898719154.

[7] A. Ames and S. Sastry. Hybrid cotangent bundle reduction of simple hybrid mechanical systems with symmetry. In *2006 American Control Conference*. IEEE, 2006. doi: 10.1109/acc.2006.1656622.

[8] A. Ames and S. Sastry. Hybrid routhian reduction of lagrangian hybrid systems. In *2006 American Control Conference*. IEEE, 2006. doi: 10.1109/acc.2006.1656621.

[9] A. Ames, A. Abate, and S. Sastry. Sufficient conditions for the existence of zeno behavior. In *Proceedings of the 44th IEEE Conference on Decision and Control*. IEEE, 2005. doi: 10.1109/cdc.2005.1582237.

[10] A. D. Ames. *A categorical theory of hybrid systems*. Phd thesis, Citeseer, 2006. URL `http://ames.caltech.edu/A%20categorical%20theory.pdf`.

[11] V. I. Arnold. *Ordinary differential equations*. Springer Berlin, Heidelberg, May 1992.

[12] F. Asano, M. Yamakita, N. Kamamichi, and Z.-W. Luo. A novel gait generation for biped walking robots based on mechanical energy constraint. *IEEE Transactions on Robotics and Automation*, 20(3): 565–573, June 2004. ISSN 1042-296X. doi: 10.1109/tra.2004.824685.

[13] R. Bellman. *Dynamic programming*. Princeton Univ. Pr., Princeton, NJ, 1957. ISBN 069107951X.

[14] J. T. Betts. *Practical methods for optimal control and estimation using nonlinear programming*. Society for Industrial and Applied Mathematics, Jan. 2010. ISBN 9780898718577. doi: 10.1137/1.9780898718577.

[15] F. Bizzarri, A. Colombo, F. Dercole, and G. S. Gajani. Necessary and sufficient conditions for the noninvertibility of fundamental solution matrices of a discontinuous system. *SIAM Journal on Applied Dynamical Systems*, 15(1):84–105, Jan. 2016. doi: 10.1137/140959031.

[16] R. Blickhan. The spring-mass model for running and hopping. *Journal of Biomechanics*, 22(11-12):1217–1227, Jan. 1989. doi: 10.1016/0021-9290(89)90224-8.

[17] K. E. Brenan, S. L. Campbell, and L. R. Petzold. *Numerical solution of initial-value problems in differential-algebraic equations*. Society for Industrial and Applied Mathematics, Jan. 1995. ISBN 9781611971224. doi: 10.1137/1.9781611971224.

[18] J. Breuling. Projected and partitioned runge-kutta methods for nonsmooth mechanical systems with frictional contact and impacts, 2024.

[19] B. Brogliato. *Nonsmooth Mechanics: Models, Dynamics and Control*. Springer International Publishing, 2016. ISBN 9783319286648. doi: 10.1007/978-3-319-28664-8.

[20] S. A. Burden, S. S. Sastry, D. E. Koditschek, and S. Revzen. Event–selected vector field discontinuities yield piecewise–differentiable flows. *SIAM Journal on Applied Dynamical Systems*, 15(2):1227–1267, Jan. 2016. doi: 10.1137/15m1016588.

[21] S. A. Burden, T. Libby, K. Jayaram, S. Sponberg, and J. M. Donelan. Why animals can outrun robots. *Science Robotics*, 9(89), Apr. 2024. ISSN 2470-9476. doi: 10.1126/scirobotics.adi9754.

[22] G. A. Cavagna, H. Thys, and A. Zamboni. The sources of external work in level walking and running. *The Journal of Physiology*, 262(3):639–657, Nov. 1976. ISSN 1469-7793. doi: 10.1113/jphysiol.1976.sp011613.

[23] P. H. Channon, S. H. Hopkins, and D. T. Pham. A variational approach to the optimization of gait for a bipedal robot. *Proceedings of the Institution of Mechanical Engineers, Part C: Journal of Mechanical Engineering Science*, 210(2):177–186, Mar. 1996. ISSN 2041-2983. doi: 10.1243/pime_proc_1996_210_184_02.

[24] A. E. Charalampakis, G. C. Tsiatas, and P. Tsopelas. New insights on rocking of rigid blocks: Analytical solutions and exact energy-based overturning criteria. *Earthquake Engineering & Structural Dynamics*, 51(9):1965–1993, Apr. 2022. doi: 10.1002/eqe.3649.

[25] A. Chatterjee, R. Pratap, C. Reddy, and A. Ruina. Persistent passive hopping and juggling is possible even with plastic collisions. *The International Journal of Robotics Research*, 21(7):621–634, July 2002. ISSN 1741-3176. doi: 10.1177/027836402322023213.

[26] A. Cherubini, A. Papini, R. Vertechy, and M. Fontana. Airborne wind energy systems: A review of the technologies. *Renewable and Sustainable Energy Reviews*, 51:1461–1476, Nov. 2015. ISSN 1364-0321. doi: 10.1016/j.rser.2015.07.053.

[27] C. L. Colin Christopher. *Limit cycles of differential equations*. Birkhäuser Basel, 1 edition, 2007. ISBN 9783764384098. doi: 10.1007/978-3-7643-8410-4.

[28] S. Collins, A. Ruina, R. Tedrake, and M. Wisse. Efficient bipedal robots based on passive-dynamic walkers. *Science*, 307(5712):1082–1085, Feb. 2005. ISSN 1095-9203. doi: 10.1126/science.1107799.

[29] L. J. Colombo and M. E. E. Irazú. Symmetries and periodic orbits in simple hybrid routhian systems. *Nonlinear Analysis: Hybrid Systems*, 36:100857, May 2020. doi: 10.1016/j.nahs.2020.100857.

[30] K. de Payrebrune, K. Flaßkamp, T. Ströhla, T. Sattel, D. Bestle, B. Röder, P. Eberhard, S. Peitz, M. Stoffel, G. Rutwik, B. Aditya, M. Wohlleben, W. Sextro, M. Raff, C. D. Remy, M. Yadav, M. Stender, J. van Delden, T. Lüddecke, S. C. Langer, J. Schultz, and C. Blech. The impact of ai on engineering design procedures for dynamical systems. *Technische Mechanik*, 2025. doi: 10.24352/UB.OVGU-2025-037.

[31] E. Delassus. Mémoire sur la théorie des liaisons finies unilatérales. In *Annales scientifiques de l'École normale supérieure*, volume 34, pages 95–179, 1917.

[32] R. P. Dickinson and R. J. Gelinas. Sensitivity analysis of ordinary differential equation systems—a direct method. *Journal of Computational Physics*, 21(2):123–143, June 1976. doi: 10.1016/0021-9991(76)90007-3.

[33] L. Dieci and L. Lopez. Fundamental matrix solutions of piecewise smooth differential systems. *Mathematics and Computers in Simulation*, 81(5):932–953, Jan. 2011. doi: 10.1016/j.matcom.2010.10.012.

[34] M. Diehl, H. Bock, H. Diedam, and P.-B. Wieber. *Fast direct multiple shooting algorithms for optimal robot control*, pages 65–93. Springer Berlin Heidelberg, 2006. ISBN 9783540361183. doi: 10.1007/978-3-540-36119-0_4.

[35] E. J. Doedel, R. C. Paffenroth, H. B. Keller, D. J. Dichmann, J. Galán-Vioque, and A. Vanderbauwhede. Computation of periodic solutions of conservative systems with application to the 3-body problem. *International Journal of Bifurcation and Chaos*, 13(06):1353–1381, June 2003. doi: 10.1142/s0218127403007291.

[36] H. Ebel, J. van Delden, T. Lüddecke, A. Borse, R. Gulakala, M. Stoffel, M. Yadav, M. Stender, L. Schindler, K. M. de Payrebrune, M. Raff, C. D. Remy, B. Röder, and P. Eberhard. Data publishing in mechanics and dynamics: Challenges, guidelines, and examples from engineering design. *Data-Centric Engineering*, 6, 2025. doi: 10.1017/dce.2025.13.

[37] C. T. Farley and D. P. Ferris. 10 biomechanics of walking and running: Center of mass movements to muscle action. *Exercise and sport sciences reviews*, 26(1):253–286, 1998.

[38] Y. Feng, Z. Ji, Y. Gao, H. Zheng, and J. Tan. An energy-saving optimization method for cyclic pick-and-place tasks based on flexible joint configurations. *Robotics and Computer-Integrated Manufacturing*, 67:102037, Feb. 2021. ISSN 0736-5845. doi: 10.1016/j.rcim.2020.102037.

[39] R. P. Feynman. *The Meaning of It All: Thoughts of a Citizen Scientist*. Perseus Books, Reading, Mass., 1998. Original work by Richard Phillips Feynman, 1918–1988.

[40] Z. Fu, A. Kumar, J. Malik, and D. Pathak. Minimizing energy consumption leads to the emergence of gaits in legged robots, 2021.

[41] R. J. Full and D. E. Koditschek. Templates and anchors: neuromechanical hypotheses of legged locomotion on land. *Journal of Experimental Biology*, 202(23):3325–3332, Dec. 1999. ISSN 1477-9145. doi: 10.1242/jeb.202.23.3325.

[42] Z. Gan, Z. Jiao, and C. D. Remy. On the dynamic similarity between bipeds and quadrupeds: A case study on bounding. *IEEE Robotics and Automation Letters*, 3(4):3614–3621, Oct. 2018. ISSN 2377-3774. doi: 10.1109/lra.2018.2854923.

[43] Z. Gan, Y. Yesilevskiy, P. Zaytsev, and C. D. Remy. All common bipedal gaits emerge from a single passive model. *Journal of The Royal Society Interface*, 15(146):20180455, Sept. 2018. doi: 10.1098/rsif.2018.0455.

[44] M. Garcia, A. Chatterjee, A. Ruina, and M. Coleman. The simplest walking model: stability, complexity, and scaling. *Journal of Biomechanical Engineering*, 120(2):281–288, Apr. 1998. ISSN 1528-8951. doi: 10.1115/1.2798313.

[45] M. Geilinger, D. Hahn, J. Zehnder, M. Bächer, B. Thomaszewski, and S. Coros. Add: analytically differentiable dynamics for multi-body systems with frictional contact. *ACM Transactions on Graphics*, 39(6): 1–15, Nov. 2020. ISSN 1557-7368. doi: 10.1145/3414685.3417766.

[46] E. Gilbert and D. Lyons. The improvement of aircraft specific range by periodic control. In *Guidance and Control Conference*. American Institute of Aeronautics and Astronautics, Aug. 1981. doi: 10.2514/6.1981-1748.

[47] R. Goebel, R. G. Sanfelice, and A. R. Teel. Hybrid dynamical systems. *IEEE Control Systems*, 29(2):28–93, Apr. 2009. doi: 10.1109/mcs.2008.931718.

[48] M. W. Gomes. *Collisionless rigid body locomotion models and physically based homotopy methods for finding periodic motions in high degree of freedom models*. Cornell University, 2005.

[49] G. Gorni and G. Zampieri. Revisiting noether's theorem on constants of motion. *Journal of Nonlinear Mathematical Physics*, 21(1):43, 2021. doi: 10.1080/14029251.2014.894720.

[50] G. Gorni, M. Scomparin, and G. Zampieri. Nonlocal constants of motion in lagrangian dynamics of any order. *Partial Differential Equations in Applied Mathematics*, 5:100262, June 2022. doi: 10.1016/j.padiff.2022.100262.

[51] A. Goswami, B. Espiau, and A. Keramane. Limit cycles in a passive compass gait biped and passivity-mimicking control laws. *Autonomous Robots*, 4(3):273–286, 1997. ISSN 0929-5593. doi: 10.1023/a:1008844026298.

[52] J. W. Grizzle, C. Chevallereau, R. W. Sinnet, and A. D. Ames. Models, feedback control, and open problems of 3d bipedal robotic walking. *Automatica*, 50(8):1955–1988, Aug. 2014. doi: 10.1016/j.automatica.2014.04.021.

[53] J. Guddat, F. G. Vazquez, and H. T. Jongen. *Parametric optimization: Singularities, pathfollowing and jumps*. Vieweg+Teubner Verlag, 1990. ISBN 9783663121602. doi: 10.1007/978-3-663-12160-2.

[54] E. Hairer, M. Roche, and C. Lubich. *The numerical solution of differential-algebraic systems by Runge-Kutta methods*. Springer Berlin Heidelberg, 1989. ISBN 9783540468325. doi: 10.1007/bfb0093947.

[55] P. Hartman. *Ordinary differential equations*. Society for Industrial and Applied Mathematics, Jan. 2002. doi: 10.1137/1.9780898719222.

[56] S. Heim, M. Millard, C. Le Mouel, and A. Badri-Spröwitz. A little damping goes a long way: a simulation study of how damping influences task-level stability in running. *Biology Letters*, 16(9):20200467, Sept. 2020. ISSN 1744-957X. doi: 10.1098/rsbl.2020.0467.

[57] M. E. Henderson. Multiple parameter continuation: Computing implicitly defined k-manifolds. *International Journal of Bifurcation and Chaos*, 12(03):451–476, Mar. 2002. doi: 10.1142/s0218127402004498.

[58] H. M. Herr and A. M. Grabowski. Bionic ankle–foot prosthesis normalizes walking gait for persons with leg amputation. *Proceedings of the Royal Society B: Biological Sciences*, 279(1728):457–464, July 2011. ISSN 1471-2954. doi: 10.1098/rspb.2011.1194.

[59] M. Hildebrand. The adaptive significance of tetrapod gait selection. *American Zoologist*, 20(1):255–267, Feb. 1980. ISSN 0003-1569. doi: 10.1093/icb/20.1.255.

[60] M. Hildebrand. The quadrupedal gaits of vertebrates. *BioScience*, 39 (11):766–775, Dec. 1989. ISSN 1525-3244. doi: 10.2307/1311182.

[61] F. J. M. Horn and R. C. Lin. Periodic processes: A variational approach. *Industrial and Engineering Chemistry Process Design and Development*, 6(1):21–30, Jan. 1967. ISSN 1541-5716. doi: 10.1021/i260021a005.

[62] B. Houska and B. Chachuat. Branch-and-lift algorithm for deterministic global optimization in nonlinear optimal control. *Journal of Optimization Theory and Applications*, 162(1):208–248, Sept. 2013. ISSN 1573-2878. doi: 10.1007/s10957-013-0426-1.

[63] G. W. Housner. The behavior of inverted pendulum structures during earthquakes. *Bulletin of the Seismological Society of America*, 53(2): 403–417, Feb. 1963. ISSN 0037-1106. doi: 10.1785/bssa0530020403.

[64] D. F. Hoyt and C. R. Taylor. Gait and the energetics of locomotion in horses. *Nature*, 292(5820):239–240, July 1981. ISSN 1476-4687. doi: 10.1038/292239a0.

[65] M. Hutter, C. Gehring, D. Jud, A. Lauber, C. D. Bellicoso, V. Tsounis, J. Hwangbo, K. Bodie, P. Fankhauser, M. Bloesch, R. Diethelm, S. Bachmann, A. Melzer, and M. Hoepflinger. Anymal - a highly mobile and dynamic quadrupedal robot. In *2016 IEEE/RSJ International Conference on Intelligent Robots and Systems (IROS)*, pages 38–44. IEEE, Oct. 2016. doi: 10.1109/iros.2016.7758092.

[66] S. Hyon and T. Emura. Symmetric walking control: invariance and global stability. In *Proceedings of the 2005 IEEE International Conference on Robotics and Automation*. IEEE, 2005. doi: 10.1109/robot.2005.1570318.

[67] A. Isidori. *Nonlinear control systems*. Springer London, 1995. ISBN 9781846286155. doi: 10.1007/978-1-84628-615-5.

[68] A. M. Johnson, S. A. Burden, and D. E. Koditschek. A hybrid systems model for simple manipulation and self-manipulation systems. *The International Journal of Robotics Research*, 35(11):1354–1392, May 2016. doi: 10.1177/0278364916639380.

[69] S. Kajita, F. Kanehiro, K. Kaneko, K. Yokoi, and H. Hirukawa. The 3d linear inverted pendulum mode: a simple modeling for a biped walking pattern generation. In *Proceedings 2001 IEEE/RSJ International Conference on Intelligent Robots and Systems. Expanding the Societal Role of Robotics in the the Next Millennium (Cat. No.01CH37180)*, volume 1 of *IROS-01*, pages 239–246. IEEE, 1995. doi: 10.1109/iros.2001.973365.

[70] D. Kalman. Leveling with lagrange: An alternate view of constrained optimization. *Mathematics Magazine*, 82(3):186–196, June 2009. ISSN 1930-0980. doi: 10.1080/0025570x.2009.11953617.

[71] H. B. Keller. Lectures on numerical methods in bifurcation problems, 1987. URL `https://www.math.tifr.res.in/~publ/ln/tifr79.pdf`.

[72] M. Kelly. An introduction to trajectory optimization: How to do your own direct collocation. *SIAM Review*, 59(4):849–904, Jan. 2017. ISSN 1095-7200. doi: 10.1137/16m1062569.

[73] G. Kerschen, M. Peeters, J. Golinval, and A. Vakakis. Nonlinear normal modes, part i: A useful framework for the structural dynamicist. *Mechanical Systems and Signal Processing*, 23(1):170–194, Jan. 2009. doi: 10.1016/j.ymssp.2008.04.002.

[74] I. Khemakhem, D. Tschemernjak, M. Raff, and C. D. Remy. How leg stiffness affects energy economy in hopping. In *The 12th International Symposium on Adaptive Motion of Animals and Machines (AMAM2025) and 2nd LokoAssist Symposium*, 2025. doi: 10.48550/ARXIV.2501.03971.

[75] S. Kim and P. M. Wensing. Design of dynamic legged robots. *Foundations and Trends® in Robotics*, 5(2):117–190, 2017. ISSN 1935-8261. doi: 10.1561/2300000044.

[76] N. J. Kong, J. J. Payne, J. Zhu, and A. M. Johnson. Saltation matrices: The essential tool for linearizing hybrid dynamical systems. *Proceedings of the IEEE*, pages 1–24, 2024. ISSN 1558-2256. doi: 10.1109/jproc.2024.3440211.

[77] D. B. Kowalsky, J. R. Rebula, L. V. Ojeda, P. G. Adamczyk, and A. D. Kuo. Human walking in the real world: Interactions between terrain type, gait parameters, and energy expenditure. *PLOS ONE*, 16 (1):e0228682, Jan. 2021. ISSN 1932-6203. doi: 10.1371/journal.pone.0228682.

[78] V. V. Kozlov. First integrals and asymptotic trajectories. *Sbornik: Mathematics*, 211(1):29–54, Jan. 2020. doi: 10.1070/sm9291.

[79] M. Krack. Nonlinear modal analysis of nonconservative systems: Extension of the periodic motion concept. *Computers & Structures*, 154:59–71, July 2015. ISSN 0045-7949. doi: 10.1016/j.compstruc.2015.03.008.

[80] A. Kuo. Choosing your steps carefully. *IEEE Robotics & Automation Magazine*, 14(2):18–29, June 2007. ISSN 1070-9932. doi: 10.1109/mra.2007.380653.

[81] J. S. Lamb and J. A. Roberts. Time-reversal symmetry in dynamical systems: A survey. *Physica D: Nonlinear Phenomena*, 112(1-2):1–39, Jan. 1998. doi: 10.1016/s0167-2789(97)00199-1.

[82] R. I. Leine and H. Nijmeijer. *Dynamics and bifurcations of non-smooth mechanical systems*. Springer Berlin Heidelberg, 2004. doi: 10.1007/978-3-540-44398-8.

[83] D. Liberzon. *Calculus of variations and optimal control theory: A concise introduction*. Princeton University Press, Dec. 2011. ISBN 9780691151878. doi: 10.2307/j.ctvcm4g0s.

[84] Q. Lin, R. Loxton, and K. Lay Teo. The control parameterization method for nonlinear optimal control: A survey. *Journal of Industrial & Management Optimization*, 10(1):275–309, 2014. ISSN 1553-166X. doi: 10.3934/jimo.2014.10.275.

[85] C. Liu and C. G. Atkeson. Standing balance control using a trajectory library. In *2009 IEEE/RSJ International Conference on Intelligent Robots and Systems*. IEEE, Oct. 2009. doi: 10.1109/iros.2009.5354018.

[86] C. Liu, C. G. Atkeson, and J. Su. Biped walking control using a trajectory library. *Robotica*, 31(2):311–322, May 2012. ISSN 1469-8668. doi: 10.1017/s0263574712000203.

[87] E. N. Lorenz. On the existence of a slow manifold. *Journal of the Atmospheric Sciences*, 43(15):1547–1558, Aug. 1986. ISSN 1520-0469. doi: 10.1175/1520-0469(1986)043<1547:oteoas>2.0.co;2.

[88] D. G. Luenberger. *Optimization by vector space methods*. John Wiley & Sons, 1997.

[89] D. G. Luenberger and Y. Ye. *Linear and nonlinear programming*. Springer International Publishing, 2021. ISBN 9783030854508. doi: 10.1007/978-3-030-85450-8.

[90] I. R. Manchester, M. M. Tobenkin, M. Levashov, and R. Tedrake. Regions of attraction for hybrid limit cycles of walking robots. *IFAC Proceedings Volumes*, 44(1):5801–5806, Jan. 2011. doi: 10.3182/20110828-6-it-1002.03069.

[91] Z. Manchester and S. Kuindersma. *Variational contact-implicit trajectory optimization*, pages 985–1000. Springer International Publishing, Nov. 2019. ISBN 9783030286194. doi: 10.1007/978-3-030-28619-4_66.

[92] T. McGeer. Passive dynamic walking. *The International Journal of Robotics Research*, 9(2):62–82, Apr. 1990. ISSN 1741-3176. doi: 10.1177/027836499000900206.

[93] T. A. McMahon, G. Valiant, and E. C. Frederick. Groucho running. *Journal of Applied Physiology*, 62(6):2326–2337, June 1987. ISSN 1522-1601. doi: 10.1152/jappl.1987.62.6.2326.

[94] I. Mordatch, E. Todorov, and Z. Popović. Discovery of complex behaviors through contact-invariant optimization. *ACM Transactions on Graphics*, 31(4):1–8, July 2012. ISSN 1557-7368. doi: 10.1145/2185520.2185539.

[95] J. Moreau. Numerical aspects of the sweeping process. *Computer Methods in Applied Mechanics and Engineering*, 177(3–4):329–349, July 1999. ISSN 0045-7825. doi: 10.1016/s0045-7825(98)00387-9.

[96] P. C. Müller. Calculation of lyapunov exponents for dynamic systems with discontinuities. *Chaos, Solitons & Fractals*, 5(9):1671–1681, Sept. 1995. doi: 10.1016/0960-0779(94)00170-u.

[97] F. Muñoz-Almaraz, E. Freire, J. Galán, E. Doedel, and A. Vanderbauwhede. Continuation of periodic orbits in conservative and hamiltonian systems. *Physica D: Nonlinear Phenomena*, 181(1-2):1–38, July 2003. doi: 10.1016/s0167-2789(03)00097-6.

[98] R. Naz, I. L. Freire, and I. Naeem. Comparison of different approaches to construct first integrals for ordinary differential equations. *Abstract and Applied Analysis*, 2014:1–15, 2014. doi: 10.1155/2014/978636.

[99] M. Neunert, F. Farshidian, A. W. Winkler, and J. Buchli. Trajectory optimization through contacts and automatic gait discovery for quadrupeds. *IEEE Robotics and Automation Letters*, 2(3):1502–1509, July 2017. ISSN 2377-3774. doi: 10.1109/lra.2017.2665685.

[100] S. M. O'Connor. *The relative roles of dynamics and control in bipedal locomotion.* PhD thesis, University of Michigan, 2009.

[101] J. M. Ortega and W. C. Rheinboldt. *Iterative solution of nonlinear equations in several variables.* Society for Industrial and Applied Mathematics, Jan. 2000. doi: 10.1137/1.9780898719468.

[102] D. Owaki, M. Koyama, S. Yamaguchi, S. Kubo, and A. Ishiguro. A 2-d passive-dynamic-running biped with elastic elements. *IEEE Transactions on Robotics*, 27(1):156–162, Feb. 2011. ISSN 1941-0468. doi: 10.1109/tro.2010.2098610.

[103] A. M. Pace and S. A. Burden. Piecewise - differentiable trajectory outcomes in mechanical systems subject to unilateral constraints. In *Proceedings of the 20th International Conference on Hybrid Systems: Computation and Control.* ACM, Apr. 2017. doi: 10.1145/3049797.3049807.

[104] F. Pfeiffer and C. Glocker. *Multibody dynamics with unilateral contacts.* Wiley, Aug. 1996. ISBN 9783527618385. doi: 10.1002/9783527618385.

[105] L. Piegl and W. Tiller. *The NURBS book.* Springer Berlin Heidelberg, 1997. ISBN 9783642592232. doi: 10.1007/978-3-642-59223-2.

[106] H. Poincaré. *Thermodynamique: Leçons professées pendant le premier semestre 1888-89.* Sciences. Hachette Livre - BNF, 1908.

[107] L. Pontryagin. *Mathematical theory of optimal processes.* Routledge, May 1987. ISBN 9780203749319. doi: 10.1201/9780203749319.

[108] L. S. Pontryagin. Ordinary differential equations. *Addison-Wesley*, 1962.

[109] M. Posa, C. Cantu, and R. Tedrake. A direct method for trajectory optimization of rigid bodies through contact. *The International Journal of Robotics Research*, 33(1):69–81, Oct. 2013. ISSN 1741-3176. doi: 10.1177/0278364913506757.

[110] M. Raff and C. D. Remy. Hard vs. soft contacts in trajectory optimization of legged robots: An example with a compliant rubber foot. In *Embracing Contacts-Workshop at ICRA 2023*, 2023.

[111] J. Reher and A. D. Ames. Inverse dynamics control of compliant hybrid zero dynamic walking. In *2021 IEEE International Conference on Robotics and Automation (ICRA)*. IEEE, May 2021. doi: 10.1109/icra48506.2021.9560906.

[112] C. D. Remy, K. Buffinton, and R. Siegwart. Comparison of cost functions for electrically driven running robots. In *2012 IEEE International Conference on Robotics and Automation*, pages 2343–2350. IEEE, May 2012. doi: 10.1109/icra.2012.6224960.

[113] Remy, C. David. *Optimal exploitation of natural dynamics in legged locomotion*. PhD thesis, ETH Zurich, 2011.

[114] T. J. Roberts and E. Azizi. Flexible mechanisms: the diverse roles of biological springs in vertebrate movement. *Journal of Experimental Biology*, 214(3):353–361, Feb. 2011. ISSN 0022-0949. doi: 10.1242/jeb.038588.

[115] N. Rosa and K. M. Lynch. Extending equilibria to periodic orbits for walkers using continuation methods. In *2014 IEEE/RSJ International Conference on Intelligent Robots and Systems*. IEEE, Sept. 2014. doi: 10.1109/iros.2014.6943076.

[116] N. Rosa and K. M. Lynch. A topological approach to gait generation for biped robots. *IEEE Transactions on Robotics*, 38(2):699–718, Apr. 2022. ISSN 1941-0468. doi: 10.1109/tro.2021.3094159.

[117] N. Rosa, B. Katamish, M. Raff, and C. D. Remy. An approach for generating families of energetically optimal gaits from passive dynamic walking gaits. In *2023 IEEE/RSJ International Conference on Intelligent Robots and Systems (IROS)*. IEEE, Oct. 2023. doi: 10.1109/iros55552.2023.10342322.

[118] U. J. Römer. *Über den Einfluss der Fußgeometrie auf die Energieeffizienz beim zweibeinigen Gehen*. PhD thesis, KIT Scientific Publishing, 2019.

[119] G. Sachs, J. Lenz, and F. Holzapfel. Periodic optimal control for range maximization of powered sailplanes with retractable electric motor. In *AIP Conference Proceedings*, pages 830–837. AIP, 2012. doi: 10.1063/1.4765584.

[120] A. Sachtler, D. Calzolari, M. Raff, A. Schmidt, Y. P. Wotte, C. D. Santina, C. D. Remy, and A. Albu-Schäffer. Swing-up of a weakly actuated double pendulum via nonlinear normal modes. In *2024 European Control Conference (ECC)*, pages 2392–2398. IEEE, June 2024. doi: 10.23919/ecc64448.2024.10590854.

[121] C. D. Santina, D. Calzolari, A. M. Giordano, and A. Albu-Schaffer. Actuating eigenmanifolds of conservative mechanical systems via bounded or impulsive control actions. *IEEE Robotics and Automation Letters*, 6(2):2783–2790, Apr. 2021. doi: 10.1109/lra.2021.3061391.

[122] E. Schumann, N. Smit-Anseeuw, P. Zaytsev, R. Gleason, K. A. Shorter, and C. D. Remy. Effects of foot stiffness and damping on walking robot performance. In *2019 International Conference on Robotics and Automation (ICRA)*, pages 3698–3704. IEEE, May 2019. doi: 10.1109/icra.2019.8794050.

[123] B. Sengupta, K. Friston, and W. Penny. Efficient gradient computation for dynamical models. *NeuroImage*, 98:521–527, Sept. 2014. ISSN 1053-8119. doi: 10.1016/j.neuroimage.2014.04.040.

[124] J.-A. Sepulchre and R. S. MacKay. Localized oscillations in conservative or dissipative networks of weakly coupled autonomous oscillators. *Nonlinearity*, 10(3):679–713, May 1997. doi: 10.1088/0951-7715/10/3/006.

[125] L. Shampine and S. Thompson. Event location for ordinary differential equations. *Computers & Mathematics with Applications*, 39(5-6):43–54, Mar. 2000. doi: 10.1016/s0898-1221(00)00045-6.

[126] N. Smit-Anseeuw, R. Gleason, R. Vasudevan, and C. D. Remy. The energetic benefit of robotic gait selection—a case study on the robot ram*one*. *IEEE Robotics and Automation Letters*, 2(2):1124–1131, Apr. 2017. ISSN 2377-3774. doi: 10.1109/lra.2017.2661801.

[127] N. Smit-Anseeuw, R. Gleason, P. Zaytsev, and C. David Remy. Ramone: A planar biped for studying the energetics of gait. In *2017 IEEE/RSJ International Conference on Intelligent Robots and Systems*

(IROS), pages 4090–4095. IEEE, Sept. 2017. doi: 10.1109/iros.2017.8206266.

[128] W. A. Sparrow and K. M. Newell. Metabolic energy expenditure and the regulation of movement economy. *Psychonomic Bulletin & Review*, 5(2):173–196, June 1998. ISSN 1531-5320. doi: 10.3758/bf03212943.

[129] J. Speyer and R. Evans. A second variational theory for optimal periodic processes. *IEEE Transactions on Automatic Control*, 29(2): 138–148, Feb. 1984. ISSN 0018-9286. doi: 10.1109/tac.1984.1103482.

[130] J. L. Speyer. Periodic optimal flight. *Journal of Guidance, Control, and Dynamics*, 19(4):745–755, July 1996. ISSN 1533-3884. doi: 10.2514/3.21695.

[131] M. W. Spong. Passivity based control of the compass gait biped. *IFAC Proceedings Volumes*, 32(2):506–510, July 1999. ISSN 1474-6670. doi: 10.1016/s1474-6670(17)56086-3.

[132] D. E. Stewart and J. C. Trinkle. An implicit time-stepping scheme for rigid body dynamics with inelastic collisions and coulomb friction. *International Journal for Numerical Methods in Engineering*, 39(15):2673–2691, Aug. 1996. ISSN 1097-0207. doi: 10.1002/(sici)1097-0207(19960815)39:15<2673::aid-nme972>3.0.co;2-i.

[133] Y. Tassa, N. Mansard, and E. Todorov. Control-limited differential dynamic programming. In *2014 IEEE International Conference on Robotics and Automation (ICRA)*, pages 1168–1175. IEEE, May 2014. doi: 10.1109/icra.2014.6907001.

[134] R. Tedrake, T. Zhang, M. fai Fong, and H. Seung. Actuating a simple 3d passive dynamic walker. In *IEEE International Conference on Robotics and Automation, 2004. Proceedings. ICRA '04. 2004*, pages 4656–4661 Vol.5. IEEE, 2004. doi: 10.1109/robot.2004.1302452.

[135] P. M. Wensing, M. Posa, Y. Hu, A. Escande, N. Mansard, and A. D. Prete. Optimization-based control for dynamic legged robots. *IEEE Transactions on Robotics*, 40:43–63, 2024. ISSN 1941-0468. doi: 10.1109/tro.2023.3324580.

[136] E. Westervelt, J. Grizzle, and D. Koditschek. Hybrid zero dynamics of planar biped walkers. *IEEE Transactions on Automatic Control*, 48(1):42–56, Jan. 2003. doi: 10.1109/tac.2002.806653.

[137] E. R. Westervelt, J. W. Grizzle, C. Chevallereau, J. H. Choi, and B. Morris. *Feedback control of dynamic bipedal robot locomotion.* CRC Press, Oct. 2018. doi: 10.1201/9781420053739.

[138] M. Wisse, A. L. Schwab, and F. C. T. van der Helm. Passive dynamic walking model with upper body. *Robotica*, 22(6):681–688, Nov. 2004. ISSN 1469-8668. doi: 10.1017/s0263574704000475.

[139] Y. Yesilevskiy, Z. Gan, and C. D. Remy. Optimal configuration of series and parallel elasticity in a 2d monoped. In *2016 IEEE International Conference on Robotics and Automation (ICRA)*, pages 1360–1365. IEEE, May 2016. doi: 10.1109/icra.2016.7487269.

[140] Y. Yesilevskiy, Z. Gan, and C. David Remy. Energy-optimal hopping in parallel and series elastic one-dimensional monopeds. *Journal of Mechanisms and Robotics*, 10(3), Apr. 2018. ISSN 1942-4310. doi: 10.1115/1.4039496.

[141] Y. Yesilevskiy, W. Yang, and C. D. Remy. Spine morphology and energetics: how principles from nature apply to robotics. *Bioinspiration & Biomimetics*, 13(3):036002, Mar. 2018. ISSN 1748-3190. doi: 10.1088/1748-3190/aaaa9e.

[142] P. Zaytsev, T. Cnops, and C. D. Remy. A detailed look at the SLIP model dynamics: Bifurcations, chaotic behavior, and fractal basins of attraction. *Journal of Computational and Nonlinear Dynamics*, 14(8), May 2019. doi: 10.1115/1.4043453.